

Interaction between galaxy clusters and jets from cluster member galaxies

J du Preez



orcid.org 0000-0002-0551-4954

Dissertation submitted in partial fulfilment of the requirements for the degree *Master of Science in Astrophysical Sciences* at the North-West University

Supervisor: Prof JO Chibueze

Co-supervisor: Dr S Chandra

Graduation: May 2025

Abstract

This dissertation presents an observational study of five galaxy clusters: Abell 133, Abell 3266, Abell 3376, Abell 3391, and Abell 3395, using radio observations from MeerKAT and X-ray observations from *XMM-Newton*. Through detailed imaging and spectral analysis, this study investigates the interactions between radio galaxies and the intracluster medium. In Abell 133, the lobe of a radio galaxy with an ultrasteep spectrum ($\alpha \sim 2.67$) undergoes re-acceleration in the cluster core. Abell 3266 hosts several bent-tailed radio galaxies, whose jet morphologies suggest strong ram pressure driven by the complex merging state of the cluster. The jets of MRC 0600−399 in Abell 3376 brighten and exhibit spectral flattening along the jets after bending approximately 90° in the same direction, with the northern bent jet tracing a cold front edge in the X-ray emission. In the Abell 3391–Abell 3395 system, both clusters have central radio galaxies with twisting and bending jets, indicative of interactions with the disturbed intracluster medium in this merging system. High-resolution MeerKAT images reveal filamentary structures associated with radio galaxies across all five clusters.

Keywords: galaxies: clusters: general – galaxies: clusters: intracluster medium – galaxies: jets – X-rays: galaxies: clusters – radio continuum: galaxies

Acknowledgements

I would like to thank everyone who supported me in writing this dissertation, including my supervisors, lecturers, colleagues, and friends. Most of all, thank you to my family. Without your love and encouragement, this would not have been possible.

This work is based on the research supported wholly by the National Research Foundation of South Africa (Grant Number 142153).

This research is based on observations obtained with MeerKAT and *XMM-Newton*. The MeerKAT telescope is operated by the South African Radio Astronomy Observatory, which is a facility of the National Research Foundation, an agency of the Department of Science and Innovation. *XMM-Newton* is an ESA science mission with instruments and contributions directly funded by ESA Member States and NASA.

Part of the data presented here has been reduced using the CARACal pipeline, partially supported by ERC Starting grant number 679627 "FORNAX", MAECI Grant Number ZA18GR02, DST-NRF Grant Number 113121 as part of the ISARP Joint Research Scheme, and BMBF project 05A17PC2 for D-MeerKAT. Information about CARACal can be obtained online under the URL: `https://caracal.readthedocs.io`.

I acknowledge the use of the ilifu cloud computing facility (`www.ilifu.ac.za`), a partnership between the University of Cape Town (UCT), the University of the Western Cape, Stellenbosch University, Sol Plaatje University, the Cape Peninsula University of Technology and the South African Radio Astronomy Observatory. The ilifu facility is supported by contributions from the Inter-University Institute for Data Intensive Astronomy (IDIA, a partnership between UCT, the University of Pretoria and the University of the Western Cape), the Computational Biology division at UCT and the Data Intensive Research Initiative of South Africa (DIRISA).

Contents

1 Introduction **1**

2 Literature Review **4**

2.1 Galaxy Clusters 4

2.1.1 The Intracluster Medium 5

2.1.1.1 Emission Processes 5

2.1.1.2 X-ray Spectroscopy 6

2.1.1.3 Hydrostatic Equilibrium 7

2.1.1.4 Radiative Cooling 10

2.1.2 Cluster Dynamics 10

2.1.3 Shocks 11

2.1.4 Cold Fronts 13

2.1.5 Intracluster Magnetic Fields 14

2.1.5.1 Kelvin–Helmholtz Instability 15

2.1.5.2 Nonthermal Emission 15

2.2 Radio Galaxies 17

2.2.1 Emission Processes 17

2.2.1.1 Synchrotron Emission 18

2.2.1.2 Inverse-Compton Scattering 22
2.2.2 Classification Schemes 23
2.2.2.1 Fanaroff–Riley Classification 23
2.2.2.2 Bent-tailed Sources 24
2.2.2.3 Remnant and Restarted Radio Galaxies 25
2.2.3 Components of Radio Galaxies 26
2.2.3.1 Active Galactic Nuclei 26
2.2.3.2 Jets 27
2.2.3.3 Lobes and Plumes 28
2.2.3.4 Knots and Hot Spots 28
2.3 Jet–Cluster Interactions 29
2.3.1 X-ray Cavities 29
2.3.2 Ram Pressure Bending 29
2.3.3 Re-accelerated AGN Plasma Sources 30
2.4 Review of Selected Clusters 30
2.4.1 Abell 133 30
2.4.2 Abell 3266 33
2.4.3 Abell 3376 38
2.4.4 Abell 3391–Abell 3395 System 40
2.4.4.1 Abell 3391 42
2.4.4.2 Abell 3395 42

3 Methodology **45**

3.1 Radio Astronomy 45

3.1.1 The Radio Telescope . . . 46
3.1.2 Radio Interferometry . . . 48
3.1.2.1 The Two-Element Interferometer . . . 48
3.1.2.2 The Radio Interferometer Measurement Equation . . . 49
3.1.2.3 Deconvolution and Imaging . . . 50
3.1.2.4 Calibration Strategies . . . 51
3.1.3 MeerKAT . . . 52
3.1.4 Data Collection . . . 53
3.1.5 Data Reduction and Imaging . . . 53
3.1.5.1 CARACal . . . 54
3.1.5.2 killMS and DDFacet . . . 57
3.1.5.3 Accuracy of the Flux Scale . . . 58
3.1.6 Spectral Analysis . . . 59
3.2 X-ray Astronomy . . . 60
3.2.1 X-ray Telescopes . . . 60
3.2.2 X-ray Calibration . . . 62
3.2.3 *XMM-Newton* . . . 63
3.2.3.1 *XMM-Newton* Science Analysis System . . . 64
3.2.3.2 *XMM-Newton* EPIC Background . . . 64
3.2.4 Data Collection . . . 65
3.2.5 Data Reduction . . . 66
3.2.6 Spectral Analysis . . . 68
3.2.6.1 Contour Binning . . . 68

3.2.6.2 Spectrum Extraction 69
3.2.6.3 XSPEC 70
3.2.6.4 Spectral Model 71
3.2.7 Imaging Analysis 73
3.2.7.1 Image Creation 73
3.2.7.2 Gaussian Gradient Magnitude Filtering 73

4 Results **74**

4.1 Radio Analysis 74
4.1.1 Radio Continuum Images 74
4.1.1.1 Abell 133 75
4.1.1.2 Abell 3266 78
4.1.1.3 Abell 3376 80
4.1.1.4 Abell 3391 82
4.1.1.5 Abell 3395 83
4.1.2 Radio Spectral Index Maps 86
4.1.2.1 Abell 133 86
4.1.2.2 Abell 3266 87
4.1.2.3 Abell 3376 91
4.1.2.4 Abell 3391 91
4.1.2.5 Abell 3395 92
4.2 X-ray Analysis 94
4.2.1 X-ray Images 94
4.2.1.1 Abell 133 94

4.2.1.2 Abell 3266 95
4.2.1.3 Abell 3376 95
4.2.1.4 Abell 3391 96
4.2.1.5 Abell 3395 96
4.2.2 X-ray Spectral Analysis 98
4.2.2.1 Cluster Emission 98
4.2.2.2 Instrumental Lines 98
4.2.2.3 Residual SPF Background 100
4.2.2.4 Solar Wind Charge Exchange 100
4.2.2.5 Cosmic Background 103

5 Discussion **105**

5.1 Abell 133 105
5.2 Abell 3266 107
5.3 Abell 3376 109
5.4 Abell 3391 112

6 Conclusion **115**

A X-ray Spectra **142**

List of Figures

2.1 APEC model at different temperatures 7

2.2 APEC model with photoelectric absorption 8

2.3 *XMM-Newton* image of the Bullet Cluster 12

2.4 Minimum energy requirement 17

2.5 Synchrotron spectrum of a single electron 19

2.6 Synchrotron spectrum 20

2.7 Aged synchrotron spectrum 22

2.8 Fanaroff–Riley classification 24

2.9 Unified model of AGNs 27

2.10 *Chandra* image of Abell 133 with MeerKAT contours 32

2.11 eROSITA image of Abell 3266 with MeerKAT contours 35

2.12 MeerKAT image of radio galaxies in the Abell 3266 field 37

2.13 MeerKAT image of Abell 3376 39

2.14 Abell 3391–Abell 3395 system with eROSITA and ASKAP 41

3.1 Two-element interferometer 49

3.2 A MeerKAT type dish. 52

3.3 Phaseball plot of J0538−4405 55

3.4 CARACal calibration phases of Abell 3391 56

3.5 Improvement after direction-dependent calibration for Abell 3395 57

3.6 Flux density comparison with NVSS and SUMSS 59

3.7 Types of Wolter telescopes 61

3.8 *XMM-Newton* 65

3.9 Filtering periods of soft proton flaring 68

4.1 MeerKAT image of Abell 133 75

4.2 MeerKAT image of the central radio galaxy of Abell 133 76

4.3 Individual radio galaxies the Abell 133 field 77

4.4 MeerKAT image of Abell 3266 78

4.5 Individual radio galaxies in Abell 3266 79

4.6 Diffuse radio sources in Abell 3266 80

4.7 MeerKAT image of Abell 3376 81

4.8 MeerKAT image of radio galaxies in Abell 3376 81

4.9 MeerKAT image of Abell 3391 82

4.10 MeerKAT image of radio galaxies in the Abell 3391 field 83

4.11 MeerKAT image of Abell 3395 84

4.12 MeerKAT image of PKS J0626−5432 in Abell 3395 85

4.13 MeerKAT image of diffuse emission in Abell 3395 85

4.15 Spectral index map of a bent-tailed radio galaxy in Abell 133 86

4.14 Spectral index map of radio galaxy in Abell 133 87

4.16 Spectral index map of A3266-RG1 88

4.17 Spectral index map of A3266-RG2 89

4.18 Spectral index map of A3266-RG3 89

4.19 Spectral index map of A3266-RG4 90

4.20 Spectral index map of A3266-D2 90

4.21 Spectral index map of radio galaxy in Abell 3376 91

4.22 Spectral index map of radio galaxy in Abell 3391 92

4.23 Spectral index map of radio galaxy in Abell 3395 93

4.24 Spectral index map of radio sources in Abell 3395 93

4.25 *XMM-Newton* image of Abell 133 94

4.26 *XMM-Newton* image of Abell 3266 95

4.27 *XMM-Newton* image of Abell 3376 96

4.28 *XMM-Newton* image of Abell 3391 97

4.29 *XMM-Newton* image of Abell 3395 97

4.30 Abell 133 spectral analysis 99

4.31 Abell 3266 spectral analysis 100

4.32 Abell 3376 spectral analysis 101

4.33 Abell 3391 spectral analysis 102

4.34 Abell 3395 spectral analysis 104

5.1 Composite radio, optical, and X-ray image of Abell 133 106

5.2 GGM image of Abell 133 107

5.3 Composite radio, optical, and X-ray image of Abell 3266 108

5.4 GGM image of Abell 3266 109

5.5 Composite radio, optical, and X-ray image of Abell 3376 110

5.6 GGM image of Abell 3376 110

5.7 Temperature map of Abell 3376 111

5.8 Spectral index and flux density profiles of A3376-RG1 111

5.9 Composite radio, optical, and X-ray image of Abell 3391 112

5.10 GGM image of Abell 3391 113

5.11 Temperature map of Abell 3391 114

5.12 Spectral index and flux density profiles of a radio galaxy in Abell 3391 114

A.1 All spectra of Abell 133 143

A.2 All spectra of Abell 3266 144

A.3 All spectra of Abell 3376 145

A.4 All spectra of Abell 3391 146

A.5 All spectra of Abell 3395 147

List of Tables

3.1 Summary of MeerKAT observations 53

3.2 Summary of *XMM-Newton* observations 66

3.3 Parameters used in contour binning. 69

3.4 Cluster parameters used in spectral fitting 71

3.5 Energies of the SWCX emission lines. 72

4.1 Statistics of radio images 75

4.2 Best-fit parameters for spectral fitting for Abell 133 99

4.3 Best-fit parameters for spectral fitting for Abell 3266 101

4.4 Best-fit parameters for spectral fitting for Abell 3376 102

4.5 Best-fit parameters for spectral fitting for Abell 3391 103

4.6 Best-fit parameters for spectral fitting for Abell 3395 104

List of Abbreviations

1GC	First-generation calibration
2GC	Second-generation calibration
3GC	Third-generation calibration
AGN	Active galactic nucleus
APEC	Astrophysical Plasma Emission Code
ARF	Ancillary response file
ASCA	*Advanced Satellite for Cosmology and Astrophysics*
ASKAP	Australian Square Kilometre Array Pathfinder
ATCA	Australia Telescope Compact Array
BCG	Brightest cluster galaxy
BRATS	Broadband Radio Astronomy Tools
CARACal	Containerized Automated Radio Astronomy Calibration
CASA	Common Astronomy Software Applications
CCD	Charge-coupled device
CCF	Current Calibration File
CMB	Cosmic microwave background
DDE	Direction-dependent effect
DSA	Diffusive shock acceleration
ECC	Eastern Core Component
EPIC	European Photon Imaging Cameras
ESAS	Extended Source Analysis Software
FOV	Field of view
FR-I	Fanaroff–Riley Class I
FR-II	Fanaroff–Riley Class II
FWHM	Full width at half maximum
GGM	Gaussian Gradient Magnitude

IC Inverse-Compton

ICM Intracluster medium

KH Kelvin–Helmholtz

LHB Local Hot Bubble

MFS Multi-frequency synthesis

MGCLS MeerKAT Galaxy Cluster Legacy Survey

MHD Magnetohydrodynamics

MOS Metal-oxide-semiconductor

MS Measurement Set

MWA Murchison Widefield Array

MWH Milky Way Halo

NAT Narrow-angle tail

NRF National Research Foundation

NVSS NRAO VLA Sky Survey

NWS Northwest Substructure

ODF Observation Data File

OOT Out-of-time

pn $p-n$ junction

PyBDSF Python Blob Detection and Source Finder

QPB Quiescent particle background

RASS *ROSAT* All Sky Survey

RFI Radio frequency interference

RIME Radio interferometer measurement equation

RMF Redistribution matrix file

RMS Root mean square

ROSAT *Roentgen Satellite*

SAS *XMM-Newton* Science Analysis System

SKA Square Kilometre Array

SNR Signal-to-noise ratio

SPF Soft proton flares

SSC *XMM-Newton* Survey Science Centre

SUMSS Sydney University Molonglo Sky Survey

SWCX Solar wind charge exchange

VLA Very Large Array

WAT Wide-angle tail

WCC Western Core Component

WHIM Warm–hot intergalactic medium

Chapter 1

Introduction

At the current epoch, a large fraction of all baryonic matter in the Universe is predicted to lie in the diffuse warm–hot intergalactic medium (WHIM) (Eckert *et al.*, 2015). The WHIM creates a vast network of filaments and sheets that make up the large-scale structure of the Universe, known as the "cosmic web" (Bond *et al.*, 1996). High-density nodes appear at the intersection of these filaments, each containing hundreds of galaxies bound by gravity, forming some of the largest structures in the Universe (Feretti *et al.*, 2002). These clusters of galaxies are permeated by the intracluster medium (ICM)—a hot, diffuse plasma that emits strong X-ray radiation. The wide variety of highly energetic astrophysical processes occurring in galaxy clusters and the ongoing accretion and mergers along the filaments leave imprints in the ICM. This allows scientists to use galaxy clusters as cosmic "laboratories" for studying subjects such as dark matter (Sand *et al.*, 2004), theories of gravity (Zhao *et al.*, 2013; Rosselli *et al.*, 2023), interactions between plasma and radiation, as well as the chemical enrichment of the Universe (Mernier *et al.*, 2020).

Radio galaxies exhibiting bipolar synchrotron-emitting jets are often found within these galaxy clusters (Massaro *et al.*, 2019). The jets originate from relativistic outflows of material near black holes at the centres of galaxies (Contopoulos *et al.*, 2015). They can extend up to megaparsec scales (Subrahmanyan *et al.*, 1996; Machalski *et al.*, 2008), far beyond the limits of the galaxy, and into the ICM that fills the space between galaxies in a galaxy cluster. The physical properties of the ICM strongly affect the propagation of the jets through this medium. Bulk motion in the ICM, intracluster magnetic fields, shocks, and cold fronts—discontinuities in the ICM at the boundaries of gas moving through hotter, less dense gas—have all been shown to cause observable effects in jets, such as jet bending or *in situ* particle acceleration (Mendygral *et al.*,

2012; Chibueze *et al.*, 2021). This makes radio galaxy jets a powerful tool to probe the dynamics of galaxy clusters.

In the past few decades since the development of radio and X-ray astronomy, extensive research has been done on radio galaxies and the X-ray emitting ICM. However, these studies were limited by the sensitivity and resolution of the telescopes at the time. Modern radio interferometers, such as MeerKAT (Jonas and the MeerKAT Team, 2016), the Low-Frequency Array (van Haarlem *et al.*, 2013), the Karl G. Jansky Very Large Array (Perley *et al.*, 2011), the recently upgraded Giant Metrewave Radio Telescope (Gupta *et al.*, 2017), and the upcoming Square Kilometre Array (SKA) (Grainge *et al.*, 2017), are leading to groundbreaking improvements in our observational capabilities. The ability of these telescopes to study previously unobservable details of jets (Delhaize *et al.*, 2021) could revolutionise our understanding of how radio galaxies interact with their cluster environments. An opportunity to do so comes from the MeerKAT Galaxy Cluster Legacy Survey (MGCLS) (Knowles *et al.*, 2022), a series of observations made by MeerKAT of 115 galaxy clusters in the southern sky.

The aim of this dissertation is to utilise the MGCLS, along with X-ray data from *XMM-Newton*, to gain a deeper understanding of the interactions between radio galaxies and the ICM in galaxy clusters. Observations from this survey are used to search for the presence of large-scale radio galaxy jets in the observed galaxy clusters. *XMM-Newton* X-ray data of the same clusters are analysed to determine the dynamical state of the clusters and to reveal phenomena such as shocks, cold fronts, and cavities in the ICM, due to merger events and other energetic processes. The morphology of the radio galaxy jets from MeerKAT is then compared with the cluster features in the *XMM-Newton* data to identify regions where jets are interacting with the ICM. The energy spectra of the radio galaxies and the ICM are studied to understand the emission processes in the jets and the thermal properties of the ICM. Using this approach, this work aims to investigate various ways the ICM affects the propagation of the jets, and how the jets affect the ICM in return.

This dissertation is structured into six chapters. This introduction is followed by **Chapter 2**, which provides an overview of the existing literature in the field to contextualise the research. First, galaxy clusters, the ICM, and the emission processes occurring in the ICM are reviewed. It then delves into the physical properties of the ICM and mathematical models to describe these properties. The chapter then discusses the dynamics of clusters, the factors affecting them, and observational evidence for their dynamical states. Next, the current understanding of radio galaxies, their components, emission mechanics, and classification schemes are discussed.

Some of the ways in which radio galaxies can interact with the ICM are then explored. Finally, previous research on the five clusters at the focus of this work—Abell 133, Abell 3266, Abell 3376, Abell 3391, and Abell A3395—is reviewed.

Next, **Chapter 3** provides a detailed account of the methodology employed in this research, in order to ensure its transparency and reproducibility. The chapter introduces important concepts in radio and X-ray astronomy, including information on the operating principles of radio and X-ray telescopes, the technique of radio interferometry, the calibration and imaging of interferometric data, as well as X-ray spectral analysis and imaging methods. It provides information on MeerKAT and *XMM-Newton* and details of the collection, calibration, and analysis of data from these telescopes.

The results of this research are presented in **Chapter 4**. These include X-ray and radio images of the cluster environments. These images show the detailed morphology and structure of the clusters and radio galaxies inside the clusters. Radio spectral index maps of the radio galaxies, and profiles of the spectral index along the jets, provide information on the variation in synchrotron emission of the radio galaxies. From the X-ray images, radial surface brightness profiles were constructed, describing the distribution of the ICM. Furthermore, the results of a detailed X-ray spectral analysis across regions following the surface brightness contours of the clusters are presented here, offering insight into the temperature gradient in the clusters and its implications for the dynamics of the system.

These results are discussed in detail in **Chapter 5**. It critically examines the radio and X-ray observations to determine the spectral and morphological properties of jets, and the physical conditions and dynamics within clusters, and explores possible interpretations of it. This chapter also compares the findings with past studies to find any discrepancies or anomalies, and investigates potential reasons for this.

Finally, **Chapter 6** presents the main conclusions of this work. It reflects on the significance of the results and the contribution this dissertation has made to our understanding of how radio galaxy jets interact with their cluster environments. This chapter also discusses the limitations of the research and suggestions for future work that could build on it.

Chapter 2

Literature Review

2.1 Galaxy Clusters

Galaxy clusters are vast formations containing hundreds of galaxies, bound together by gravity within a radius of $1-2\,\mathrm{Mpc}$ (Markevitch and Vikhlinin, 2007). They form hierarchically through mergers of smaller structures and the accretion of matter along the filaments of the cosmic web. The masses of galaxy clusters typically range from $10^{14}-10^{15}\,M_{\odot}$, making them among the most massive gravitationally bound structures in the Universe (Markevitch and Vikhlinin, 2007). Apart from stars, which make up only about 3% of their mass content, clusters are also composed of approximately 85% dark matter and 12% hot plasma, which permeates the space between galaxies within the cluster (Pratt *et al.*, 2019).

The study of clusters rapidly developed in the 20th century, after Hubble (1926) proved the extragalactic nature of many objects that were previously simply classified as "nebulae". Soon after, the study of the Coma Cluster led Zwicky (1933) to postulate the existence of dark matter. Later, a catalogue of 2712 galaxy clusters in the northern sky was compiled by Abell (1958). It was posthumously expanded to an all-sky catalogue of 4073 clusters (Abell *et al.*, 1989). These catalogues are still in common use today. In the second half of the 20th century, the development of X-ray astronomy led to the discovery of the X-ray emitting ICM. Modern multi-wavelength observational capabilities offer invaluable insights into cluster evolution and dynamics, the nature of dark matter, and the large-scale structure of the Universe.

2.1.1 The Intracluster Medium

The ICM is a hot, diffuse plasma filling the space between galaxies in a cluster. It is composed of fully ionised hydrogen and helium, enriched with trace amounts of highly ionised heavier elements (Markevitch and Vikhlinin, 2007). These elements are typically found at about one-third of their solar abundances throughout most of the cluster, but their abundances can reach solar levels toward the cluster core (Werner and Mernier, 2020). Observational data of clusters typically indicate densities ranging from approximately $10^{-2}\,\mathrm{cm}^{-3}$ in the core to $10^{-4}\,\mathrm{cm}^{-3}$ in the outskirts of the cluster (Markevitch and Vikhlinin, 2007). The high temperatures of the ICM, which typically range from $T \sim 10^7 - 10^8\,\mathrm{K}$ (or equivalently[1] $kT \sim 1 - 10\,\mathrm{keV}$), result in bright emission at X-ray energies (Markevitch and Vikhlinin, 2007; Longair, 2010).

2.1.1.1 Emission Processes

At temperatures $kT \gtrsim 2\,\mathrm{keV}$, the X-ray emission of the ICM primarily results from thermal bremsstrahlung, or free-free emission, produced by the deceleration of free electrons in the plasma as they are deflected from their trajectories by the electrostatic fields of ions (Werner and Mernier, 2020). This process, occurring for electrons deflected at various angles and velocities, results in a continuum of photon energies. The emissivity of bremsstrahlung at a photon energy $h\nu$ is

$$\epsilon_\nu^{\mathrm{ff}} = \frac{32\pi Z^2 e^6 n_e n_i}{3 m_e c^3}\sqrt{\frac{2\pi}{3kTm_e}}\, e^{-h\nu/kT}\bar{g}_{\mathrm{ff}}, \tag{2.1}$$

where h is Planck's constant, ν is the frequency, e is the elementary charge, Ze is the charge of the ions, n_e and n_i are the number densities of the electrons and ions respectively, m_e is the electron mass, c is the speed of light, and $\bar{g}_{\mathrm{ff}} \approx \frac{3}{\sqrt{\pi}} \ln\left(\frac{9kT}{4h\nu}\right)$ is the Gaunt factor, a quantum-mechanical correction factor (Rybicki and Lightman, 1991; Schneider, 2014). At energies $h\nu \lesssim kT$, the emissivity scales approximately with n_e^2. Assuming solar abundances, the total bremsstrahlung emission is (Schneider, 2014)

$$\epsilon^{\mathrm{ff}} = \int_0^\infty \epsilon_\nu^{\mathrm{ff}}\,\mathrm{d}\nu \approx 3.0 \times 10^{-27}\sqrt{\frac{T}{1\,\mathrm{K}}}\left(\frac{n_e}{1\,\mathrm{cm}^{-3}}\right)^2 \mathrm{erg\,cm^{-3}\,s^{-1}}. \tag{2.2}$$

In addition to the continuum emission, the ICM emits line emission through various atomic processes, such as collisional excitation and radiative recombination. Line emission can dominate

[1] By convention, temperatures are typically expressed as kT, where k is the Boltzmann constant, in units of keV.

in regions where the ICM temperature is $kT \lesssim 2\,\mathrm{keV}$, such as in cluster outskirts (Reiprich *et al.*, 2013; Schneider, 2014). Similar to continuum emission, the emissivity of line emission is proportional to n_e^2 (Peterson and Fabian, 2006; Böhringer and Werner, 2010).

Because of its low density, the ICM is optically thin, allowing most of the emitted photons to escape the cluster without interacting with ions or electrons, apart from occasional resonant scattering in dense cluster cores (Böhringer and Werner, 2010; Werner and Mernier, 2020). This means that a soft X-ray image of a cluster approximately maps the square of the column density of the ICM (Markevitch and Vikhlinin, 2007). For a spherically symmetric cluster, the observed X-ray surface brightness at a projected radius R from the centre of the cluster is the line-of-sight integral of the X-ray emissivity,

$$S_X(R) \propto \int_R^\infty \frac{\epsilon_\nu(r) r}{\sqrt{r^2 - R^2}}\,\mathrm{d}r. \tag{2.3}$$

2.1.1.2 X-ray Spectroscopy

X-ray spectroscopy is an important tool in determining the physical properties of the ICM. Plasma radiation codes commonly used for this purpose include the Astrophysical Plasma Emission Code (APEC) (Smith *et al.*, 2001) and MEKAL (Mewe *et al.*, 1995). The normalisation of the spectrum is determined by the emission measure

$$\mathrm{EM}_e = \int n_e^2\,\mathrm{d}V, \tag{2.4}$$

where V is the volume of the emitting plasma. It is sometimes expressed instead as

$$\mathrm{EM}_H = \int n_e n_H\,\mathrm{d}V, \tag{2.5}$$

where n_H is the hydrogen number density (Böhringer and Werner, 2010). In APEC, the normalisation of the observed X-ray spectrum is proportional to EM_H and is defined as

$$\mathrm{norm} = \frac{10^{-14}}{4\pi\left[D_A(1+z)\right]^2} \int n_e n_H\,\mathrm{d}V, \tag{2.6}$$

where D_A is the angular diameter distance to the source in units of cm and z is the redshift. By making assumptions about the distribution and ionisation state of the emitting plasma, such as assuming a uniformly distributed spherical source with $n_e = 1.2 n_H$, it is possible to calculate the ICM density.

The shape of the continuum emission can be used to determine the average electron temperature along the line of sight (Markevitch and Vikhlinin, 2007). The spectrum is relatively flat at low

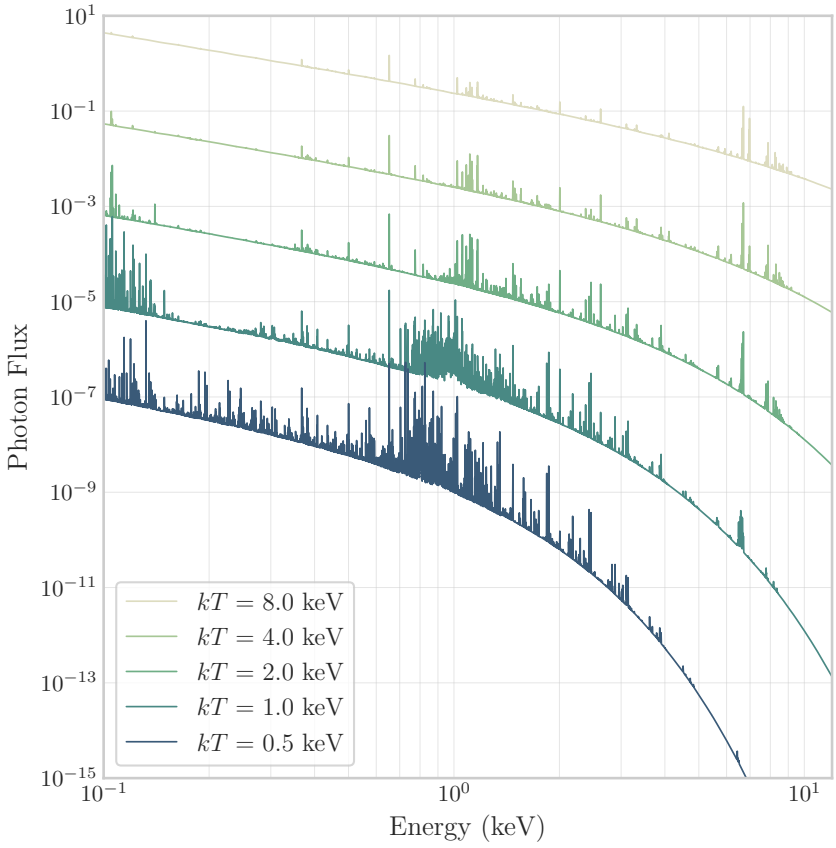

Figure 2.1: APEC model at different temperatures, with metal abundances at a third of their solar value, as typically found in clusters. The photon flux is given in arbitrary units and the graphs have been shifted vertically for clarity.

energies, but decreases exponentially at energies $h\nu \gtrsim kT$ (Schneider, 2014). This is demonstrated in Figure 2.1, which shows results from the APEC model at different temperatures.

A plasma model such as APEC alone is not sufficient for describing the observed spectrum, as X-rays travelling towards the Earth will undergo photoelectric absorption, primarily by the interstellar medium. This absorption causes a cut-off in the spectrum at lower energies, as shown in Figure 2.2. Furthermore, various instrumental and cosmic background components must be accounted for, including thermal emission from the circumgalactic medium of the Milky Way (Bluem *et al.*, 2022) and nonthermal emission from extragalactic point sources (Lumb *et al.*, 2002).

2.1.1.3 Hydrostatic Equilibrium

After a major merging event, it takes approximately the sound-crossing time of the cluster for perturbations induced by the merger to dissipate. The ICM then returns to approximately hydrostatic equilibrium, achieved when the inward gravitational force and outward pressure are

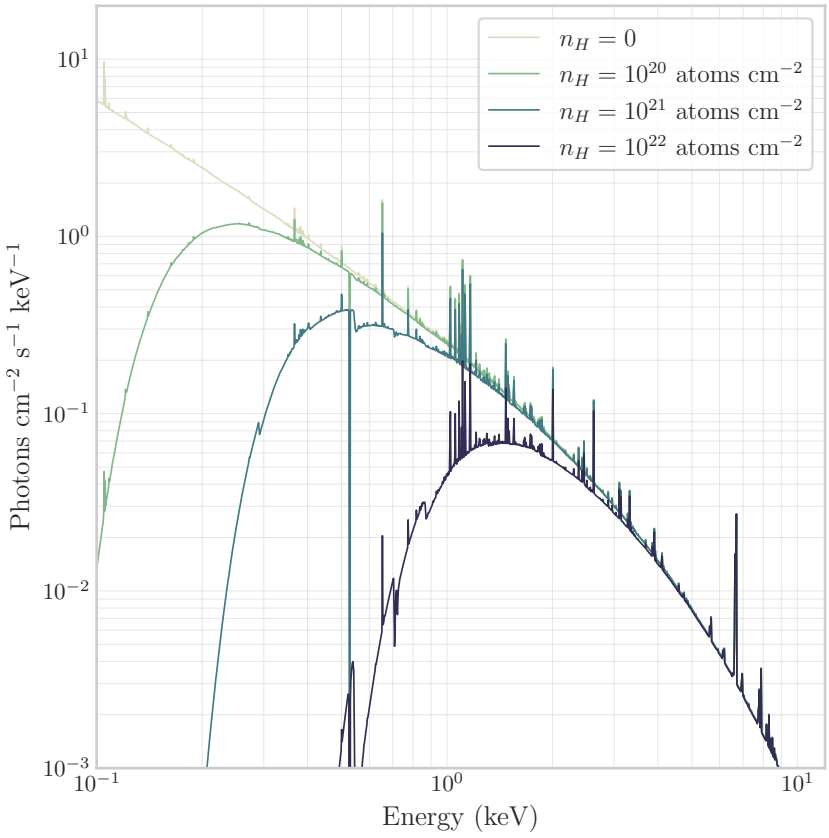

Figure 2.2: APEC model with the Tuebingen-Boulder ISM absorption model at different hydrogen column densities n_H, using a temperature of 3 keV and abundances at a third of their solar value for the APEC model.

balanced (Schneider, 2014). In this state, the pressure P and mass density ρ of the ICM satisfy the equation

$$\nabla P = -\rho \nabla \Phi, \tag{2.7}$$

where Φ is the gravitational potential of the cluster (Schneider, 2014). For a spherically symmetric cluster, the hydrostatic equilibrium equation simplifies to

$$\frac{\mathrm{d}P}{\mathrm{d}r} = -\frac{GM(r)\rho}{r^2}, \tag{2.8}$$

where G is the gravitational constant and $M(r)$ is the total mass of a cluster enclosed inside a radius r. The ICM can be well-approximated by an ideal gas, described by the ideal gas law,

$$P = nkT = \left(\frac{\rho}{\mu m_p}\right) kT. \tag{2.9}$$

where n is the number density of the gas, m_p is the proton mass, and μm_p is the average mass per particle (Longair, 2010; Schneider, 2014). Combining the ideal gas law with the hydrostatic equilibrium equation under spherical symmetry yields

$$\frac{\mathrm{d}P}{\mathrm{d}r} = \frac{kT\rho}{\mu m_p}\left(\frac{\mathrm{d}\ln\rho}{\mathrm{d}r} + \frac{\mathrm{d}\ln T}{\mathrm{d}r}\right) = -\frac{GM(r)\rho}{r^2}. \tag{2.10}$$

If the temperature and density profiles of the cluster are known, its mass can be calculated with

$$M(r) = -\frac{kTr^2}{G\mu m_p}\left(\frac{\mathrm{d}\ln\rho}{\mathrm{d}r} + \frac{\mathrm{d}\ln T}{\mathrm{d}r}\right). \tag{2.11}$$

If the gas distribution is isothermal, equation (2.10) reduces to

$$\frac{\mathrm{d}\ln\rho}{\mathrm{d}r} = -\frac{\mu m_p}{kT}\frac{GM(r)}{r^2}. \tag{2.12}$$

Similarly, for the galaxies (or dark matter particles) in the cluster,

$$\frac{\mathrm{d}\ln\rho_G}{\mathrm{d}r} = -\frac{1}{\sigma_v^2}\frac{GM(r)}{r^2}, \tag{2.13}$$

where ρ is the mass density of the galaxies and σ_v^2 is the velocity dispersion (Schneider, 2014). Comparing equations (2.12) and (2.13), the gas density ρ can be related to the galaxy density ρ_G with

$$\frac{\mathrm{d}\ln\rho}{\mathrm{d}r} = \beta\frac{\mathrm{d}\ln\rho_G}{\mathrm{d}r}, \tag{2.14}$$

or equivalently,

$$\rho(r) \propto [\rho_G(r)]^{\beta}, \tag{2.15}$$

where $\beta \equiv \left(\frac{\mu m_p \sigma_v^2}{kT}\right)$. King (1962, 1966) derived a radial density distribution commonly used to describe the galaxy or dark matter mass density distribution of galaxy clusters, in the form

$$\rho_G(r) = \rho_{G0}\left[1 + \left(\frac{r}{r_c}\right)^2\right]^{-3/2}, \tag{2.16}$$

where ρ_{G0} is the central mass density of the galaxies or dark matter particles and r_c is the core radius. Using equation (2.15), the King profile can be adapted to describe the radial density profile of the ICM,

$$\rho(r) = \rho_0\left[1 + \left(\frac{r}{r_c}\right)^2\right]^{-3\beta/2}, \tag{2.17}$$

where ρ_0 is the central gas density. This is known as the β-model, first proposed by Cavaliere and Fusco-Femiano (1976, 1978), and is widely used to describe the gas density profiles in galaxy clusters. The β-model can also be expressed in terms of surface brightness (see equation (2.3)),

$$S_X(R) = S_0\left[1 + \left(\frac{R}{r_c}\right)^2\right]^{-3\beta+1/2}, \tag{2.18}$$

where S_0 is the central surface brightness. The β-model assumes an isothermal gas distribution, but can still be applied to clusters with varying temperatures by considering only the surface brightness in the low-energy band, where the emissivity does not strongly depend on the temperature (Arnaud, 2009). Fitting the β-model to X-ray emission from clusters typically yields a core radius $r_c = 0.1 - 0.3\,h^{-1}\,\mathrm{Mpc}$ and $\beta \approx 0.65$ (Schneider, 2014).

2.1.1.4 Radiative Cooling

The ICM cools as it emits radiation and cannot remain in hydrostatic equilibrium indefinitely. The gas cooling timescale due to thermal bremsstrahlung is

$$t_{\rm cool} = \frac{u}{\epsilon^{\rm ff}} \approx 8.5 \times 10^{10}\,{\rm yr} \left(\frac{n_e}{10^{-3}\,{\rm cm}^{-3}}\right)^{-1} \left(\frac{T}{10^{8}\,{\rm K}}\right)^{1/2}, \tag{2.19}$$

where $u = 3nkT/2$ is the energy density of the gas (Schneider, 2014). For most of the cluster, the cooling timescale of the ICM is longer than the Hubble time and hydrostatic equilibrium is preserved. However, in the core, the density is high enough that in certain cases cooling can occur effectively. To maintain pressure equilibrium, gas is expected to flow inward, further increasing the core density and the cooling rate (Cowie and Binney, 1977; Fabian and Nulsen, 1977). While many clusters have cool cores, high-resolution spectroscopy with *XMM-Newton* and *Chandra* revealed that cooling-flow models significantly overestimate cooling rates (Molendi and Pizzolato, 2001; Peterson *et al.*, 2003). One possible heating mechanism that can counteract cooling flows is feedback from active galactic nuclei (AGNs), particularly from the massive brightest cluster galaxies (BCGs) typically found at the centres of cool-core clusters (McNamara and Nulsen, 2012; Hardcastle and Croston, 2020).

2.1.2 Cluster Dynamics

The Lambda Cold Dark Matter model predicts that galaxy clusters originated as density peaks in the density fluctuations in the early Universe, growing hierarchically through the accretion of matter and merging of structures (Werner and Mernier, 2020). After clusters form, they continue to experience accretion and mergers along the filaments of the cosmic web. Major cluster mergers (mergers between clusters with similar masses) are among the most energetic events since the Big Bang (Valdarnini and Sarazin, 2021). This energy is converted into shocks, turbulence, the amplification of magnetic fields, and the acceleration of relativistic particles (Markevitch and Vikhlinin, 2007).

Clusters are broadly categorised as either relaxed or disturbed based on their dynamical state. Relaxed clusters typically have symmetrical X-ray morphologies, with bright, cool cores, whereas disturbed clusters tend to have asymmetrical or elongated morphologies and often show other observational evidence of recent merging events, such as shocks and cold fronts.

2.1.3 Shocks

A shock is a disturbance propagating through a medium at a speed v exceeding the local speed of sound c_s. This speed ratio is known as the Mach number, $\mathscr{M} \equiv v/c_s$. Shocks are characterised by abrupt discontinuities in the pressure, temperature, and density of the medium before and after the shock front (Longair, 2010). The Rankine–Hugoniot conditions describe the conservation of mass, energy, and momentum across these discontinuities, relating the mass density, pressure, speed, and specific enthalpy of the upstream and downstream[2] gas (see Longair, 2010 for more information).

For a perfect gas, these conditions can be used to derive the upstream-to-downstream ratio of the temperature, mass density, and pressure, in terms of the Mach number (Longair, 2010),

$$\frac{T_2}{T_1} = \frac{\left(2\gamma\mathscr{M}^2 - (\gamma-1)\right)\left(2 + (\gamma-1)\mathscr{M}^2\right)}{(\gamma+1)^2\mathscr{M}^2}, \tag{2.20}$$

$$\frac{\rho_2}{\rho_1} = \frac{\gamma+1}{(\gamma-1) + 2/\mathscr{M}^2}, \tag{2.21}$$

$$\frac{P_2}{P_1} = \frac{2\gamma\mathscr{M}^2 - (\gamma-1)}{(\gamma+1)}, \tag{2.22}$$

where γ is the adiabatic index, and the subscripts 1 and 2 denote the upstream and downstream quantities, respectively. The first two equations can be combined to show the relation between the temperature ratio and the density ratio (Markevitch and Vikhlinin, 2007),

$$\frac{T_2}{T_1} = \frac{\left(\frac{\gamma+1}{\gamma-1}\right) - \left(\frac{\rho_1}{\rho_2}\right)}{\left(\frac{\gamma+1}{\gamma-1}\right) - \left(\frac{\rho_2}{\rho_1}\right)}, \tag{2.23}$$

or equivalently,

$$\left(\frac{\rho_2}{\rho_1}\right)^{-1} = \left[\frac{1}{4}\left(\frac{\gamma+1}{\gamma-1}\right)^2\left(\frac{T_2}{T_1}-1\right)^2 + \frac{T_2}{T_1}\right]^{1/2} - \frac{1}{2}\frac{\gamma+1}{\gamma-1}\left(\frac{T_2}{T_1}-1\right). \tag{2.24}$$

For a monatomic gas, $\gamma = 5/3$, so $(\gamma+1)/(\gamma-1) = 4$. In the limit of very strong shocks ($\mathscr{M} \gg 1$), the density ratio in equation (2.21) then becomes $\rho_2/\rho_1 = (\gamma+1)/(\gamma-1) = 4$, constraining the maximum density increase over a shock front. In contrast, the temperature and the pressure can become arbitrarily large (Longair, 2010).

Markevitch and Vikhlinin (2007) reviewed a number of ways in which X-ray studies of shocks can be used to study the conditions of the ICM. This includes using shocks to determine the velocities and trajectories of merging subclusters, estimate the intracluster magnetic field

[2]The flow is described in the reference frame of the shock front, where the medium is approaching it with speed v. The descriptors *upstream* and *downstream* refer to the undisturbed and the shocked gas, respectively.

strength, and gain insight into the properties of dark matter. Ideal for these purposes are merger shocks sent into the ICM as clusters experience mergers, which heat up and compress the ICM, increasing the entropy, often defined[3] as

$$K \equiv \frac{kT}{n^{2/3}}, \tag{2.25}$$

in studies of hot atmospheres (Werner and Mernier, 2020). These collisions can have velocities around $2000\,\mathrm{km\,s^{-1}}$ (Markevitch *et al.*, 1999; Ricker and Sarazin, 2001), but due to the high speed of sound in clusters, merger shocks have Mach numbers $\mathscr{M} \lesssim 3$ (Markevitch and Vikhlinin, 2007). Gabici and Blasi (2003) suggested that in major mergers, where the masses of the merging subclusters are comparable, merger shocks are only moderately supersonic ($\mathscr{M} \sim 1$).

One of the first clear examples of a cluster merger shock was the "Bullet Cluster" (1E 0657-56) (Markevitch *et al.*, 2002). The X-ray image of this cluster, shown in Figure 2.3, features a bullet-like structure exiting the main cluster core to the west, the result of a merger event where a subcluster, initially approaching from the east, passed the main core $0.1-0.2\,\mathrm{Gyr}$ ago (Markevitch *et al.*, 2002). To the west, a prominent bow shock with $\mathscr{M} = 2-3$ (Markevitch *et al.*, 2002; Di Mascolo *et al.*, 2019) is propagating ahead of the bullet structure.

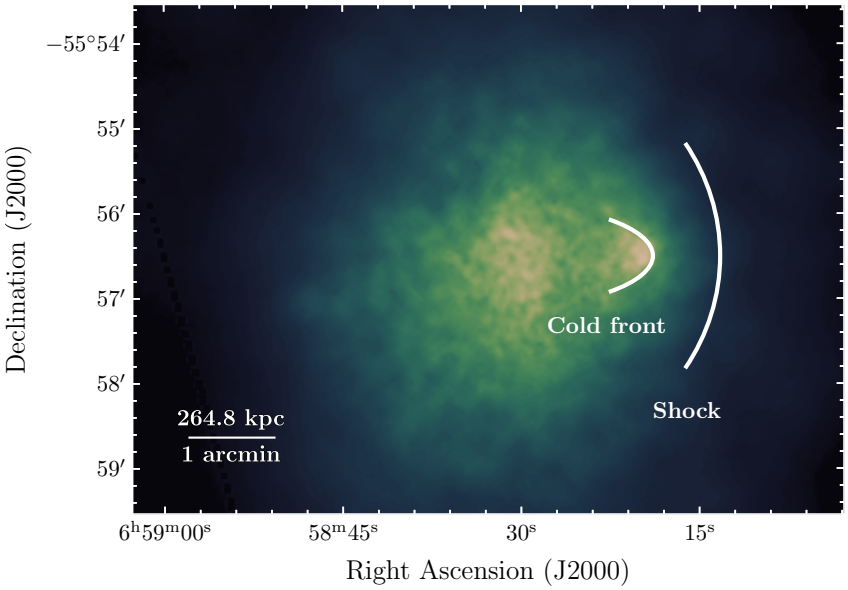

Figure 2.3: Adaptatively smoothed *XMM-Newton* X-ray image of the Bullet Cluster at $0.5-2.0$ keV. Point sources have been cosmetically masked. The sharp brightness edge of the bullet-structure is a cold front. The jump in brightness across the cold front implies an increase in density, but the temperature decreases. The fainter brightness edge to the west of the structure is a bow shock. Bow shocks are a characteristic feature of merging clusters. Both the temperature and the density increase across the shock front.

[3]This definition of entropy is related to, but not identical to the definition of entropy in thermodynamics (Werner and Mernier, 2020).

Other shocks found in galaxy clusters include weak ($\mathscr{M} \sim 1$) shocks in central regions generated by bubbles created by AGNs (Markevitch and Vikhlinin, 2007), and strong shocks with $\mathscr{M} \sim 10$ in the cluster outskirts from the continuous infall of the WHIM (Hong *et al.*, 2014). Neither of these are ideal for studying ICM properties, as the discontinuities are too weak for the former, while the latter usually appears in regions with too low X-ray surface brightness for statistically significant observations.

2.1.4 Cold Fronts

Early observations from the *Chandra* X-ray Observatory provided evidence that certain sharp X-ray brightness discontinuities appearing in merging clusters were not shock fronts, as previously thought, but rather boundaries of cool gas clouds moving subsonically or transonically through hotter and less dense surrounding gas (Markevitch *et al.*, 2000). Vikhlinin *et al.* (2001a) termed this phenomenon a *cold front*. Unlike shock fronts, where the temperature, density, and pressure all increase across the front, only the density increases across a cold front, while the temperature drops and the pressure remains relatively constant (Feretti *et al.*, 2002; Markevitch and Vikhlinin, 2007). Cold fronts are found in most clusters experiencing mergers in the plane of the sky, but also in many seemingly relaxed clusters (Ghizzardi *et al.*, 2010).

In merging clusters, cold fronts are often interpreted as the cool, dense remnants of infalling substructures, such as clusters or galaxies. An infalling substructure moving with speed v relative to the ICM with density ρ will experience ram pressure with strength $P_{\rm ram} = \rho v^2$ (ZuHone and Su, 2024). For an infalling cool-core cluster, ram pressure progressively strips away the gas from the outer regions of the subcluster, leaving only remnants of the cool, dense core, confined by the shocked ambient gas flowing around it (Markevitch and Vikhlinin, 2007). Substructure remnants may have extended tails of unstripped gas, as the downstream gas is more shielded from ram pressure stripping (Roediger *et al.*, 2015; Sheardown *et al.*, 2019).

One example of a merger remnant cold front is the iconic bullet structure in the Bullet Cluster (Markevitch *et al.*, 2002), shown in Figure 2.3. Optical images show that the cold gas of the bullet lags behind the subcluster galaxies (Markevitch *et al.*, 2004). Both the cold front and the bow shock have a density jump by a factor of around 3, but there is a significant drop in the entropy across the cold front and nearly continuous pressure, while there is a large pressure jump and an increase in the entropy across the shock (Markevitch *et al.*, 2002; Markevitch and Vikhlinin, 2007).

At a later stage, as the subcluster approaches the apocentre of its orbit, it will slow down and also enter less dense regions of the ambient medium. If the cool gas remnant survives the pericentre passage it will experience a rapid decrease in ram pressure, and the trailing cool gas will overtake the dark matter peak like a slingshot (Markevitch and Vikhlinin, 2007; Sheardown *et al.*, 2019). This can lead to cold fronts *ahead* of the subcluster peak (Hallman and Markevitch, 2004). Unlike tails stripped by ram pressure, tracing the path of the infalling structure, the X-ray tails that form during slingshots are also shaped by tidal forces and can be arc-shaped or even point opposite to the infall direction. For this reason, the direction of X-ray tails alone may not be a good indicator of the motion of the subcluster (Sheardown *et al.*, 2019).

More subtle cold fronts are also found near the cool cores of seemingly relaxed clusters with little to no evidence of recent mergers (Markevitch *et al.*, 2001; Ghizzardi *et al.*, 2010). This is believed to be caused by the sloshing of the cool central gas. Numerical simulations have shown that sloshing in cool-core clusters can be induced by minor mergers that can disturb the cool gas in the core without leaving other evidence of a disturbance (Ascasibar and Markevitch, 2006; ZuHone *et al.*, 2019). The sloshing motion can create multiple cold fronts, resulting in a gas-sloshing spiral structure (Blanton *et al.*, 2011; Sarkar *et al.*, 2023; Gatuzz *et al.*, 2022). Gas sloshing may be a solution to the cooling flow problem, as it can mix the hot gas of the outer regions with the cool gas in the core, compensating for radiative cooling (ZuHone *et al.*, 2010).

2.1.5 Intracluster Magnetic Fields

Galaxy clusters are permeated by large-scale magnetic fields. Although these fields are not directly observable, radio observations of synchrotron emission suggest magnetic field strengths of $B \sim 1\,\mu\mathrm{G}$ and coherence scales of $\sim$10 kpc (Carilli and Taylor, 2002; Brüggen, 2013). The exact nature and origin of large-scale intracluster magnetic fields are still unclear. They may originate from a primordial seed field that formed before the epoch of recombination and has since been significantly amplified (Hutschenreuter *et al.*, 2018; Domínguez-Fernández *et al.*, 2019). Alternatively, the magnetic fields could form from astrophysical phenomena such as outflows from galaxies (Donnert *et al.*, 2009) or AGNs (Xu *et al.*, 2010). Although the magnetic pressure is much less than the thermal pressure, the weakly magnetised ICM can have a crucial effect on cluster dynamics (Lyutikov, 2006).

2.1.5.1 Kelvin–Helmholtz Instability

The Kelvin–Helmholtz (KH) instability, first described by Helmholtz (1868) and Kelvin (1871), is an instability that occurs at the interface of fluids with different velocities. Soon after the discovery of cold fronts, Vikhlinin *et al.* (2001b) noted that the sharp cold front in the galaxy cluster Abell 3667 did not appear to be disturbed by a KH instability as would be expected in the absence of any stabilising factors. They proposed that the KH instability could be suppressed by the surface tension of a 10 µG magnetic field that is aligned parallel to the front. Although this is much higher than the typical magnetic field strength of the ICM, this can be explained by the effect of magnetic draping, where a strong magnetic layer forms at the head of a cloud moving through a weakly magnetised medium (Lyutikov, 2006). Simulations show that strong magnetic fields form both outside merger cold fronts and inside sloshing cold fronts, suppressing the KH instability for many of the cold fronts that have been observed (ZuHone and Roediger, 2016).

2.1.5.2 Nonthermal Emission

Radio observations of galaxy clusters reveal the presence of extended sources of nonthermal emission associated with magnetic fields. These sources include not only radio galaxies, discussed in the next section, but also diffuse synchrotron radio emission that is not directly related to any particular galaxy. Synchrotron emission is produced by relativistic charged particles that are accelerated perpendicular to their velocity, which occurs when highly energetic charged particles gyrate in a magnetic field (Longair, 2010).

One physical mechanism for accelerating particles to such high energies is diffusive shock acceleration (DSA), also known as first-order Fermi acceleration, in which particles are reflected back and forth through the shock front by magnetic inhomogeneities around the shock, gaining energy with each crossing (Van Weeren *et al.*, 2019). This accelerates particles to a power-law spectrum of $n(E)\,\mathrm{d}E \propto E^{-p}\,\mathrm{d}E$, with power-law index $p = (r+2)/(r-1)$ where $r = \rho_2/\rho_1$ is the density ratio of the downstream and upstream gas (Caprioli, 2024). This results in a power-law synchrotron spectrum $S_\nu \propto \nu^{-\alpha}$, with spectral index $\alpha = (p-1)/2$ (see Section 2.2.1.1). For strong shocks, where $p \approx 2$, the synchrotron spectral index is $\alpha \approx 0.5$.

Van Weeren *et al.* (2019) proposed three classes of diffuse radio emission in clusters. The first class of objects is radio halos, which are extended sources located at the centres of clusters that roughly follow the X-ray emission from the ICM (Feretti *et al.*, 2001; Xie *et al.*, 2020). Although

the acceleration mechanism behind halos is still debated, giant radio halos are associated with disturbed clusters (Cassano *et al.*, 2010). The second class consists of cluster radio shocks, also known as radio relics[4]. These are elongated, strongly polarised, steep-spectrum sources of synchrotron emission that trace particles accelerated at merger shocks by a mechanism such as DSA (Van Weeren *et al.*, 2019). These sources are often found at the peripheries of clusters. The third class consists of plasma sources originally related to radio galaxy jets, which have been re-accelerated by processes unrelated to the original radio galaxy (see Section 2.3.3).

A common way of estimating the magnetic field strength of a synchrotron source is to minimise the total energy density U_{total} that can produce the observed synchrotron emission (Burbidge, 1956),

$$U_{\text{total}} = U_{\text{e}} + U_{\text{p}} + U_B, \tag{2.26}$$

where U_{e}, U_{p}, and U_B are the energy densities of the electrons, protons, and magnetic field, respectively (Govoni and Feretti, 2004). The minimum energy condition is similar to the equipartition condition, in which the particle energy density is equal to the energy density of the magnetic field, as shown in Figure 2.4. However, this method of calculating the magnetic field is inherently limited as there is not necessarily any reason to assume that the source components are near equipartition (Contopoulos *et al.*, 2015).

The same relativistic electrons creating the synchrotron radiation are also expected to scatter cosmic microwave background (CMB) photons to X-ray energies through inverse-Compton (IC) scattering. As will be shown in Section 2.2.1, the emissivity of the IC scattering is directly proportional to the energy density of the CMB photon field, whereas the emissivity of the synchrotron radiation is proportional to the energy density of the magnetic field. This provides a method of calculating magnetic field strength that is not dependent on the equipartition assumption (Carilli and Taylor, 2002). However, the detection of the IC emission is hindered by the thermal bremsstrahlung that dominates X-ray emission in galaxy clusters (Bartels *et al.*, 2015). Nevertheless, even the non-detection of IC X-ray emission can be used to derive a lower limit on the magnetic field strength (Han, 2017).

[4]While the term *relic* is often used, it is not an accurate description, as these are not necessarily old sources (Van Weeren *et al.*, 2019).

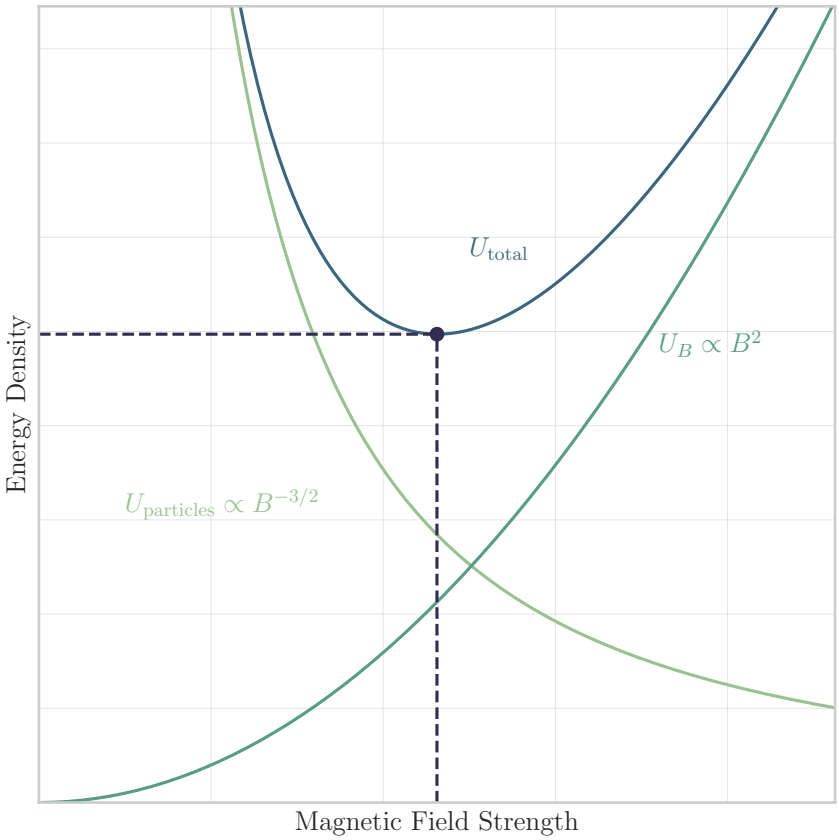

Figure 2.4: Energy content of a synchrotron source as a function of magnetic field strength in arbitrary units. The total energy density is at a minimum when $U_{\text{particles}} \equiv U_{\text{e}} + U_{\text{p}} \propto B^{-3/2}$ (see Section 2.2.1.1) is approximately equal to $U_B \propto B^2$.

2.2 Radio Galaxies

Radio galaxies are active galaxies with extended regions of radio emission driven by synchrotron-emitting jets that can extend up to megaparsec scales. Radio galaxy jets were first documented by Curtis (1918) who described a "curious straight line" extending from the nucleus of Messier 87. However, not many jets were discovered until the development of radio interferometry in the second half of the 20th century. According to the widely accepted beam model for radio galaxies, originating in the 1970s, radio galaxy jets are the manifestation of bipolar collimated outflows powered by an AGN at the centre of the galaxy (Blandford and Rees, 1974; Scheuer, 1974). These jets can expand into large-scale radio structures such as lobes or plumes.

2.2.1 Emission Processes

The radio emission from radio galaxy jets is mainly synchrotron emission from highly relativistic particles gyrating in magnetic fields. These particles can also scatter low-energy photons to X-ray energies through IC scattering. The physics of these emission processes is discussed in this

section.

2.2.1.1 Synchrotron Emission

In the absence of an electric field, a particle with rest mass m and charge Ze, moving through a uniform, static magnetic field $\boldsymbol{B}$, with velocity $\boldsymbol{v}$ and Lorentz factor $\gamma = \left(1 - \left(\frac{v}{c}\right)^2\right)^{-\frac{1}{2}}$, will experience a force (in c.g.s. units)

$$\frac{\mathrm{d}}{\mathrm{d}t}(\gamma m \boldsymbol{v}) = \frac{Ze}{c}(\boldsymbol{v} \times \boldsymbol{B}). \tag{2.27}$$

This results in acceleration perpendicular to the direction of travel of the particle (Longair, 2010; Beckmann and Shrader, 2012). The particle will then move with a constant velocity in the direction of the magnetic field while gyrating around the field lines with a constant pitch angle θ and radius

$$r_g = \frac{v_\perp \gamma m c}{ZeB}, \tag{2.28}$$

where $v_\perp$ is the velocity component perpendicular to the magnetic field. The frequency of this gyration, known as the gyrofrequency, is given by

$$\nu_g = \frac{1}{2\pi}\frac{v_\perp}{r_g} = \frac{ZeB}{2\pi\gamma mc}. \tag{2.29}$$

Such a particle then radiates a spectrum of synchrotron emission that is strongly peaked near the critical frequency

$$\nu_c = \frac{3Ze\gamma^2 B \sin\theta}{4\pi mc} = \frac{3}{2}\gamma^3 \nu_g \sin\theta. \tag{2.30}$$

The energy per unit time and unit frequency radiated by a single electron[5] is

$$P_\nu^{\mathrm{sync}} = \frac{\sqrt{3}e^3 B \sin\theta}{mc^2} F\left(\frac{\nu}{\nu_c}\right), \tag{2.31}$$

where $F\left(\frac{\nu}{\nu_c}\right)$, shown in Figure 2.5, is the function defined by

$$F(x) = x\int_x^\infty K_{5/3}(z)\,\mathrm{d}z, \tag{2.32}$$

and $K_{5/3}$ is a modified Bessel function (Rybicki and Lightman, 1991; Longair, 2010; Beckmann and Shrader, 2012). The total energy radiated by an electron per unit of time is then

$$P^{\mathrm{sync}} = \int_0^\infty P_\nu^{\mathrm{sync}}\,\mathrm{d}\nu = 2\sigma_T c U_B \gamma^2 \sin^2\theta, \tag{2.33}$$

where $\sigma_T = \frac{8\pi}{3}\left(\frac{e^2}{mc^2}\right)^2$ is the Thomson cross section and $U_B = \frac{B^2}{8\pi}$ is the magnetic energy density (Rybicki and Lightman, 1991; Longair, 2010).

[5]Discussions of synchrotron radiation are usually based on electrons (or positrons) as they radiate much more efficiently than heavier particles such as protons. The particle charge is then $Ze = e$.

For an isotropic distribution of pitch angles, this can be averaged over solid angle to give

$$P^{\text{sync}} = \frac{4}{3}\sigma_T c U_B \gamma^2. \tag{2.34}$$

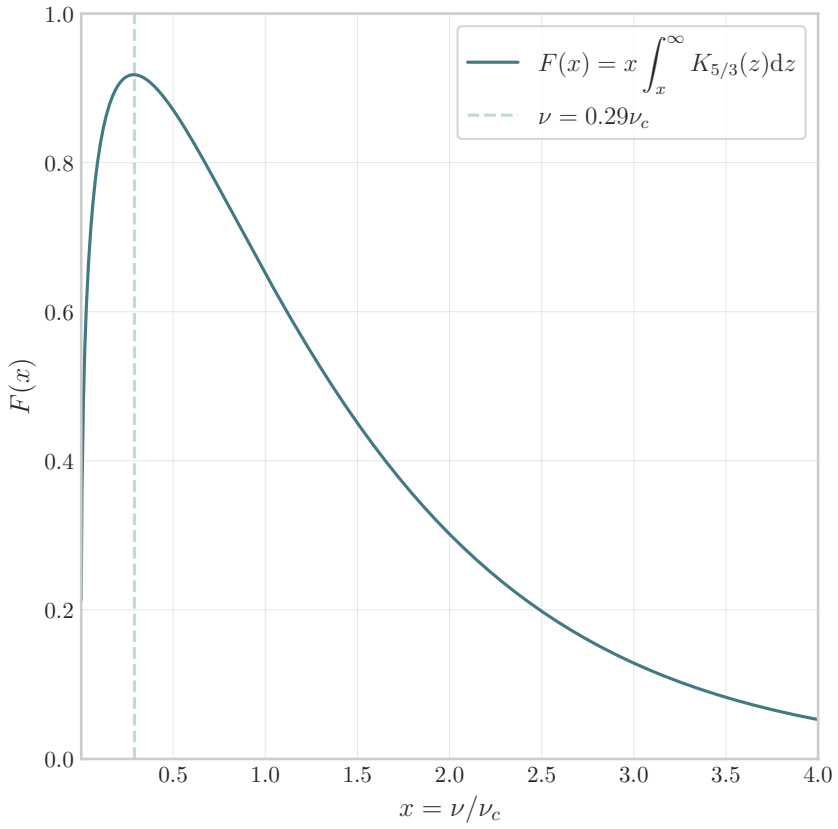

Figure 2.5: Plot of the function $F(\frac{\nu}{\nu_c})$ that determines the shape of the synchrotron spectrum of a single electron. The function peaks at $\nu \approx 0.29\nu_c$.

For a population of electrons with energies between E_{min} and E_{max}, the total synchrotron emissivity is

$$\epsilon_\nu^{\text{sync}}(\nu, \theta) = \int_{E_{\text{min}}}^{E_{\text{max}}} P_\nu^{\text{sync}}(E, \nu, \theta) n(E)\, \mathrm{d}E, \tag{2.35}$$

where $n(E)\,\mathrm{d}E$ is the number density of electrons with energies between E and $E + \mathrm{d}E$. The electron population of synchrotron sources typically follows a power-law distribution of electron energies,

$$n(E)\,\mathrm{d}E = \kappa E^{-p}\,\mathrm{d}E, \tag{2.36}$$

where κ is a normalisation factor of the power law, and p is the power-law index (Beckmann and Shrader, 2012; Longair, 2010). Assuming such a power-law distribution and an isotropic distribution of pitch angles, the emissivity is

$$\epsilon_\nu^{\text{sync}}(\nu) = \frac{16\pi^2 \kappa e^3}{(mc^2)^p} \left(\frac{3e}{4\pi mc}\right)^{\frac{p-1}{2}} B^{\frac{p+1}{2}} \nu^{-\frac{p-1}{2}} a(p) \tag{2.37}$$

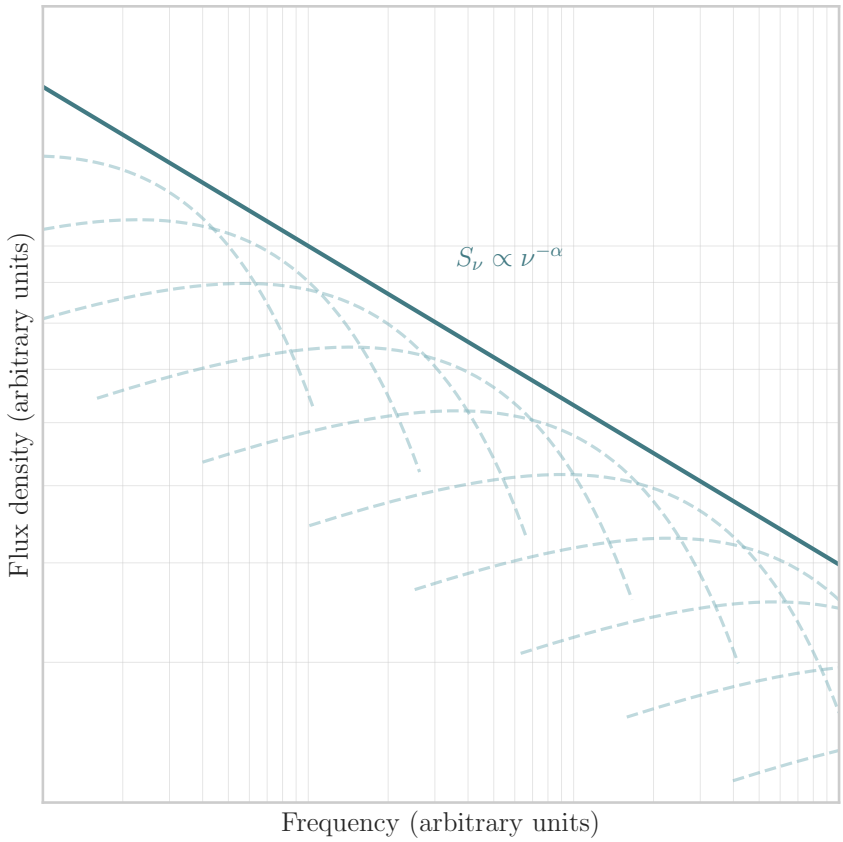

Figure 2.6: Illustration of the synchrotron spectrum on a logarithmic scale. The dashed curves represent the synchrotron spectra from electrons at specific energies. If the electron population follows a power law, the superposition of the different spectra results in a power-law spectrum.

where the function $a(p)$ depends on the gamma function $\Gamma(x)$ and is defined as

$$a(p) = \frac{2^{(p-1)/2}\sqrt{3}\Gamma\left(\frac{3p-1}{12}\right)\Gamma\left(\frac{3p+19}{12}\right)\Gamma\left(\frac{p+5}{4}\right)}{8\sqrt{\pi}(p+1)\Gamma\left(\frac{p+7}{4}\right)}, \tag{2.38}$$

with values tabulated by Blumenthal and Gould (1970). Therefore, the flux density at frequency ν follows a power-law spectrum, shown in Figure 2.6, that can be described as

$$S_\nu \propto \nu^{-\alpha}, \tag{2.39}$$

where $\alpha = (p-1)/2$ is known as the spectral index (Longair, 2010). The gradient of the synchrotron spectrum can be used to determine the slope of the electron energy distribution (Beckmann and Shrader, 2012).

The energy density of an electron population described by equation (2.36) is

$$U_\mathrm{e} = \int_{E_\mathrm{min}}^{E_\mathrm{max}} n(E)E\,\mathrm{d}E \propto E_\mathrm{max}^{2-p} - E_\mathrm{min}^{2-p}. \tag{2.40}$$

Since an electron with energy E emits most of its radiation at a frequency $\nu \sim \nu_c \propto E^2 B$, this is approximately equivalent to

$$U_\mathrm{e} \propto B^{\frac{p-2}{2}}\left(\nu_\mathrm{max}^{(2-p)/2} - \nu_\mathrm{min}^{(2-p)/2}\right). \tag{2.41}$$

Because the total integrated flux is

$$S = \int_{\nu_{\min}}^{\nu_{\max}} S_\nu \, \mathrm{d}\nu \propto B^{\frac{p+1}{2}} \left(\nu_{\max}^{(2-p)/2} - \nu_{\min}^{(2-p)/2} \right), \tag{2.42}$$

the electron energy density can be written as

$$U_\mathrm{e} \propto S B^{-\frac{3}{2}}. \tag{2.43}$$

Assuming that the proton energy density is $U_\mathrm{p} = \eta U_\mathrm{e}$, the energy density of the particles can be described as

$$U_\mathrm{particles} = U_\mathrm{e} + U_\mathrm{p} \propto (1+\eta) S B^{-\frac{3}{2}}. \tag{2.44}$$

The total energy density in equation (2.26) then has a minimum when

$$U_B = \frac{3}{4} U_\mathrm{particles} = \frac{3}{4}(1+\eta) U_\mathrm{e}. \tag{2.45}$$

By assuming that the total energy density is at a minimum, or that the magnetic and particle energy densities are near equipartition, the magnetic field can be estimated.

As time (t) passes, electrons lose energy by radiating synchrotron emission. From equation (2.33), the energy loss rate for an electron with energy $E = \gamma m c^2$ is $-\frac{\mathrm{d}E}{\mathrm{d}t} \propto \gamma^2 \propto E^2$, which means that energetic electrons will lose energy faster than less energetic electrons. This creates a break in the spectrum from which the age of the source can be estimated. Assuming a single injection of electrons, an aged electron population can be described with

$$n(E,t) = \kappa E^{-p} \left(1 - ECt\right)^{p-2}, \tag{2.46}$$

where C is the constant such that $\frac{\mathrm{d}E}{\mathrm{d}t} = -CE^2$ (Harwood *et al.*, 2013). The value of C used in spectral ageing models depends on the presence (Jaffe and Perola, 1973) or absence (Kardashev, 1962; Pacholczyk and Roberts, 1971) of pitch angle scattering. Figure 2.7 shows the ageing of a synchrotron spectrum with the free-streaming Tribble (1993) model, where the losses described by Jaffe and Perola (1973) are integrated over a Maxwell–Boltzmann distribution of magnetic field strengths (Harwood *et al.*, 2013; Hardcastle, 2013).

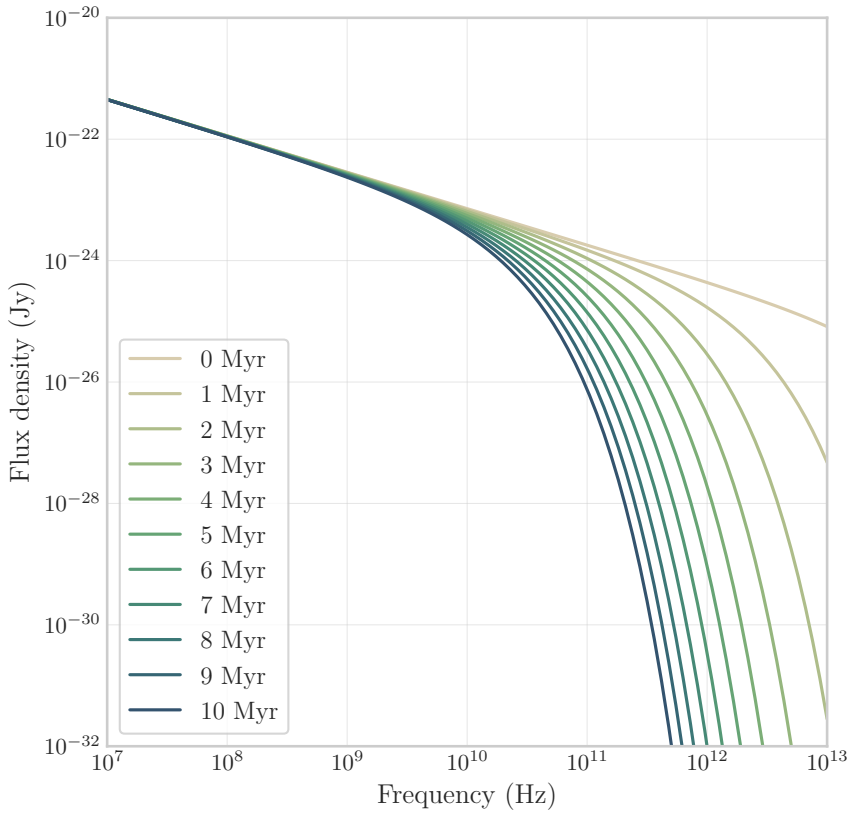

Figure 2.7: Synchrotron spectra for different spectral ages using the Tribble model (Tribble, 1993), created with BRATS (Harwood *et al.*, 2013, 2015).

2.2.1.2 Inverse-Compton Scattering

IC scattering occurs when low-energy photons are scattered to high energies by relativistic electrons. In the lobes of radio galaxies, the dominant photon population is the CMB, while synchrotron self-Compton—where synchrotron photons are upscattered by the same electron population that produced the synchrotron radiation—is more significant in the hot spots (Croston *et al.*, 2005). In the Thomson limit, where the photon energy is much lower than the electron energy in the rest frame of the electron, the total energy per unit time radiated by the electron due to IC scattering is

$$P^{\mathrm{IC}} = \frac{4}{3}\sigma_T c U_{\mathrm{rad}} \gamma^2, \tag{2.47}$$

where U_{rad} is the energy density of the radiation (Longair, 2010). This is identical to equation (2.34), apart from the energy density of radiation replacing the magnetic energy density; therefore,

$$\frac{P^{\mathrm{sync}}}{P^{\mathrm{IC}}} = \frac{U_B}{U_{\mathrm{rad}}} = \frac{1}{8\pi}\frac{B^2}{U_{\mathrm{rad}}}. \tag{2.48}$$

Studying IC emission provides a method of estimating the magnetic field without relying on equipartition assumptions. However, this is not trivial, especially in galaxy clusters where the

thermal emission from the ICM dominates (Hardcastle and Croston, 2010). In addition, the relativistic particles responsible for synchrotron radiation at the frequencies of telescopes like MeerKAT scatter photons to much higher energies than detectable by soft X-ray telescopes like *XMM-Newton*. Directly calculating the magnetic field in this way requires low-frequency radio and hard X-ray observations, or the assumption that the power-law electron population in equation (2.36) holds down to low energies (Bartels *et al.*, 2015).

2.2.2 Classification Schemes

The radio morphology of radio galaxies can vary significantly. Some of the observed characteristics are due to inherent properties of the jets, such as their initial power. Others are indicative of the jet's interaction with the ICM, or just a result of the viewing angle. This section describes different classification schemes for radio galaxies based on their morphological and spectral characteristics.

2.2.2.1 Fanaroff–Riley Classification

Fanaroff and Riley (1974) proposed a classification scheme for radio galaxies based on the morphology and radio luminosity of the emission. Radio galaxies with low radio luminosities, typically less than $10^{32}\,\mathrm{erg\,s^{-1}\,Hz^{-1}}$ at 1.4 GHz (Schneider, 2014), with the brightest regions close to the core, became known as Fanaroff–Riley Class I (FR-I) sources, while higher-luminosity radio galaxies with the brightest regions towards the edges were classified as Fanaroff–Riley Class II (FR-II). Most of the emission from FR-II sources comes from bubbles of material inflated by the jets, known as lobes, while FR-I jets often fade into wider plumes or tails as they extend into the ICM, or inflate weaker lobes (Laing *et al.*, 2011). This classification shaped the framework for studying extragalactic radio sources, and is still used extensively in literature (Fanaroff *et al.*, 2021). The two classes are illustrated in Figure 2.8.

However, some radio galaxies do not fit clearly into this dichotomy, including hybrid radio galaxies with two lobes with different Fanaroff–Riley morphologies (Gopal-Krishna and Wiita, 2000), and low-luminosity, core-dominated "FR-0" radio galaxies, lacking the kiloparsec-scale extended radio emission present in FR-I sources (Baldi, 2023).

Similar to the Fanaroff–Riley classification, jets are sometimes described as strong-flavoured or weak-flavoured. Strong-flavoured jets are usually associated with FR-II sources. These are well-collimated jets found in powerful sources that usually form luminous lobes. As strong-

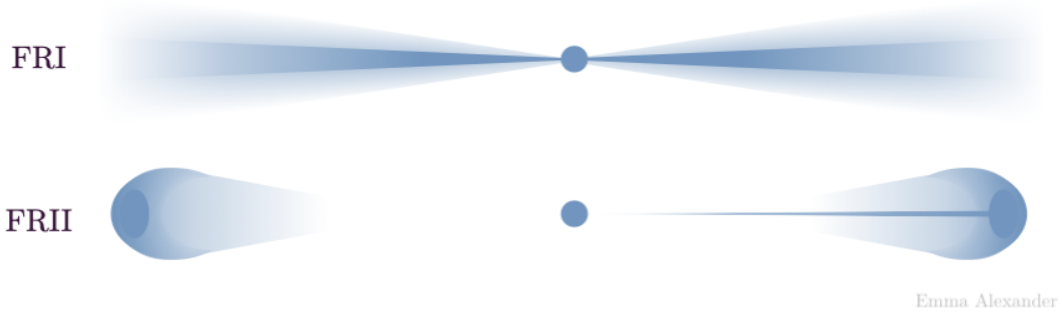

Figure 2.8: FR-I and FR-II radio galaxies by Alexander (2022a). FR-I sources are centre-brightened, while FR-II sources are edge-brightened.

flavoured jets are narrow, these jets are more difficult to detect. Weak-flavoured jets, found in FR-I sources, are easier to detect. These jets are initially well-collimated and faint, but then brighten and flare, often before recollimating. They usually terminate in diffuse lobes or winding plumes. While jets of both flavours are initially relativistic, it is believed that weak-flavoured jets decelerate to subrelativistic speeds faster than strong-flavoured jets (Böttcher *et al.*, 2012; Laing and Bridle, 2014).

2.2.2.2 Bent-tailed Sources

Some radio galaxies exhibit bent jets, which often end in tails similar to those in FR-I sources. Bent-tailed radio galaxies are strongly, though not exclusively, associated with galaxy clusters (Garon *et al.*, 2019), and with merging clusters in particular (Gómez *et al.*, 1997). In cluster environments, jets interact with the ICM in various ways, leading to complex jet morphologies, including V-shaped or U-shaped radio galaxies, where the jets are bent in the same direction, S-shaped radio galaxies with jets bent in opposite directions, and sources with twists that are too convoluted for simple descriptions. Bent-tailed sources can be produced by ram pressure due to the motion of the host galaxy relative to the ICM or due to cluster mergers. Recently, Chibueze *et al.* (2021) used three-dimensional magnetohydrodynamics (MHD) simulations to show that intracluster magnetic fields can cause the bending of jets. The interaction between jets and the ICM is further discussed in Section 2.3.

Radio galaxies with jets bent in the same direction are sometimes divided into wide-angle tail (WAT) radio galaxies and narrow-angle tail (NAT) radio galaxies. WATs are often associated with the BCG in a cluster and typically have higher radio luminosities than NATs, closer to FR-II luminosities (Owen and Rudnick, 1976; O'Donoghue *et al.*, 1993; Missaglia *et al.*, 2019). In some definitions of these classes, radio galaxies are grouped based on the opening angle between

the jets, with WATs typically having angles greater than 90° (Sasmal *et al.*, 2022). However, this is subject to misclassification due to projection effects. Other definitions of WATs require the inner jets to remain well-collimated on kiloparsec scales before abruptly transforming into diffuse bending plumes (Hardcastle and Sakelliou, 2004; Jetha *et al.*, 2005; Saikia, 2022). While the inner parts of WATs in this definition resemble FR-II radio galaxies, the disruption of the jet occurs at the base of the plume, not at the end of the source (Hardcastle and Sakelliou, 2004).

Some authors treat WATs and NATs as entirely different types of objects (O'Dea and Owen, 1985; O'Dea and Baum, 2023), while others believe that the distinction is highly subjective and prefer to use the term *bent-tailed radio galaxies* for all radio galaxies with bent jets (Dehghan *et al.*, 2014; Riseley *et al.*, 2022). This work will adopt this latter umbrella term and use the terms WATs or NATs only in the context of the historical classification of sources.

2.2.2.3 Remnant and Restarted Radio Galaxies

At a certain point in the lifetime of a radio galaxy, it enters a remnant phase as the activity at the AGN slows down or stops, and the outflow of material ceases. These radio galaxies are known as remnant radio galaxies (Duchesne and Johnston-Hollitt, 2019; Quici *et al.*, 2021), dying radio galaxies (Murgia *et al.*, 2011; Oozeer *et al.*, 2021), or relic[6] radio galaxies (Cordey, 1987; Komissarov and Gubanov, 1994). When this phase starts, the compact components of the radio galaxy will begin to fade, but the extended lobes can remain detectable for more than $\sim 10^7$ years at low frequencies (Shulevski *et al.*, 2017; Brienza *et al.*, 2017). Once the injection of new particles ends, the spectrum of the lobes will rapidly steepen, since high-energy electrons lose energy faster than low-energy electrons due to synchrotron losses (see equation (2.33)) (Komissarov and Gubanov, 1994).

After a period of AGN quiescence, the jet activity may start up again (Saikia and Jamrozy, 2010). If the remnant lobes have not completely faded by this time, the restarted radio galaxy can have two (or more) pairs of lobes, such as the double–double radio galaxies identified by Schoenmakers *et al.* (2000).

[6]The term *relic* is often ambiguously used for a variety of steep-spectrum sources including remnant radio galaxies, cluster radio shocks (see Section 2.1.5.2), and phoenix sources (see Section 2.3.3) (Kempner *et al.*, 2004).

2.2.3 Components of Radio Galaxies

In the basic beam model, radio galaxies consist of AGNs at their centres that power large-scale jets. The jets, interacting with their environments, can inflate lobes or fade into wide plumes. Bright, compact knots and hotspots along the jets and lobes are usually interpreted as the manifestation of internal shocks along the jets. These components are discussed in detail here.

2.2.3.1 Active Galactic Nuclei

Radio galaxies are a type of active galaxy. These are galaxies that emit strong radiation across the electromagnetic spectrum, originating mainly from powerful AGNs at their centres (Schneider, 2014). AGNs are believed to be powered by the accretion of matter from an accretion disc onto supermassive black holes. In some AGNs, the accretion disc produces two collimated relativistic jets of ionised matter launched in opposite directions from the vicinity of the disc.

While the exact nature of the formation of jets is still unknown, they are believed to be launched from close to the accretion disc as rotational energy is extracted from the black hole. An important mechanism for powering the jets is the Blandford-Znajek process (Blandford and Znajek, 1977). In this process, a rotating black hole drags the magnetic field lines threading the accretion disc, accelerating matter into relativistic jets along the direction of the rotation axis as the field lines tighten (Beckmann and Shrader, 2012).

Less than 1% of AGNs have a radio-to-optical flux ratio greater than 10 (Padovani, 2011) and are commonly classified in literature as radio-loud[7] AGNs. A significant portion of the radio emission in radio-loud AGNs is associated with synchrotron emission from jets, whereas jets are absent or weak in radio-quiet AGNs (Contopoulos *et al.*, 2015).

The presence or absence of strong jets, their orientation with respect to the observer, and the amount of obscuration by a dusty torus surrounding the nucleus can lead to large variations in the observed properties of AGNs. This has led to many distinct historical classifications that are now believed to describe objects that are intrinsically the same under the currently favoured unified models of AGNs (Urry and Padovani, 1995; Padovani *et al.*, 2017). Blazars, which are powerful sources of emission across the electromagnetic spectrum, are AGNs with a jet pointing very close to the line of sight of the observer ($\lesssim 15-20^{\circ}$) (Padovani *et al.*, 2017). The high brightness of blazars can be attributed to relativistic beaming of the nonthermal radiation of

[7] Some authors argue against the *radio-loud* and *radio-quiet* classification and instead suggest the use of *jetted* and *non-jetted* (Padovani, 2017).

the jet pointed towards the observer (Padovani *et al.*, 2017). In contrast, radio galaxies have jets that are pointed close to perpendicular to the line of sight. This orientation makes it possible to observe the extended structure of the jets. Active galaxies with less prominent or absent jets include Seyfert galaxies. Historically, Seyfert galaxies exhibiting broad emission lines and those that don't, were classified as Seyfert Type I and II galaxies, respectively (Khachikian and Weedman, 1974). Most Seyfert galaxies are considered radio quiet (Komossa *et al.*, 2006). The unified model of AGNs is illustrated in Figure 2.9.

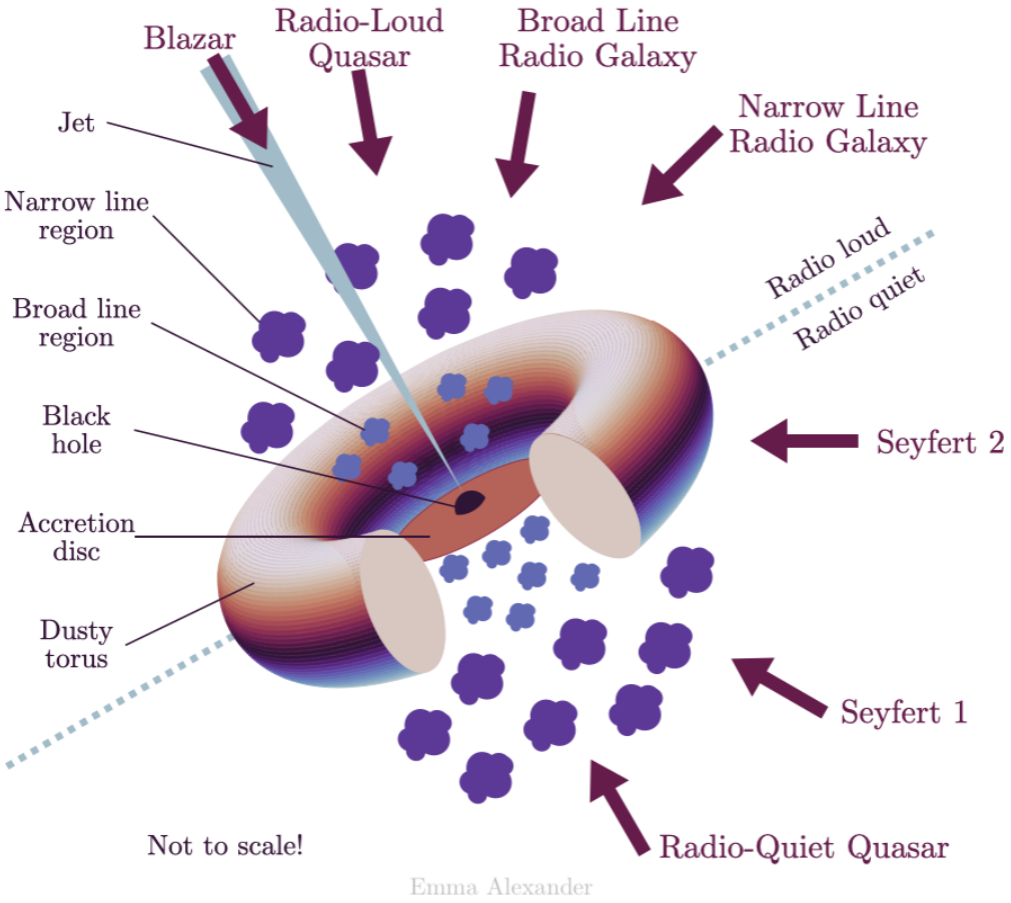

Figure 2.9: Unified model of AGNs by Alexander (2022b), adapted from Urry and Padovani (1995), showing the observed objects at different viewing angles for radio-loud and radio-quiet AGN.

2.2.3.2 Jets

The exact composition of the jets is still unclear. While jets are believed to be initially dominated by Poynting flux, they are later converted into particle-dominated plasma (Saikia, 2022). Possible compositions discussed in the literature include electron-positron pair plasma, electron-proton plasma, and electron-positron-proton plasma (Petropoulou *et al.*, 2019).

Jets are initially collimated and accelerated within $\lesssim 10^6$ gravitational radii of the black hole,

after which they often change from parabolic to conical in shape (Kovalev *et al.*, 2020; Park *et al.*, 2021; Yi *et al.*, 2024). After the initial expansion, jets often re-collimate and can remain well-collimated on scales of hundreds of kiloparsecs (Lapenta and Kronberg, 2005).

The observed characteristics of jets are highly dependent on the viewing angle. Due to Doppler boosting, approaching jets can appear very bright, while receding jets appear faint or undetectable. Projection effects can also exaggerate or conceal bends in jets. Additionally, resolved jet components may exhibit superluminal motion, appearing to travel faster than the speed of light when observed at small angles (Böttcher *et al.*, 2012).

2.2.3.3 Lobes and Plumes

Some jets gradually widen into plumes or tails, often winding and bending as a result of their interaction with the ICM (Hardcastle *et al.*, 2005). Others end in extended radio lobes surrounding the jets, inflated by material that passed along the jet (Contopoulos *et al.*, 2015).

Spectral ageing studies of lobes are often used to estimate the age of radio galaxies. However, these studies tend to underestimate the ages by an order of magnitude compared to those determined through dynamical arguments (Eilek, 1996). Spectral ageing studies of 100-kiloparsec-scale lobes tend to give ages of $\sim$10 Myr, while estimates based on the size and expansion rate can reach 100 Myr (Hardcastle and Croston, 2020). This is likely due to a combination of factors such as *in situ* particle acceleration, an overestimation of magnetic field strengths with equipartition arguments, and the mixing of old and young electron populations in lobes (Hardcastle and Croston, 2020).

2.2.3.4 Knots and Hot Spots

Many radio galaxies have bright, compact regions or knots along their jets or lobes. The brightest of these regions are known as hot spots. Bridle *et al.* (1994) define a hot spot as the brightest feature in a lobe, with surface brightness more than four times greater than that of its surroundings, and a linear full width at half maximum (FWHM) that is less than 5% of the largest diameter of the source. Hot spots typically appear in the lobes of FR-II radio galaxies, where they are interpreted to be the manifestation of shocks that form when the relativistic beam of particles abruptly decelerates (Blandford and Rees, 1974; Meisenheimer *et al.*, 1989).

2.3 Jet–Cluster Interactions

Radio galaxies in clusters interact with their environments in ways that shape the physical properties of both the jets and the surrounding ICM. This section explores some of these interactions, including the formation of X-ray cavities, the effect of ram pressure on jets, and particle re-acceleration in radio galaxy plasma.

2.3.1 X-ray Cavities

One of the clearest signs of interaction between radio galaxies and the ICM is the formation of X-ray cavities where expanding radio lobes displace the X-ray-emitting ICM (Bîrzan *et al.*, 2004). These cavities manifest as depressions in the X-ray surface brightness of the ICM emission. The formation of cavities may contribute to the quenching of cooling flows (Bîrzan *et al.*, 2004; Pandge *et al.*, 2021).

2.3.2 Ram Pressure Bending

Radio galaxies can experience ram pressure due to the motion of the host galaxy relative to the cluster, or the bulk motion of ICM as a result of cluster mergers. The ram pressure could bend the jets in the direction opposite to the direction of motion. This bending can be described by the equation

$$\frac{\rho_{\rm jet} v_{\rm jet}^2}{R} \approx \frac{\rho_{\rm ICM} v_{\rm gal}^2}{h}, \tag{2.49}$$

where $\rho_{\rm jet}$ and $\rho_{\rm ICM}$ are the densities of the jet and ICM respectively, $v_{\rm jet}$ is the velocity of the jet, $v_{\rm gal}$ is the velocity of the galaxy relative to the ICM, R is the radius of curvature of the bending, and h is the radius of the jet (Burns and Owen, 1980; Garon *et al.*, 2019; O'Dea and Baum, 2023). However, ram pressure alone is often not able to explain the degree of bending of jets associated with the BCG, which usually do not have a large velocity relative to the ICM (Garon *et al.*, 2019; Gendron-Marsolais *et al.*, 2021). In some extreme cases, jets bend in the same direction as the motion of the radio galaxy relative to the ICM, and alternative explanations are needed to explain the bending (Chibueze *et al.*, 2022).

2.3.3 Re-accelerated AGN Plasma Sources

Interaction with the ICM can re-accelerate plasma from radio galaxies. Radio phoenices are revived sources of fossil plasma from remnant radio galaxies that have been re-accelerated through adiabatic compression by a passing shock wave (Ensslin *et al.*, 2001; Kempner *et al.*, 2004; Van Weeren *et al.*, 2009; de Gasperin *et al.*, 2015). They often have irregular filamentary morphologies (Van Weeren *et al.*, 2019).

Radio galaxy jets can also experience 'gentle' re-acceleration, such as the gently re-energised tail source studied by de Gasperin *et al.* (2017). This source is a radio galaxy tail that shows unexpected brightening and spectral flattening, contrary to what is expected from synchrotron losses. A similar case of brightening and spectral flattening in the tail of a bent-tailed radio galaxy was reported by Chibueze *et al.* (2021) (see Section 2.4.3).

2.4 Review of Selected Clusters

This section provides an overview of the galaxy clusters that will be studied in this work: Abell 133, Abell 3266, Abell 3376, and the interacting system of clusters Abell 3391 and Abell 3395. These clusters have been selected due to their complex X-ray morphologies and the presence of unusual radio galaxies, suggesting intricate underlying dynamical processes. The following sections summarise the key characteristics of each cluster and review previous findings relevant to understanding their dynamical states and the interactions between radio galaxies and the ICM.

2.4.1 Abell 133

Abell 133 is a cool-core galaxy cluster located at a redshift of $z = 0.0569$ (Planck Collaboration, 2015). Observations from *Chandra* (Fujita *et al.*, 2002) and *XMM-Newton* (Fujita *et al.*, 2004) revealed a "tongue" of X-ray emission from cool gas extending from the centre of the cluster towards the northwest, with faint "wings" extending northeast and southwest, forming a bird-like structure. Fujita *et al.* (2004) reported a cold front towards the southeast of the core and a possible weak shock that passed from southeast to northwest through the core. Randall *et al.* (2010) also reported a weak surface brightness edge surrounding the core, consistent with a

sloshing cold front. The BCG is a cD galaxy[8], with an optical position that aligns with the peak X-ray emission but is located southeast of the X-ray centroid on large scales (Fujita *et al.*, 2004). This complex morphology is indicative of a highly disturbed cluster core (Randall *et al.*, 2010).

In a *Chandra* study of Abell 133 up to a radius of $r \simeq 1000\,\mathrm{kpc}$, Vikhlinin *et al.* (2005) reported a nearly solar metallicity ($Z_\odot$) at the centre of the cluster, which decreases to $Z \simeq 0.2\,Z_\odot$ at larger radii. They also reported a temperature of $T = 4.60 \pm 0.15\,\mathrm{keV}$ at a radius of $r = 170\,\mathrm{kpc}$, decreasing to $T = 1.8 \pm 0.6\,\mathrm{keV}$ towards the outskirts. Within the inner 70 kpc, the temperature drops sharply, likely due to radiative cooling.

Abell 133 is associated with extremely steep-spectrum radio emission with a complex morphology, the nature of which has long been debated (Rizza *et al.*, 2000; Slee *et al.*, 2001; Randall *et al.*, 2010). A compact radio source coincides with the optical position of the cD galaxy. A filamentary structure with a very steep spectral index appears roughly 30 arcsec north of this position. This structure is often classified in the literature as a radio relic (Slee *et al.*, 2001; Fujita *et al.*, 2004). While Rizza *et al.* (2000) used 1.4 GHz Very Large Array (VLA) observations to suggest the existence of a bridge of emission between the compact source and the relic, Slee *et al.* (2001) found no convincing evidence of such a connection with higher sensitivity and resolution VLA observations at the same frequency. However, Randall *et al.* (2010) detected a possible connection in their 330 MHz VLA image.

There is partial overlap between the filamentary structure and the X-ray tongue. Fujita *et al.* (2002, 2004) proposed that the tongue could be produced either by Kelvin-Helmholtz instabilities as the cold gas surrounding the cD galaxy interacts with the hot, lower-density ICM or by being uplifted by the motion of a buoyant bubble of nonthermal plasma, which they identified with the filamentary radio structure. The second possibility is supported by Randall *et al.* (2010), who also suggested that it may be a gas-sloshing spiral viewed edge-on instead. Fujita *et al.* (2004) argued that the wings of the bird-like structure could have formed as a weak shock passed through the core, but Randall *et al.* (2010) suggested that the wings result from two X-ray cavities on either side of the tongue, formed by the displacement of X-ray gas by the radio relic.

Other prominent compact radio sources include those 54 arcsec west and 1.53 arcmin southeast of the cD galaxy (Randall *et al.*, 2010; Slee *et al.*, 2001). Redshift calculations of their optical

[8] cD is a galaxy classification, where *D* refers to an elliptical-like nucleus surrounded by an extensive envelope, and the prefix *c* is given to the very large galaxies that appear in clusters (Matthews *et al.*, 1964).

counterparts place the former inside the cluster at $z = 0.0563$ (Slee *et al.*, 1996) and the latter at $z = 0.2930$ (Owen *et al.*, 1995). Randall *et al.* (2010) discovered large-scale radio structures extending north and south of the southern compact source, which they interpreted as the jets of a radio galaxy. As shown in Figure 2.10, the northern jet extends up to the cluster core. The "relic" could be the northern lobe of the radio galaxy or overlap with it in projection. The southern jet terminates in a diffuse lobe roughly 3.2 arcmin south of the southern compact source.

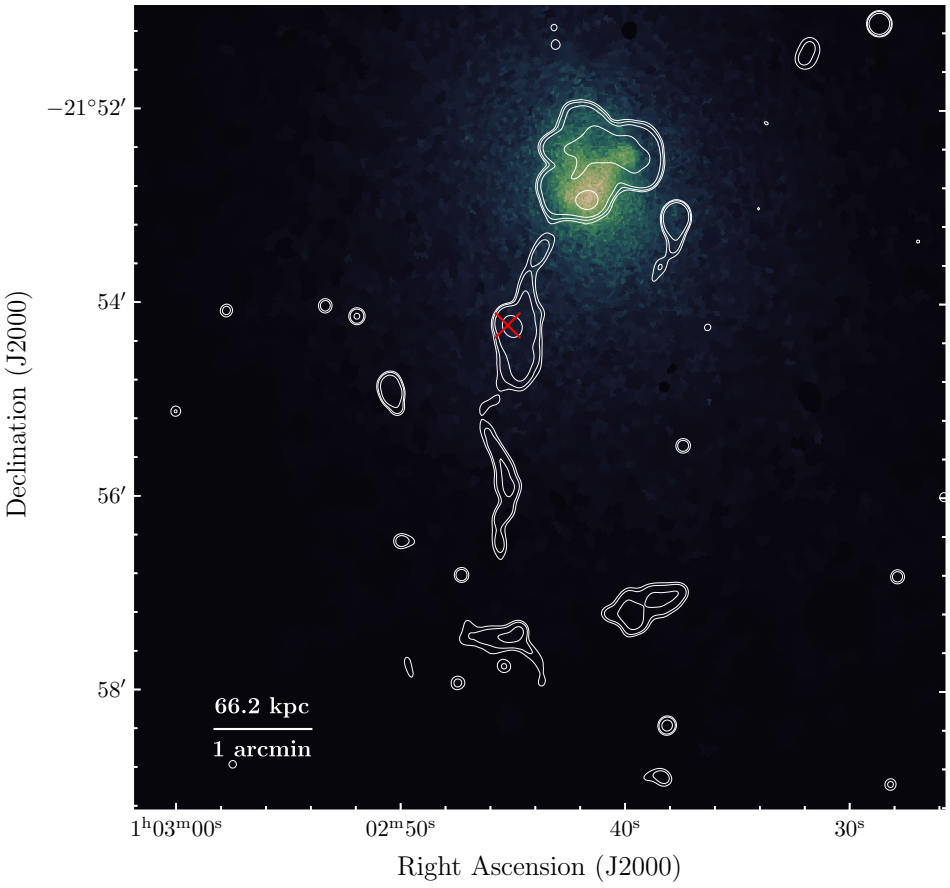

Figure 2.10: *Chandra* image of Abell 133 in the 0.5 – 3.0 keV, reproduced from Zhu *et al.* (2023), with contours of the 1.28 GHz MGCLS Data Release 1 image (Knowles *et al.*, 2022) overlaid. The red cross marks the position of an optical galaxy at redshift $z = 0.2930$.

Even before the discovery of the large-scale radio structures, Slee *et al.* (2001) considered the possibility that the relic could be a lobe with a counterpart to the southeast. However, this was dismissed as the relic is shown to be interacting with the cluster at $z = 0.0569$, while the emission towards the southeast was associated with the galaxy at $z = 0.2930$. This is still an unresolved problem, for which Randall *et al.* (2010) considered three possible solutions: the radio galaxy could be associated with Abell 133, with merely coincidental overlap with the optical galaxy and the relic; the core and the jet could be associated with the optical source at $z = 0.2930$, with coincidental alignment with lobes unrelated to this source; or the radio galaxy, including the

lobes, is located at $z = 0.2930$, with coincidental overlap between the relic and the northern lobe. They concluded that the third possibility required the fewest coincidences to occur, implying a giant radio galaxy with a total extent of 1.6 Mpc, compared to 400 kpc at $z = 0.0569$.

The radio emission from the cD galaxy and the southern compact source has a relatively flat spectrum (though quite steep for cores) with a spectral index of $\alpha \lesssim 1.2$, while the extended emission in the jets and lobes is very steep with $\alpha \gtrsim 2$. Randall *et al.* (2010) suggested that some steepening in the compact sources might be due to contamination from nearby diffuse emission, as the flattest spectral index values in these regions are slightly offset from the cores in the opposite direction than the brightest diffuse emission. In the framework of a giant radio galaxy at $z = 0.2930$, Randall *et al.* (2010) calculated that the background northern lobe would not significantly affect the spectral index of the relic if the two lobes have equal flux, although the authors acknowledged that this assumption might not be valid.

Despite the thorough evaluation by Randall *et al.* (2010), the proposed scenario requires the unusual overlap between a relic and a radio galaxy with a similar anomalously steep spectrum. Therefore, it would be valuable to consider an alternative interpretation where the radio galaxy is indeed at the redshift of the cluster. In this scenario, the northern lobe might contribute to, or in itself be, the so-called relic.

2.4.2 Abell 3266

Abell 3266, often referred to in older literature as Sérsic 40/6, is a massive galaxy cluster and a very bright X-ray source, with a mass of $6.64^{+0.11}_{-0.12} \times 10^{14}\,\mathrm{M}_\odot$ (Planck Collaboration, 2016) and a flux of $5.8 \times 10^{-11}\,\mathrm{erg\,s^{-1}\,cm^{-1}}$ at $0.1-2.4\,\mathrm{keV}$ (Reiprich and Boehringer, 2002). Located at a redshift of $z = 0.0589$ (Planck Collaboration, 2015), Abell 3266 is a member of the Horologium-Reticulum supercluster, one of the largest superclusters in the local Universe, containing over 20 Abell clusters (Fleenor *et al.*, 2005). It is a well-known merging cluster with a complex X-ray morphology (De Grandi and Molendi, 1999; Henriksen and Tittley, 2002; Sanders *et al.*, 2022), a central cD galaxy with a dumbbell shape (Quintana *et al.*, 1996), and several radio structures, including a large-scale halo, a cluster radio shock, fossil plasma sources, and multiple radio galaxies (Rudnick *et al.*, 2021; Riseley *et al.*, 2022; Duchesne *et al.*, 2022). It is a hot cluster, with temperatures $\sim$8 keV reported near the centre, decreasing to $\sim$4 keV at larger radii (Sanders *et al.*, 2022). The X-ray surface brightness of the central region of the cluster is elongated in the northeast–southwest direction, which is typically considered the merger axis (Henriksen *et al.*, 2000). The position of the cD galaxy aligns with the peak X-ray emission,

which is offset from the larger centroid of the emission (Henriksen and Tittley, 2002).

Abell 3266 has been a topic of interest since the early days of X-ray astronomy (Maccagni *et al.*, 1978; Quintana and Melnick, 1982). Significant substructure detected in X-ray observations (Mohr *et al.*, 1993), simulations of cluster formation (Evrard, 1990), and optical studies showing a radial gradient in the velocity dispersion of the galaxies in the cluster (Quintana *et al.*, 1996) provided some of the first evidence of a merging event along the northeast–southwest axis. This has since been confirmed by numerous studies using instruments such as *BeppoSAX* (De Grandi and Molendi, 1999), the *Advanced Satellite for Cosmology and Astrophysics* (*ASCA*) (Henriksen *et al.*, 2000), *Chandra* (Henriksen and Tittley, 2002), and *XMM-Newton* (Sauvageot *et al.*, 2005; Finoguenov *et al.*, 2006).

Sauvageot *et al.* (2005) favoured a merging scenario where a subcluster approached the main cluster from the northeast and passed its core approximately $0.15-0.20\,\mathrm{Gyr}$ ago. Henriksen and Tittley (2002) identified an extended filamentary region of slightly cooler gas running through the central cD galaxy along the merger axis. This corresponds to an extended region of low-entropy gas detected by Finoguenov *et al.* (2006), who concluded that it is likely stripped gas from the infalling subcluster. An alternative scenario, where the subcluster initially approached from the southwest, was proposed by Henriksen *et al.* (2000) and Sauvageot *et al.* (2005). In this case, Sauvageot *et al.* (2005) suggested that the subcluster would have passed the core around $0.8\,\mathrm{Gyr}$ ago and would now be nearing turnaround. While some sources disagree (Roettiger and Flores, 2000), there is a general consensus that the merger occurred in or close to the plane of the sky (Henriksen *et al.*, 2000; Henriksen and Tittley, 2002; Sauvageot *et al.*, 2005; Dehghan *et al.*, 2017).

More recently, Sanders *et al.* (2022) reported a detailed study of the cluster with eROSITA. Their $0.3-2.0\,\mathrm{keV}$ image is shown in Figure 2.11. They concluded that the northeast–southwest merger is an oversimplification, and that there are at least three structures merging with the main cluster: the low-entropy gas extending northeast as a result of a northeast–southwest merger, low-entropy filamentary structures extending to a brighter region 9.5 arcmin west of the core, and an extended structure 20 arcmin northwest of the core that has probably passed through the cluster before. The filamentary structures, identified by Henriksen and Tittley (2002) as X-ray "fingers", could be the stripped gas from a group passing near the cluster core, or alternatively be cavities caused by AGN feedback. Riseley *et al.* (2022) found a region of diffuse radio emission associated with the fingers. Sanders *et al.* (2022) reported a possible shock $1.1\,\mathrm{Mpc}$ towards the southeast of the cluster with $\mathscr{M} \sim 1.5-1.7$. They also considered

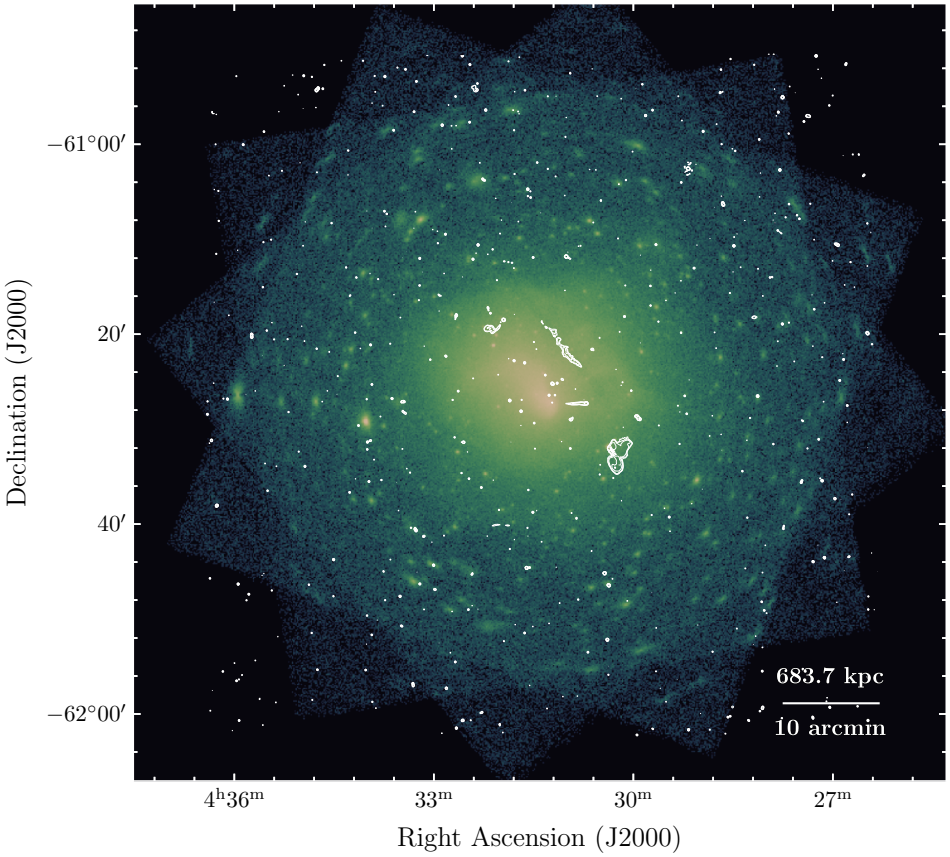

Figure 2.11: eROSITA count image of Abell 3266 in the 0.3 – 2.0 keV band, reproduced from Sanders *et al.* (2022), with contours of the 1.28 GHz MGCLS Data Release 1 image (Knowles *et al.*, 2022) overlaid.

the possibility of a merger shock just west of the cluster core, but were unable to find conclusive evidence.

Such a complex, disturbed dynamical state aligns with the spectroscopic structure analysis[9] reported by Dehghan *et al.* (2017). They analysed 880 galaxies observed with the optical Anglo-Australian Telescope within a 2° field around Abell 3266, identifying six groups and filaments surrounding the cluster core. The core itself comprises the Western Core Component (WCC) and the Eastern Core Component (ECC). The member galaxies of the ECC are more scattered and have a slightly lower average redshift than those of the WCC. The ECC also exhibits a velocity distribution with two peaks, allowing for the further decomposition of the ECC into two structures known as the Southeast Substructure and the Northwest Substructure (NWS). The NWS seems to have merged with the cluster from either the northeast or the southwest, consistent with the northeast–southwest merging theories from X-ray studies. However, Dehghan *et al.* (2017) disagreed with the notion that a subcluster approaching from the northeast has already passed the core (Sauvageot *et al.*, 2005). Overall, Dehghan *et al.* (2017) concluded

[9]See Dehghan *et al.* (2017) for an interactive three-dimensional visualisation of the different structures.

that X-ray and optical analyses alone might be insufficient to determine the complex merger dynamics of Abell 3266 definitively.

Radio observations provide additional insight into the dynamical history of Abell 3266. Giant radio halos are often found in massive merging clusters like Abell 3266 (Duchesne *et al.*, 2022). While a halo could not be detected by Bernardi *et al.* (2015) in 1.86 GHz observations performed with the 7-element Karoo Array Telescope, nor by Duchesne *et al.* (2022) in 88 – 216 MHz observations taken with the Murchison Widefield Array (MWA), a large-scale (up to 1.09 Mpc) radio halo was recently discovered by Riseley *et al.* (2022) in their spatially-filtered Australian Square Kilometre Array Pathfinder (ASKAP) map at 943 MHz. The brightest component of the halo is a faint, steep-spectrum ridge near the centre of the cluster, the nature of which is still unclear. Riseley *et al.* (2022) considered the possibility of this ridge, hereafter A3266-D1, being either a mini-halo or re-accelerated fossil plasma, potentially from the cD galaxy or from a one-sided radio galaxy west of the ridge, hereafter A3266-RG1, with a steep spectrum tail that blends with the diffuse emission from the ridge. A3266-RG1 is shown in Figure 2.12 (a).

The southeastern shock reported by Sanders *et al.* (2022) coincides with a cluster radio shock (relic) (Riseley *et al.*, 2022), A3266-D2, that was first tentatively identified by Murphy (1999) using Molonglo Observatory Synthesis Telescope observations, and has since been clearly detected by telescopes including MeerKAT (Knowles *et al.*, 2022), the MWA (Duchesne *et al.*, 2022), ASKAP, and Australia Telescope Compact Array (ATCA) (Riseley *et al.*, 2022). A3266-D2 has an unusual morphology, with a concave shape that would suggest the movement of a shock propagating from south to north, but a brightness distribution declining towards the north that would suggest shock propagation in the opposite direction (Riseley *et al.*, 2022).

The MGCLS data revealed the highly unusual morphology of a radio galaxy, or possibly multiple radio galaxies, northwest of the cluster centre, along the edge of the central low-entropy gas (Rudnick *et al.*, 2021; Knowles *et al.*, 2022), shown in Figure 2.12 (b). Like the elongated X-ray emission, this source, hereafter A3266-RG2, is aligned with the northeast–southwest axis. The northeastern part resembles a double-lobed radio galaxy with a compact core, referred to as the "triple". The southwestern part of the source shows quasi-periodic widening and brightening, with thin transverse "ribs" extending from it. The two parts are seemingly connected by a series of thin filamentary "tethers". The host galaxy is believed to be J043045.37−612335.8 at $z = 0.06282$ (Dehghan *et al.*, 2017), located at the southwestern point of the source. Rudnick *et al.* (2021) reported a spectral index of $\alpha \sim 0.6$ that steepens along the source, reaching $\alpha \sim 3.4$, apart from flattening to $\alpha = 1.4$ at the compact source in the centre of the triple. Riseley *et al.*

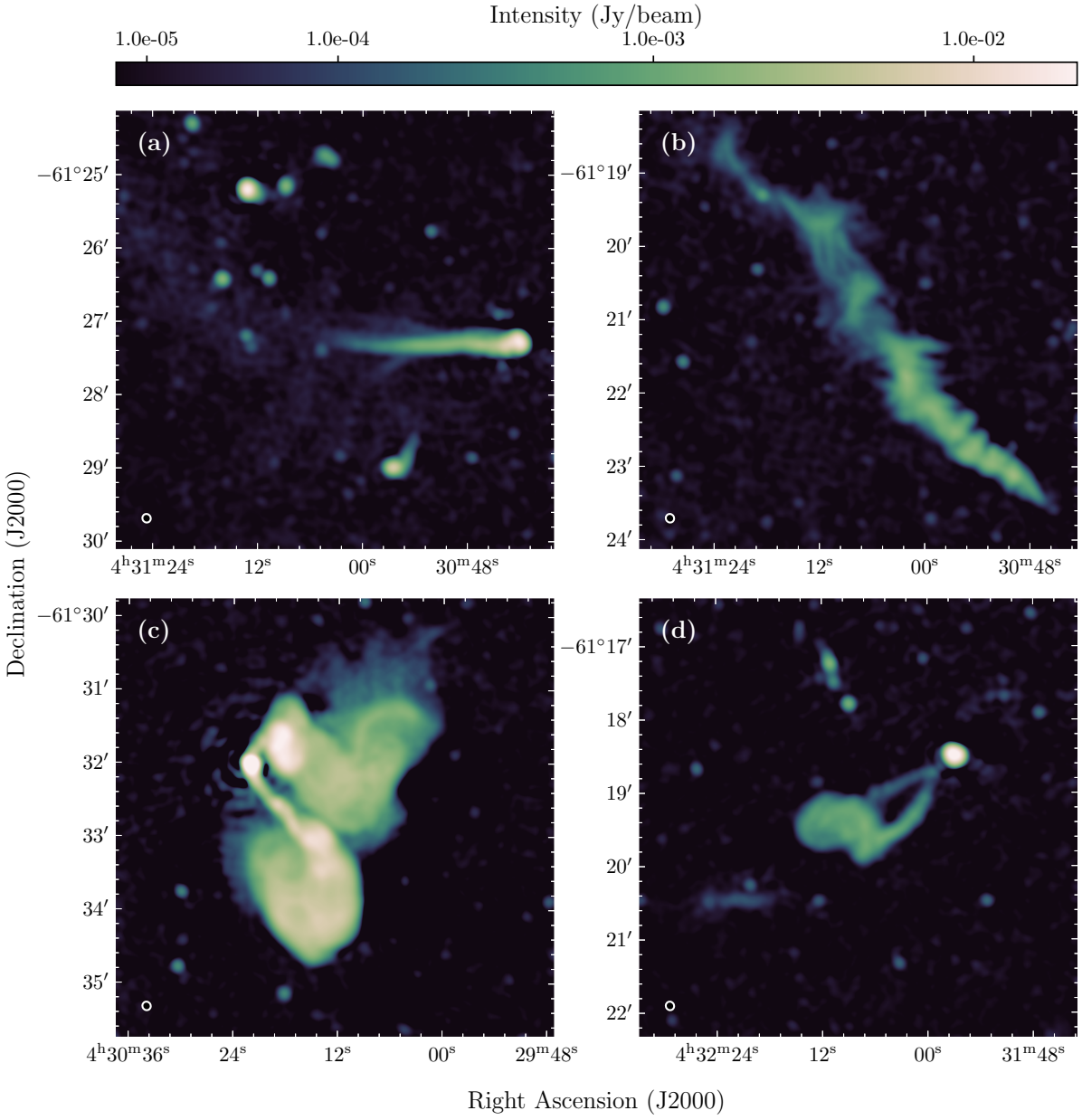

Figure 2.12: Individual radio galaxies in the 1.28 GHz MGCLS Data Release 1 image of Abell 3266 (Knowles *et al.*, 2022). The white ellipse in the corner shows the $7\farcs1 \times 6\farcs7$ beam size. These sources are referred to throughout this work as **(a)** A3266-RG1, **(b)** A3266-RG2, **(c)** A3266-RG3, and **(d)** A3266-RG4.

(2022) derived similar spectral indices using ASKAP and ATCA data. The compact source in the triple coincides with the galaxy WISEA J043118.50−611918.2 at $z = 0.78$. While this could imply that the triple is an unrelated background radio galaxy, the similar spectra (Rudnick *et al.*, 2021; Riseley *et al.*, 2022) and Faraday rotation measures (Rudnick *et al.*, 2021) between the different parts suggest that the extended emission is a single source, with a coincidental background point source in the triple.

The bent-tailed radio galaxy shown in Figure 2.12 (c), A3266-RG3, is located southwest of the

cluster core. Usually classified as a WAT (Duchesne *et al.*, 2022), the source has two jets pointing southwest and northwest, with a projected opening angle of around 95°, before terminating in complex, bending lobes. Riseley *et al.* (2022) reported a hook-like feature near the edge of the western lobe. The host galaxy, J043022.01−613200.2, is located at a redshift of $z = 0.0557$ (Dehghan *et al.*, 2017), near the outermost edge of the WCC (Riseley *et al.*, 2022). A second bent-tailed radio galaxy associated with J043157.29−611825.8 at $z = 0.0593$ (Dehghan *et al.*, 2017) is located northeast of the core (Riseley *et al.*, 2022). This source, hereafter A3266-RG4, is shown in Figure 2.12 (d). Both jets point southeast, with a small projected opening angle between them. The southern jet is much brighter than the northern jet, suggesting that the northern jet might be pointing somewhat away from us. The jets blend into a lobe that abruptly bends north and then back eastwards. Riseley *et al.* (2022) could not determine a reason for this twisted morphology.

To the west of A3266-RG3, Duchesne *et al.* (2022) discovered ultrasteep emission with $\alpha = 2.4 \pm 0.4$ at $118 - 216$ MHz, which they classified as a fossil source. It is unclear if this source is a remnant of a past episode of the radio galaxy or re-accelerated plasma. This source could not be clearly detected by ASKAP at $0.8 - 1.1$ GHz or ATCA at $1.1 - 3.1$ GHz, which is expected for such a steep spectrum (Riseley *et al.*, 2022). Duchesne *et al.* (2022) also discovered a second fossil source, hereafter A3266-D3, towards the north of the cluster, with $\alpha = 1.70 \pm 0.14$. Riseley *et al.* (2022) could detect this source with ASKAP, but not with ATCA. They identified J043041.92−611709.7 (Dehghan *et al.*, 2017) as a potential original host of the remnant radio galaxy.

2.4.3 Abell 3376

Abell 3376 is a merging galaxy cluster at $z = 0.0468$. It is well known for two megaparsec-scale arc-like radio shocks, or relics, located at the outskirts of this cluster (Bagchi *et al.*, 2006; Kale *et al.*, 2012). The X-ray morphology of the cluster is elongated along the northeast–southwest axis, forming a distinct cometary shape that points northeast. The northeastern brightness edge that forms the head of the cometary shape has been confirmed to be a cold front (Urdampilleta *et al.*, 2018; Chibueze *et al.*, 2021). Interestingly, the BCG is located far southwest of the peak X-ray emission, while the second-brightest galaxy, WINGS J060209.73−395659.7 at $z = 0.04591$ (Moretti *et al.*, 2017), is near this peak, at the head of the cometary shape. This galaxy is associated with the radio galaxy MRC 0600−399 (Large *et al.*, 1981), hereafter A3376-RG1, whose unusual jets extend north and south before both bending 90° towards the east, with

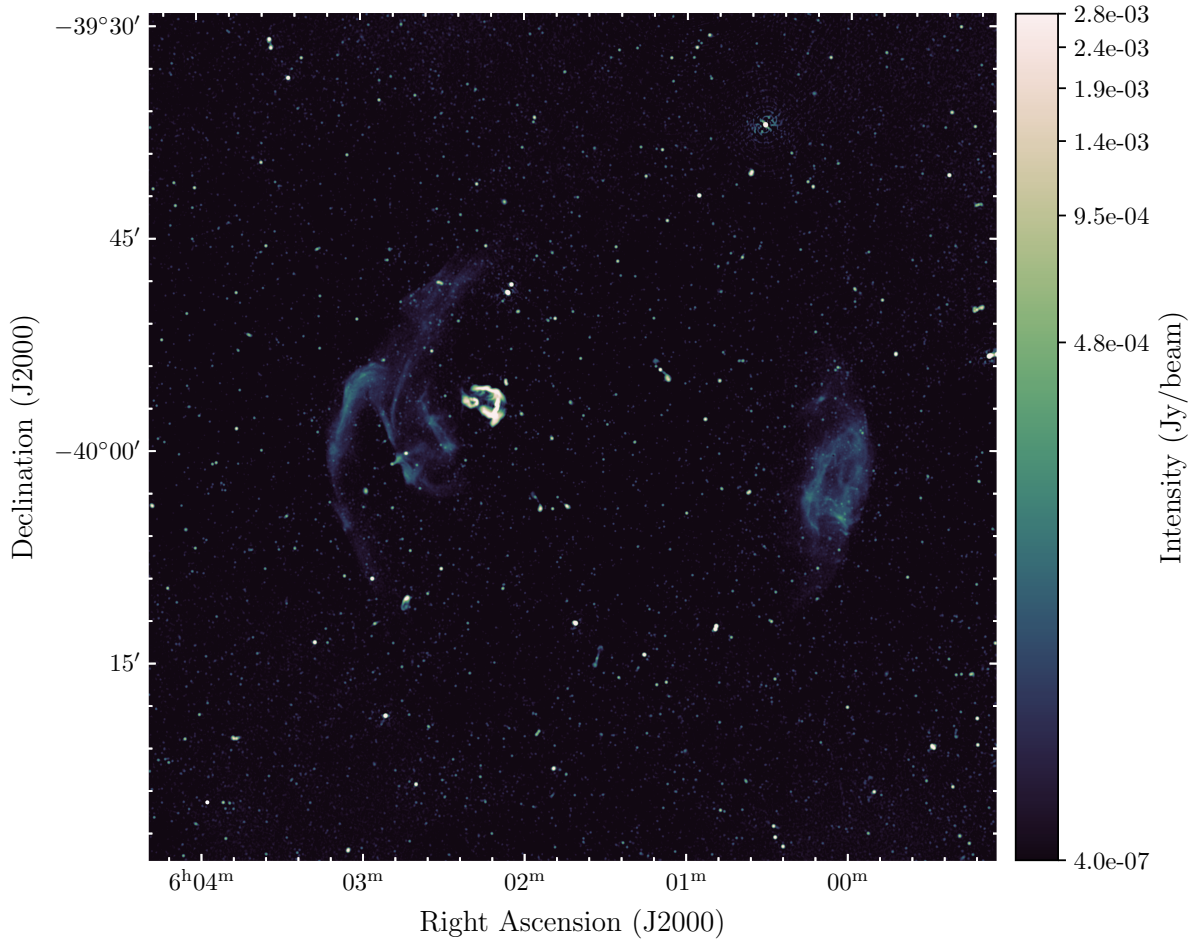

Figure 2.13: 1.28 GHz MGCLS Data Release 1 image (Knowles *et al.*, 2022) MeerKAT image of Abell 3376.

some elongated diffuse emission extending west, forming a "double-scythe" structure (Chibueze *et al.*, 2021). A smaller radio galaxy, A3376-RG2, with similarly bent jets lies just east of MRC 0600−399 and is associated with WINGS J060217.27−395634.2 at $z = 0.04813$ (Moretti *et al.*, 2017).

Simulations predict that a merger likely occurred between the main cluster, which hosted the BCG, and a more dense subcluster approaching from the southwest, hosting the second BCG. This subcluster appears to have overtaken the core of the main cluster while retaining its own gaseous core (Machado and Lima Neto, 2013; Monteiro-Oliveira *et al.*, 2017). Using the two BCGs as proxies for the dark matter peaks, Machado and Lima Neto (2013) used N-body adiabatic hydrodynamical simulations to model a head-on collision between two spherically symmetric clusters. They successfully reproduced the observed X-ray morphology by simulating a merger with a mass ratio between $\frac{1}{6}$ and $\frac{1}{8}$ and a density ratio of 4, with a 40° inclination with the plane of the sky, as viewed ∼0.5 Gyr after pericentric passage took place. A subsequent study, incorporating weak lensing and spectroscopic analysis, suggested a merger angle of around

10° and placed the pericentric passage at approximately 0.9 Gyr before it is observed (Monteiro-Oliveira *et al.*, 2017).

However, the eastward bending of the jets of the two radio galaxies, against the expected direction of ram pressure, seems to contradict this merging scenario. The jets of A3376-RG1 in particular, remain collimated for roughly 100 kpc after bending southwards. Bagchi *et al.* (2006) proposed that a small structure merging with the main cluster from the east-northeast would explain the jet morphology. However, it seems more likely that the subcluster initially approached from the southwest, as predicted in the simulations, and then experienced a ram pressure slingshot, discussed in Section 2.1.4, causing the jets to bend eastwards due to the bulk motion of the surrounding gas (Chibueze *et al.*, 2021).

A different explanation was put forward by Chibueze *et al.* (2021), who used three-dimensional MHD simulations to demonstrate that the 90° bending of the jets of A3376-RG1 could result from interactions with the intracluster magnetic fields. The northern jet, in particular, appears to bend along the cold front at the head of the X-ray emission, where an amplified magnetic field layer is expected to form (see Section 2.1.5.1). In these simulations, the supersonic jet encounters a $\sim$10 µG magnetic arch at the cold front, where its motion is suppressed by magnetic tension and its flow diverges along the arch. The magnetic field suppresses the KH instability of the flow, allowing the jet to remain collimated. This interpretation is supported by an observed increase in flux and a flattening of the spectrum at the bend point, potentially due to magnetic reconnection.

2.4.4 Abell 3391–Abell 3395 System

The galaxy clusters Abell 3391 and Abell 3395, with an average redshift of $\langle z \rangle = 0.053$ (Koulouridis *et al.*, 2021) and separated by a projected distance of approximately 3 Mpc, are part of an interacting system of galaxy clusters connected by large-scale filamentary X-ray emission (Tittley and Henriksen, 2001). This system also includes several smaller galaxy groups and clusters, often referred to as *clumps* in the literature. These include the cluster MCXC J0621.7−5242, known as the Northern Clump (Reiprich *et al.*, 2021), the Little Southern Clump galaxy group (Veronica *et al.*, 2024), and the galaxy group ESO 161-IG 006, located in the region of a filamentary gas bridge that connects Abell 3391 and Abell 3395 (Tittley and Henriksen, 2001).

This bridge was initially discovered by Tittley and Henriksen (2001) using data from the *Advanced Satellite for Cosmology and Astrophysics* and the *Roentgen Satellite*, and has since been

studied with several other X-ray telescopes, including *Suzaku* (Sugawara *et al.*, 2017; Tümer *et al.*, 2022), *XMM-Newton* (Alvarez *et al.*, 2018; Tümer *et al.*, 2022), *Chandra* (Alvarez *et al.*, 2018; Tümer *et al.*, 2022), and eROSITA (Reiprich *et al.*, 2021). The eROSITA observations revealed that the bridge is part of a much larger network of continuous diffuse X-ray emission with a projected length of ∼15 Mpc (Reiprich *et al.*, 2021). The eROSITA image of the system is shown in Figure 2.14, with ASKAP radio contours overlaid.

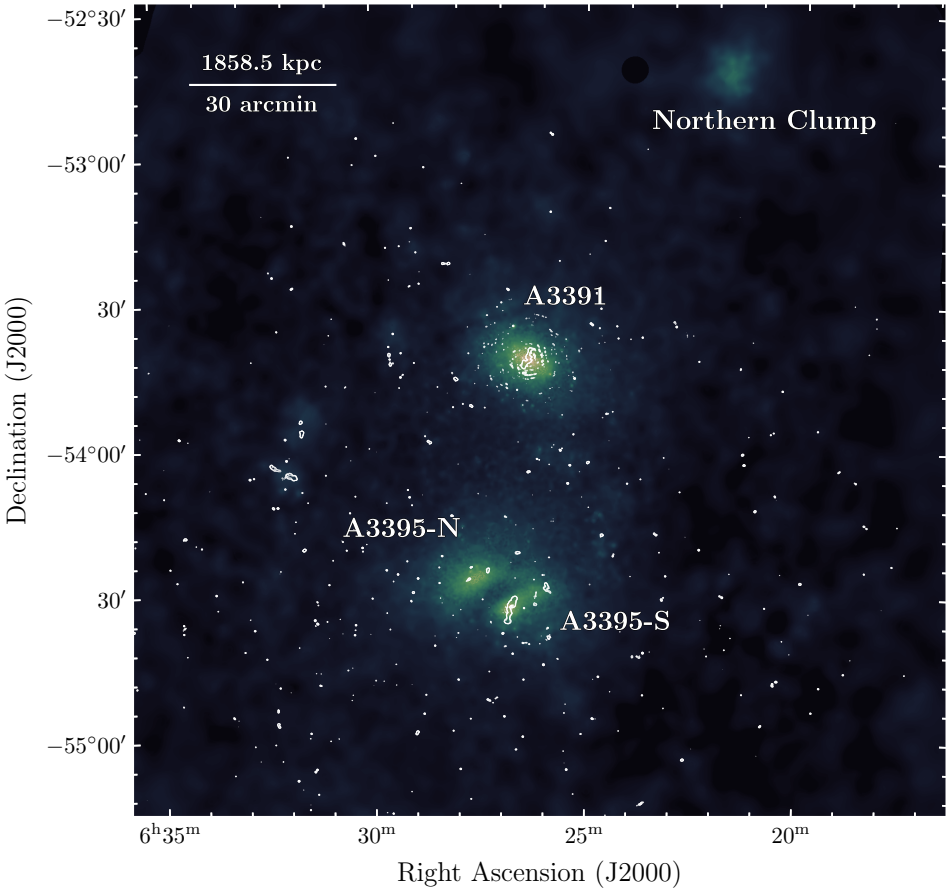

Figure 2.14: Adaptatively smoothed 0.3 − 2.0 keV eROSITA image of the Abell 3391–Abell 3395 system, reproduced from Veronica *et al.* (2024), overlaid with contours of the 887 MHz ASKAP image by Wilber *et al.* (2023b). The eROSITA image has been corrected for Galactic absorption, exposure, and particle-background, and point sources have been cosmetically masked.

A non-detection of diffuse radio emission in the bridge region with ASKAP enabled Brüggen *et al.* (2021) to derive an upper limit for the radio emissivity at 1 GHz of $1.2 \times 10^{-44}\,\mathrm{W\,Hz^{-1}\,m^{-3}}$. They also identified 20 giant radio galaxies in the field, all of which are background sources except for the radio galaxy EMU ES J0621−5647, located in the far south. Both Abell 3391 and Abell 3395 host approximately 300-kiloparsec-scale bent-tailed radio galaxies. ASKAP also detected several other radio galaxies associated with the other components of the system.

2.4.4.1 Abell 3391

The main northern component of the system, Abell 3391, located at a redshift of $z = 0.0550$ (Koulouridis *et al.*, 2021), exhibits an elliptical morphology elongated in the east–west direction (Veronica *et al.*, 2024). It is a non-cool-core cluster with an average temperature of approximately 4.88 keV between 181 – 452.5 kpc from the core (Zhang *et al.*, 2016). The density profile of the cluster follows a β-model (see equation (2.17)) with $\beta \approx 0.56$ and a core radius of $r_c \approx 230$ kpc (Otani *et al.*, 1998; Gliozzi *et al.*, 1999; Reiprich and Boehringer, 2002). The BCG of Abell 3391 is a dumbbell galaxy located at the cluster centre, with a bright eastern component coinciding with the peak X-ray emission. This component is also the host of the central radio source MRC 0625−536 (Otani *et al.*, 1998; Brüggen *et al.*, 2021).

MRC 0625−536 is a bright bent-tailed radio galaxy with a total extent of more than 4.5 arcmin (Brüggen *et al.*, 2021). It is typically classified as an FR-I (Mingo *et al.*, 2014; Brüggen *et al.*, 2021) and/or a WAT (Mingo *et al.*, 2014; Massaro *et al.*, 2023). It has twisting and bending jets initially pointing north and south, believed to be shaped by the ICM (Otani *et al.*, 1998; Brüggen *et al.*, 2021). Mingo *et al.* (2017) identified a potential X-ray cavity at the northern lobe of the source, where a slight decrease in the ICM emission is observed in the *Chandra* image of the cluster.

At the western outskirts of the cluster, the large, asymmetric radio galaxy PMN J0622−5334 is associated with the host galaxy WISEA J062255.56−533434.5 at $z = 0.0567$. The morphology of the radio lobes suggests that the galaxy may be infalling into Abell 3391 (Brüggen *et al.*, 2021). This galaxy has been identified as the BCG of the Abell *et al.* (1989) cluster S0584 (Coziol *et al.*, 2009). However, Tittley and Henriksen (2001) could not find a significant enhancement in galaxy density or X-ray flux at this location, calling into question the existence of such a cluster.

2.4.4.2 Abell 3395

The double-peaked merging cluster Abell 3395 is located approximately 3 Mpc south of the X-ray peak of Abell 3391, at redshift $z = 0.0510$ (Koulouridis *et al.*, 2021). The northeast and southwest subclusters, labelled A3395-N and A3395-S in Figure 2.14, are both elongated in the northwest–southeast direction. A3395-S has a prominent "finger" of emission extending northwest of the peak cluster emission (Reiprich *et al.*, 2021). The finger is connected to the western part of A3395-N by a filamentary band of emission (Lakhchaura *et al.*, 2011; Reiprich *et al.*, 2021), with an average temperature of approximately 6.5 keV (Lakhchaura *et al.*, 2011).

Markevitch *et al.* (1998) proposed that the two main subclusters could be heading for an offset merger, with A3395-N and A3395-S moving west and east, respectively. Lakhchaura *et al.* (2011) considered the extension of A3395-S to be a potential separate subcluster, A3395-W, and suggested two possible merger scenarios. Firstly, the cluster could be in a pre-merger phase, with both A3395-S and A3395-W falling into the more massive A3395-N. However, they could not find an explanation for the filament connecting A3395-N and A3395-W under this assumption. Alternatively, it could be that the cluster is seen post-merger, in which case the filament and A3395-W could be the result of different phases of ram pressure stripping.

The BCG of A3395-S, which is slightly offset from the X-ray peak, is associated with the bright, 5.5 arcmin radio galaxy, PKS J0626−5432, sometimes classified as a WAT (Lakhchaura *et al.*, 2011) or an FR-I source (Brüggen *et al.*, 2021). The jets of the radio galaxy initially extend northwest and southwest before sharply bending back after approximately 90 kpc to align with the north–south axis (Lakhchaura *et al.*, 2011). At the end of the southern jet, it expands spherically and the brightness drops as the jet enters less dense X-ray gas. Brüggen *et al.* (2021) interpreted this as the possible onset of an X-ray cavity. They found steep gradients in the X-ray surface brightness near both ends of the jets. Lakhchaura *et al.* (2011) calculated the equipartition magnetic field of the northern and southern peaks of emission closest to the core to be $\sim$20 µG and $\sim$14 µG, respectively. They also estimated an average equipartition magnetic field across the whole source of $\sim$6 µG. Using the Jaffe and Perola (1973) model, they estimated the spectral age of the radio galaxy to be $\sim$10 Myr.

West of the central radio galaxy, ASKAP observations revealed a complex conglomerate of faint radio sources that are candidates for radio phoenices or cluster radio shocks (Brüggen *et al.*, 2021; Wilber *et al.*, 2023a). This includes a diffuse, L-shaped source with arms extending north and west for 4 arcmin and a faint radio core (Brüggen *et al.*, 2021). The core does not coincide with a known optical source, but the cluster member galaxy WINGS J062610.49−543226.6 at $z = 0.05461$ (Moretti *et al.*, 2017), located just south of the core, could be responsible for feeding the source (Brüggen *et al.*, 2021). Wilber *et al.* (2023a) suggested that the ICM could have disturbed and shifted old AGN emission from this galaxy. Spectral index maps by Wilber *et al.* (2023a) show relatively flat emission near the core, and ultrasteep emission in the northern arm, while the western arm could not be well-resolved.

Faint filaments stretching out from the L-shaped source reach a second complex source (Brüggen *et al.*, 2021). The brightest spot on this source is near the northern tip and coincides with the galaxy NFP J062557.1−542750 ($z = 0.06030$; Smith *et al.*, 2004). Faint emission stretches

northwest from this point before turning and forming a linear structure extending 6 arcmin southwest (Brüggen *et al.*, 2021). At the end of the linear structure, there is a short extension that bends $\sim 90^{\circ}$ southeast just as it enters a high-temperature region of the ICM (Reiprich *et al.*, 2021).

Chapter 3

Methodology

This chapter describes the methodology employed to study a sample of galaxy clusters—Abell 133, Abell 3266, Abell 3376, Abell 3391, and Abell 3395—and to explore the interactions between the ICM and radio galaxies within these environments. An observational radio and X-ray approach was adopted, utilising observations from MeerKAT and *XMM-Newton* to examine both the thermal and nonthermal components of the clusters. MeerKAT was selected for its high-sensitivity imaging capabilities, while *XMM-Newton* was chosen for its large collecting area, sensitivity to extended emission, and extensive archival data. The chapter is divided into two main sections, Section 3.1: Radio Astronomy and Section 3.2: X-ray Astronomy, each detailing the relevant observational techniques, specifics of the data collection, and the data reduction and analysis methods used.

3.1 Radio Astronomy

Radio astronomy is the branch of astronomy that studies electromagnetic radiation at the lowest frequencies of the electromagnetic spectrum. The radio waveband can be roughly defined as all frequencies below 3 THz, with the observable radio frequencies for ground-based astronomy limited to the so-called "radio window" of 15 MHz to 1.5 THz, where the atmosphere is transparent to radio waves (Wilson *et al.*, 2009).

Radio waves are produced by charged particles undergoing acceleration. Most astronomical sources emit radio waves (Condon and Ransom, 2016), through a variety of radiation mechanisms, including both thermal and nonthermal processes. Thermal emission refers to electromagnetic radiation produced by matter in local thermodynamic equilibrium, i.e., matter that

is in thermal equilibrium with itself (Rybicki and Lightman, 1991). This includes thermal Bremsstrahlung, also known as free-free emission, which is the radiation produced by the acceleration of a charged particle in the Coulomb field of another charged particle However, most forms of radiation at radio wavelengths are of nonthermal origin and cannot be described by thermal physics (Wilson *et al.*, 2009). The most common nonthermal radio emission mechanism is synchrotron radiation, which is the radiation produced by relativistic particles accelerated in a magnetic field (Rybicki and Lightman, 1991).

Early radio astronomy revolutionised astronomy by extending the field beyond the visible spectrum. It led to the discovery of various astronomical sources such as radio galaxies, quasars, pulsars, masers and the CMB. Radio waves can penetrate interstellar clouds and Compton-thick layers of neutral gas, allowing for the detection of sources that are obscured in other wavebands. This property also allows for long-wavelength radio observations even in overcast weather conditions, as clouds are mostly transparent to radio waves. As a further advantage, radio observations can be conducted during the day, unlike most of optical astronomy.

However, radio astronomy faces the significant challenge of dealing with radio frequency interference (RFI) which is introduced into the observed spectrum through both natural and human-made phenomena. In recent years, RFI has become dominated by communication systems worldwide that also exploit the advantageous properties of radio waves for communication, such as cellular networks, television, and radio broadcasts. In most cases, the RFI is much stronger than the astronomical sources being studied. The International Telecommunications Union allocates specific frequency bands for specific uses (Wilson *et al.*, 2009). To minimise the inevitable RFI that will enter the system, radio telescopes must be built in remote areas where there is less RFI, and frequency ranges known to contain RFI must be removed from the data.

3.1.1 The Radio Telescope

In the 1930s, Karl Jansky first discovered cosmic radio waves coming from the Milky Way, using a directional antenna he built (Burke *et al.*, 2019). This telescope consisted of an array of dipoles and reflectors, which were mounted on a turntable that allowed it to rotate in any direction. Grote Reber, inspired by Jansky's work, built the first parabolic dish radio telescope in 1937, a design that has since become the most common type of radio telescope.

At radio wavelengths, the low energy of photons makes it very hard to detect them individually. Consequently, radio astronomy treats radiation as classical electromagnetic waves instead

of focusing on counting individual photons (Burke *et al.*, 2019). Astronomical sources emit spherical waves, but at sufficiently great distances[1], the curvature becomes negligible and the waves can be approximated by plane waves. In the simplest form of a parabolic dish radio telescope, the reflective surface of the dish reflects these incoming plane waves to a single focal point, where they are collected by a small feed antenna that is connected to receivers (Condon and Ransom, 2016). In order to gain a longer focal length, and consequently a bigger field of view (FOV), subreflector systems are often added to these telescopes. These systems include a convex secondary reflector, known as a Cassegrain subreflector, located below the prime focus, and a concave secondary reflector, known as a Gregorian subreflector, located above the prime focus. These subreflectors reflect waves to a secondary focus close to the vertex of the parabolic dish, where they enter the feed.

The incoming electromagnetic radiation induces a fluctuating electric current in the antenna, which is then amplified for easier processing. The amplified signal then passes through a band-pass filter to select the desired frequency range of interest. The power in this signal is then measured by squaring the noise voltage and averaging the result over time (Burke *et al.*, 2019). However, the measured power is not directly related to radiation emitted by the source being studied. The noise is influenced by various factors, including radiation from the CMB, the Milky Way, and the atmosphere, as well as radiation picked up by the beam's sidelobes and noise linked to losses in the antenna and receiver system.

The system noise temperature T_{sys} is the sum of all the various noise components (Burke *et al.*, 2019). By the Nyquist sampling theorem, T_{sys} should be independently sampled $2\Delta\nu\tau$ times in a time interval τ, where $\Delta\nu$ is the bandwidth. For a single sample of T_{sys}, the root mean square (RMS) error is $\sqrt{2}T_{\text{sys}}$ (Condon and Ransom, 2016). When averaging many independent samples, this value is divided by the square of the number of samples, as a consequence of the central limit theorem. As a result, the RMS fluctuations in the signal after averaging is

$$\sigma_T \approx \frac{T_{\text{sys}}}{\sqrt{\Delta\nu\tau}}, \tag{3.1}$$

an equation known as the ideal radiometer equation. This value determines the threshold for the minimum strength of the signal needed for a successful detection of a source.

A telescope with an aperture diameter of d, observing at wavelength λ, can distinguish between

[1]Spherical waves with wavelength λ can be accurately approximated as plane waves when observed by a telescope with an aperture diameter d if the source is located at a distance equal to or greater than the Rayleigh distance (also called the far-field distance), $R_{\text{ff}} = 2d^2/\lambda$ (Burke *et al.*, 2019).

two point sources when they are separated at minimum by an angular distance of

$$\theta \approx \frac{\lambda}{d}, \tag{3.2}$$

where θ is the angular resolution, a condition called the Rayleigh criterion. At the long wavelengths of radio waves, the aperture size must be very large to give an angular resolution comparable to that achieved with optical astronomy. However, increasing aperture size reduces the FOV, creating a trade-off between resolution and sky coverage. Building such large radio telescopes is also impractical and expensive. This has led to the development of radio interferometry as an alternative.

3.1.2 Radio Interferometry

Instead of increasing the size of the dish to improve the angular resolution, radio interferometry combines the signal from multiple dishes spread over a distance to achieve the same effect. In this case, the limiting factor for the angular resolution,

$$\theta \approx \frac{\lambda}{b}, \tag{3.3}$$

is the baseline length b between the dishes, rather than the aperture diameter.

3.1.2.1 The Two-Element Interferometer

The most basic interferometer consists of only two antennae, as illustrated in Figure 3.1. In this setup, the baseline vector $\mathbf{b}$ connects the phase centres of the two antennae, while the unit vector $\mathbf{s}_0$ points in the direction of the phase tracking centre, close to the direction of the source $\mathbf{s} = \mathbf{s}_0 + \boldsymbol{\sigma}$, where $\boldsymbol{\sigma}$ is a small vector normal to $\mathbf{s_0}$. The physical path length difference between waves emitted at $\mathbf{s}_0$ arriving at the different antennae is given by $\mathbf{b} \cdot \mathbf{s_0}$. This path length difference corresponds to a time delay of

$$\tau_g = \frac{\mathbf{b} \cdot \mathbf{s_0}}{c}, \tag{3.4}$$

where c is the speed of light. The baseline vector is often described in units of wavelength as $\mathbf{b}_\lambda \equiv \mathbf{b}/\lambda$. The components of this dimensionless baseline can be expressed in the right-handed rectilinear coordinate system (u, v, w), where u and v are in the projected direction of right ascension and declination, respectively, and $\mathbf{s_0}$ defines the direction of w (Burke *et al.*, 2019). Furthermore, (l, m, n) can be defined as the direction cosines of $\mathbf{s}$ with respect to the (u, v, w) coordinate system, with $n = \sqrt{1 - l^2 - m^2}$. However, unlike the (u, v, w) coordinate system, which is in the spatial frequency domain, (l, m, n) is in the spatial domain (Burke *et al.*, 2019).

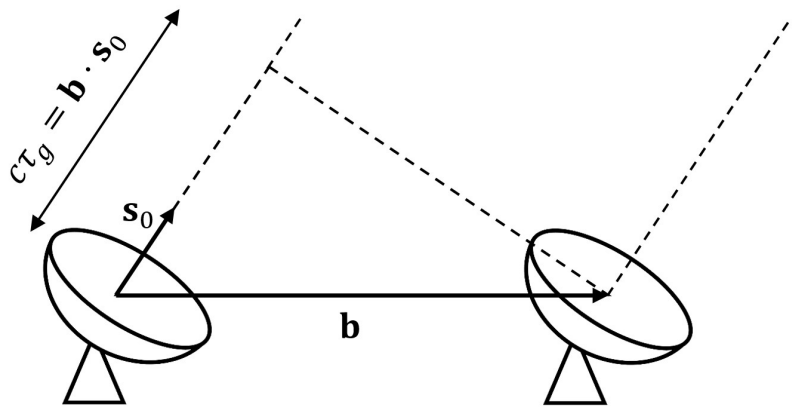

Figure 3.1: The geometry of the two-element interferometer.

To account for the geometrical time delay, the output voltage of the antenna closer to the source is intentionally delayed by τ_g using a delay circuit in the receiver, before the signal can be combined (Burke *et al.*, 2019). The correlator finds the cross-correlation by multiplying the two voltages, one delayed by τ_g, and averaging it over time, forming complex visibilities.

3.1.2.2 The Radio Interferometer Measurement Equation

The radio interferometer measurement equation (RIME), first formulated by Hamaker *et al.* (1996), serves as the mathematical foundation for calibration methods in radio interferometry, using the Jones calculus (Jones, 1941) as its basis. This equation relates the visibilities measured to the corresponding brightness distribution, while accounting for the various factors that distort the signal. Within this framework, these distortion effects are represented by chains of Jones matrices, applied to a brightness matrix $\mathbf{B}$ through a series of matrix multiplications. The brightness matrix is related to the Stokes I, Q, U and V parameters by the equation:

$$\mathbf{B} = \begin{bmatrix} I+Q & U+iV \\ U-iV & I-Q \end{bmatrix}, \tag{3.5}$$

where i represents the imaginary number (Smirnov, 2011). For a two-element interferometer with antennae p and q, Smirnov (2011) gives the general full-sky RIME:

$$\mathcal{V}_{pq} = \mathbf{G}_p \left[\iint\limits_{lm} \frac{1}{n} \bar{\mathbf{E}}_p \, \mathbf{B} \, \bar{\mathbf{E}}_q^H \, \mathrm{e}^{-2\pi i(u_{pq}l + v_{pq}m + w_{pq}(n-1))} \, \mathrm{d}l\mathrm{d}m \right] \mathbf{G}_q^H, \tag{3.6}$$

where H represents the Hermitian transpose. $\mathcal{V}_{pq}$ represents the visibility matrix containing the pairwise correlations between the components of the complex voltages measured by antennae p and q. For each antenna k, $\mathbf{G}_k$ represents the Jones chain of all relevant direction-independent

Jones matrices, including bandpass gain and instrumental gain. $\bar{\mathbf{E}}_k$ represents the chain of direction-dependent Jones matrices, such as ionospheric and tropospheric effects. The exponential function corrects for the phase-delay effect.

This function is not a two-dimensional Fourier transform, but can be changed into one by decomposing the non-coplanarity term $w_{pq}(n-1)$ into per-antenna terms $W_k = \frac{1}{\sqrt{n}}\mathrm{e}^{-2\pi i w_k(n-1)}$, which can be considered direction-dependent Jones matrices and can be absorbed into the direction-dependent term by defining $\mathbf{E}_k = \bar{\mathbf{E}}_k W_k$. Equation (3.6) can then be written as

$$\mathcal{V}_{pq} = \mathbf{G}_p \left[\iint_{lm} \mathbf{B}_{pq} \mathrm{e}^{-2\pi i(u_{pq}l + v_{pq}m)} \mathrm{d}l\mathrm{d}m \right] \mathbf{G}_q^H, \tag{3.7}$$

where $\mathbf{B}_{pq} \equiv \mathbf{E}_p \mathbf{B} \mathbf{E}_q^H$. This equation is a two-dimensional Fourier transform of the apparent sky as seen by baseline pq (Smirnov, 2011). This result, that the visibility function is the Fourier transform of the sky brightness distribution, is known as the van Cittert-Zernike theorem (Thompson *et al.*, 2017).

The discussion has so far focused on a simple two-element interferometer. However, this concept can be expanded to an N-element interferometer, which can be treated as a combination of $N(N-1)/2$ independent two-element interferometers (Condon and Ransom, 2016). The interferometer then samples the complete, continuous visibility function $\mathcal{V}(u, v)$ at different discrete points in the (u, v) plane. In any physical interferometer, there are always gaps in the (u, v) coverage, which inevitably lead to distortions in the image (Burke *et al.*, 2019).

3.1.2.3 Deconvolution and Imaging

The sampling can be described by a spatial frequency transfer function $S(u, v)$, which can be weighted to prioritise either short or long baselines. Commonly used weighting schemes include natural, uniform, and robust weighting, which is an intermediate between the aforementioned two. Uniform weighting results in higher angular resolution, while natural weighting results in a better signal-to-noise ratio (SNR) (Wilson *et al.*, 2009). The sampled "dirty" visibility is given by

$$\mathcal{V}_D(u, v) = \mathcal{V}(u, v) \times S(u, v). \tag{3.8}$$

The corresponding "dirty" image is then the inverse Fourier transform $B_D(l, m) = \mathcal{F}^{-1}\{\mathcal{V}(u, v) \times S(u, v)\}$. However, by the convolution theorem, this is equivalent to the convolution between the clean image $B(l, m)$ and the "dirty beam" or point spread function, defined as $s(l, m) \equiv$

$\mathcal{F}^{-1}\{S(u,v)\}$ (Burke *et al.*, 2019), where

$$B_D(l,m) = B(l,m) * s(l,m). \tag{3.9}$$

The "clean" image $B(l,m)$ can be recovered using deconvolution theorems such as CLEAN (Högbom, 1974). This works by iteratively identifying the brightest point source in the image, fitting a scaled dirty beam to the point source, subtracting this from the image and recording the position and amplitude of the component until there are no point sources left that are significantly brighter than the general noise level of the image. The point sources are then returned to the image in the form of clean beam functions with corresponding amplitudes, where the clean beam is usually a Gaussian with the same FWHM as the dirty beam (Thompson *et al.*, 2017).

One way of substantially improving (u,v) coverage, and by extension image quality, is through a technique called multi-frequency synthesis (MFS) (Conway *et al.*, 1990). Since the baseline vector $\mathbf{b}_\lambda$ is directly dependent on the observing frequency, different frequencies will produce different coverage of the (u,v) plane. By separately imaging at even just a few different frequencies and combining the results, it is possible to fill large parts of the gaps in the (u,v) coverage of a single frequency.

3.1.2.4 Calibration Strategies

Techniques for calibrating radio interferometric data are often divided into the three generations defined by Noordam and Smirnov (2010). The first-generation calibration (1GC) involves deriving corrections for instrumental and propagation effects from well-known calibrator sources observed alongside the target source. These corrections are then applied to the target data. This is known as cross-calibration. Second-generation calibration (2GC) improves results obtained using 1GC by iteratively using the target data itself to calculate gain solutions in a process known as self-calibration (Cornwell and Wilkinson, 1981). Both 1GC and 2GC are direction-independent calibration techniques.

Direction-dependent effects (DDEs) manifest as artefacts around bright sources. Third-generation calibration (3GC) was developed to address the DDEs. This is done using methods such as "peeling" the bright sources by subtracting a model of the source and its DDEs from the visibility data, or breaking the field into different facets and separately determining calibration solutions for each facet (Tasse *et al.*, 2018). While 2GC was usually sufficient for older telescopes, 3GC is often needed to achieve the full potential of highly-sophisticated modern interferometers such

as MeerKAT.

3.1.3 MeerKAT

MeerKAT is a radio interferometer located in the Karoo, in the Northern Cape Province of South Africa, at approximately 21°26′E, 30°42′S (Camilo *et al.*, 2018). It was constructed as a precursor to the SKA by the National Research Foundation (NRF) of South Africa and is operated by the South African Radio Astronomy Observatory, a National Facility managed by the NRF. It was designed to be the most sensitive decimeter-wavelength radio interferometer array in the world before the advent of SKA1-mid (Jonas and the MeerKAT Team, 2016).



Figure 3.2: A MeerKAT type dish, illustrated by Morganoshell (2016), featuring a "feed-down" offset Gregorian configuration.

The full MeerKAT array currently consists of 64 "feed-down" offset Gregorian parabolic dishes, as illustrated in Figure 3.2, with additional dishes planned as part of the MeerKAT Extension Project. In this design, incoming radio waves are reflected from the main reflector to a small, concave secondary reflector, positioned away from the centre of the dish. This configuration was chosen for the MeerKAT dishes for its numerous advantages, including high aperture efficiency, low far sidelobes, reduced spill-over from ground radiation, and easy access to the receiver systems for installation and maintenance (Jonas and the MeerKAT Team, 2016).

The dishes are equipped with receivers in the UHF-band (544 – 1088 MHz), L-band (856 – 1712 MHz), and S-band (1.75 – 3.5 GHz) (Heywood *et al.*, 2022). Each of the dishes has a projected diameter of 13.5 m (Jonas and the MeerKAT Team, 2016). Of the 64 dishes, 48 are concentrated within a core region of 1 km diameter, while the remaining 16 are spread within a radius of 4 km from

the centre (Mauch *et al.*, 2020). The shortest baseline formed is 29 m, while the longest reaches 7.7 km (Jonas and the MeerKAT Team, 2016). The concentrated core enables MeerKAT to observe extended emission, while the long baselines simultaneously provide the angular resolution to observe compact sources. This enables observers to study a wide range of sources and phenomena.

3.1.4 Data Collection

The radio galaxies studied in this work were chosen from the MGCLS (Knowles *et al.*, 2022). This survey consists of long-track observations of 115 galaxy clusters carried out by MeerKAT shortly after starting operations in 2018. The observations were made with the L-band receiver, using 4096 channels and 8 s integrations. For this study, clusters from the MGCLS hosting extended radio sources with large-scale jets or lobes were identified. These clusters were cross-referenced with archival *XMM-Newton* data, to choose a sample of five clusters that host radio galaxies that could show evidence of interaction with the ICM. The MeerKAT data for these clusters were recalibrated up to 3GC. The sample of MGCLS clusters used in this work is listed in Table 3.1. Further information on the corresponding X-ray observations is discussed in Section 3.2.4.

Table 3.1: Summary of the MGCLS observations used for this study. In the MGCLS, Abell 3266, Abell 3391, Abell 3395 are referred to as J0431.4−6126, J0626.3−5341 and J0627.2−5428, respectively, but their Abell designations will be used throughout this work for consistency.

Cluster	Date	Block ID	Antennae	On-source (h)	Bandpass and delay calibrator	Gain calibrator
Abell 133	2018-10-01	1538415237	61	7.17	J0408−6545	J0025−2602
Abell 3266	2019-03-03	1551621148	59	5.94	J0408−6545, J1938−6341	J0420−6223
Abell 3376	2019-03-06	1551885425	58	6.17	J0408−6545	J0616−3456
Abell 3391	2019-02-08	1549637106	60	6.67	J0408−6545, J1938−6341	J0538−4405
Abell 3395	2019-03-15	1552662853	58	6.00	J0408−6545	J0538−4405

3.1.5 Data Reduction and Imaging

The 1GC and 2GC data processing for the MeerKAT data were done using the CARACal[2] (Józsa *et al.*, 2020) pipeline. The 3GC capabilities of CARACal are still under development, so direction-dependent calibration and imaging were done with killMS (Tasse, 2023) and DDFacet (Tasse *et al.*, 2023) outside of the CARACal pipeline.

[2] `https://caracal.readthedocs.io`

3.1.5.1 CARACal

CARACal is a collection of STIMELA[3] scripts capable of reducing data from any radio interferometer, but specifically developed for MeerKAT. STIMELA is a PYTHON-based scripting framework for radio interferometry, making use of container technology such as DOCKER or SINGULARITY (Makhathini, 2018). CARACal uses several data reduction software packages, including the Common Astronomy Software Applications (CASA) package (Bean *et al.*, 2022), WSCLEAN (Offringa *et al.*, 2014), TRICOLOUR (Hugo *et al.*, 2022), and CUBICAL (Kenyon *et al.*, 2018). Each individual CARACal STIMELA script is called a worker. The parameters of the workers are specified in a YAML configuration file.

Each run of CARACal started with preparing the workspace and setting up the necessary directories for the data processing with the `general` worker. The names of the files that were to be processed were provided to the `getdata` worker, which then ensured that the visibility data were in the CASA Measurement Set (MS) format required by CARACal. MeerKAT MS files include observations of primary calibrators for bandpass and flux calibration, and secondary gain calibrators. Information about the target and calibrator names were extracted from the MS file using the `obsconf` worker.

The calibrator data must be cleaned before it can be used to determine the necessary corrections. The `transform` worker was used to create MS files containing only the calibrator data. These files were then prepared for processing using `prep`. This included fixing the calibrator coordinates when necessary. The `flag` worker was used to flag out any parts of the calibrator data that were not usable. This worker made use of the CASA task `flagdata` to flag autocorrelations, shadowed antennae, and the known RFI channels 856 – 880 MHz, 1658 – 1800 MHz, and 1419.8 – 1421.3 MHz. It also used a static mask to flag out known MeerKAT RFI[4]. In addition to this, it used TRICOLOUR, an RFI flagging software specifically developed for MeerKAT, with a strict flagging strategy[5], to remove any remaining RFI.

The `crosscal` worker was used for 1GC processing of the data, following the calibration strategy in the sample continuum configuration developed for MeerKAT[6]. Using this strategy, this worker

[3] https://github.com/ratt-ru/Stimela

[4] https://github.com/caracal-pipeline/caracal/blob/master/caracal/data/meerkat_files/meerkat.rfimask.npy

[5] https://github.com/caracal-pipeline/caracal/blob/master/caracal/data/meerkat_files/stalin.yaml

[6] https://github.com/caracal-pipeline/caracal/blob/master/caracal/sample_configurations/meerkat-continuum-defaults.yml

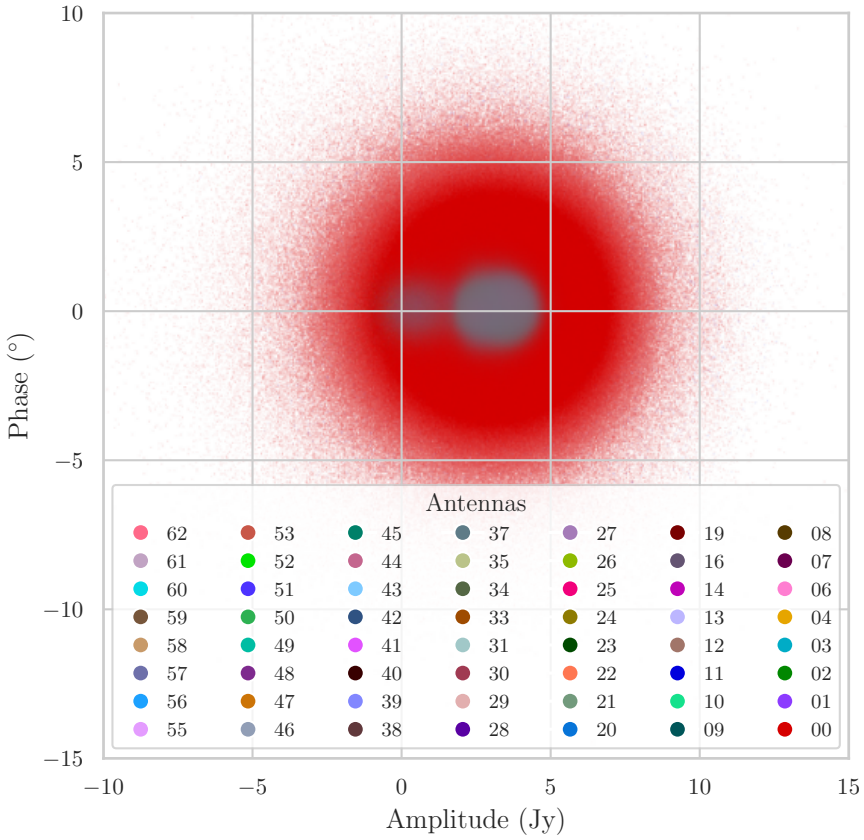

Figure 3.3: Phaseball plot of J0538−4405 for the observation of Abell 3395. This calibrator has a known flux density of 2.16 ± 0.05 Jy at 1.4 GHz (Taylor and Legodi, 2021).

made use of the CASA task `gaincal` to calculate delay and gain corrections, and the CASA task `bandpass` to calculate bandpass corrections of the primary calibrator, using a local sky model developed for MeerKAT. After applying these corrections, the data were flagged again, using the CASA task `flagdata`. This was followed by a second round of delay, gain, and bandpass calibration. Similarly, the secondary calibrators went through two rounds of delay and gain calibration, with flagging in between. After this, the flux of the secondary calibrator is scaled to that of the primary calibrator using the CASA task `fluxscale`. These solutions were then applied to the calibrator visibilities.

After cross-calibration, the quality of the calibrated calibrator visibilities was verified using the `inspect` worker. This produced a variety of diagnostic plots using SHADEMS[7], including so-called "phaseball" plots of the phase versus amplitude for the different antennas. Properly calibrated data would produce phaseball plots tightly clustered around a phase of zero and an amplitude corresponding to the known flux density of the calibrator, as in Figure 3.3.

[7] `https://github.com/ratt-ru/shadeMS`

After ensuring that the cross-calibration was satisfactory, the `transform` worker was used to create target-only MS files, while simultaneously applying the cross-calibration solutions on-the-fly with the CASA task `mstransform`. This also frequency-averaged the target data to 5 channels per frequency bin, in order to reduce the computational power required for further data processing. The MS files were then prepared for calibration and imaging with the worker `prep`. The target visibilities were then flagged with `flag`. Auto-correlations, shadowed antennae, and known RFI channels were removed, and additional RFI was flagged out by TRICOLOUR, with a more lenient flagging strategy[8].

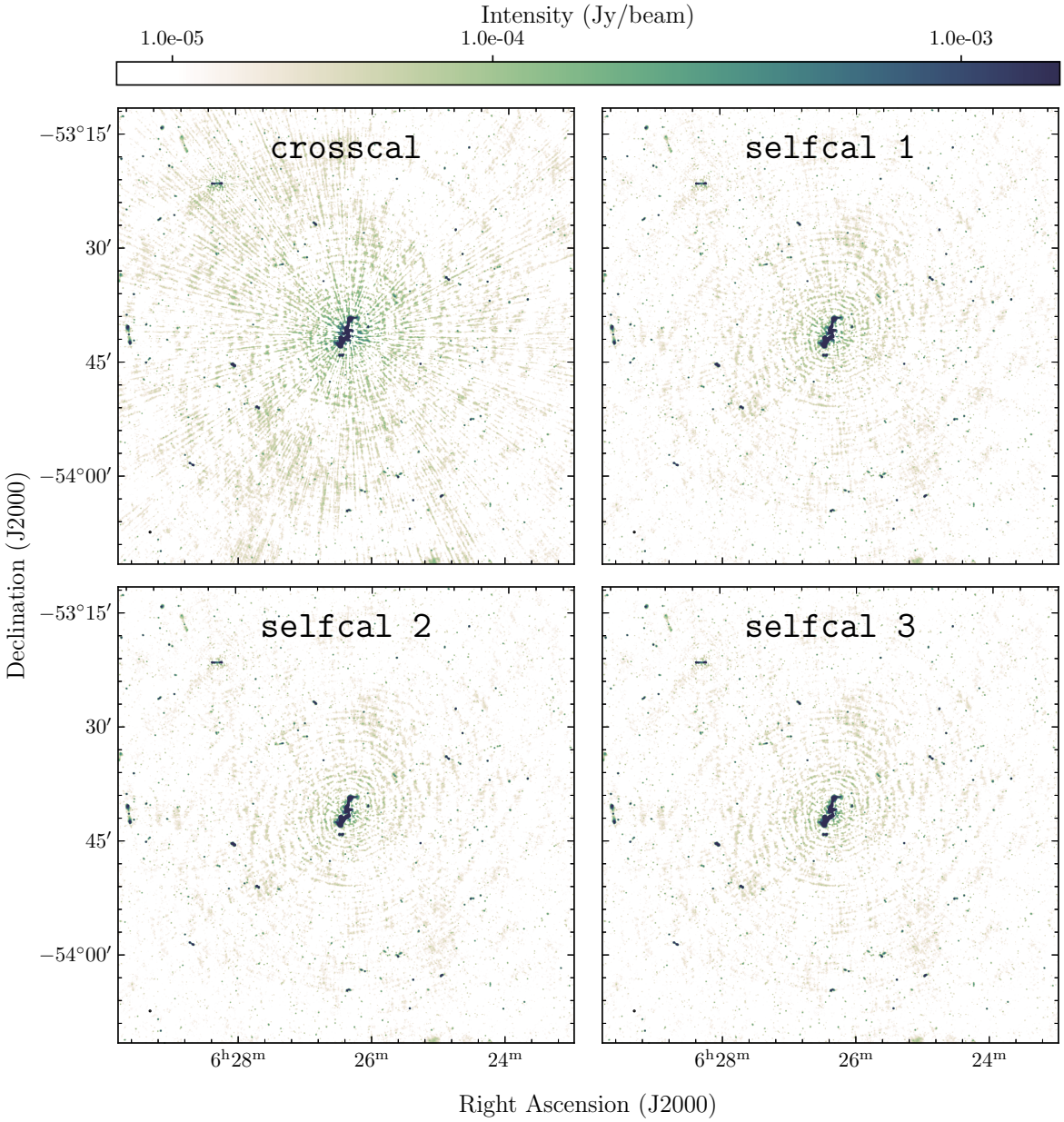

Figure 3.4: MeerKAT images of Abell 3391 after different CARACal calibration phases.

[8] `https://github.com/caracal-pipeline/caracal/blob/master/caracal/data/meerkat_files/gorbachev.yaml`

The 2GC data processing was then done with `selfcal`. This worker performed three iterations of self-calibration, each time imaging with WSClean and calibrating with CubiCal. Five sub-band images were used to create the MFS images. Each image was created with 6000×6000 pixels in an area of $1.^{\circ}75 \times 1.^{\circ}75$, with each pixel being $1.''05 \times 1.''05$ in size. Figure 3.4 shows the images after each calibration round for Abell 3391.

3.1.5.2 killMS and DDFacet

killMS is a direction-dependent calibration package, implementing algorithms described by Tasse (2014) and Smirnov and Tasse (2015) to solve the direction-dependent terms of the RIME. This was used in conjunction with DDFacet, a facet-based imaging and deconvolution package, to create the final 3GC images. Figure 3.5 demonstrates the improvement in image quality after direction-dependent calibration for Abell 3395.

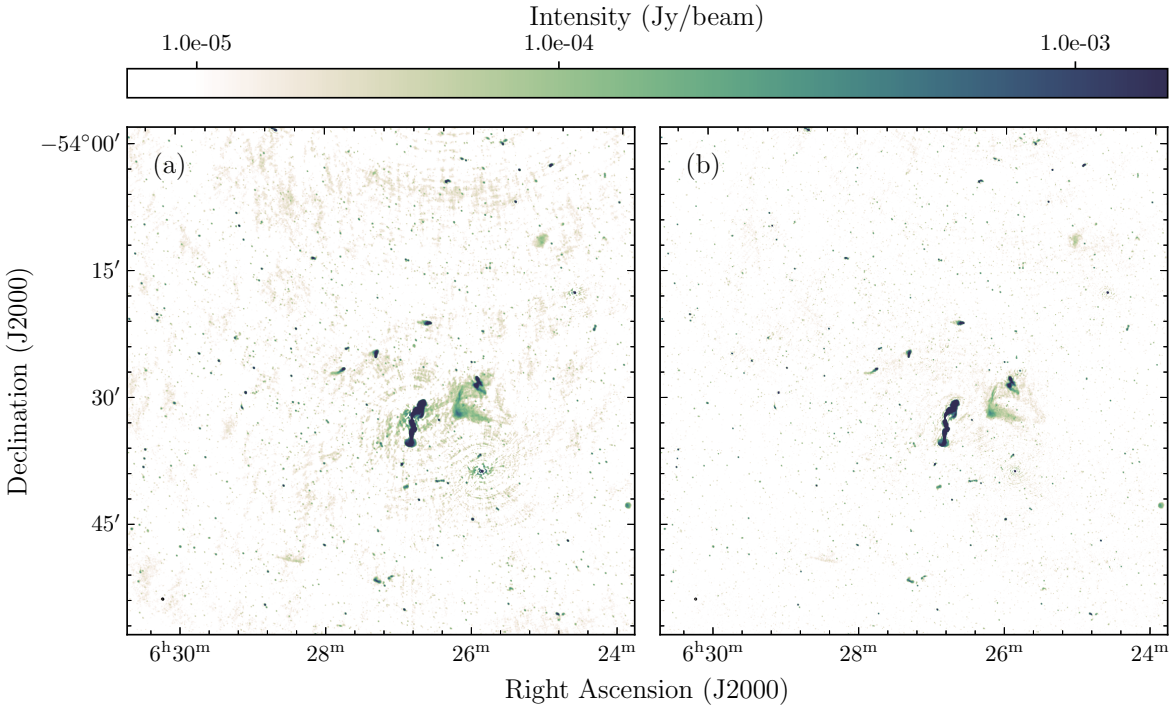

Figure 3.5: MeerKAT images of Abell 3395 **(a)** before and **(b)** after direction-dependent calibration.

First, a "dirty" image was created from the 2GC data with DDFacet. In each cluster, approximately six of the brightest sources that were responsible for the DDEs, were manually identified. The `MakeModel.py` script[9] used these regions to create a tessellation pattern to define the directions in which calibration solutions were determined at a later stage. Next, DDFacet was used to run two major cycles of deconvolution with the SSD2 deconvolver and

[9] `https://github.com/saopicc/DDFacet/blob/master/SkyModel/MakeModel.py`

apply auto-masking. An external mask was then created with the `MakeMask.py` script[10], and another cycle of DDFacet was used for a deeper deconvolution of the image. killMS derived the direction-dependent Jones matrices with the `KAFCA` solver, across 10 frequency intervals and 5-minute time intervals. Finally, DDFacet created a 3GC MFS image at 1284 MHz from 10 sub-band images with central frequencies of 899, 984, 1070, 1155, 1241, 1327, 1412, 1498, 1583, and 1669 MHz.

3.1.5.3 Accuracy of the Flux Scale

To determine the uncertainty in the flux scale of the calibrated images, the integrated flux densities of point sources within the MeerKAT primary beam were compared with those from the NRAO VLA Sky Survey (NVSS) (Condon *et al.*, 1998) and Sydney University Molonglo Sky Survey (SUMSS) (Mauch *et al.*, 2003) catalogues.

The source detection for the MeerKAT images was done with the Python Blob Detection and Source Finder (PyBDSF) (Mohan and Rafferty, 2015), with the images convolved to the $45''$ resolution of NVSS and SUMSS using the CASA task `imsmooth`. Sources with an SNR below 50, and sources determined to be extended sources were rejected from the resulting PyBDSF catalogue.

The flux densities of the 1.4 GHz NVSS and 843 MHz SUMSS catalogues were scaled to the 1.28 GHz central frequency of the MeerKAT images, assuming a power-law spectrum with a spectral index of $\alpha = 0.7$ (Smolčić *et al.*, 2017). The scaled catalogues were then cross-matched with sources in the PyBDSF catalogue within a $22\farcs5$ radius, using the Tool for Operations on Catalogues and Tables (Taylor, 2011).

The MeerKAT flux density versus the scaled catalogue flux densities is shown in Figure 3.6. Fitting a linear least-squares regression line in log space gives

$$\log S_{\mathrm{MeerKAT}} = (0.97 \pm 0.02) \log S_{\mathrm{scaled_cat}} - (0.03 \pm 0.03) \tag{3.10}$$

This is close to a one-to-one correspondence between S_{MeerKAT} and $S_{\mathrm{scaled_cat}}$, although the MeerKAT flux densities are, on average, 11.9% lower than that of the catalogues.

[10] `https://github.com/saopicc/DDFacet/blob/master/SkyModel/MakeMask.py`

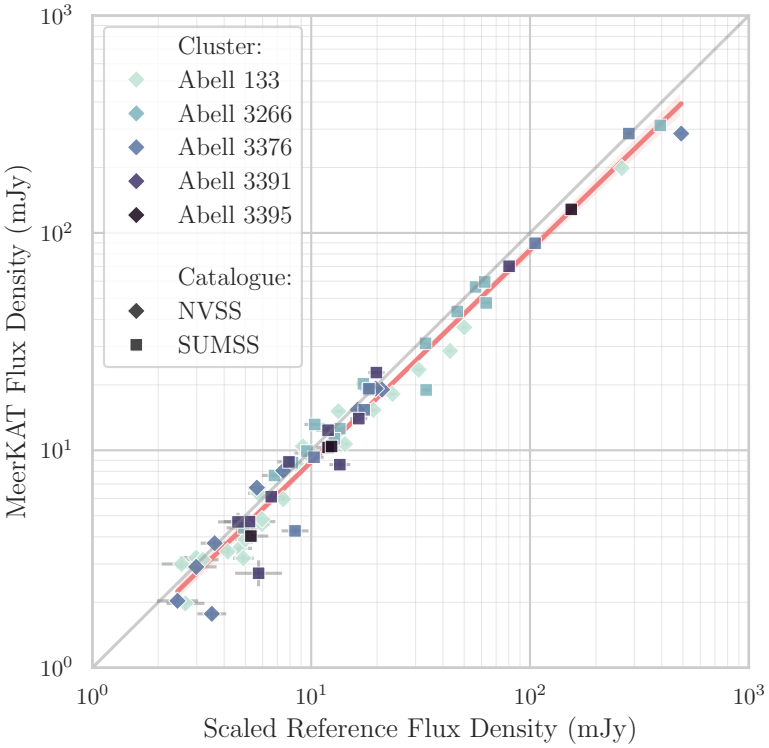

Figure 3.6: Flux density comparison with NVSS and SUMSS.

3.1.6 Spectral Analysis

The spectral analysis of the radio galaxies was performed with the Broadband Radio Astronomy Tools (BRATS)[11] (Harwood *et al.*, 2013, 2015) on a pixel-by-pixel basis using the 10 sub-band images smoothed to the resolution of the 899 MHz image with the CASA task `imsmooth`. Pixels with intensities below three times the RMS noise level calculated from a large off-source region were excluded from the analysis. The power-law synchrotron spectrum in equation (2.39) can be written as a straight line in log space, given by

$$\log S_\nu = -\alpha \log \nu + C, \tag{3.11}$$

for some constant C. BRATS calculated the spectral index for each pixel with a weighted least-squares linear regression fitting using the GNU Scientific Library functions `wlinear` and `linear_est`, with weights given by the reciprocal of the square of the error on a given intensity. BRATS then plotted the calculated spectral index as a function of position to create spectral index maps.

[11] `https://www.askanastronomer.co.uk/brats/`

3.2 X-ray Astronomy

X-ray astronomy studies celestial objects and phenomena at energies from 100 eV to 100 keV, corresponding to wavelengths of approximately 10 nm to 10 pm (Longair, 2010). Earth's atmosphere is opaque to X-rays, necessitating space-based X-ray observatories.

X-rays are produced in highly energetic processes in a variety of astronomical sources, such as accretion onto black holes, high-temperature gas in galaxy clusters, supernovae, and supernova remnants. The X-ray energy spectrum has many components of both continuum and line emission and absorption. The continuum spectrum mainly arises from thermal Bremsstrahlung, synchrotron radiation, and IC scattering of lower-energy photons by relativistic electrons.

On the other hand, line emission occurs when electrons transition between energy levels in atoms or ions. These transitions emit X-rays at specific energies corresponding to the energy differences between the levels. Nearly all astrophysically abundant elements have atomic transitions at X-ray energies, with most of these transitions involving inner-shell electrons (Arnaud *et al.*, 2011). In addition to this, the X-ray spectrum also shows absorption lines. This is a result of X-rays passing through material that absorbs photons with specific energies. This can then lead to the presence of fluorescent emission lines. The full X-ray spectrum provides insight into the physical processes and chemical composition of astronomical sources and the intervening medium.

The biggest constraint in the advancement of X-ray astronomy is the challenges and risks associated with conducting research from space-based observatories. There is a strict limitation on the size and weight of the instruments, as these factors can greatly increase the cost of launching the spacecraft. This requires the careful design and optimisation of X-ray telescopes and a trade-off between having a good angular resolution or a large collecting area (Arnaud *et al.*, 2011). Additionally, these spacecraft are usually unmanned, adding a significant challenge to the control and maintenance of the observatories.

3.2.1 X-ray Telescopes

X-ray astronomy developed in the 1960s and 1970s, using stratospheric balloons and rockets, which were often repurposed equipment from World War II, to carry Geiger counters to altitudes near or beyond the boundary of the atmosphere (Trümper and Hasinger, 2008). The Geiger counters were later replaced by proportional counters, enabling astronomers to measure the energy of incoming photons (Arnaud *et al.*, 2011). In recent times, X-ray astronomy is pre-

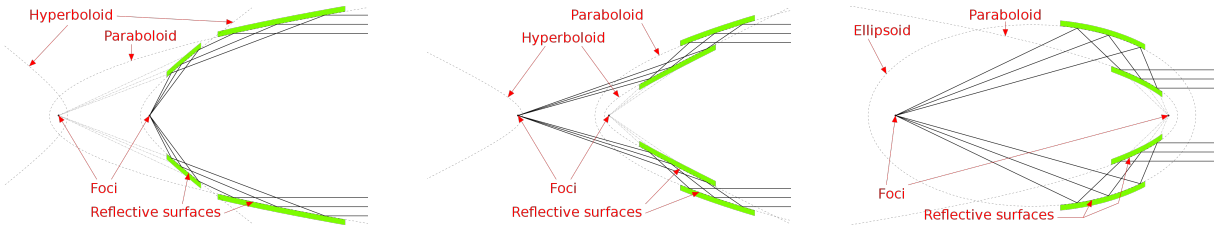

(a) Wolter I **(b)** Wolter II **(c)** Wolter III

Figure 3.7: The different types of Wolter telescopes, as illustrated by Andreas 9384 (2017a,b,c).

dominantly conducted using satellite observatories. Although large-area proportional counters are still used occasionally, most X-ray observatories use focusing optics.

Unlike radio waves, X-ray photons have sufficiently high energies to be treated as particles (Longair, 2010), and their relatively low flux makes it possible to count individual photons (Arnaud *et al.*, 2011). Consequently, X-ray detectors record individual photon events rather than integrated flux. The event data typically include information about the photon's energy (or a quantity related to the energy), time, direction of arrival, and polarisation angle (Trümper and Hasinger, 2008).

Generally, X-ray photons can penetrate most materials on which they are incident, and will be absorbed if the material is thick enough (Arnaud *et al.*, 2011). This makes focusing optics challenging, as traditional methods using mirrors and lenses are impossible at X-ray energies. However, X-rays can be reflected if they are incident at small grazing angles. Photons with energies ranging from $0.1-10\,\mathrm{keV}$ require grazing angles of $0.5-1^\circ$ for effective reflection. Wolter (1952) introduced three telescope designs, known as Wolter type I, II, or III, utilising such small grazing angles. These telescopes are illustrated in Figure 3.7. Modern X-ray astronomy predominantly makes use of Wolter type I or II telescope designs, with Wolter I mirrors being particularly favoured for their ability to be combined to create nested structures with large effective aperture areas (Trümper and Hasinger, 2008).

As photon energies increase, the angles at which reflection is possible become smaller, which necessitates the use of longer focal lengths. For a Wolter I telescope, the ratio between the aperture size D and the focal length f is

$$\frac{D}{2f} = \sin 4\alpha, \tag{3.12}$$

where α represents the slope angle of the first mirror element (Trümper and Hasinger, 2008). The grazing angle also determines the maximum FOV of the telescope (Arnaud *et al.*, 2011).

The position, energy, and arrival time of the focused photons are measured by charge-coupled

devices (CCDs). CCDs are integrated circuits of linked capacitors. Incoming photons interact with a semiconductor substrate, generating electric charge which is stored in a pixel. The charge is transferred from pixel to pixel until it reaches a readout amplifier where the time, position, and pulse height of the charge are recorded and digitised (Arnaud *et al.*, 2011). There are two types of CCDs used in X-ray telescopes: conventional metal-oxide-semiconductor (MOS) CCDs and $p-n$ junction (pn) CCDs.

Each event that is recorded is assigned a pattern or grade characterising the morphology of pulse height at the centre of the event and the pixels surrounding it. These patterns can be used to filter out events associated with the charged-particle background, such as cosmic rays. Charged particles tend to produce large shapes, such as blobs or streaks, whereas photons produce point-like patterns (Arnaud *et al.*, 2011). The level of the charged-particle background depends on the orbit. Satellites in low-Earth orbit experience a relatively low particle background, and have the added benefit of being cheap and easy to put into orbit compared to other orbits, but Earth being in the way makes continuous coverage impossible. Other options such as eccentric orbits have improved efficiency and coverage, but a high particle background, making it crucial to have a proper background-filtering method.

3.2.2 X-ray Calibration

X-ray telescopes measure the pulse heights instead of directly measuring the energy of incoming photons. However, the relationship between pulse height and energy can be non-linear. This relationship is described by the redistribution function $R(h, E)$, which gives the probability that an incoming photon with energy E would be observed in a specific bin of pulse heights h (Arnaud *et al.*, 2011). For a telescope with an effective area $A(E)$, observing for an effective exposure time τ, the observed counts $C(h)$ in a spectral channel can be related to the intrinsic spectrum $s(E)$ by the equation (Davis, 2001)

$$C(h) = \tau \int R(h, E) A(E) s(E) \, \mathrm{d}E. \tag{3.13}$$

Unfortunately, this equation cannot be inverted to calculate the spectrum directly. Instead, a forward-folding approach is used, where a possible model spectrum is chosen based on the physics of the source. The expected number of counts per spectral channel is then calculated using equation (3.13) and compared to the observed values by using a goodness-of-fit test. The model parameters are then iteratively adjusted until the best fit is achieved (Arnaud *et al.*, 2011).

In practice, information about the redistribution function and the effective area is usually stored in files known as the redistribution matrix file (RMF) and the ancillary response file (ARF), respectively. Spectral analysis software such as XSPEC (Arnaud, 1996) use these files to model the spectrum.

3.2.3 *XMM-Newton*

XMM-Newton is an X-ray space observatory that was launched by the European Space Agency in December 1999. It follows a highly eccentric orbit around Earth in a period of approximately 48 hrs, enabling long, continuous observations. The observations are only briefly interrupted when the spacecraft passes through Earth's radiation belts (Jansen *et al.*, 2001).

The observatory is equipped with three X-ray telescopes with European Photon Imaging Cameras (EPICs) at their foci (Turner *et al.*, 2001). Two of these cameras, referred to as EPIC-MOS 1 and EPIC-MOS 2, each make use of seven MOS-CCDs (Turner *et al.*, 2001), while the third camera, EPIC-pn, makes use of twelve pn CCDs (Strüder *et al.*, 2001). The two MOS cameras have orthogonal CCDs and the pn CCDs are rotated 45° relative to them. This means that the gaps between the CCDs in one camera can be covered by the other two, providing full coverage of the field (Turner *et al.*, 2001). In addition to these cameras, the spacecraft is equipped with Reflection Grating Spectrometers fitted to the same telescopes as the MOS cameras (Turner *et al.*, 2001), and an Optical Monitor for simultaneous optical observations.

Each of the three X-ray telescopes consists of 58 nested, coaxial, and confocal Wolter I mirrors with grazing angles ranging from 17 to 42 arcmin. Each mirror is coated with gold. These telescopes each have a focal length of 7.5 m, and the largest mirrors have a diameter of 70 cm (Jansen *et al.*, 2001). The X-ray telescopes have a FOV of 30 arcmin and a useful quantum efficiency in the energy range of $0.2 - 10$ keV (Turner *et al.*, 2001).

The EPIC cameras can operate in different readout modes with various integration times and frame sizes, depending on the extent and brightness of the source being observed. If the source is very bright, there is an increased chance that more than one photon will interact with pixels close to each other before the image is read out. The different photons will then be registered as one event with erroneously high energy, an effect known as pile-up (Arnaud *et al.*, 2011). To prevent pile-up, a faster readout time can be achieved by using a smaller FOV. In order of increasing readout time, the different imaging modes include 'small window', 'large window', 'full frame', and in the case of EPIC-pn, 'extended full frame'. The cameras can also be operated in

'timing mode', which retains spatial information in only one dimension for faster readout times (Strüder *et al.*, 2001; Turner *et al.*, 2001).

3.2.3.1 *XMM-Newton* Science Analysis System

XMM-Newton data calibration is primarily done with the *XMM-Newton* Science Analysis System (SAS). This system consists of various tools, scripts, and libraries tailored specifically for handling data from the *XMM-Newton* observatory. The development, maintenance, and distribution of SAS are overseen by the *XMM-Newton* Survey Science Centre (SSC) (Gabriel *et al.*, 2004). The Extended Source Analysis Software (ESAS) was developed for handling the background of extended sources that cover a significant part of the FOV. It is currently in the process of being fully integrated with SAS. The discussions on ESAS follow mostly from Kuntz and Snowden (2008), Snowden *et al.* (2008), and the ESAS manual (Snowden and Kuntz, 2014, 2023).

3.2.3.2 *XMM-Newton* EPIC Background

The charged-particle EPIC background consists of a highly variable component created by soft protons (with energies less than a few 100 keV) and a more stable component created by high-energy particles interacting with the detector and its surrounding material (Snowden *et al.*, 2008). Most of the contamination caused by soft proton flares (SPF) can be removed by filtering out periods of flaring, but the latter component is variable on timescales much longer than the typical observation time, and is considered "quiescent".

High-energy particles directly striking the detector result in a continuum spectrum, while those interacting with the surrounding material produce fluorescent line emission that can be detected by the instruments. ESAS is equipped to model and subtract most of the quiescent particle background (QPB), following the methodology described in Kuntz and Snowden (2008). The regions in the corners of the detectors are shielded from focused X-rays, but not from X-rays and secondary electrons generated within the vicinity of the detector, providing a measure of the normalisation and shape of the QPB spectrum. In addition, the EPIC cameras are each equipped with a filter wheel system. When the filter wheel is closed, X-rays and soft protons originating outside the instrument are not detected, while high-energy particles capable of penetrating to the detectors are. The filter-wheel closed data provide the distribution of the QPB events across the FOV.

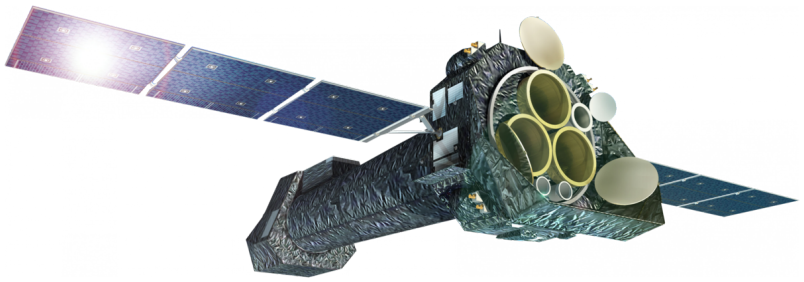

Figure 3.8: An artistic depiction of the *XMM-Newton* spacecraft (ESA/*XMM-Newton*, 2005).

While many of the fluorescent lines are included in the model QPB spectrum, some strong emission lines can not be well modelled in this way, and are excised from the model spectrum, including the Kα ($E \sim 1.49\,\mathrm{keV}$) and Si K$\alpha$ lines ($E \sim 1.75\,\mathrm{keV}$) in the EPIC-MOS spectra, and Al Kα and several lines in the $7.0-9.0\,\mathrm{keV}$ range in the EPIC-pn spectrum. These lines, along with the remaining background components, including residual contamination from SPF, the cosmic background, and potential solar wind charge exchange (SWCX), can be accounted for by fitting them alongside the source spectrum during spectral analysis. SWCX occurs when solar wind ions gain excited-state electrons from their interactions with neutral atoms, which leads to line emission as these electrons return to their ground states (Carter and Sembay, 2008).

The distribution of the SPF across the FOV was determined by Kuntz and Snowden (2008) and the distribution for the SWCX is given by the standard exposure map, but the normalisations of the SPF and the SWCX must be obtained by fitting the spectrum across the entire FOV. Therefore, spectral analysis is necessary to produce background-subtracted images of extended sources with *XMM-Newton*.

3.2.4 Data Collection

This study made use of archival data from *XMM-Newton*. The EPIC cameras provide detailed views of the extended X-ray emission from the hot ICM within the host clusters of radio galaxies. To select suitable targets, radio galaxies from the MGCLS were cross-referenced with the *XMM-Newton* Science Archive[12] to find galaxy clusters with existing X-ray data. Emphasis was placed on identifying clusters that exhibit signs of shock fronts, cold fronts, or other perturbations in the X-ray brightness or temperature distributions. Details of the selected *XMM-Newton* observations are presented in Table 3.2. Information about the corresponding radio data was provided in Section 3.1.4.

[12] `http://nxsa.esac.esa.int/`

Table 3.2: Summary of the *XMM-Newton* observations used for this study, including the observation date, the observation identifier (ObsID), the Right Ascension (RA) and Declination (Dec) of the pointing in degrees, and the duration of the observation in seconds.

Cluster	Date	ObsID	RA (deg)	Dec (deg)	Duration (s)
Abell 133	2002-12-22	0144310101	15.67125	-21.87972	33917
	2013-06-11	0723801301	15.67375	-21.88061	89278
	2013-06-14	0723802001	15.67375	-21.88061	88462
Abell 3266	2000-10-01	0105260701	68.11125	-61.31278	22192
	2000-10-11	0105260801	67.81583	-61.25917	21821
	2000-10-09	0105260901	67.59834	-61.50889	15015
	2000-09-27	0105261001	67.55542	-61.35056	15414
	2000-09-25	0105261101	68.14792	-61.48361	15015
	2000-09-23	0105262001	67.90417	-61.56722	9294
	2000-09-25	0105262101	68.14792	-61.48361	9688
	2000-09-27	0105262201	67.55542	-61.35056	9291
	2003-03-15	0105262501	67.90417	-61.56722	13624
	2023-06-15	0921880401	67.71858	-61.56517	132900
	2023-06-29	0921880801	67.71858	-61.56517	76900
Abell 3376	2003-04-01	0151900101	90.53583	-39.95500	46113
	2007-08-24	0504140101	90.21312	-40.02544	47206
Abell 3391	2005-10-19	0300211001	96.59242	-53.69369	35014
	2008-02-25	0505210401	96.59242	-53.69369	27915
	2013-06-14	0720252301	96.59479	-53.69550	12913
Abell 3395	2007-01-24	0400010301	96.79730	-54.46633	29910

3.2.5 Data Reduction

XMM-Newton datasets are available in the form of Observation Data Files (ODFs), the uncalibrated quantities in FITS format, and Pipeline Processing System products, scientific products created by the SSC. Calibrating ODFs requires calibration data in the form of a Current Calibration File (CCF). All CCFs are available from a continuously updated public repository[13]. SAS version 21.0 was used for most of the data reduction, apart from a few exceptions where version 20.0 was used instead. Before starting data reduction, the SAS task `cifbuild` was used to create a CCF Index File containing an up-to-date list of the relevant calibration files. The task `odfingest` then prepared the ODFs for processing by extending the ODF summary file to include information from the calibration database and the instrument housekeeping files containing the status of the detector and satellite.

[13] `https://www.cosmos.esa.int/web/xmm-newton/current-calibration-files`

The tasks `emchain` and `epchain` were used to perform the basic calibration of the ODFs and create calibrated event lists for EPIC-MOS and EPIC-pn, respectively. For EPIC-pn, `epchain` was also used to create an out-of-time (OOT) event list. OOT events occur during the short time frame when the pn CCDs are being clocked out. These events are recorded, but not associated with the correct positions, which can cause problems if not accounted for.

Occasionally, some of the MOS CCDs will malfunction, resulting in a significant increase in the background at energies below 1 keV. The task `emanom` was used to detect if any of the MOS CCDs were operating in an anomalous state. These CCDs were later excluded when creating the spectra and images. Due to micrometeorite strikes on 9 March 2005 and 11 December 2012, affecting EPIC-MOS 1 CCD 6 and CCD 3, respectively, these CCD were also excluded from observations after these dates.

The task `espfilt` was used to filter out most of the SPF. This created light curves in the 2.5 – 8.5 keV energy band from the full FOV data and the corner data, as well as a histogram of the count rate of the full FOV, as shown in the example in Figure 3.9. The histogram will typically have an approximately Gaussian peak at the nominal count rate during time intervals without SP flaring (Kuntz and Snowden, 2008). The `espfilt` task fitted a Gaussian to these data. It then created a good time interval file containing all time intervals with count rates within 3.0 times the standard deviation from the peak of the Gaussian. Some contamination from SPF is often still present after this temporal filtering and must be accounted for when fitting the spectrum.

For EPIC-MOS, the filters `PATTERN<=12` and `((FLAG & 0x766aa000) == 0)` were used to select single, double, triple, and quadruple pixel events that passed conservative screening to filter out bad events. For EPIC-pn, only single and double events pixels were selected with `PATTERN<=4`, and bad events filtered out with `((FLAG & #XMMEA_EP) == 0)`.

Since only the diffuse cluster emission is of interest, point sources were identified and removed from the data. This can be done with the SAS task `cheese`, which creates source lists and FITS "cheese" masks. To capture the same point sources in all observations, `cheese` was used to run point source detection for each observation, as well as on merged event lists of all the observations. The source lists were then combined and augmented with data from Wang *et al.* (2016), and a subset of the `cheese` routine was used to create masks for each observation.

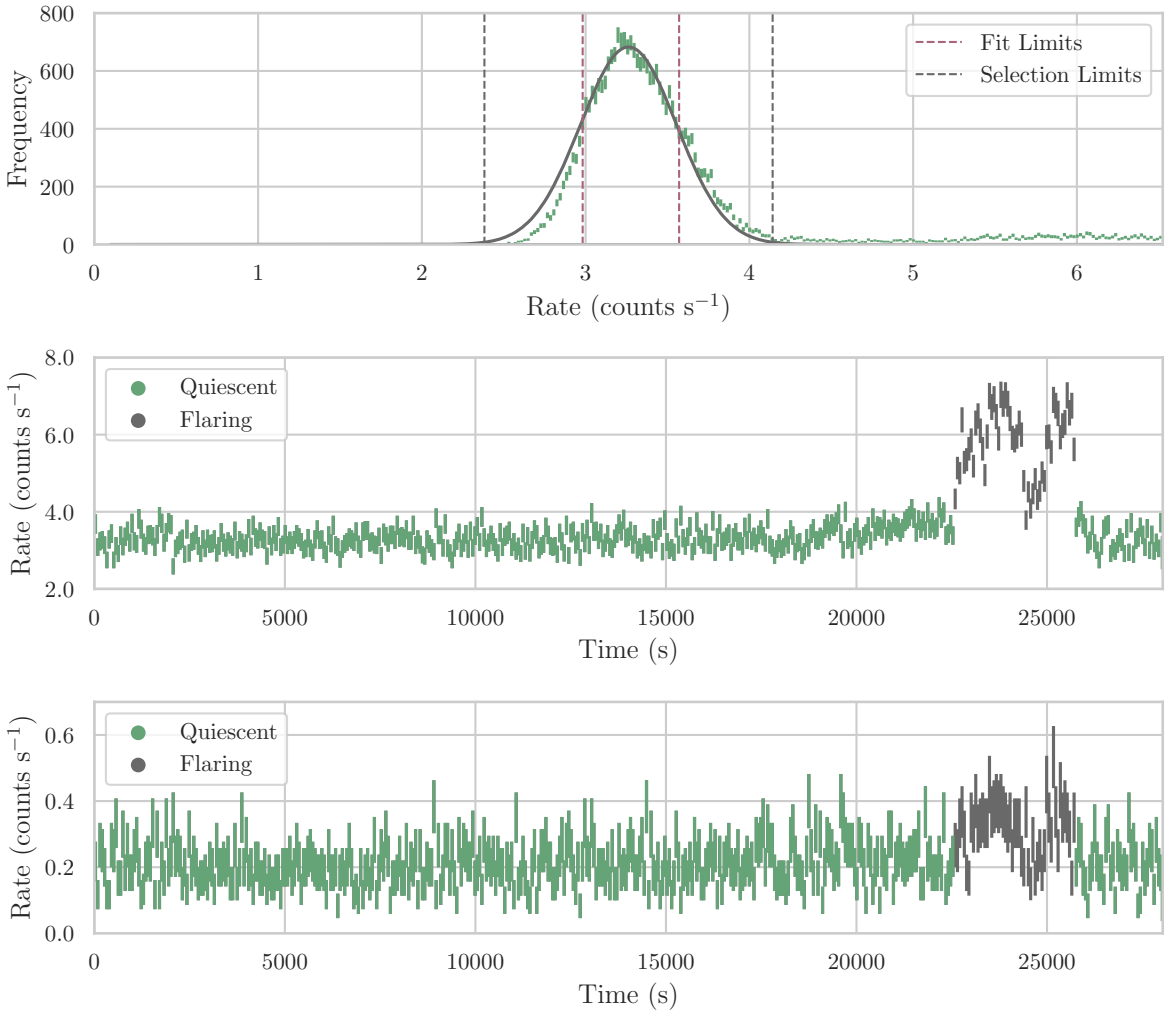

Figure 3.9: Count rate histogram (*top*), FOV light curve (*middle*), and corner light curve (*bottom*) for Abell 3395, ObsID 0400010301, demonstrating the selection of good time intervals that are free of SPF.

3.2.6 Spectral Analysis

Because X-ray telescopes like *XMM-Newton* record the position and energy of individual photons, it is possible to apply a region filter to an event list and extract a spectrum from events in that region. X-ray spectroscopy of different regions of a cluster reveals the variation of the physical properties, such as the ICM temperature, over the extent of a cluster. It also makes it possible to identify and characterise any residual soft proton or SWCX contamination. These components can then be subtracted when creating clean images of the cluster.

3.2.6.1 Contour Binning

In spectral analyses of clusters, common choices for the regions from which the spectra are extracted include sectors, boxes, ellipses, or concentric annuli around the cluster core. The

latter is a good option for studying how the properties of the ICM change with distance from the centre of spherically or elliptically symmetric clusters. However, many clusters are not symmetric and have significant spectral variation in different directions. To address this, Sanders (2006) developed a technique to define regions by following contours on a smoothed image[14]. This method assumes that spectral changes are associated with changes in surface brightness rather than distance from the cluster centre.

This contour binning software was used to define 15 regions for each cluster with approximately equal SNR, using mosaic images created from all the observations. To prevent the regions from becoming too elongated, the geometrical constraint factor `constrainval` was set to the values in Table 3.3.

Table 3.3: Parameters used in contour binning.

Cluster	SNR	Geometrical Constraint
Abell 133	400	2.0
Abell 3266	600	2.0
Abell 3376	275	2.5
Abell 3391	545	1.9
Abell 3395	545	1.9

To make the contour binning software work in the context of *XMM-Newton* and ESAS, several adjustments were necessary. By default, the software creates a FITS map of the binned regions, which it converts to region files compatible with the *Chandra* Interactive Analysis of Observations software package, composed of smaller box regions. However, `mosspectra` and `pnspectra` require region inputs in detector coordinates, which differ for each instrument and observation. In addition, since a mosaic input image was used, some regions fall outside the FOV of some of the observations, making the casting of the sky coordinates to detector coordinates problematic. The modified software created detector coordinate FITS region files for each instrument of each observation of only the regions that overlap with the FOV of that image.

3.2.6.2 Spectrum Extraction

For each of the 15 regions defined with the contour binning software, spectra and QPB spectra were extracted for all instruments and observations where that region is in the FOV and the statistics were sufficient for a model QPB spectrum to be created. The spectra and QPB background spectra were created from the cleaned event lists, with point sources removed and

[14] `https://github.com/jeremysanders/contbin`

OOT events subtracted, in a two-step process with `mosspectra` and `mosback` for EPIC-MOS and `pnspectra` and `pnback` for EPIC-pn. This also created the RMFs and ARFs needed for spectral analysis.

3.2.6.3 XSPEC

The spectral fitting was done with XSPEC, using abundances by Wilms *et al.* (2000) and photoionisation cross sections by Verner *et al.* (1996). XSPEC is an interactive, command-driven program that uses TCL as its user interface.

XSPEC calculates the predicted count spectrum $C_p(h)$ from a user-supplied model spectrum (see equation (3.13)), and varies the model parameters until the predicted count spectrum adequately describes the observed count spectrum $C(p)$. XSPEC has different goodness-of-fit statistical test options, such as the chi-squared test,

$$\chi^2 = \sum \frac{(C(h) - C_p(h))^2}{(\sigma(h))^2}, \tag{3.14}$$

where $\sigma(h)$ is the uncertainty for a channel. In general, for a fit to be considered good, the χ^2 value must be approximately equal to the number of degrees of freedom, calculated by XSPEC as the number of channels minus the number of model parameters (Arnaud *et al.*, 2024). However, the chi-squared test is invalid when channels have low counts (Cash, 1979). To ensure that each channel had sufficient counts, channels were binned with the optimal binning method of Kaastra and Bleeker (2016).

XSPEC models can be created by users from built-in or user-defined components. These components can be additive, multiplicative, mixing, or convolutions. During spectral fitting, the parameters of each component can be free to vary, frozen to a specific value, or linked to another parameter. XSPEC models can also be fitted to multiple data files simultaneously.

All spectra from the different regions, instruments, or observations were simultaneously fitted, with the QPB background subtracted. The relevant model parameters were linked for the different spectra or frozen to their expected values, minimising the amount of free parameters. The full model, described in the next section, has thousands of parameters in its simplest form. It becomes even more complex when multiple observations are included. As it is impractical to set this up interactively, it was scripted with PyXspec, an object-oriented PYTHON interface of XSPEC.

3.2.6.4 Spectral Model

The spectral model consisted of five components: the cluster emission, the cosmic background, instrumental lines, SWCX, and residual SPF contamination. The cluster emission was modelled with APEC, with absorption described by the Tuebingen-Boulder ISM absorption model (Wilms *et al.*, 2000), which calculates the absorption based on the hydrogen column density. In pseudo-XSPEC terms, this is

$$M_1 = \texttt{TBabs} \times \texttt{apec}.$$

The parameters of APEC in XSPEC are the plasma temperature, the metal abundances, the redshift, and a normalisation factor given by equation (2.6). Determining the temperature of the ICM is one of the main objectives of the spectral analysis.

The Galactic hydrogen column densities, shown in Table 3.4, were estimated with the $\mathrm{NH_{tot}}$ tool[15], which uses the HI maps of Kalberla *et al.* (2005) with a correction for molecular hydrogen added using the method of Willingale *et al.* (2013).

Table 3.4: The redshift, z, and the total Galactic column density, n_H of each cluster. The hydrogen column density is given in XSPEC units of $10^{22}\,\mathrm{atoms\,cm^{-2}}$.

Cluster	z	n_H
Abell 133	0.0569	1.65×10^{-2}
Abell 3266	0.0589	1.72×10^{-2}
Abell 3376	0.0468	6.05×10^{-2}
Abell 3391	0.0550	7.58×10^{-2}
Abell 3395	0.0510	1.01×10^{-1}

The cosmic background consists of emission from extragalactic AGNs, modelled with an absorbed power law with a photon index of 1.45 (Lumb *et al.*, 2002), unabsorbed thermal emission from the Local Hot Bubble (LHB), modelled with APEC, and absorbed thermal emission from the Milky Way Halo (MWH), modelled with two APEC components,

$$M_2 = \texttt{apec} + \texttt{TBabs}(\texttt{apec} + \texttt{apec} + \texttt{powerlaw}).$$

The normalisation of the power law is known to be $\sim$10.5 keV cm^{-2} s^{-1} sr^{-1} keV^{-1}. In XSPEC, this is $8.88 \times 10^{-7}\,\mathrm{photons\,cm^{-2}\,s^{-1}\,keV^{-1}\ arcmin^{-2}}$ at 1 keV. However, since point sources were excluded when extracting the spectrum, the expected normalisation was estimated with the SAS task `point-source` to be $1.09 \times 10^{-7}\,\mathrm{photons\,cm^{-2}\,s^{-1}\,keV^{-1}\ arcmin^{-2}}$.

To constrain the cosmic background, the cosmic background model was also fitted simultaneously

[15] `https://www.swift.ac.uk/analysis/nhtot/docs.php`

to a *ROSAT* All Sky Survey (RASS) spectrum extracted in a $0.5-1.0^{\circ}$ annulus surrounding the cluster centre, using the High Energy Astrophysics Science Archive Research Center X-ray Background Tool[16].

There are some emission lines by the material surrounding the detectors that are too strong to be modelled properly by ESAS. These lines have been removed from the QPB spectra and must be modelled explicitly with Gaussians. For EPIC-MOS, this is done with two Gaussians at energies $E \sim 1.49$ and $E \sim 1.75$, for the Al Kα and Si Kα fluorescent lines, respectively. For EPIC-pn, the normalisation of the Si Kα line was set to zero, and energies in the $7.0-9.0$ keV range were excluded from the spectrum to avoid fitting several lines in this range. In pseudo-XSPEC terms, the instrumental line model is

$$M_3 = \texttt{gaussian} + \texttt{gaussian}.$$

Potential emission lines due to SWCX, listed in Table 3.5, were also modelled with Gaussian components, using

$$M_4 = \texttt{gaussian} + \texttt{gaussian} + \texttt{gaussian} + \texttt{gaussian} + \texttt{gaussian}.$$

Table 3.5: Energies of the SWCX emission lines.

Line	Energy (keV)
O VII	0.57
O VIII	0.65
O VIII	0.81
Ne IX	0.92
Mg XI	1.35

Although the bulk of the SPF component is removed by filtering out periods of flaring, some contamination still remains. This can be modelled reasonably well with a broken power law,

$$M_5 = \texttt{bknpower}.$$

As this component is created by protons rather than photons, the broken power law is not folded through the ARF, and uses an RMF for an infinitely narrow line spread function.

In order to link the relevant normalisations of the model components for the different instruments or observations, all the model components were multiplied with two constant components, `constant*constant`. The first of these was included to normalise the area of the region to 1 arcmin and the second constant ($\sim$1) was to account for small calibration differences between instruments and observations.

[16] `https://heasarc.gsfc.nasa.gov/cgi-bin/Tools/xraybg/xraybg.pl`

3.2.7 Imaging Analysis

As discussed in Section 2.1.1.1, at soft X-ray energies, an image of a cluster is an approximate map of the square of the ICM column density. These images reveal the complex morphology and density distributions of the ICM, including substructures, shocks, and cold fronts.

3.2.7.1 Image Creation

Apart from creating the spectra, `mosspectra`/`pnspectra` and `mosback`/`pnback` were also used to create count images, QPB images, and exposure maps of the clusters in the $400-1300\,\mathrm{eV}$ energy range. Using the spectral analysis results, the ESAS tasks `proton` and `swcx` were used to create images of the SPF and SWCX background, respectively. The background images were created in detector coordinates, and were rotated to sky coordinates with `rotdet2sky`. The data of the different observations and instruments were then combined with `mosaicmerge` to create a single count image, exposure map, point source mask, QPB image, SPF image, and SWCX image. These components were combined to create a background-subtracted, exposure-corrected count rate mosaic with `binadaptmerge`. This task was also used to create adaptively smoothed images, for cosmetic purposes only, after filling the regions where point sources were masked with values from the surrounding pixels[17]. For Abell 3395, where only one observation was used, `combimage` and `binadapt` were used instead of `mosaicmerge` and `binadaptmerge`.

3.2.7.2 Gaussian Gradient Magnitude Filtering

To highlight variations in the surface brightness and detect edges related to filamentary structures, cold fronts, and shocks, a Gaussian Gradient Magnitude (GGM) filter (Sanders *et al.*, 2016a,b, 2022) was applied to the images. This works by computing the gradient of the image assuming Gaussian derivatives. The Gaussian width can be adjusted to detect gradients on different scales. To prevent the GGM filtering from becoming noisier at the outskirts of clusters, where there are fewer X-ray counts per pixel, a larger width is needed than in the cluster centres. To do this, the adaptive GGM filtering[18] described by Sanders *et al.* (2022) was used to adjust the scale dynamically based on the SNR at that region.

[17] The tool to mask point sources cosmetically was based on `hideregions2` (see `https://github.com/jeremysanders/ggm`), but adapted to work with the FITS image masks created by `cheese` rather than region files.

[18] `https://github.com/jeremysanders/ggm`

Chapter 4

Results

This chapter describes the main results of the radio and X-ray analysis of the galaxy clusters Abell 133, Abell 3266, Abell 3376, Abell 3391, and Abell 3395. Section 4.1.1 presents the radio continuum MeerKAT images of each galaxy cluster, highlighting specific radio galaxies in each field. The radio spectral index maps of these sources are shown in Section 4.1.2. The *XMM-Newton* X-ray images of the clusters are discussed in Section 4.2.1. Section 4.2.2 describes the regions used in the X-ray spectral fitting and summarises the spectral analysis results.

4.1 Radio Analysis

4.1.1 Radio Continuum Images

This section presents high-resolution continuum MeerKAT images of the clusters, revealing the detailed structures of radio galaxies in each field. The images have been corrected for direction-dependent effects. On average, the dynamic range, defined as the ratio of the peak intensity to the global RMS, improved by 25.6% after 3GC. The RMS and dynamic range values are shown in Table 4.1. Although 3GC significantly reduced the DDEs, some artefacts still remain, particularly around the bright central radio galaxy of Abell 3391.

Table 4.1: Global RMS in units of mJy beam^{-1} and dynamic range for each cluster after 2GC and 3GC.

Cluster	RMS		Dynamic Range	
	2GC	3GC	2GC	3GC
Abell 133	0.26	0.21	650.30	927.88
Abell 3266	0.52	0.42	632.33	745.94
Abell 3376	0.43	0.32	650.30	833.77
Abell 3391	1.68	1.04	341.58	366.55
Abell 3395	0.90	0.70	382.42	505.16

4.1.1.1 Abell 133

Figure 4.1 presents the MeerKAT image of Abell 133, showing several radio galaxies within and around the cluster. The most prominent source is the radio galaxy discovered by Randall *et al.* (2010), spanning approximately 6.5 arcmin. A zoomed-in view of this source is provided in Figure 4.2. This radio galaxy has two narrow jets extending in the north–south direction, terminating in two similarly sized lobes.

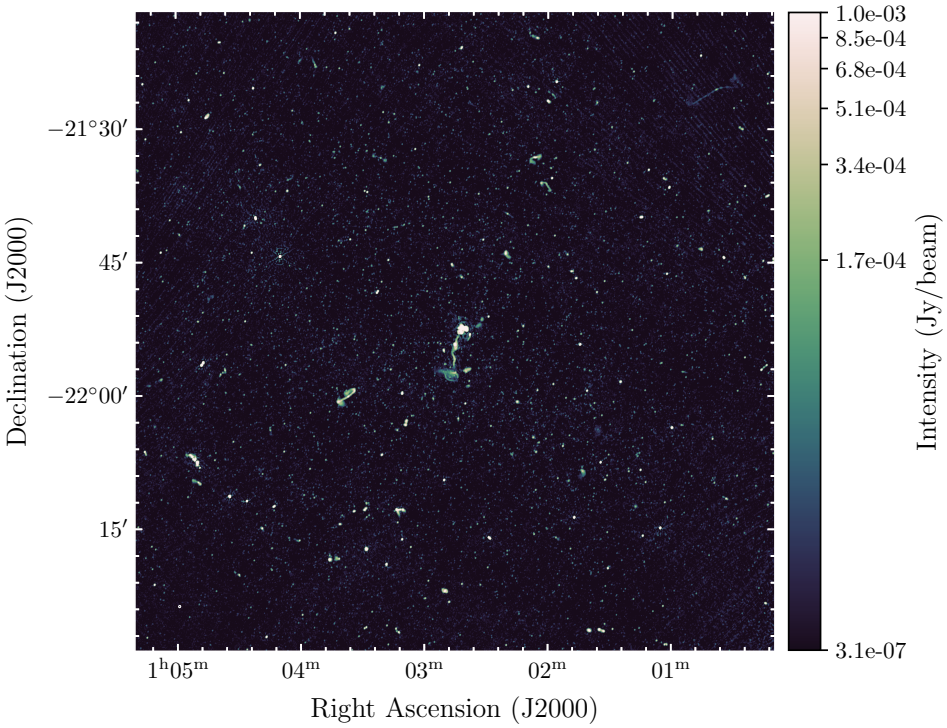

Figure 4.1: $7\farcs7 \times 6\farcs5$ resolution MeerKAT total intensity image of Abell 133. The off-source RMS noise level is 4.2 µJy beam^{-1}.

Both jets fade and become unresolved before reaching the lobes. The brightest region in the faint southern lobe is likely the point where the jet connects with the lobe. The lobe has sharp boundaries, with some diffuse emission extending eastward.

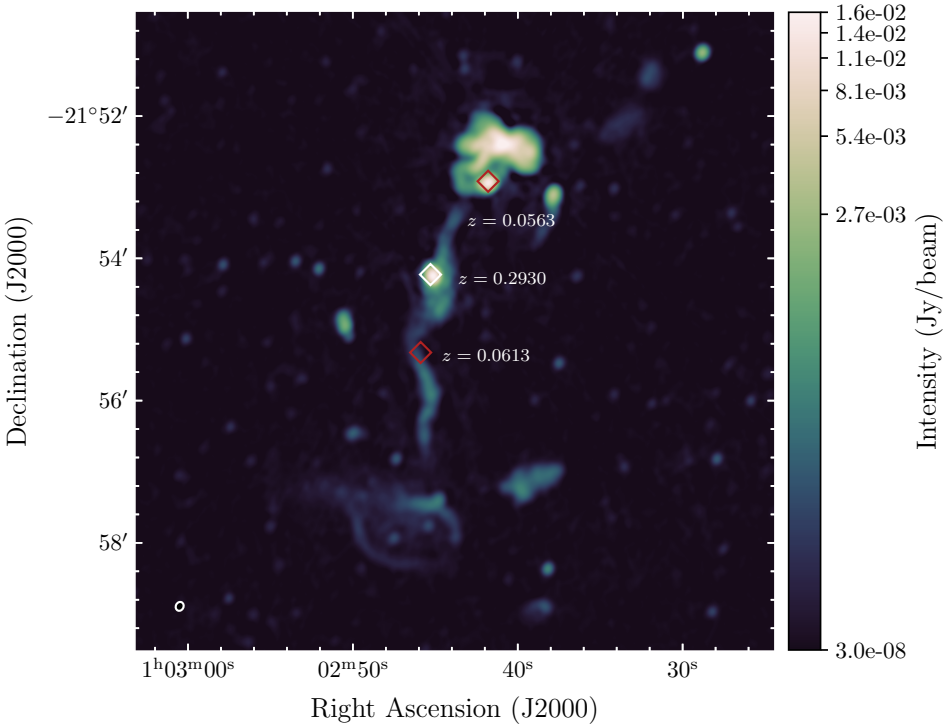

Figure 4.2: MeerKAT total intensity image of the central galaxy of Abell 133. The white ellipse in the bottom left corner shows the $7\farcs7 \times 6\farcs5$ beam size. The red diamonds show the positions of the cluster member galaxies KGS J010242−215234 (Carroll *et al.*, 2016) at $z = 0.0563$ and NFP J010245.9−215520 (Smith *et al.*, 2004) at $z = 0.0613$. The white diamond marks the position of 2MASX J01024529−2154137 (Skrutskie *et al.*, 2006) at $z = 0.2930$.

The northern lobe overlaps in projection with the peak X-ray emission of the cluster (see Section 4.2.1.1). The radio emission from this region is much brighter than that of the jets or the southern lobe and was considered a radio relic before the discovery of the extended jets to the south (Slee *et al.*, 2001). It has an irregular but sharply defined morphology. A compact radio source corresponding to the BCG is embedded in this emission.

The jets exhibit several small bends and twists. Near the projected centre of the radio galaxy, there is a prominent bend with an opening angle of approximately 135°. A cluster member galaxy appears slightly offset from the bend point, but there is no evidence of a radio core to suggest that this could be the host galaxy. Alternatively, a bright compact radio source approximately 1 arcmin northwest of the bend point may be the host galaxy. However, this would place the radio galaxy outside the cluster, at $z = 0.2930$.

Several other radio galaxies are present in the field, some of which are shown in Figure 4.3. Panel (a) depicts a radio galaxy with a sharply bending jet. While a bright compact region is visible, no optical counterpart has been identified to confirm the location of the host galaxy.

Panel (b) reveals the knotty structure of the radio galaxy PMN J0104−2208. Panel (c) shows

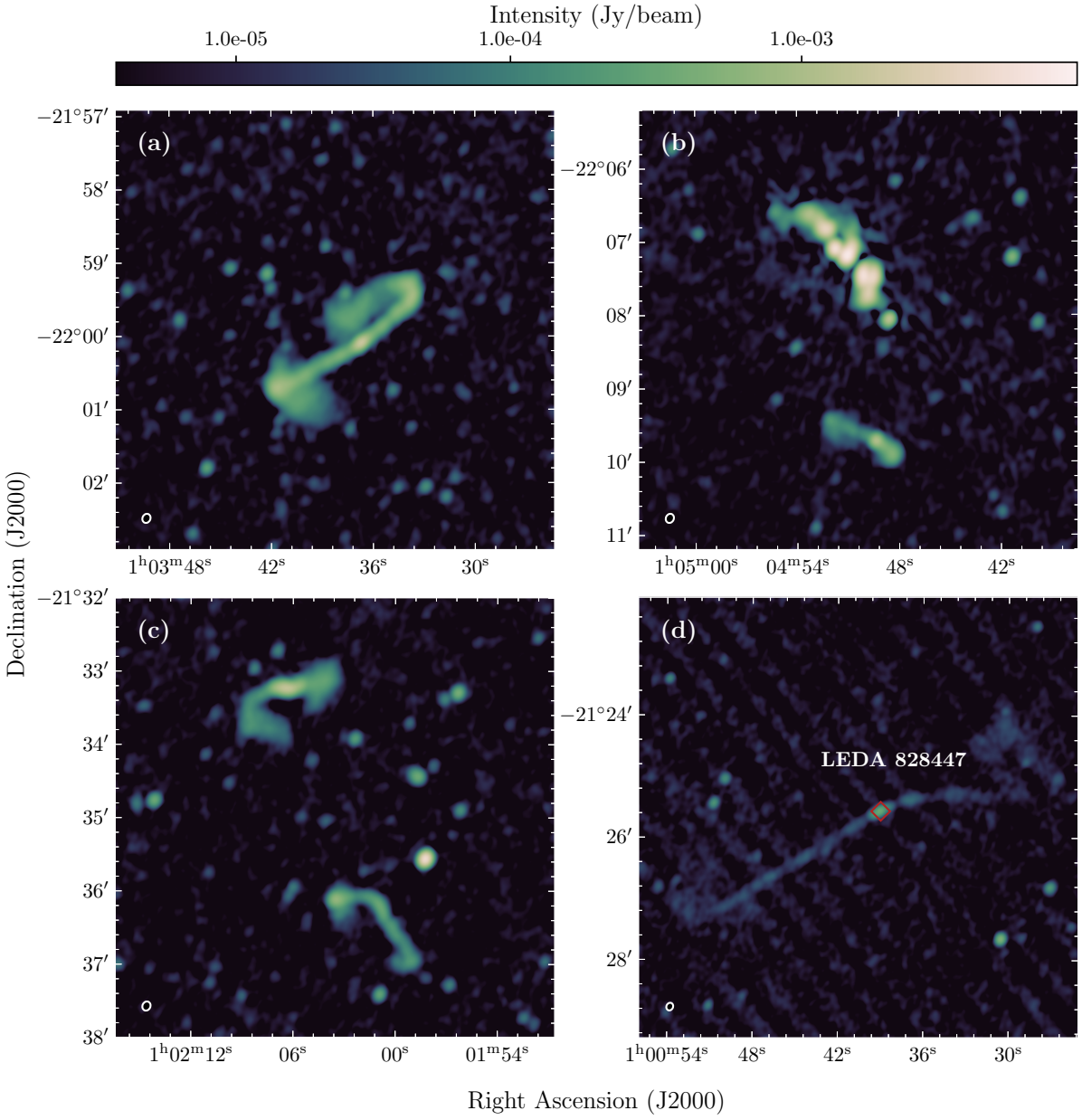

Figure 4.3: MeerKAT total intensity images of individual radio galaxies in the Abell 133 field. The white ellipses in the bottom left corner of each panel show the $7\farcs7 \times 6\farcs5$ beam size. The red diamond in panel **(d)** shows the position of LEDA 828447 at $z = 0.193$ (Paturel *et al.*, 2003).

two other radio galaxies with bent jets and no known counterparts. Panel (d) reveals a faint source with a compact core and two collimated jets terminating in radio lobes. The northeast–southwest lines visible in this panel are calibration artefacts. The compact core coincides with LEDA 828447 at $z = 0.193$ (Dálya *et al.*, 2018). At this redshift, its angular size of ∼6.5 arcmin corresponds to ∼1.3 Mpc, classifying it as a giant radio galaxy.

4.1.1.2 Abell 3266

Several radio galaxies and other radio sources are visible in the MeerKAT image of Abell 3266, shown in Figure 4.4. Magnified versions of the most prominent radio galaxies in the field, A3266-RG1, A3266-RG2, A3266-RG3, and A3266-RG4 are shown in Figure 4.5.

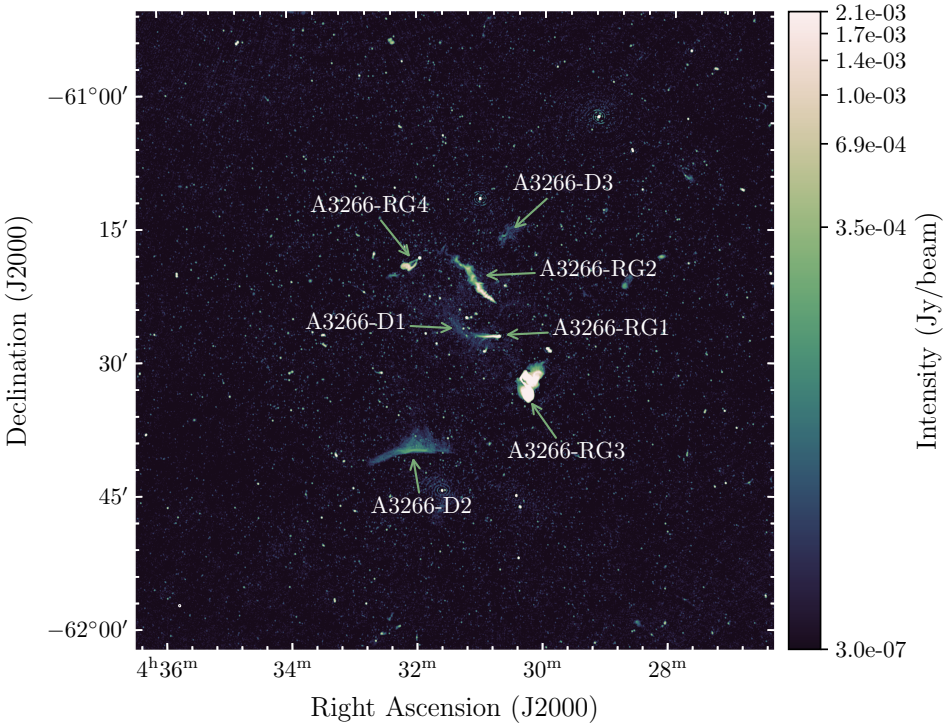

Figure 4.4: $7\farcs4 \times 6\farcs6$ resolution MeerKAT total intensity image of Abell 3266. The off-source RMS noise level is $6.9\,\mu\text{Jy beam}^{-1}$.

Figure 4.5 (a) shows A3266-RG1, with a bright core and a thin one-sided jet extending east towards the centre of the cluster for approximately 3 arcmin, before blending into the diffuse emission from A3266-D1, bending north. Faint wisps of emission extend northeast and southeast from the collimated jet, approximately 1.2 arcmin and 1.6 arcmin from the core, respectively.

The unusual radio galaxy—or possibly multiple radio galaxies—A3266-RG2 is shown in Figure 4.5 (b). This source, oriented in the northeast–southwest direction, has a bright, knotty southwestern half, the so-called "ribbed-tail" (Rudnick *et al.*, 2021; Knowles *et al.*, 2022), and a faint northeastern half. Four filamentary tethers are visible, connecting the northeastern "triple" with the rest of the source.

The bent-tailed source A3266-RG3, shown in Figure 4.5 (c), has a bright core aligned with its optical counterpart, J043022.01−613200.2, and two jets bending westward. The southwestern jet remains collimated for approximately 1.2 arcmin before brightening and expanding into a

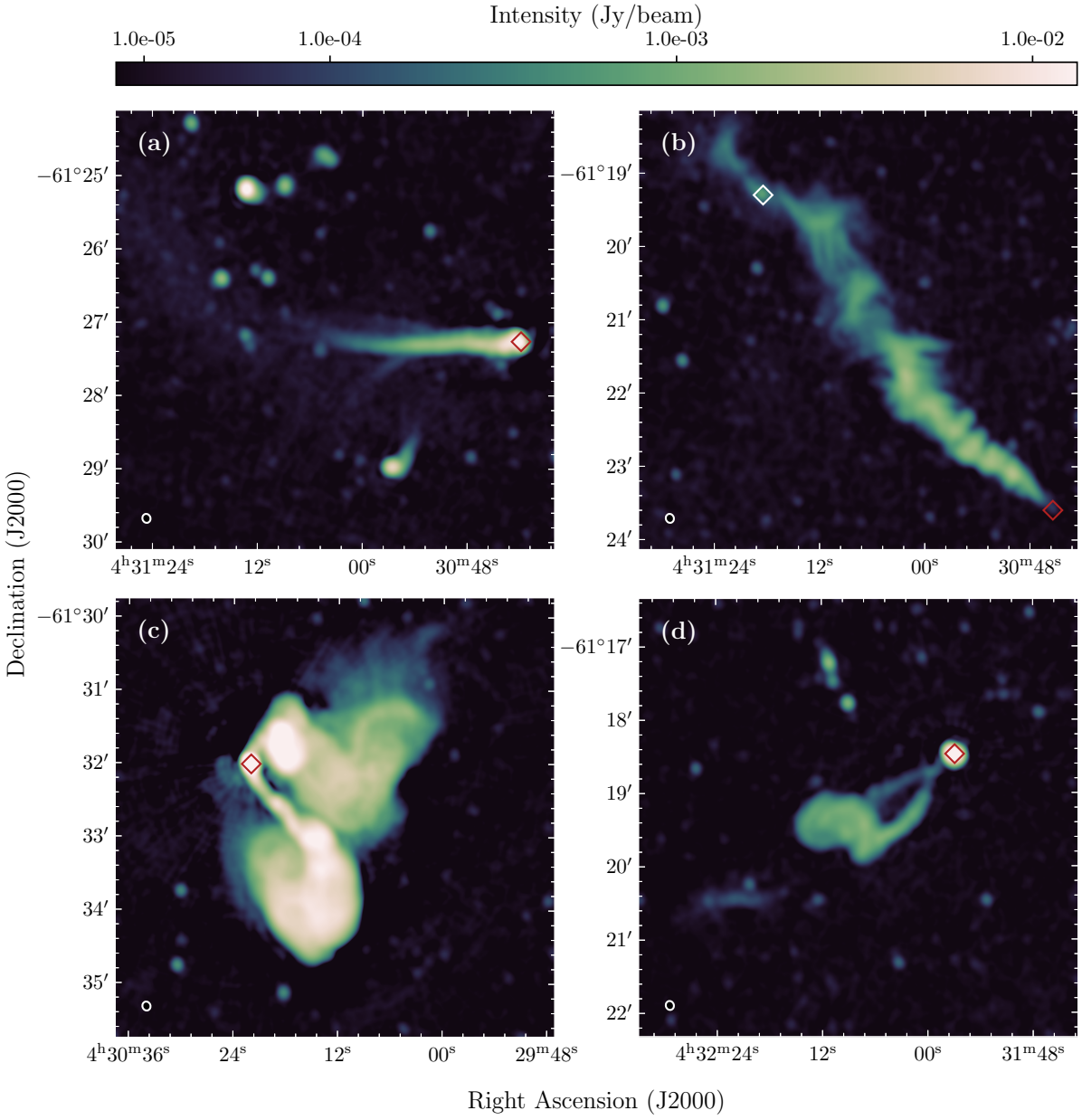

Figure 4.5: MeerKAT total intensity images of the radio galaxies **(a)** A3266-RG1, **(b)** A3266-RG2, **(c)** A3266-RG3, and **(d)** A3266-RG4. The tail of A3266-RG1 leads into the diffuse ridge, A3266-D1. The red diamonds mark the optical positions of the likely host galaxies (Gaia Collaboration, 2023). The white diamond in panel **(b)** shows the position of WISEA J043118.50−611918.2 at $z = 0.78$. The white ellipses in the bottom left corner of each panel show the $7\farcs4 \times 6\farcs6$ beam size.

lobe that curves back northeast. The northwestern jet extends approximately 0.4 arcmin before becoming indistinguishable from a lobe that first stretches southwest before bending back northwest. The region where the jet meets the lobe is very bright. The hook-like feature identified by Riseley *et al.* (2022) appears near the end of the northwestern lobe. Filamentary emission extends further north.

A3266-RG4, shown in Figure 4.5 (d), has a bright compact core coinciding with the position of

its optical counterpart and two jets bending southeast, with an opening angle of approximately 27°. About 1.4 arcmin from the core, the jets connect with a lobe. It appears to be connected to the bright southern jet, but there could also be some contribution from the northern jet.

Other sources of interest include the cluster radio shock, A3266-D2, and the diffuse source northwest of the core, A3266-D3, shown in Figure 4.6. The ultrasteep emission west of A3266-RG3, discovered by Duchesne *et al.* (2022), could not be detected.

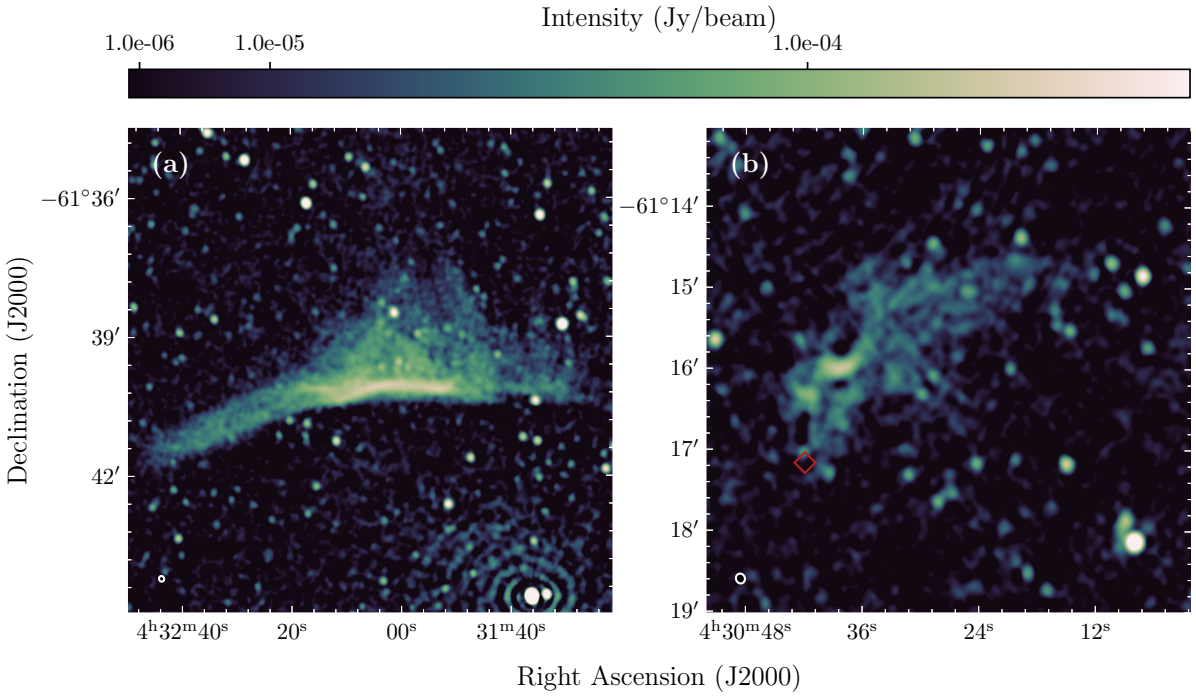

Figure 4.6: MeerKAT total intensity image of the diffuse radio sources **(a)** A3266-D2 and **(b)** A3266-D3. The red diamond in panel **(b)** shows the position of the optical galaxy identified by Riseley *et al.* (2022) as the potential source of the diffuse emission. The white ellipses in the bottom left corner of each panel show the $7''.4 \times 6''.6$ beam size.

4.1.1.3 Abell 3376

The MeerKAT image of Abell 3376 is presented in Figure 4.7. This displays the two large-scale cluster radio shocks at the outskirts of the cluster. Several radio galaxies appear in the field, most notably the bent-tailed source A3376-RG1 and the small radio galaxy east of it, A3376-RG2, shown in Figure 4.8.

A3376-RG1 has two jets extending north and south of the optical position of its unresolved core. The inner jets, extending ∼15 arcsec from the optical position of the host galaxy, are exceptionally bright and bend slightly eastward. Beyond this point, the jets align parallel and progressively dim, until they abruptly bend 90° to the east, approximately ∼60 arcsec north

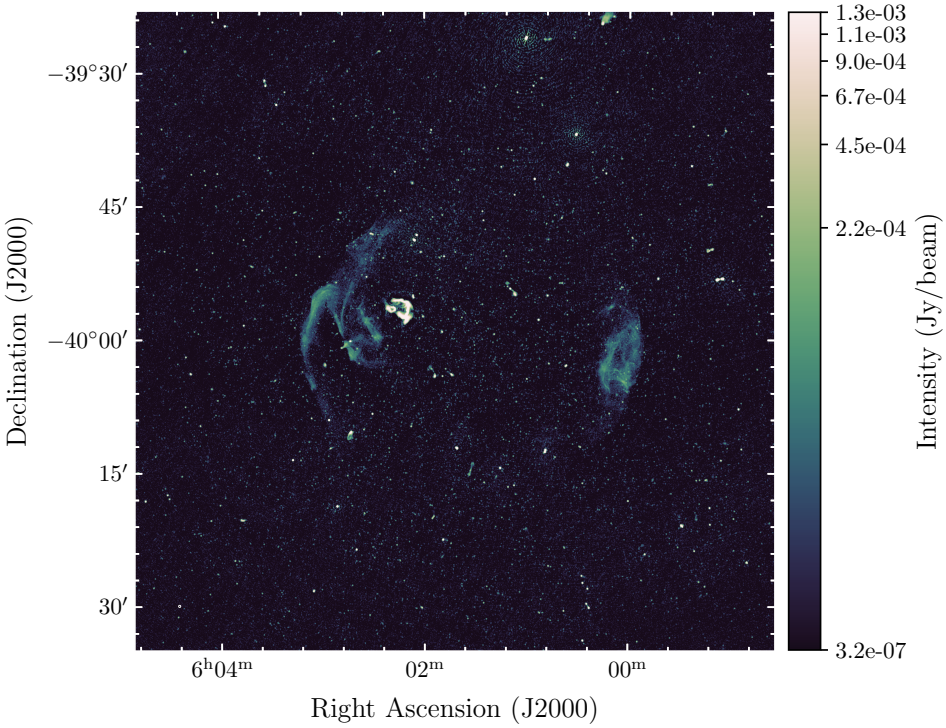

Figure 4.7: $6\farcs3 \times 6\farcs1$ resolution MeerKAT total intensity image of Abell 3376. The off-source RMS noise level is $4.9\,\mu\mathrm{Jy\,beam^{-1}}$.

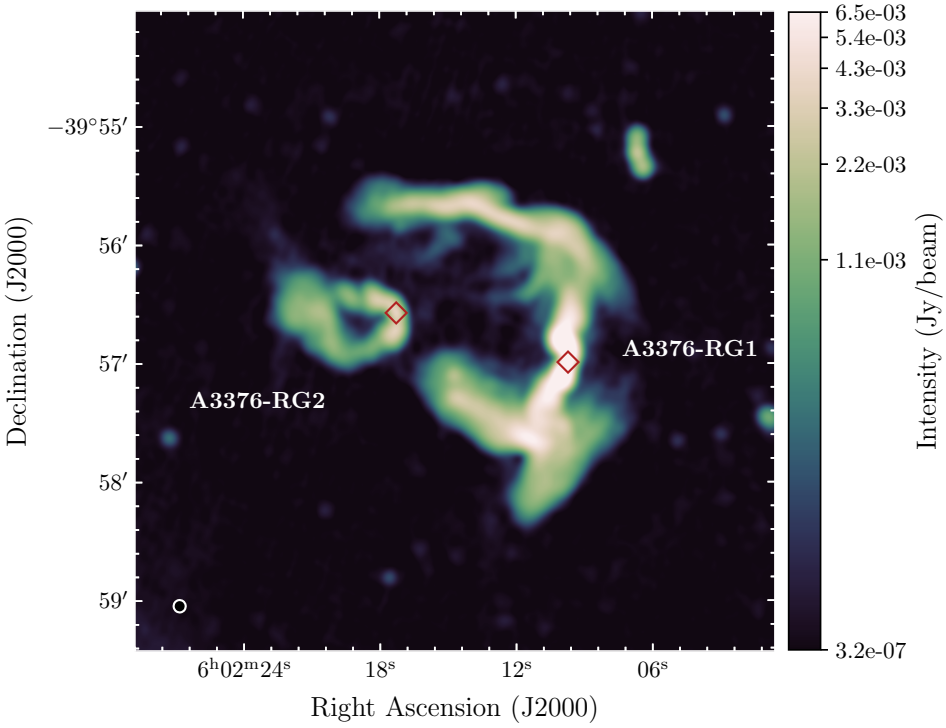

Figure 4.8: MeerKAT total intensity image of radio galaxies A3376-RG1 and A3376-RG2. The red diamonds mark the positions of the host galaxies of A3376-RG1 and A3376-RG2 (Gaia Collaboration, 2023). The white ellipse in the bottom left corner shows the $6\farcs3 \times 6\farcs1$ beam size.

and ∼40 arcsec south of the core.

After the bend point, the northern jet brightens and remains straight and well-collimated for a further ∼50 arcsec, before bending slightly and continuing for another ∼60 arcsec. The southern jet brightens at the bend point and extends northeast for ∼60 arcsec. Diffuse emission extends away from the jets at both bend points. Filamentary structures appear around the bend point of the northern jet.

A3376-RG2 also exhibit jets bending eastward, with an opening angle of approximately 40°. Both jets extend roughly 30 arcsec before the southern jet expands into a lobe that curves northward.

4.1.1.4 Abell 3391

The MeerKAT image of Abell 3391, presented in Figure 4.9, exhibits the most severe DDEs among the clusters in the sample, with ring-like appearing around the bright central radio galaxy MRC 0625−536. Similar artefacts appear in ASKAP images of the same source (Brüggen *et al.*, 2021; Wilber *et al.*, 2023a).

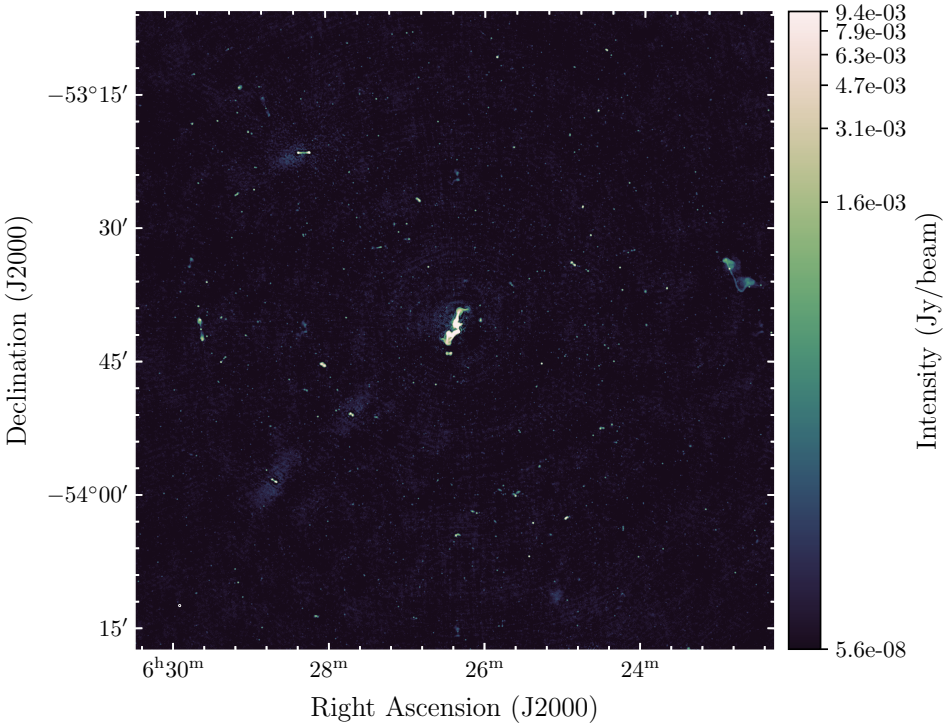

Figure 4.9: 6″.2 × 5″.9 resolution MeerKAT total intensity image of Abell 3391. The off-source RMS noise level is 10 µJy beam^{-1}.

MRC 0625−536, shown in Figure 4.10 (a), lacks a resolved core, but features bright, twisting

jets extending from the position of the BCG of Abell 3391. The jets initially curve eastward but align in a northwest–southeast orientation after undergoing several bends and twists. Although initially wide, the jets gradually narrow and collimate further out. A straight filament extends 30 arcsec southeast from one of the bend points along the southern jet.

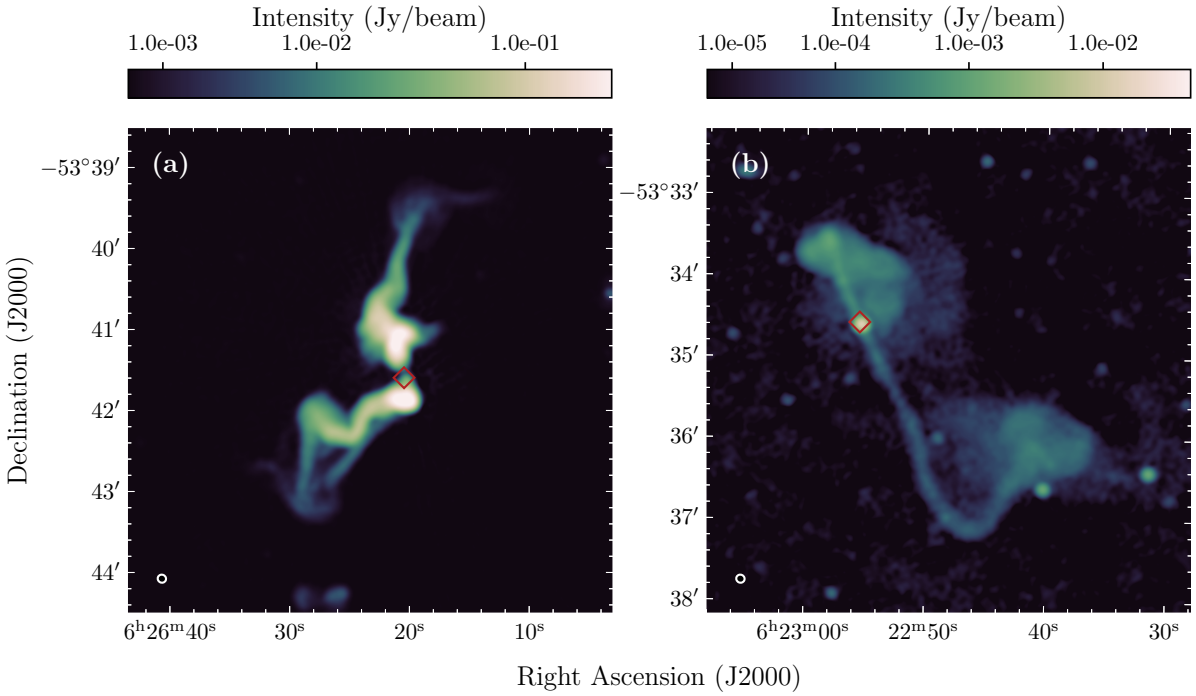

Figure 4.10: MeerKAT total intensity image of radio galaxies in the Abell 3391 field. The red diamonds mark the position of the host galaxies (Skrutskie *et al.*, 2006; Petrov *et al.*, 2019). The white ellipses in the bottom left corner of each panel show the $6\farcs2 \times 5\farcs9$ beam size.

Figure 4.10 (b) shows the radio galaxy PMN J0622−5334 located in the western outskirts of the cluster. It has two collimated jets initially extending northeast and southwest from a compact core associated with WISEA J062255.56−533434.5 at $z = 0.0567$. Approximately 3 arcmin from the core, the southern jet bends sharply west, with an opening angle of about 50°. It remains collimated for a further ∼1 arcmin before expanding into a diffuse lobe. North of the core, the jet remains collimated for 1.2 arcmin before abruptly terminating. The entire northern jet and core are embedded in a diffuse lobe. This could be a result of the viewing angle.

4.1.1.5 Abell 3395

The MeerKAT image of Abell 3395 is presented in Figure 4.11. The most prominent feature in the image is PKS J0626−5432, the radio galaxy associated with the BCG of A3395-S, also displayed in Figure 4.12.

This radio galaxy has a compact core with thin inner jets that expand into wider, brighter

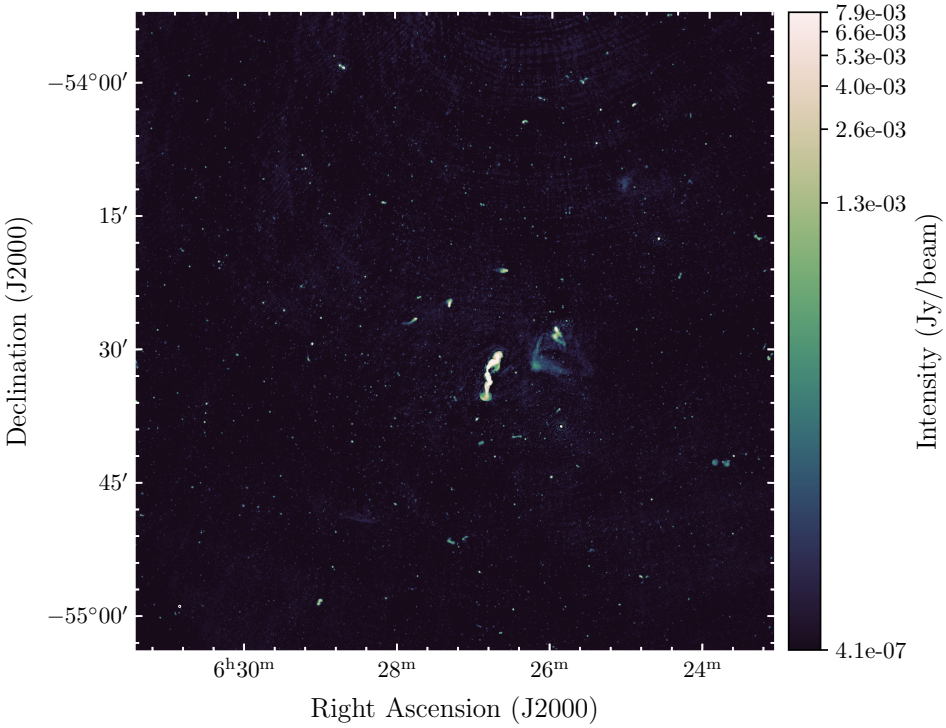

Figure 4.11: $6\farcs6 \times 6\farcs0$ resolution MeerKAT total intensity image of Abell 3395. The off-source RMS noise level is $4.2\,\mu\mathrm{Jy\,beam}^{-1}$.

jets after approximately 9.5 arcsec. The jets then bend slightly westward, extending for about 1.2 arcmin. Beyond this, the northern jet bends further west and then northward, terminating in a diffuse lobe. Faint emission also extends south of this final bend point. The southern jet bends eastward and then southward for a further ∼1.5 arcmin in two distinct "legs", before forming a diffuse lobe.

Figure 4.13 (a) shows the complex radio emission observed northwest of this radio galaxy. The northern arm of the L-shaped source consists of two thin, filamentary strands, while the western arm appears more diffuse. The source (or sources) located further northwest has a complex, twisted morphology. A single jet seems to extend southwest from the galaxy NFP J062557.1−542750. Approximately 1 arcmin south of the core, an enlarged region of emission is visible, with two filaments—or possibly jets—extending from it. The southern 'filament' crosses the jet originating from the core. It is difficult to determine whether this originates from a single source or not.

Diffuse emission, shown in Figure 4.13 (b), is observed north of the cluster, along the X-ray filament. Although very faint, this emission is unlikely to be a calibration artefact, as enhanced emission in this region is also present in ASKAP images of the source (Wilber *et al.*, 2023b; Brüggen *et al.*, 2021).

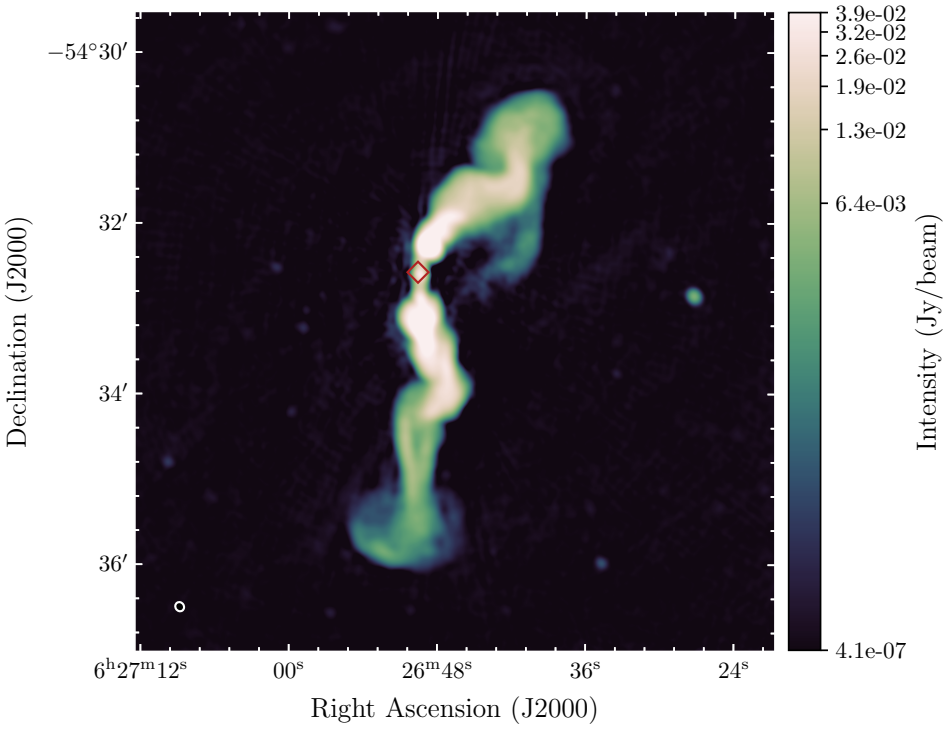

Figure 4.12: MeerKAT total intensity image of the radio galaxy PKS J0626−5432 in Abell 3395. The red diamond shows the position of the host galaxy (Gaia Collaboration, 2023). The white ellipse in the bottom left corner shows the $6\farcs6 \times 6\farcs0$ beam size.

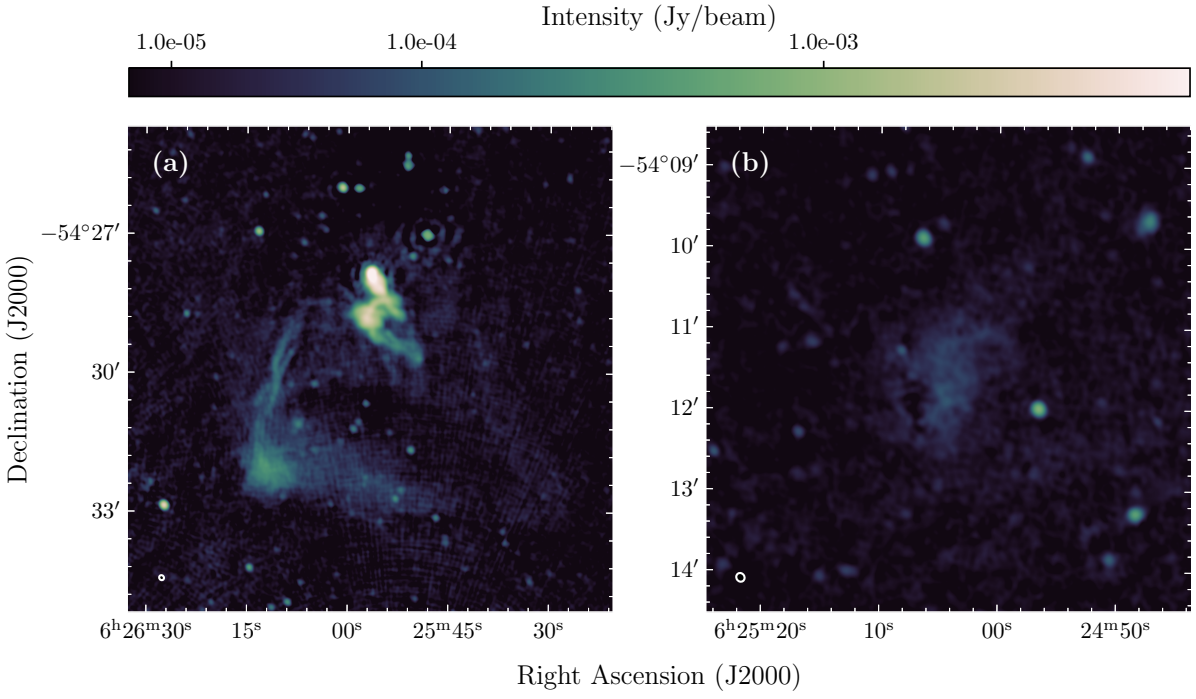

Figure 4.13: MeerKAT total intensity image of diffuse radio sources in Abell 3395. The white ellipses in the bottom left corner of each panel show the $6\farcs6 \times 6\farcs0$ beam size.

4.1.2 Radio Spectral Index Maps

This section presents the spectral index maps and spectral index error maps of individual radio sources created with BRATS using 10 sub-band images with central frequencies of 899, 984, 1070, 1155, 1241, 1327, 1412, 1498, 1583, and 1669 MHz. The error maps include only statistical uncertainties from the fit. The spectral index was only calculated for pixels with intensities above three times the off-source RMS noise level.

4.1.2.1 Abell 133

Figure 4.14 presents the spectral index map and corresponding error map of the central radio galaxy in Abell 133. This source exhibits an anomalously steep spectrum, with parts of the jets and southern lobe being too faint to yield reliable spectral index measurements. In the northern lobe, the spectral index has an average value of $\alpha = 1.77 \pm 0.02$, steepening to $\alpha = 2.03 \pm 0.02$ when the contribution from the cD galaxy is excluded. The jets, apart from the compact $\alpha = 0.89 \pm 0.02$ source, have an average spectral index of $\alpha = 2.69 \pm 0.08$. For the regions of the southern lobe where the spectral index could be determined, the average value is $\alpha = 2.54 \pm 0.11$. This ultrasteep spectrum is characteristic of a dying or remnant radio galaxy.

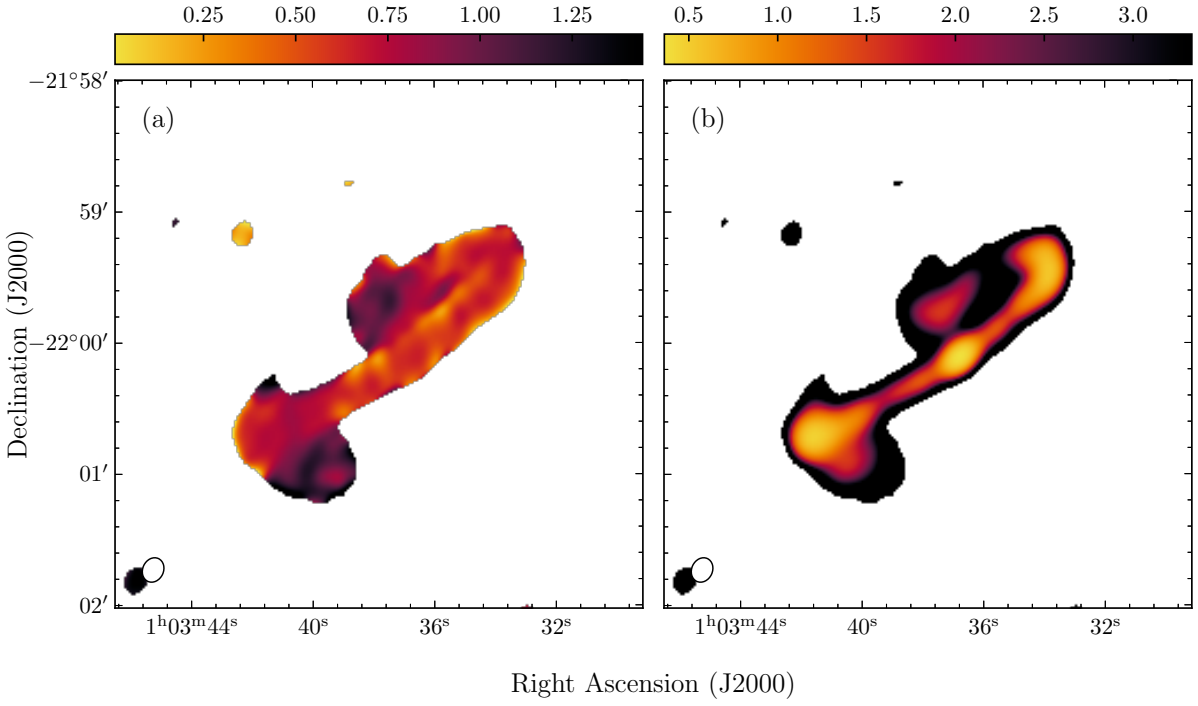

Figure 4.15: **(a)** Spectral index map and **(b)** spectral index error map of the small bent-tailed radio galaxy southeast of the core of Abell 133. The ellipses in the lower left corners show the $11\farcs5 \times 9\farcs5$ beam size of the 899 – 1669 MHz sub-band images used to create the maps.

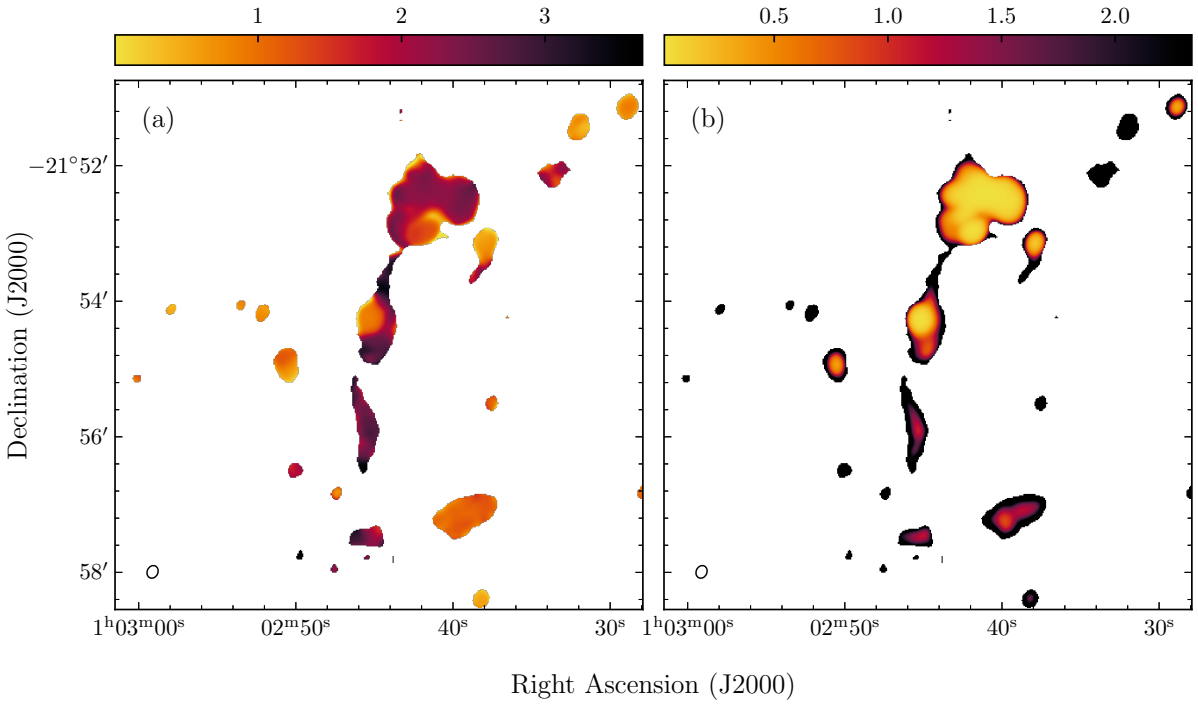

Figure 4.14: **(a)** Spectral index map and **(b)** spectral index error map of the central radio galaxy in Abell 133. The maps were created from 10 sub-band images between 899 – 1669 MHz smoothed to a common resolution of $11\farcs5 \times 9\farcs5$ using CASA `imsmooth`. The ellipses in the lower left corners show the beam size of the smoothed images.

In contrast, Figure 4.15 shows a radio galaxy with spectral index values more typical of an active system. This source, previously shown in Figure 4.3 (a), exhibits an average spectral index of $\alpha = 0.58 \pm 0.01$ along the jets, steepening to $\alpha = 0.91 \pm 0.08$ in the lobes. The remaining radio galaxies shown in Figure 4.3 were either too faint or located too far from the centre of the field for reliable spectral index calculations.

4.1.2.2 Abell 3266

The spectral index map of A3266-RG1 is presented in Figure 4.16. The spectrum is relatively flat in the core, with an average value of $\alpha = 0.82$, but steepens rapidly to $\alpha \sim 2.6$ over a distance of approximately 2.5 arcmin. Beyond this region, the emission becomes too faint for reliable spectral index measurements.

Figure 4.17 shows the spectral index map of A3266-RG2. At the southern tip, near the potential host galaxy J043045.37−612335.8, the spectrum is relatively flat with $\alpha \sim 0.9$. Along the jet, the spectral index steepens to $\alpha > 2$ toward the northern tip, except for a compact region at the position of WISEA J043118.50−611918.2, where the spectrum flattens to $\alpha \sim 1.5$. The diffuse

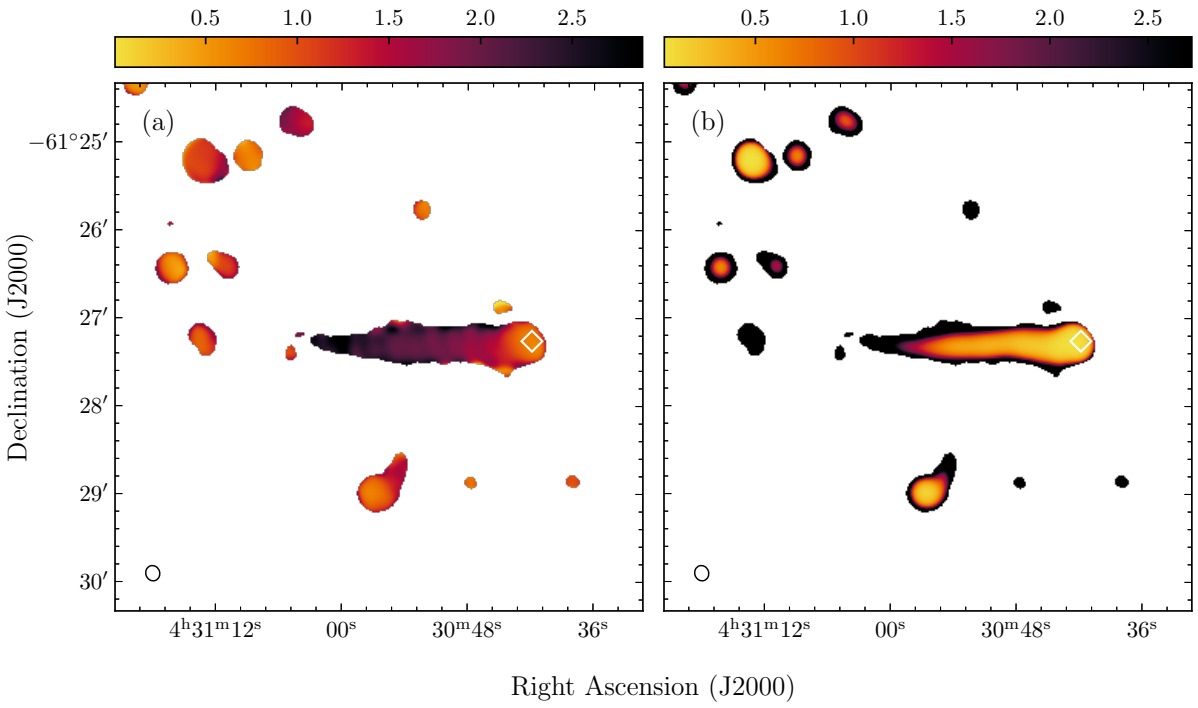

Figure 4.16: **(a)** Spectral index map and **(b)** spectral index error map of A3266-RG1. The white diamond shows the position of the host galaxy. The ellipses in the lower left corners show the $10\farcs5 \times 9\farcs5$ beam size of the 899 – 1669 MHz sub-band images used to create the maps.

source northwest of A3266-RG2, A3266-D3, was too faint to calculate its spectral index.

The spectral index map of A3266-RG3, displayed in Figure 4.18, reveals a flat spectrum in the core with an average value of $\alpha = 0.232 \pm 0.001$. The bright regions where the northern and southern jets connect to the lobes exhibit average spectral indices of $\alpha = 0.748 \pm 0.001$ and $\alpha = 0.91 \pm 0.06$, respectively. The spectral index steepens to $\alpha \sim 1.7$ in the northern lobe and $\alpha \sim 1.2$ in the southern lobe.

A3266-RG4, shown in Figure 4.19, has an average core spectral index of $\alpha = 0.63 \pm 0.01$. The southern jet displays an average spectral index of $\alpha = 1.46 \pm 0.04$, steepening to $\alpha \sim 1.7$ in the lobe. The northern jet is too faint for the spectral index to be determined.

The spectral index map of the cluster radio shock, A3266-D2, is shown in Figure 4.20. Only the bright edge of the source appears in the spectral index map. The measured spectral index fluctuates between $\alpha \sim 0.9$ and $\alpha \sim 1.3$. However, these values are subject to large uncertainties and might not be reliable.

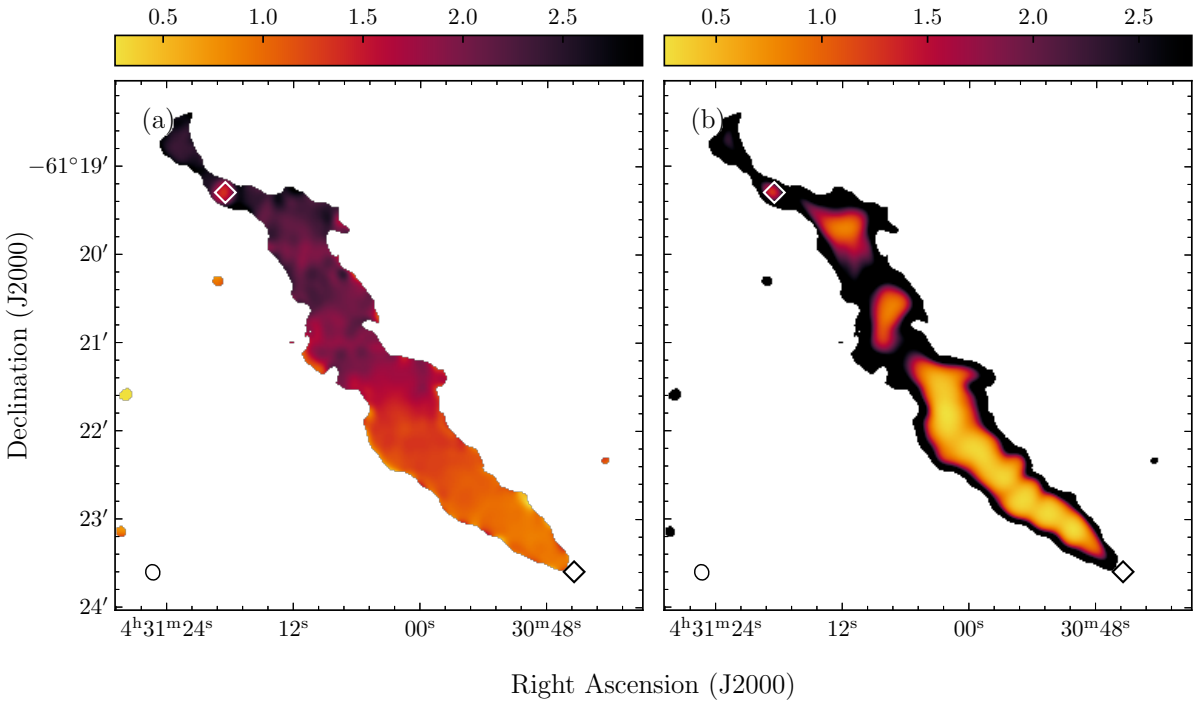

Figure 4.17: **(a)** Spectral index map and **(b)** spectral index error map of A3266-RG2. The white and black diamonds show the position of the background galaxy WISEA J043118.50−611918.2 and the possible host galaxy J043045.37−612335.8, respectively. The ellipses in the lower left corners show the $10\farcs5 \times 9\farcs5$ beam size of the 899 – 1669 MHz sub-band images used to create the maps.

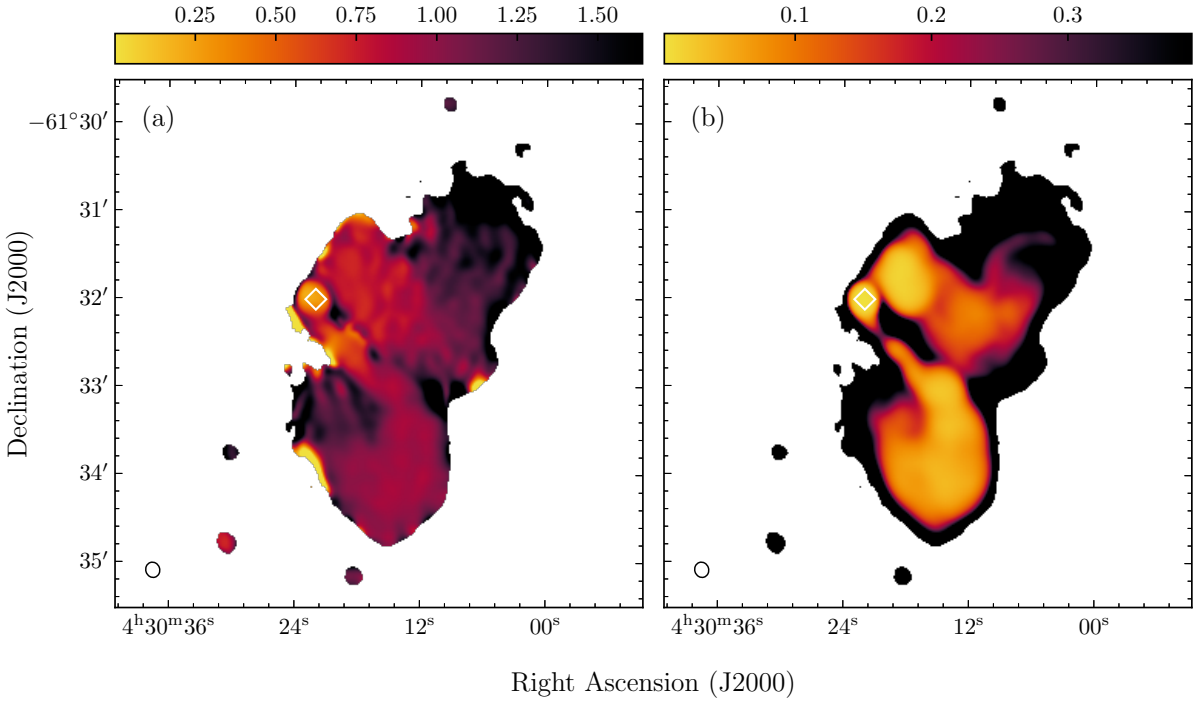

Figure 4.18: **(a)** Spectral index map and **(b)** spectral index error map of A3266-RG3. The white diamond shows the position of the host galaxy. The ellipses in the lower left corners show the $10\farcs5 \times 9\farcs5$ beam size of the 899 – 1669 MHz sub-band images used to create the maps.

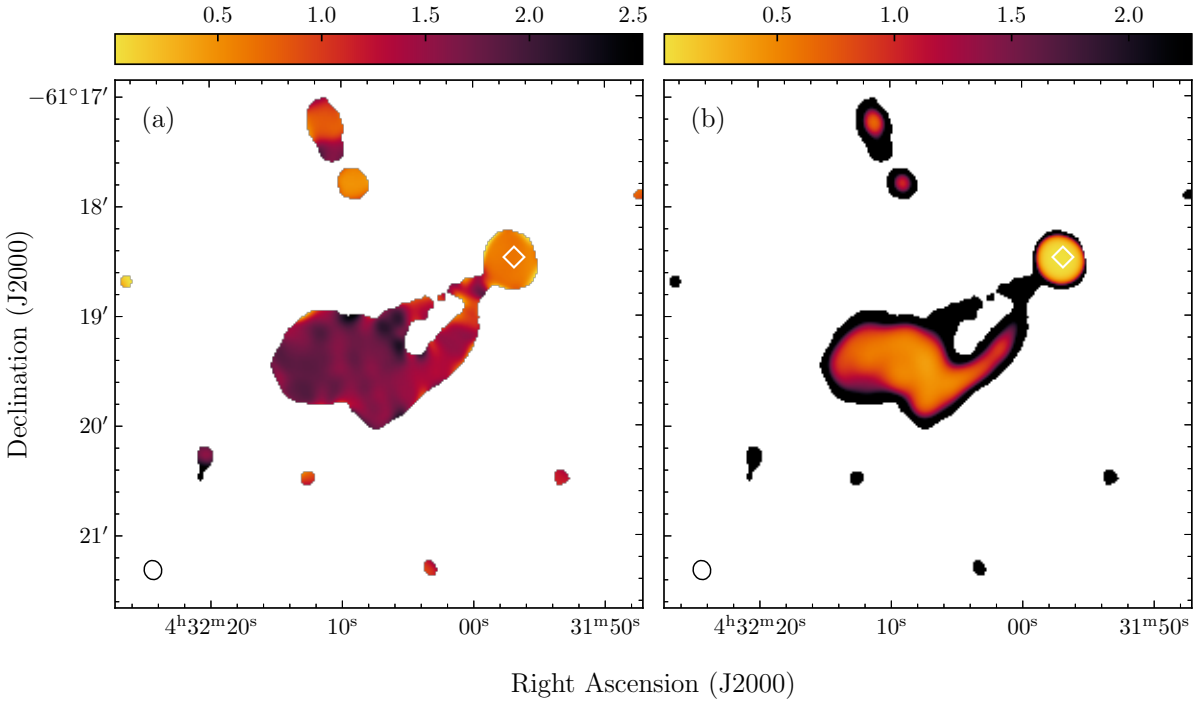

Figure 4.19: **(a)** Spectral index map and **(b)** spectral index error map of A3266-RG4. The white diamond shows the position of the host galaxy. The ellipses in the lower left corners show the $10\farcs5 \times 9\farcs5$ beam size of the 899 – 1669 MHz sub-band images used to create the maps.

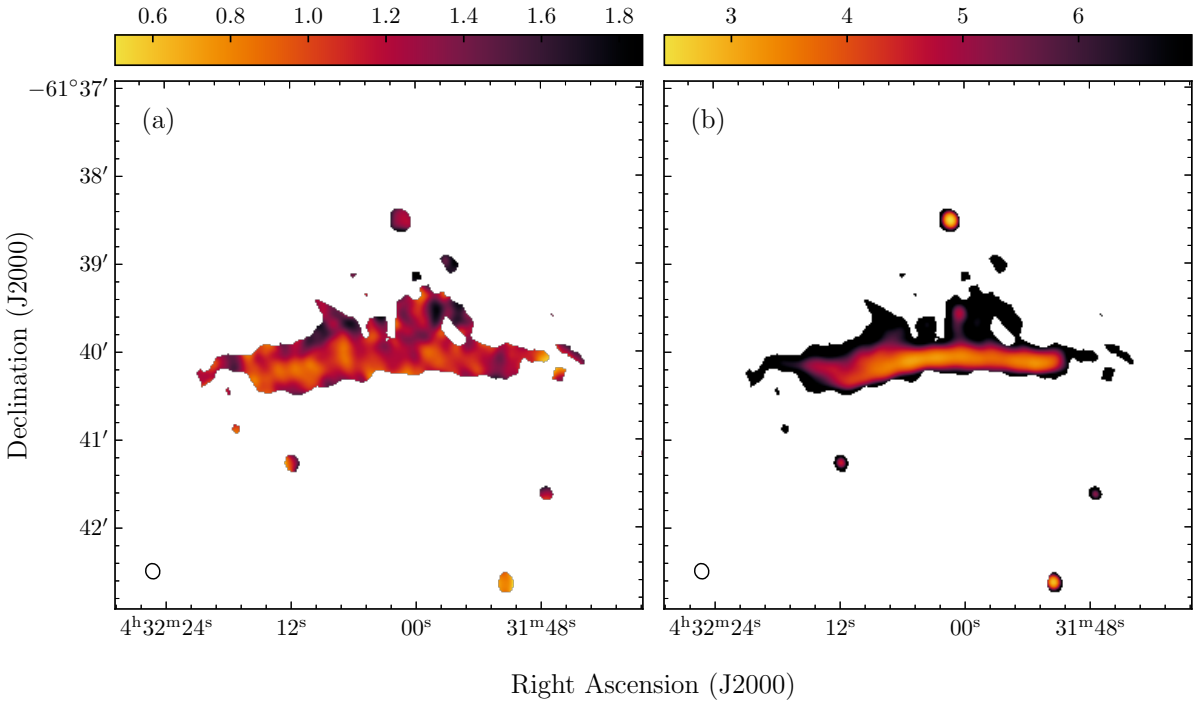

Figure 4.20: **(a)** Spectral index map and **(b)** spectral index error map of the cluster radio shock A3266-D2. The ellipses in the lower left corners show the $10\farcs5 \times 9\farcs5$ beam size of the 899 – 1669 MHz sub-band images used to create the maps.

4.1.2.3 Abell 3376

The spectral index map of A3376-RG1 and A3376-RG2 is shown in Figure 4.21. A3376-RG1 exhibits a flat spectrum in the core, with $\alpha = 0.55 \pm 0.01$. The spectral index steepens along the jets, reaching $\alpha \sim 1.7$ in the northern jet and $\alpha \sim 1.3$ in the southern jet. Similarly, A3376-RG2 has an average spectral index of $\alpha = 0.54 \pm 0.02$ at the core, which steepens to $\alpha \sim 1.4$ toward the ends of the jets.

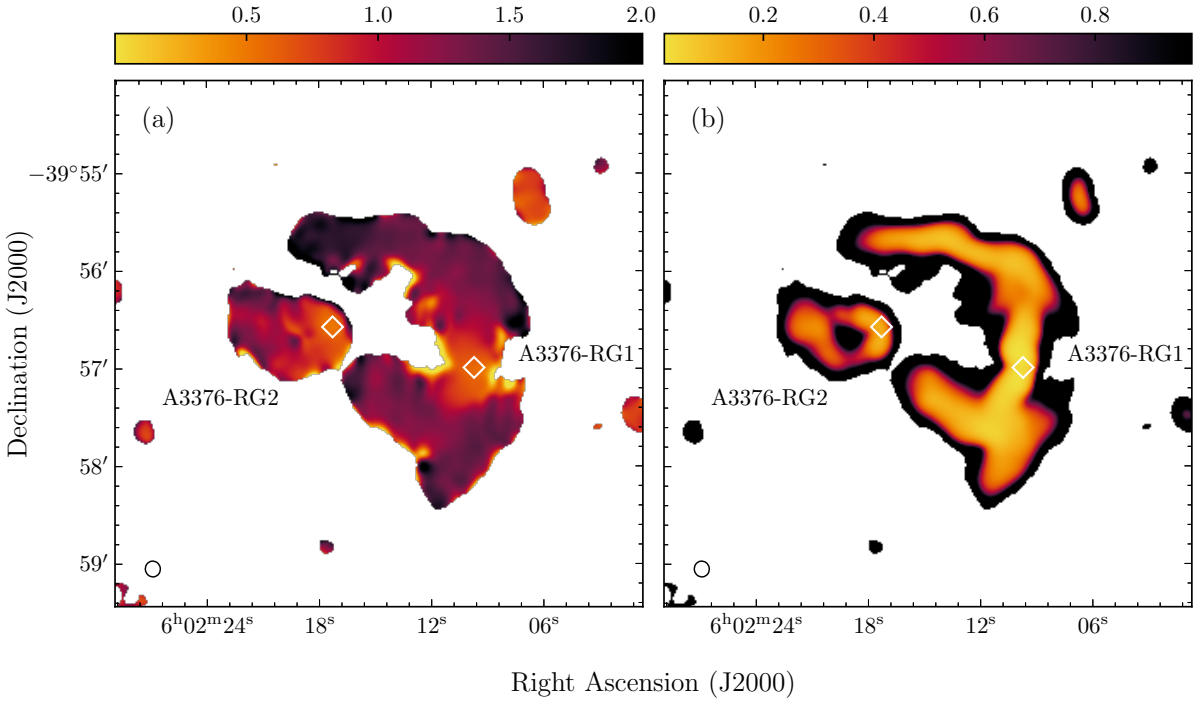

Figure 4.21: **(a)** Spectral index map and **(b)** spectral index error map of the radio galaxies A3376-RG1 and A3376-RG2. The maps were created from 10 sub-band images between 899 – 1669 MHz smoothed to a common resolution of $9\farcs7 \times 9\farcs2$ using CASA `imsmooth`. The white diamonds show the positions of the host galaxies. The ellipses in the lower left corners show the beam size of the smoothed images.

4.1.2.4 Abell 3391

Figure 4.22 presents the spectral index map of MRC 0625−536, the central radio galaxy in Abell 3391. The spectral index is flat in the unresolved core, with $\alpha \sim 0.4$, and gradually steepens to $\alpha \sim 2$ toward the ends of the lobes. A thin flat-spectrum edge is visible, which may suggest minor underlying misalignments between the sub-band images.

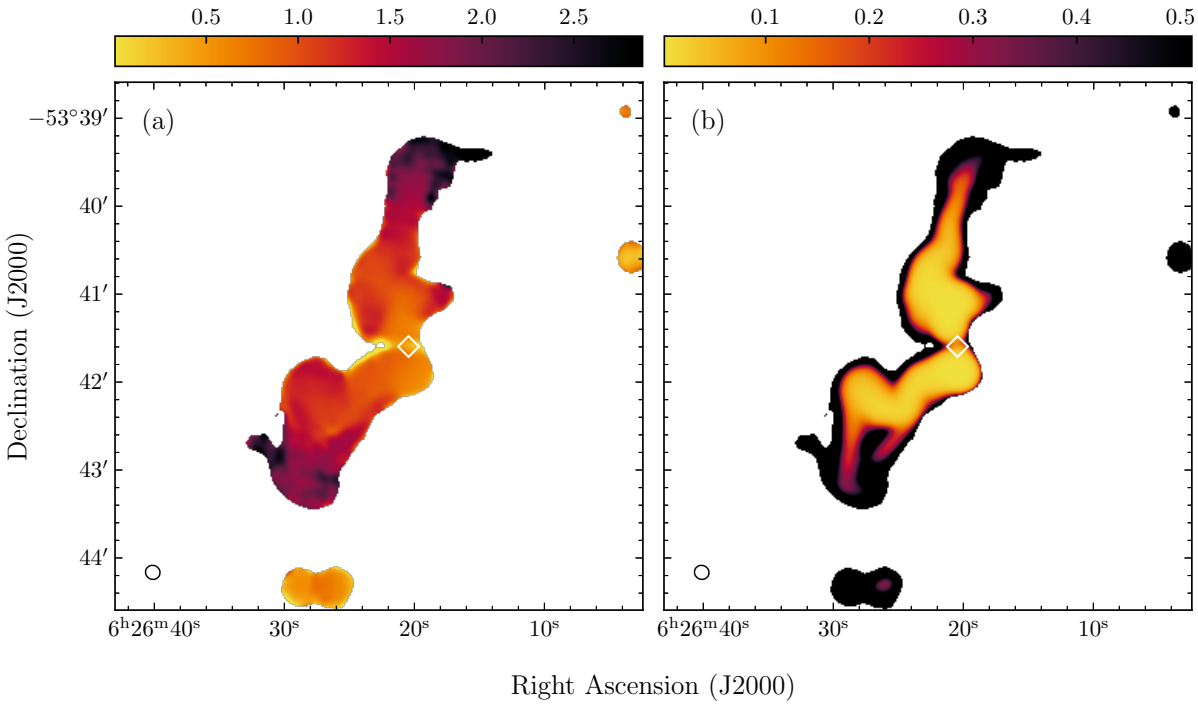

Figure 4.22: **(a)** Spectral index map and **(b)** spectral index error map of MRC 0625−536 in Abell 3391. The maps were created from 10 sub-band images between 899 − 1669 MHz smoothed to a common resolution of $10\farcs0 \times 9\farcs5$ using CASA `imsmooth`. The white diamond shows the position of the host galaxy. The ellipses in the lower left corners show the beam size of the smoothed images.

4.1.2.5 Abell 3395

Figure 4.23 presents the spectral index map of PKS J0626−5432, associated with the BCG of Abell 3395. The spectral index gradually steepens along the jets, from $\alpha \sim 0.4$ near the core to $\alpha \sim 1.5$ and $\alpha \sim 2.0$ in the northern and southern lobes, respectively. The core has an exceptionally flat spectrum with $\alpha = 0.067 \pm 0.005$. The average spectral index in the backflow is $\alpha = 1.71 \pm 0.03$. Similar to Figure 4.22, a thin flat-spectrum border is visible, likely due to minor misalignment between the sub-band images.

The spectral index map of the conglomerate of sources west of PKS J0626−5432 is shown in Figure 4.24. The arms of the L-shaped source, only partially visible in the spectral index map, exhibit steep emission with $\alpha > 2$. The core of this source is relatively flat, with $\alpha \sim 1$. The source to the northwest has a spectral index of $\alpha \sim 0.8$ at the northern tip, which gradually steepens along the source to $\alpha \sim 2.6$ at the southern tip.

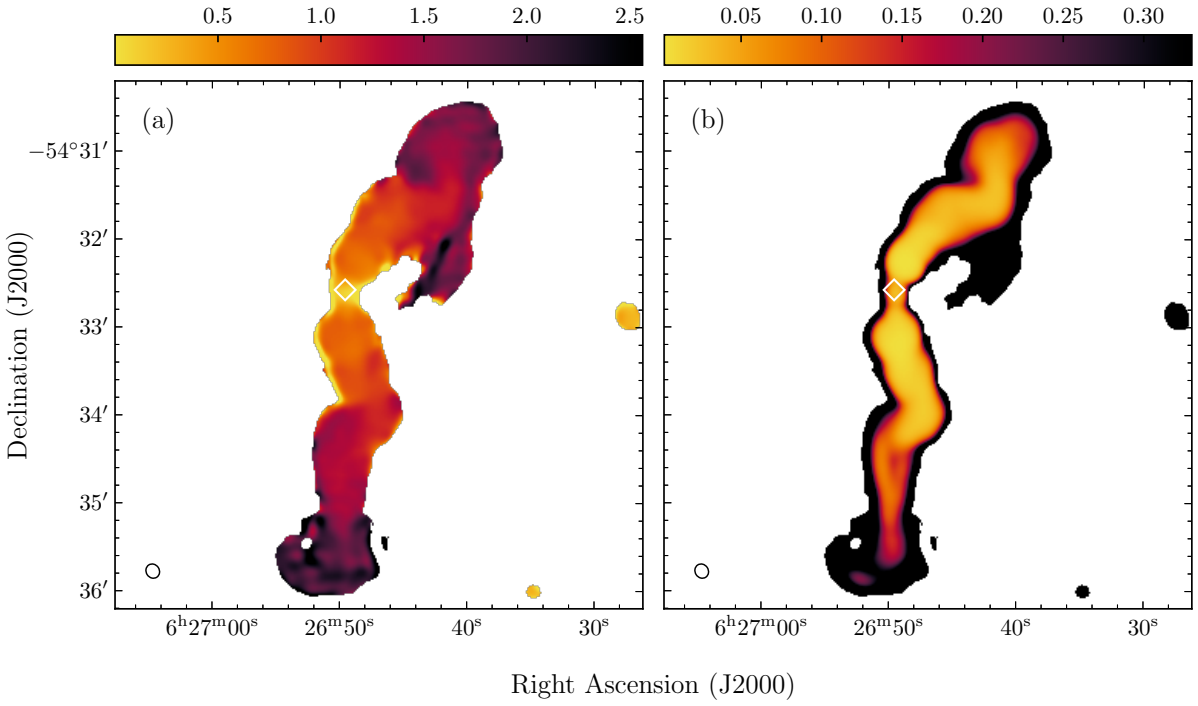

Figure 4.23: **(a)** Spectral index map and **(b)** spectral index error map of the radio galaxy PKS J0626−5432 in Abell 3395. The maps were created from 10 sub-band images between 899 – 1669 MHz smoothed to a common resolution of $10\farcs0 \times 9\farcs0$ using CASA `imsmooth`. The white diamond shows the position of the host galaxy. The ellipses in the lower left corners show the beam size of the smoothed images.

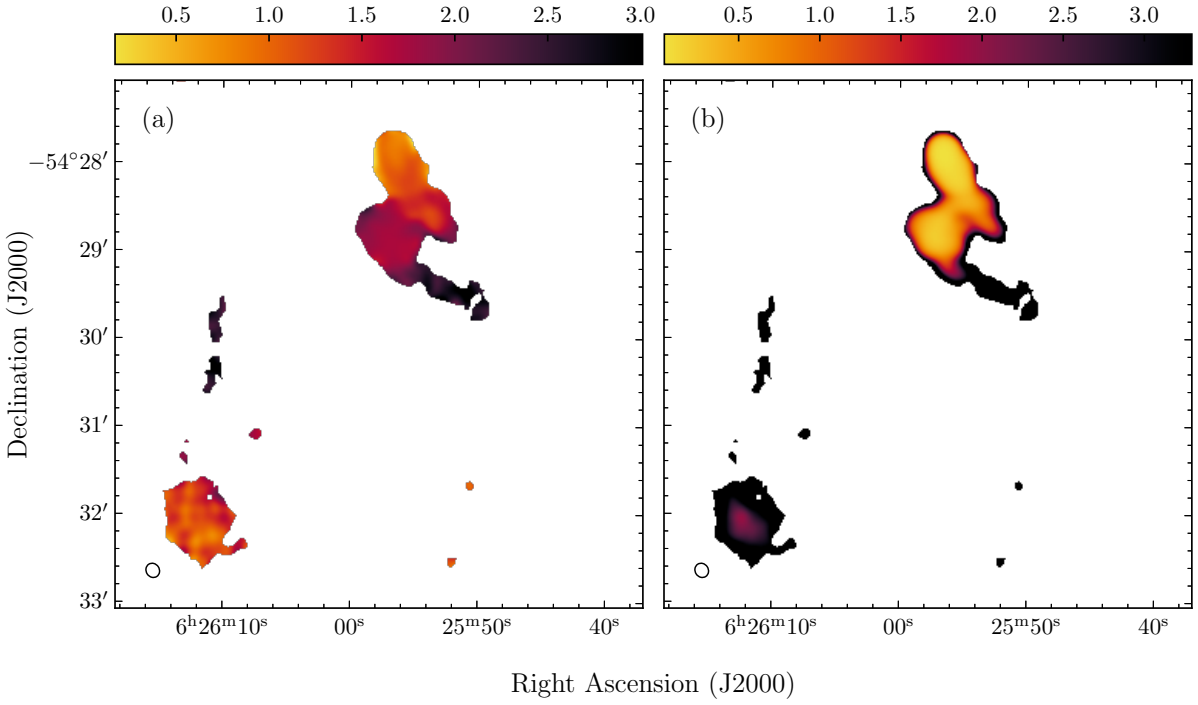

Figure 4.24: **(a)** Spectral index map and **(b)** spectral index error map of the conglomerate of radio sources west of PKS J0626−5432 in Abell 3395. The ellipses in the lower left corners show the $10\farcs0 \times 9\farcs0$ beam size of the 899 – 1669 MHz sub-band images used to create the maps.

4.2 X-ray Analysis

4.2.1 X-ray Images

This section presents the *XMM-Newton* background-subtracted, exposure-corrected count rate mosaics of the clusters, created by combining the data from the different observations and the three EPIC instruments.

4.2.1.1 Abell 133

The soft X-ray mosaic of Abell 133 is presented in Figure 4.25. The cluster is slightly elongated along the northeast–southwest axis, and exhibits a relatively relaxed morphology with a bright, centrally concentrated core. The bird-like structure identified by Fujita *et al.* (2002) is visible at the centre of the core. This structure consists of bright, compact X-ray emission, aligning with the optical position of the BCG, a tongue-like extension stretching northwest, and faint emission extending to the northeast and southwest, resembling the wings of a bird.

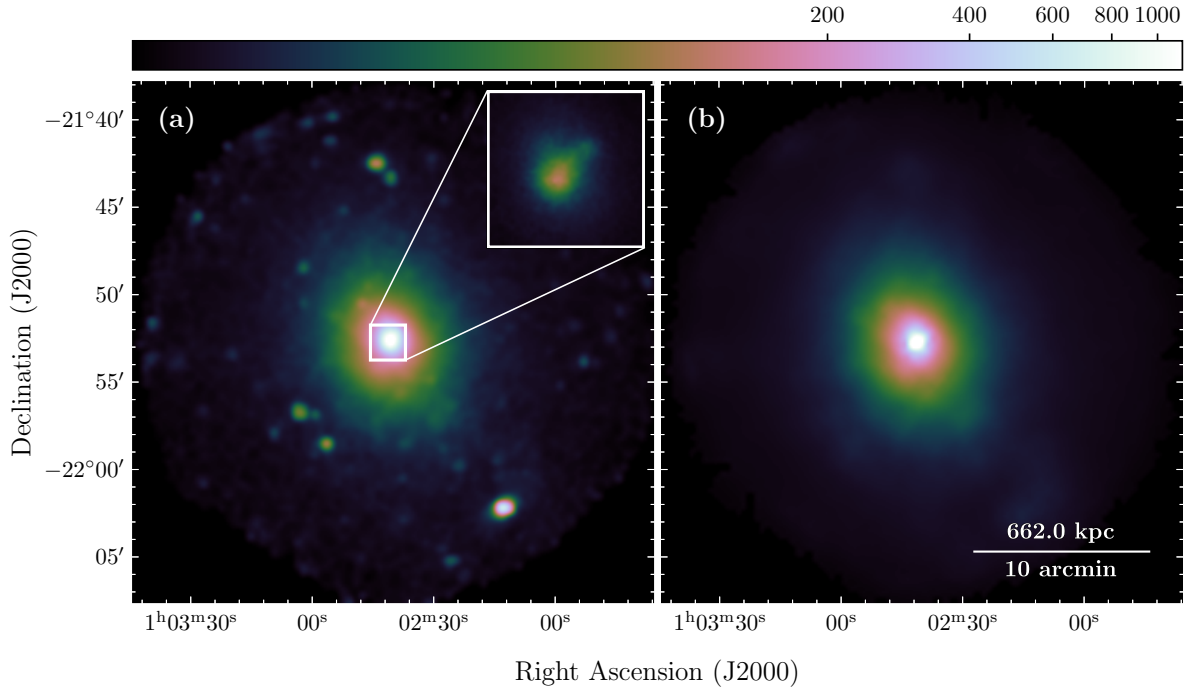

Figure 4.25: **(a)** Background-subtracted, exposure-corrected *XMM-Newton* count rate image of Abell 133 in the 0.4 – 1.3 keV band. **(b)** Same as panel **(a)**, but with point sources cosmetically masked and the image smoothed using the accumulative smoothing method of Sanders (2006), achieving an SNR of 15. The inset in panel **(a)** highlights the bird-like structure in the cluster core.

4.2.1.2 Abell 3266

The *XMM-Newton* image of Abell 3266, presented in Figure 4.26, shows the complex dynamical state of this cluster. The bright X-ray core, offset to the southeast of the cluster centroid, has a sharp edge along its southern and western boundaries, and a tail extending northeast. To the west of the cluster centre, filamentary X-ray "fingers" extend more than 400 kpc northwest. Faint emission is visible northwest of these filaments. Northeast and southwest of the filaments, two 300-kiloparsec-scale cavities are visible.

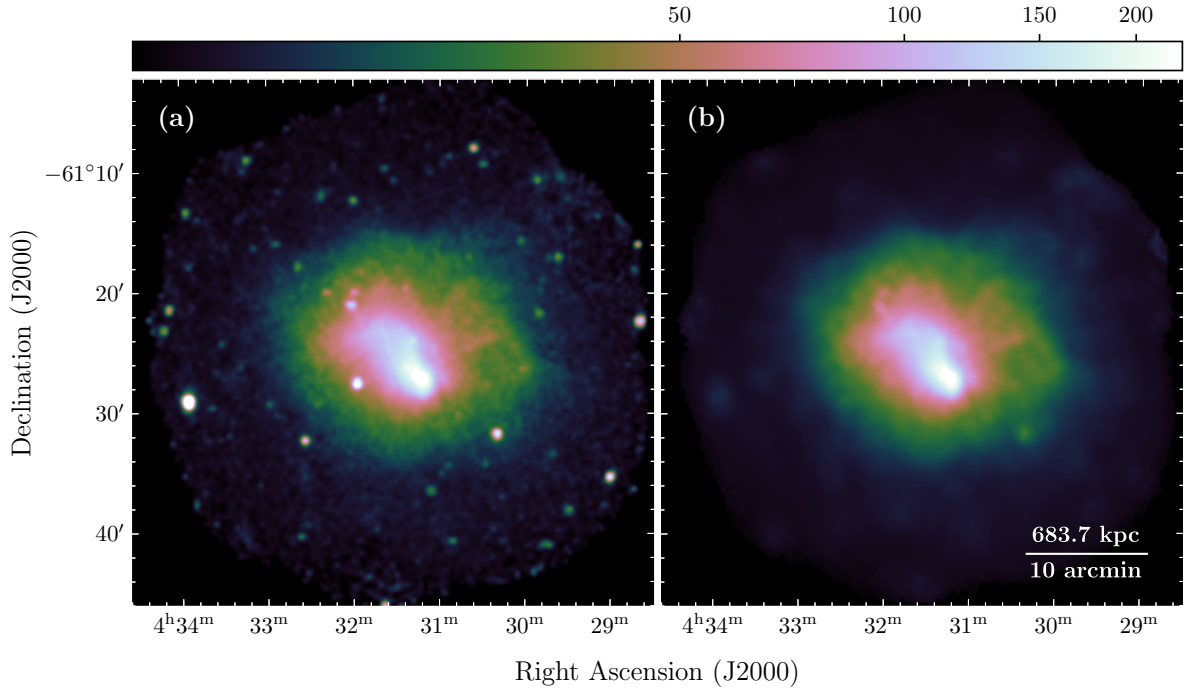

Figure 4.26: **(a)** Background-subtracted, exposure-corrected *XMM-Newton* count rate image of Abell 3266 in the 0.4 – 1.3 keV band. **(b)** Same as panel **(a)**, but with point sources cosmetically masked and the image smoothed using the accumulative smoothing method of Sanders (2006), achieving an SNR of 15.

4.2.1.3 Abell 3376

Figure 4.27 shows the cometary X-ray structure of Abell 3376, indicative of a northeast–southwest merger. A sharp edge appears at the head of this structure, to the northeast, where the peak X-ray emission is concentrated. This edge, known to be a cold front (Urdampilleta *et al.*, 2018; Chibueze *et al.*, 2021), is likely the result of cool, dense gas from the core of a merging subcluster moving northeast.

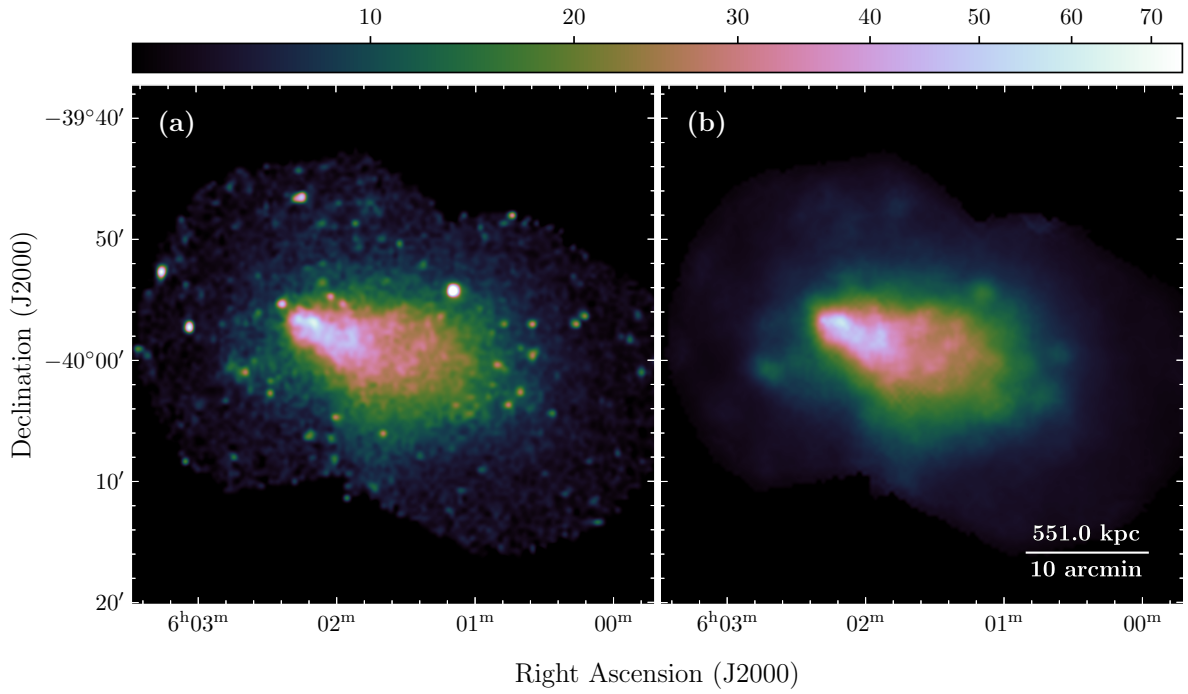

Figure 4.27: **(a)** Background-subtracted, exposure-corrected *XMM-Newton* count rate image of Abell 3376 in the 0.4 – 1.3 keV band. **(b)** Same as panel **(a)**, but with point sources cosmetically masked and the image smoothed using the accumulative smoothing method of Sanders (2006), achieving an SNR of 15.

4.2.1.4 Abell 3391

Figure 4.28 presents the *XMM-Newton* image of Abell 3391. This cluster exhibits a relatively relaxed morphology, despite its elongation along the northeast–southwest axis, with a bright central core. A surface brightness edge is visible approximately 350 kpc southwest of the cluster core, potentially indicative of a cold front or a shock. Although not visible in this image, the large-scale filamentary structure connecting Abell 3391 with Abell 3395 is known to intersect the cluster on its southwestern side.

4.2.1.5 Abell 3395

Figure 4.29 shows the *XMM-Newton* image of the double-peaked Abell 3395. Both of the main subclusters, A3395-N and A3395-S, are elongated along the northwest–southeast axis. In A3395-N, the peak X-ray emission is concentrated near its centre. In contrast, A3395-S exhibits a bright core offset to the southeast, with an extension stretching northwest. Although this extension is fainter than the core, it exhibits sharp boundaries, suggesting a well-defined substructure. Filamentary emission to the northwest connects A3395-N with A3395-S.

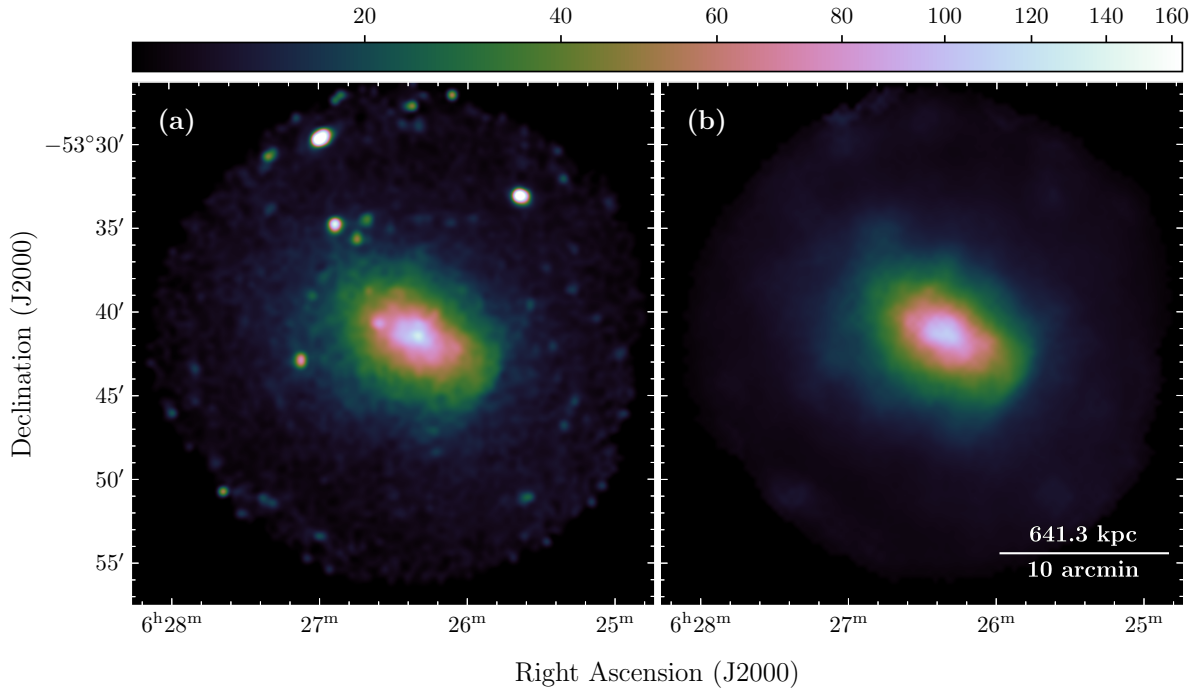

Figure 4.28: **(a)** Background-subtracted, exposure-corrected *XMM-Newton* count rate image of Abell 3391 in the 0.4 – 1.3 keV band. **(b)** Same as panel **(a)**, but with point sources cosmetically masked and the image smoothed using the accumulative smoothing method of Sanders (2006), achieving an SNR of 15.

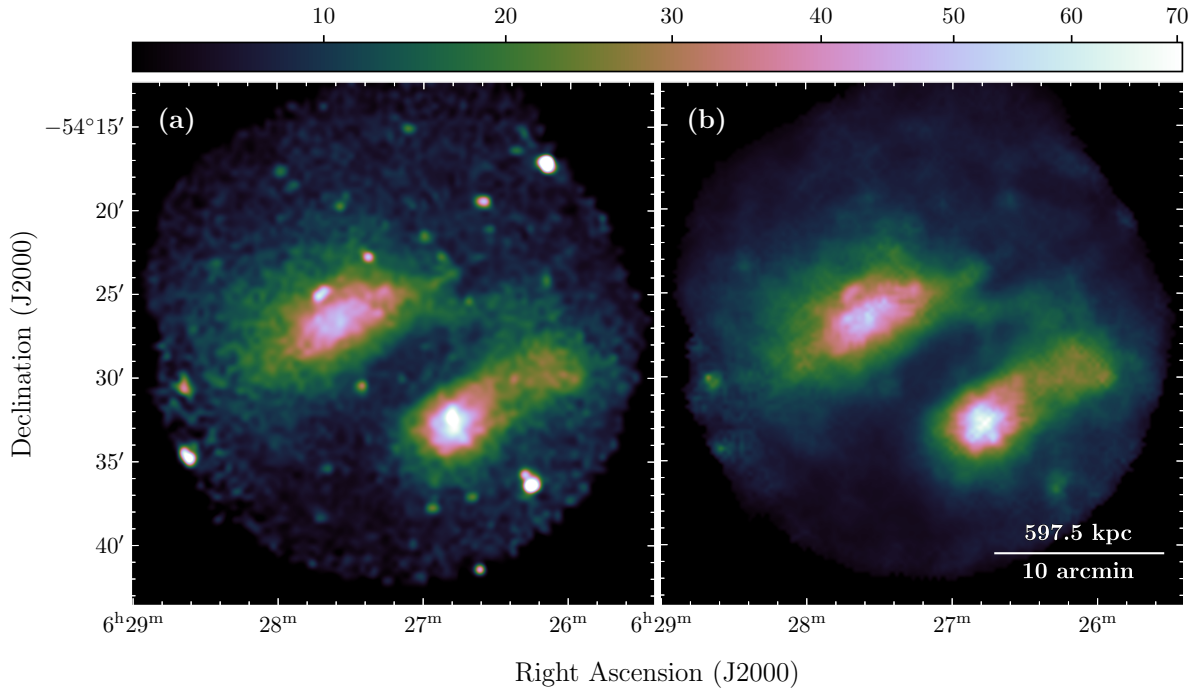

Figure 4.29: **(a)** Background-subtracted, exposure-corrected *XMM-Newton* count rate image of Abell 3395 in the 0.4 – 1.3 keV band. **(b)** Same as panel **(a)**, but with point sources cosmetically masked and the image smoothed using the accumulative smoothing method of Sanders (2006), achieving an SNR of 15.

4.2.2 X-ray Spectral Analysis

This section presents the results of the X-ray spectral analysis. For each cluster, 15 regions were defined, following the contours of the X-ray image after point sources were masked, as explained in Section 3.2.6.1. From each of these regions, spectra and model QPB spectra were extracted for all observations where it was possible to do so. All the spectra of all the regions of a cluster were fitted simultaneously in XSPEC. To account for the differences in the sizes of the regions and small calibration mismatches between instruments or observations, all the model components were multiplied by `constant`×`constant`, where the first constant is the area of the region in units of arcmin^2 and the second constant ($\sim$1) accounts for small calibration discrepancies. This way, many of the normalisations of the model components could be tied for the different spectra, reducing the amount of free parameters. The region selections for the different clusters are shown in Figures 4.30 to 4.34. These figures also show example spectra of the different regions for one instrument of one observation. All of the spectra are shown in Appendix A.

4.2.2.1 Cluster Emission

For each region, the parameters of the (absorbed) cluster emission model, `TBabs`×`apec`, were linked for all observations and instruments during the spectral fitting. The redshifts and hydrogen column densities were fixed to the values in Table 3.4. During the initial fitting, the abundances of the outer regions were linked to those of the inner regions, and allowed to vary once a good fit was achieved. The best-fit parameters for the different clusters are shown in Tables 4.2 to 4.6. Errors are reported at a 90% confidence level.

4.2.2.2 Instrumental Lines

While many of the instrumental lines are included in the model QPB spectrum, the Si Kα line at $\sim$1.75 keV in the EPIC-MOS spectra and the Al Kα line at $\sim$1.49 keV in both the EPIC-MOS and EPIC-pn spectra were explicitly fitted in XSPEC with `gaussian` components. The EPIC-pn spectra have several strong instrumental lines in the 7.0 – 9.0 keV energy range. Instead of fitting each of these lines, this range was excluded from the EPIC-pn spectra. During the fit, the line energies were initially fixed to their expected values and the line width to zero[1] and were only allowed to vary after a reasonable fit was obtained. The widths and energies were linked for all

[1] XSPEC treats `gaussian` components with zero width as delta functions.

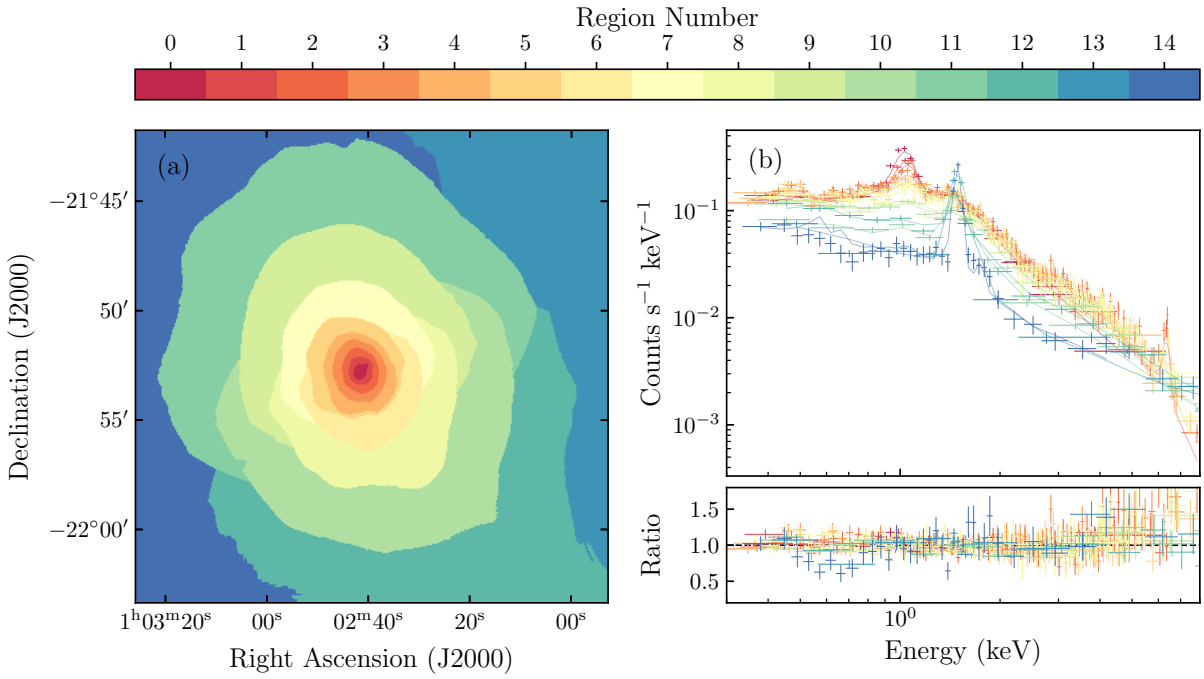

Figure 4.30: **(a)** Configuration of the regions used for spectral analysis of Abell 133. **(b)** EPIC-pn spectra for ObsID 0144310101, each coloured the same as the region it was extracted from. The spectra of all the observations of Abell 133 for all instruments are shown in Figure A.1.

Table 4.2: Best-fit cluster emission parameters for the regions of Abell 133 shown in Figure 4.30.

Region	***kT*** **(keV)**	**Normalisation** $(\mathbf{10^{-5}cm^{-5}\,arcmin^{-2}})$	***Z*** $(Z_\odot)$
0	$2.37^{+0.03}_{-0.03}$	432^{+4}_{-4}	$1.66^{+0.03}_{-0.04}$
1	$2.69^{+0.02}_{-0.02}$	215^{+1}_{-1}	$1.29^{+0.02}_{-0.02}$
2	$3.26^{+0.04}_{-0.04}$	115^{+1}_{-1}	$1.12^{+0.02}_{-0.02}$
3	$3.66^{+0.05}_{-0.05}$	$69.9^{+0.3}_{-0.3}$	$0.83^{+0.02}_{-0.02}$
4	$3.88^{+0.05}_{-0.05}$	$49.5^{+0.2}_{-0.2}$	$0.61^{+0.02}_{-0.02}$
5	$3.83^{+0.06}_{-0.05}$	$31.60^{+0.15}_{-0.15}$	$0.59^{+0.02}_{-0.02}$
6	$4.12^{+0.07}_{-0.07}$	$20.70^{+0.11}_{-0.11}$	$0.56^{+0.03}_{-0.03}$
7	$3.96^{+0.06}_{-0.06}$	$13.00^{+0.07}_{-0.07}$	$0.51^{+0.02}_{-0.02}$
8	$3.97^{+0.08}_{-0.08}$	$8.08^{+0.05}_{-0.05}$	$0.40^{+0.03}_{-0.03}$
9	$3.74^{+0.08}_{-0.08}$	$4.80^{+0.03}_{-0.03}$	$0.50^{+0.03}_{-0.03}$
10	$3.64^{+0.12}_{-0.11}$	$2.76^{+0.02}_{-0.02}$	$0.43^{+0.04}_{-0.04}$
11	$3.42^{+0.14}_{-0.13}$	$1.21^{+0.02}_{-0.02}$	$0.77^{+0.05}_{-0.05}$
12	$3.2^{+0.2}_{-0.2}$	$0.66^{+0.01}_{-0.01}$	$0.68^{+0.08}_{-0.08}$
13	$2.4^{+0.7}_{-0.2}$	$0.05^{+0.01}_{-0.01}$	$0.3^{+0.6}_{-0.6}$
14	$3.5^{+0.3}_{-0.2}$	$0.21^{+0.01}_{-0.01}$	$0.3^{+0.2}_{-0.2}$

the regions of the same instrument and observation, reducing the amount of free parameters.

4.2.2.3 Residual SPF Background

The residual SPF emission still remaining after filtering out periods with high amounts of flaring was modelled with a `bknpower` component that has not been folded through the instrumental response. During spectral fitting, the break energy was initially fixed at energy ∼3.0 keV. The break energy and power-law indices were linked together for all the spectra belonging to a certain instrument and observation, and the normalisation scaled according to the distribution of the SPF across the CCDs.

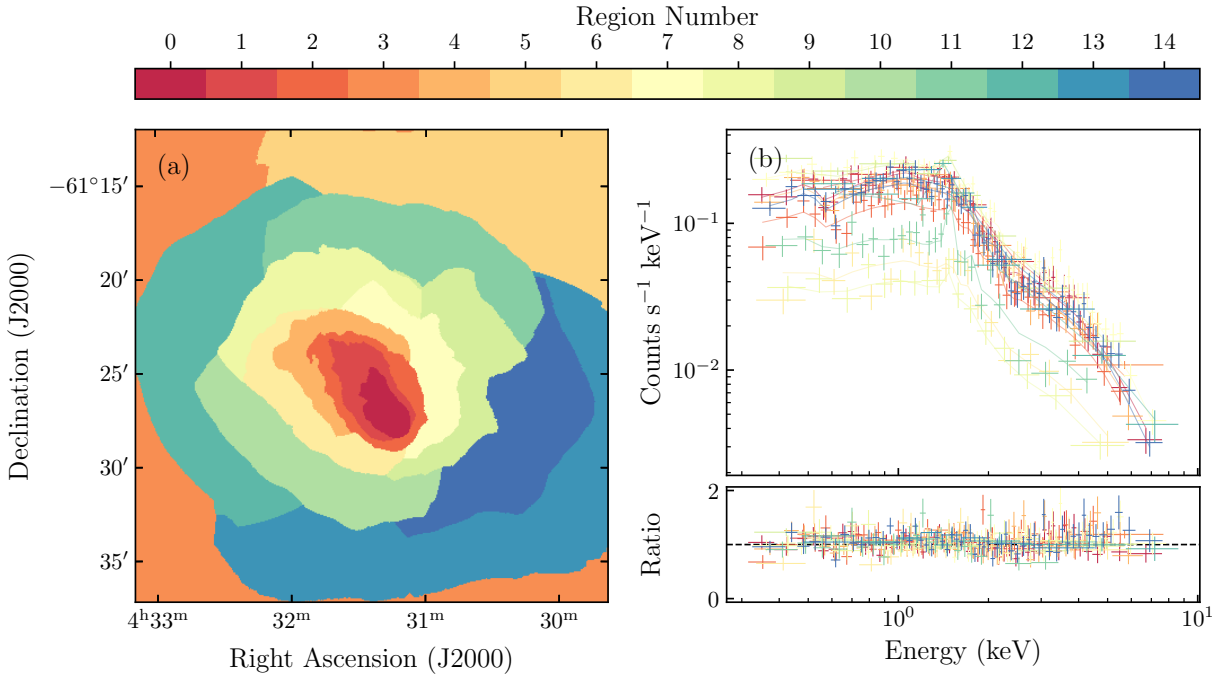

Figure 4.31: (a) Configuration of the regions used for spectral analysis of Abell 3266. **(b)** EPIC-MOS 1 spectra for ObsID 0105262101, each coloured the same as the region it was extracted from. The spectra of all the observations of Abell 3266 for all instruments are shown in Figure A.2.

4.2.2.4 Solar Wind Charge Exchange

To account for potential SWCX, `gaussian` components were with zero width and energies fixed to the values in Table 3.5. The normalisations were linked for all spectra of the same observation, with the appropriate scaling applied with `constant` × `constant`.

Table 4.3: Best-fit cluster emission parameters for the regions of Abell 3266 shown in Figure 4.31.

Region	kT (keV)	Normalisation (10^{-5}cm^{-5} arcmin^{-2})	Z ($Z_\odot$)
0	$7.1^{+0.2}_{-0.2}$	$82.1^{+0.4}_{-0.4}$	$0.46^{+0.03}_{-0.03}$
1	$6.9^{+0.2}_{-0.2}$	$53.8^{+0.3}_{-0.3}$	$0.53^{+0.03}_{-0.03}$
2	$7.2^{+0.2}_{-0.2}$	$40.5^{+0.2}_{-0.2}$	$0.39^{+0.03}_{-0.03}$
3	$5.3^{+0.3}_{-0.3}$	$0.88^{+0.01}_{-0.01}$	$0.46^{+0.08}_{-0.08}$
4	$6.5^{+0.1}_{-0.1}$	$32.5^{+0.2}_{-0.2}$	$0.37^{+0.03}_{-0.03}$
5	$6.9^{+0.3}_{-0.3}$	$2.43^{+0.02}_{-0.02}$	$0.40^{+0.06}_{-0.06}$
6	$6.63^{+0.02}_{-0.02}$	$22.60^{+0.12}_{-0.12}$	$0.33^{+0.04}_{-0.04}$
7	$8.1^{+0.2}_{-0.2}$	$24.00^{+0.12}_{-0.12}$	$0.38^{+0.04}_{-0.04}$
8	$5.7^{+0.1}_{-0.1}$	$16.80^{+0.09}_{-0.09}$	$0.36^{+0.03}_{-0.03}$
9	$7.6^{+0.2}_{-0.2}$	$16.10^{+0.09}_{-0.09}$	$0.36^{+0.04}_{-0.04}$
10	$7.2^{+0.2}_{-0.2}$	$11.20^{+0.07}_{-0.07}$	$0.24^{+0.04}_{-0.04}$
11	$6.7^{+0.2}_{-0.2}$	$9.15^{+0.06}_{-0.06}$	$0.34^{+0.04}_{-0.04}$
12	$5.5^{+0.2}_{-0.2}$	$5.31^{+0.04}_{-0.04}$	$0.41^{+0.04}_{-0.04}$
13	$7.4^{+0.3}_{-0.3}$	$3.32^{+0.03}_{-0.03}$	$0.40^{+0.07}_{-0.07}$
14	$6.7^{+0.1}_{-0.1}$	$8.43^{+0.03}_{-0.03}$	$0.41^{+0.03}_{-0.03}$

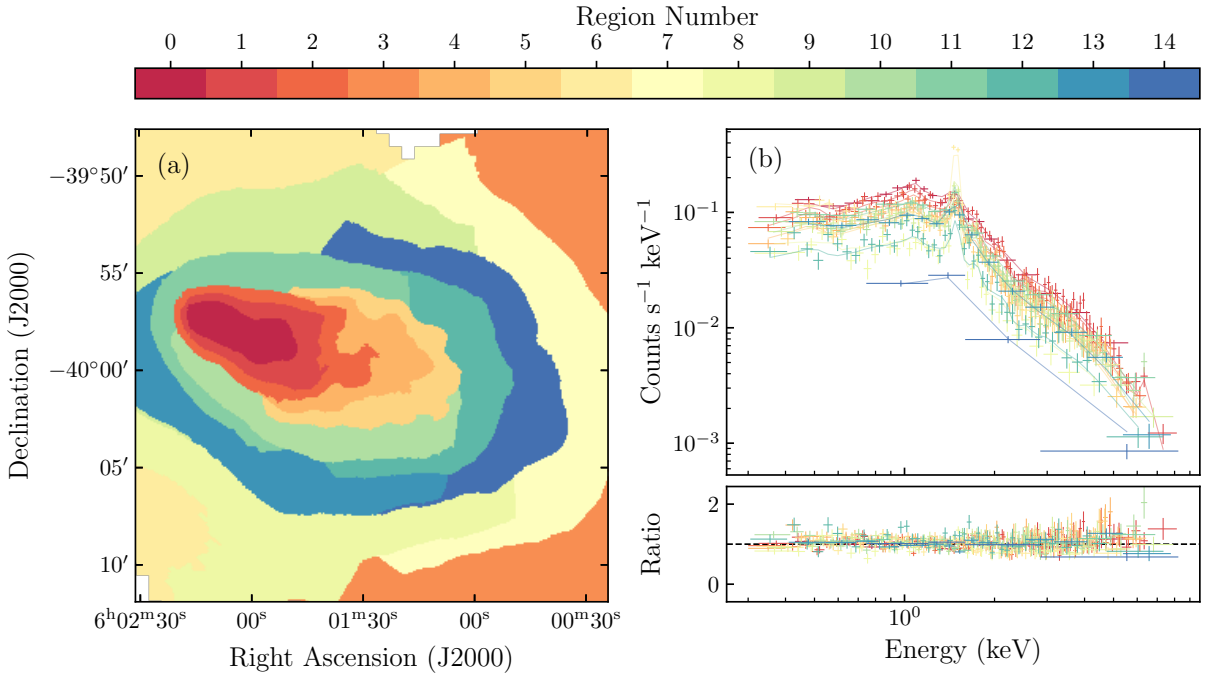

Figure 4.32: **(a)** Configuration of the regions used for spectral analysis of Abell 3376. **(b)** EPIC-MOS 1 spectra for ObsID 0151900101, each coloured the same as the region it was extracted from. The spectra of all the observations of Abell 3376 for all instruments are shown in Figure A.3.

Table 4.4: Best-fit cluster emission parameters for the regions of Abell 3376 shown in Figure 4.32.

Region	kT (keV)	Normalisation (10^{-5}cm^{-5} arcmin^{-2})	Z ($Z_\odot$)
0	$3.58^{+0.11}_{-0.11}$	$18.2^{+0.2}_{-0.2}$	$0.48^{+0.04}_{-0.05}$
1	$3.68^{+0.12}_{-0.10}$	$13.95^{+0.14}_{-0.14}$	$0.46^{+0.04}_{-0.04}$
2	$3.51^{+0.12}_{-0.11}$	$12.21^{+0.14}_{-0.13}$	$0.29^{+0.04}_{-0.04}$
3	$4.4^{+0.5}_{-0.5}$	$0.70^{+0.02}_{-0.02}$	$0.62^{+0.14}_{-0.12}$
4	$3.47^{+0.09}_{-0.08}$	$10.76^{+0.09}_{-0.09}$	$0.38^{+0.03}_{-0.03}$
5	$3.37^{+0.09}_{-0.08}$	$9.05^{+0.08}_{-0.08}$	$0.39^{+0.03}_{-0.03}$
6	$3.8^{+0.5}_{-0.2}$	$1.13^{+0.03}_{-0.02}$	$0.28^{+0.09}_{-0.08}$
7	$3.9^{+0.2}_{-0.2}$	$2.02^{+0.03}_{-0.03}$	$0.20^{+0.06}_{-0.06}$
8	$3.1^{+0.2}_{-0.2}$	$2.38^{+0.05}_{-0.05}$	$0.10^{+0.06}_{-0.06}$
9	$4.3^{+0.4}_{-0.2}$	$2.72^{+0.05}_{-0.04}$	$0.21^{+0.08}_{-0.07}$
10	$3.49^{+0.12}_{-0.10}$	$6.97^{+0.07}_{-0.07}$	$0.39^{+0.04}_{-0.04}$
11	$3.86^{+0.19}_{-0.14}$	$6.13^{+0.08}_{-0.08}$	$0.33^{+0.06}_{-0.05}$
12	$3.73^{+0.12}_{-0.11}$	$6.10^{+0.06}_{-0.06}$	$0.29^{+0.04}_{-0.04}$
13	$3.34^{+0.17}_{-0.12}$	$4.05^{+0.05}_{-0.05}$	$0.32^{+0.05}_{-0.04}$
14	$4.05^{+0.16}_{-0.14}$	$4.23^{+0.04}_{-0.05}$	$0.12^{+0.05}_{-0.05}$

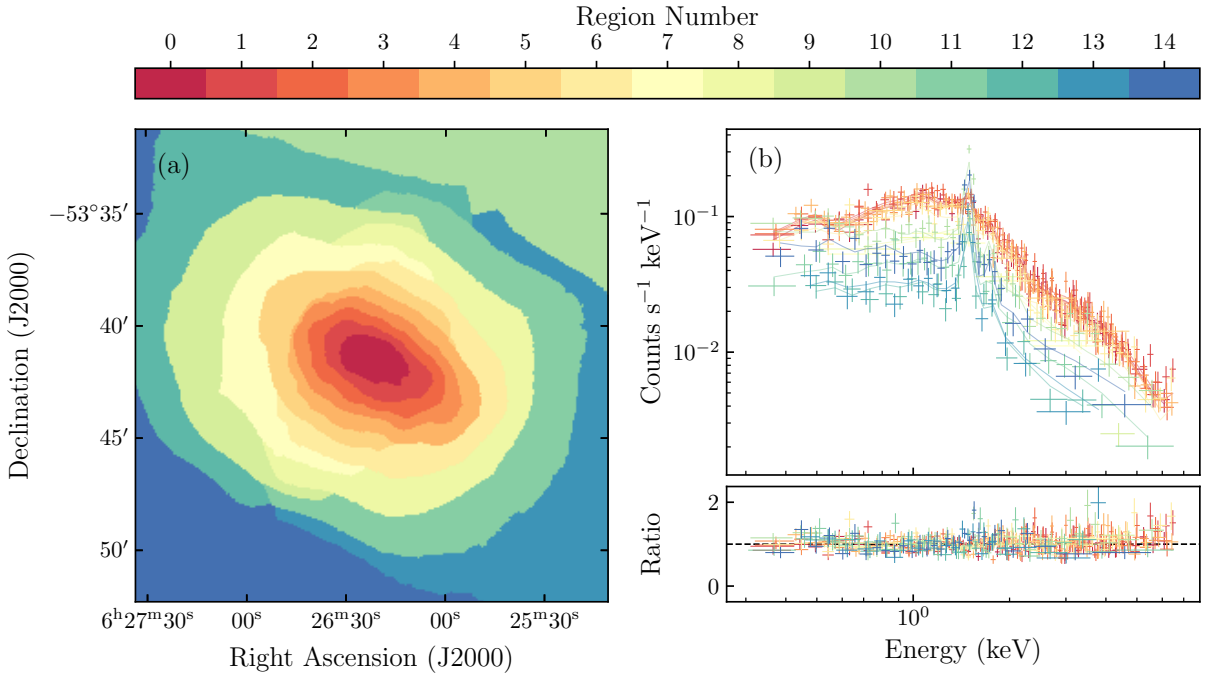

Figure 4.33: **(a)** Configuration of the regions used for spectral analysis of Abell 3391. **(b)** EPIC-MOS 1 spectra for ObsID 0720252301, each coloured the same as the region it was extracted from. The spectra of all the observations of Abell 3391 for all instruments are shown in Figure A.4.

Table 4.5: Best-fit cluster emission parameters for the regions of Abell 3391 shown in Figure 4.33.

Region	kT (keV)	Normalisation (10^{-5}cm^{-5} arcmin^{-2})	Z ($Z_\odot$)
0	$5.6^{+0.2}_{-0.2}$	$40.0^{+0.4}_{-0.4}$	$0.56^{+0.06}_{-0.06}$
1	$5.5^{+0.2}_{-0.2}$	$29.4^{+0.3}_{-0.3}$	$0.49^{+0.06}_{-0.06}$
2	$5.1^{+0.2}_{-0.2}$	$22.9^{+0.2}_{-0.2}$	$0.37^{+0.05}_{-0.05}$
3	$5.2^{+0.2}_{-0.2}$	$18.4^{+0.2}_{-0.2}$	$0.44^{+0.06}_{-0.06}$
4	$5.2^{+0.2}_{-0.2}$	$14.2^{+0.1}_{-0.1}$	$0.53^{+0.06}_{-0.06}$
5	$5.2^{+0.2}_{-0.2}$	$11.4^{+0.1}_{-0.1}$	$0.50^{+0.06}_{-0.06}$
6	$5.1^{+0.2}_{-0.2}$	$8.75^{+0.09}_{-0.09}$	$0.48^{+0.06}_{-0.06}$
7	$4.6^{+0.2}_{-0.2}$	$7.26^{+0.09}_{-0.09}$	$0.38^{+0.06}_{-0.06}$
8	$5.2^{+0.3}_{-0.3}$	$5.11^{+0.06}_{-0.06}$	$0.30^{+0.07}_{-0.07}$
9	$4.1^{+0.2}_{-0.2}$	$4.55^{+0.07}_{-0.07}$	$0.34^{+0.07}_{-0.07}$
10	$4.9^{+0.6}_{-0.5}$	$1.38^{+0.03}_{-0.03}$	$0.56^{+0.15}_{-0.15}$
11	$5.0^{+0.3}_{-0.3}$	$2.90^{+0.05}_{-0.05}$	$0.58^{+0.09}_{-0.09}$
12	$4.1^{+0.4}_{-0.3}$	$2.32^{+0.05}_{-0.05}$	$0.36^{+0.09}_{-0.09}$
13	$4.5^{+0.5}_{-0.4}$	$2.03^{+0.04}_{-0.04}$	$0.19^{+0.11}_{-0.11}$
14	$5.4^{+1.1}_{-0.8}$	$1.20^{+0.04}_{-0.04}$	$0.4^{+0.2}_{-0.2}$

4.2.2.5 Cosmic Background

To best constrain the cosmic background, a RASS spectrum extracted in a $0.5-1^\circ$ annulus around the cluster core was fitted alongside the *XMM-Newton* spectra. The Galactic cosmic background consists of unabsorbed emission from the LHB, modelled with `apec` with temperature $\sim$0.1 keV, absorbed emission from the MWH, modelled as a two-phase plasma, `TBabs`(`apec`+`apec`), with temperatures $\sim$0.1 keV and $\sim$0.6 keV. The temperatures were initially fixed to the expected values and allowed to vary once a good fit was obtained. The redshifts were set to zero and the abundances to solar. The unresolved extragalactic background was modelled with `TBabs`×`powerlaw`, where the power-law index was set to 1.45 and the normalisation was set to 1.09×10^{-7} photons cm^{-2} s^{-1} keV^{-1} arcmin^{-2} for the *XMM-Newton* spectra and to 8.88×10^{-7} photons cm^{-2} s^{-1} keV^{-1} arcmin^{-2} for the RASS spectrum. The hydrogen column densities were fixed to the values in Table 3.4. The cosmic background was assumed to be constant across the FOV, and all the model parameters, excluding the normalisation of the RASS power law, were linked for all the spectra.

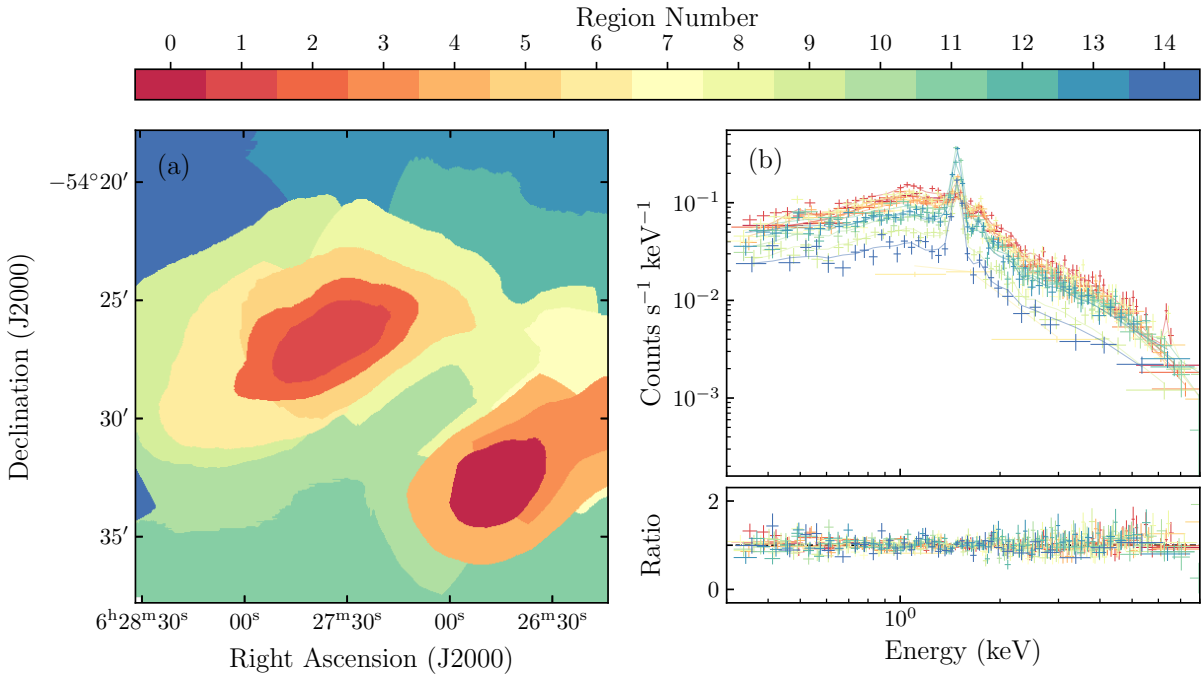

Figure 4.34: **(a)** Configuration of the regions used for spectral analysis of Abell 3395. **(b)** EPIC-MOS 1 spectra for ObsID 0400010301, each coloured the same as the region it was extracted from. The spectra of all the observations of Abell 3395 for all instruments are shown in Figure A.5.

Table 4.6: Best-fit cluster emission parameters for the regions of Abell 3395 shown in Figure 4.34.

Region	***kT*** **(keV)**	**Normalisation** $(10^{-5}\mathrm{cm}^{-5}\,\mathrm{arcmin}^{-2})$	Z $(Z_\odot)$
0	$4.9^{+0.3}_{-0.3}$	$18.4^{+0.3}_{-0.3}$	$0.59^{+0.10}_{-0.10}$
1	$4.9^{+0.3}_{-0.2}$	$18.1^{+0.3}_{-0.3}$	$0.65^{+0.09}_{-0.09}$
2	$4.3^{+0.2}_{-0.2}$	$13.2^{+0.2}_{-0.2}$	$0.45^{+0.08}_{-0.08}$
3	$5.0^{+0.4}_{-0.3}$	$12.0^{+0.2}_{-0.2}$	$0.19^{+0.11}_{-0.11}$
4	$5.0^{+0.4}_{-0.3}$	$8.0^{+0.1}_{-0.2}$	$0.26^{+0.10}_{-0.10}$
5	$4.5^{+0.2}_{-0.2}$	$8.87^{+0.10}_{-0.11}$	$0.37^{+0.06}_{-0.06}$
6	$4.1^{+0.4}_{-0.3}$	$7.00^{+0.02}_{-0.02}$	$0.68^{+0.13}_{-0.14}$
7	$5.2^{+0.5}_{-0.4}$	$6.7^{+0.1}_{-0.4}$	$0.27^{+0.13}_{-0.13}$
8	$5.2^{+0.3}_{-0.3}$	$5.2^{+0.1}_{-0.4}$	$0.58^{+0.08}_{-0.08}$
9	$3.9^{+0.2}_{-0.3}$	$4.91^{+0.08}_{-0.09}$	$0.37^{+0.08}_{-0.08}$
10	$6.6^{+0.7}_{-0.6}$	$3.4^{+0.1}_{-0.4}$	$0.9^{+0.2}_{-0.2}$
11	$5.0^{+0.6}_{-0.5}$	$1.9^{+0.1}_{-0.4}$	$0.9^{+0.2}_{-0.2}$
12	$6.4^{+0.7}_{-0.6}$	$3.1^{+0.1}_{-0.4}$	$0.4^{+0.2}_{-0.2}$
13	$4.8^{+0.4}_{-0.4}$	$2.0^{+0.1}_{-0.3}$	$1.1^{+0.3}_{-0.2}$
14	$4.8^{+0.5}_{-0.6}$	$2.2^{+0.1}_{-0.3}$	$0.8^{+0.2}_{-0.2}$

Chapter 5

Discussion

This chapter discusses possible interpretations of the results, comparing the radio and X-ray observations presented in the previous chapter to show possible signs of interaction between the radio galaxies and the ICM.

5.1 Abell 133

While seemingly relaxed, Abell 133, shown in Figure 5.1, has a complex X-ray core and unusual radio galaxy that potentially interacts with this core. A significant challenge in studying this interaction arises from the identification of the host galaxy of the radio source. Based on its redshift, the optical galaxy corresponding to the bright compact component along the jets—an obvious candidate for the host—is not a cluster member galaxy. This raises questions about whether the radio galaxy is physically associated with Abell 133.

The strongest evidence for such an association comes from the interaction between the northern lobe of the radio galaxy and the X-ray structure at the core of Abell 133. As shown in the GGM-filtered X-ray image of Abell 133 in Figure 5.2, the northern lobe closely follows a sharp X-ray edge surrounding the bright compact source and the tongue-like extension in the inner core (see Figure 4.25). Radio contours align almost perfectly with this edge, except for an extension in the lobe to the northeast.

While the main source of radio emission from this region could be unrelated to the radio galaxy lobe, as suggested by Randall *et al.* (2010), this seems unlikely, as this structure has a similar size and ultrasteep spectrum as the southern lobe. The differences that do exist in morphology,

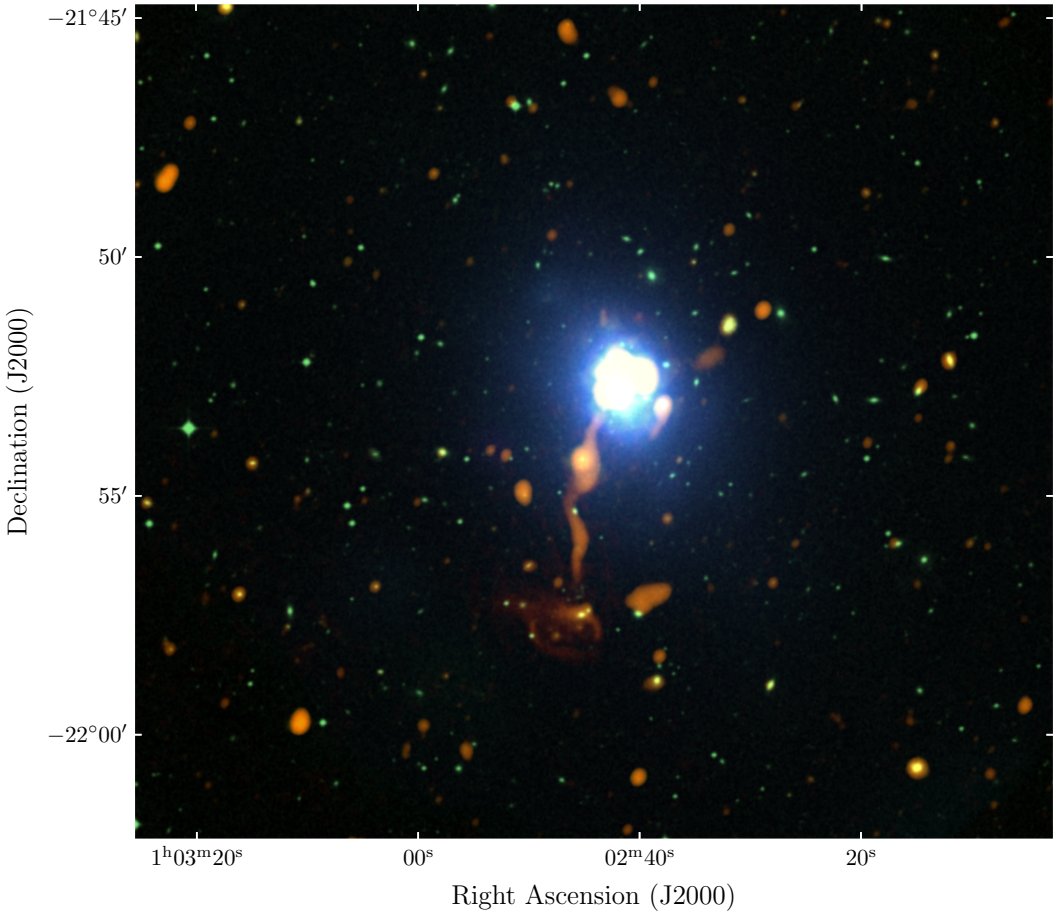

Figure 5.1: Composite radio, optical, and X-ray image of Abell 133. The radio emission, ranging from red to orange, is based on the 10 sub-band images. The optical emission, displayed in green, is from the Digitized Sky Survey, and the X-ray emission is shown in blue to purple for the energy ranges 400 – 750 eV, 750 – 1300 eV, and 2000 – 7200 eV.

spectrum, and brightness could be explained by the interaction between the lobe and the ICM at the core of Abell 133.

A possible alternative host galaxy is the cluster member galaxy NFP J010245.9−215520 near the bend point about midway between the two lobes. This bend point and a second bend further south coincide with edges in the GGM image, but the statistical significance of these edges remains uncertain, as some artefacts in the image originate from detector effects rather than physical phenomena within the cluster.

There is no radio core visible near the bend point, but if the radio galaxy is a remnant radio galaxy, as suggested by its steep spectral index, a lack of core prominence is expected. The brightening and flattening in the northern lobe could indicate re-acceleration of the fossil plasma in the lobes by processes occurring in the complex cluster core. However, the relatively collimated

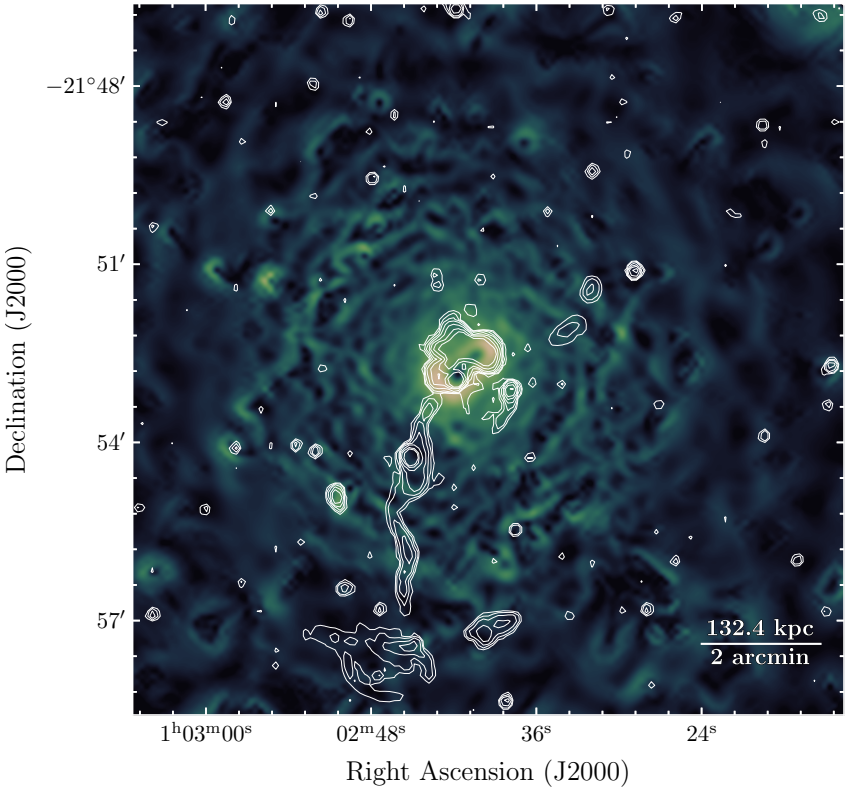

Figure 5.2: Edge-filtered X-ray image of Abell 133 with the adaptive GGM filter of Sanders *et al.* (2022), using an SNR of 15, with MeerKAT contours overlaid. Contour levels are $1, 2, 4, 8, 16, 32, 64 \times 10\sigma$ where $\sigma = 4.2\,\mu\text{Jy beam}^{-1}$. Some of the boxiness in the image is an artefact of the gaps between the *XMM-Newton* CCDs.

jets are atypical for remnant radio galaxies, which generally exhibit relaxed morphologies and lack compact jets (Brienza *et al.*, 2017), warranting further investigation into the nature of this source.

5.2 Abell 3266

Abell 3266, shown in Figure 5.3, has a complex X-ray morphology and several unusual radio galaxies, making it ideal for studying the interaction between these radio galaxies and the ICM. The bending lobes in some of these radio galaxies could be the result of ram pressure from the complex cluster merger.

The GGM image of the cluster is shown in Figure 5.4, revealing gradients in the X-ray surface brightness. While GGM images can contain artefacts, for example from the gaps between the CCDs, this one can be verified by comparing it to the GGM-filtered eROSITA image of the cluster by Sanders *et al.* (2022). Some of the boxiness and straight lines are artefacts, but

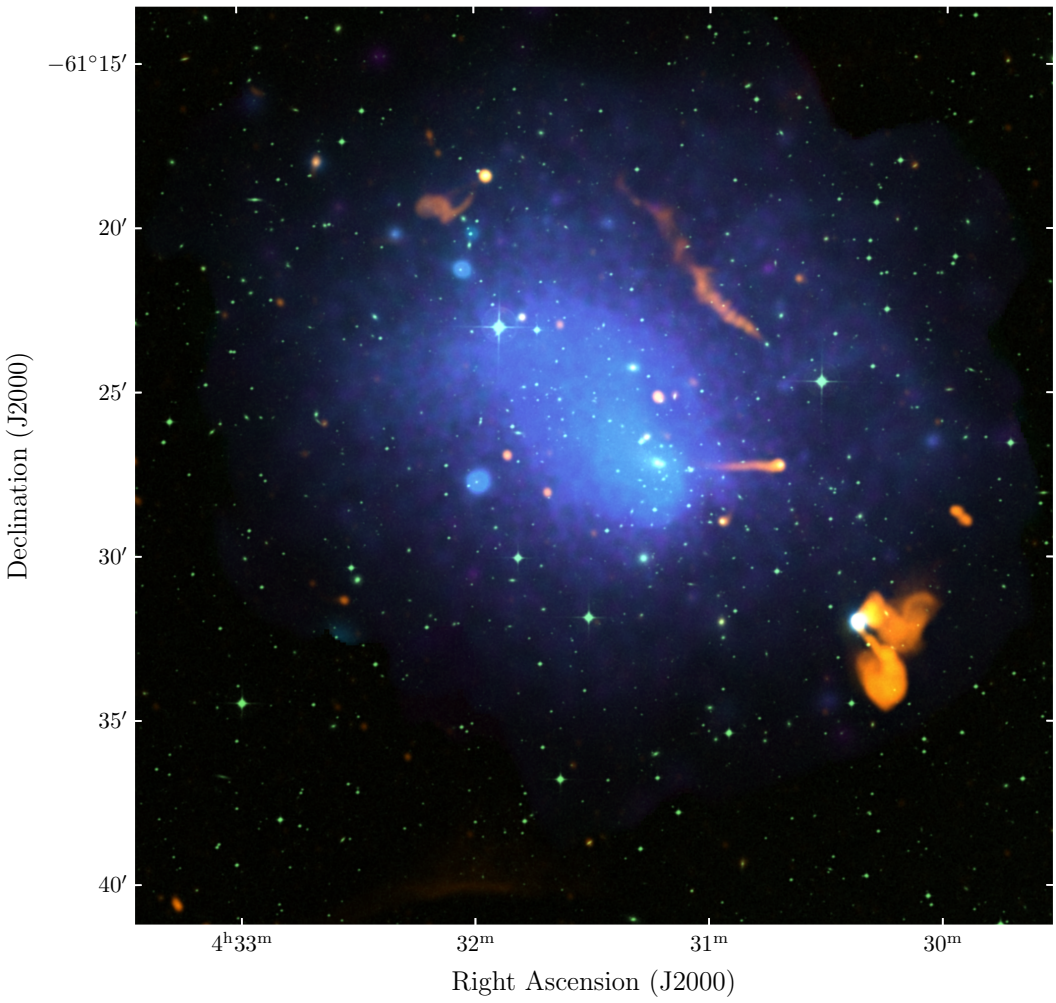

Figure 5.3: Composite radio, optical, and X-ray image of Abell 3266. The radio emission, ranging from red to orange, is based on the 10 sub-band images. The optical emission, displayed in green, is from the Digitized Sky Survey, and the X-ray emission is shown in blue to purple for the energy ranges 400 – 750 eV, 750 – 1300 eV, and 2000 – 7200 eV.

most of the strong features are also present in the eROSITA image, including the strong edge south and west of the cluster core, the large-scale cavity north of A3266-RG3, and the edges corresponding to the "fingers" of emission reaching northwest from the cluster core. The edge from the northern fingers passes through A3266-RG2, at the point halfway through this source where the faint northeastern and bright southwestern sides connect. While the fingers do not have the appearance of typical cluster shocks, the morphology of A3266-RG2 resembles a jet that has interacted with a shock. The jets of A3266-RG3 bend back near the location of an outer edge in the GGM image. While weak, this structure is also visible in the GGM image of Sanders *et al.* (2022).

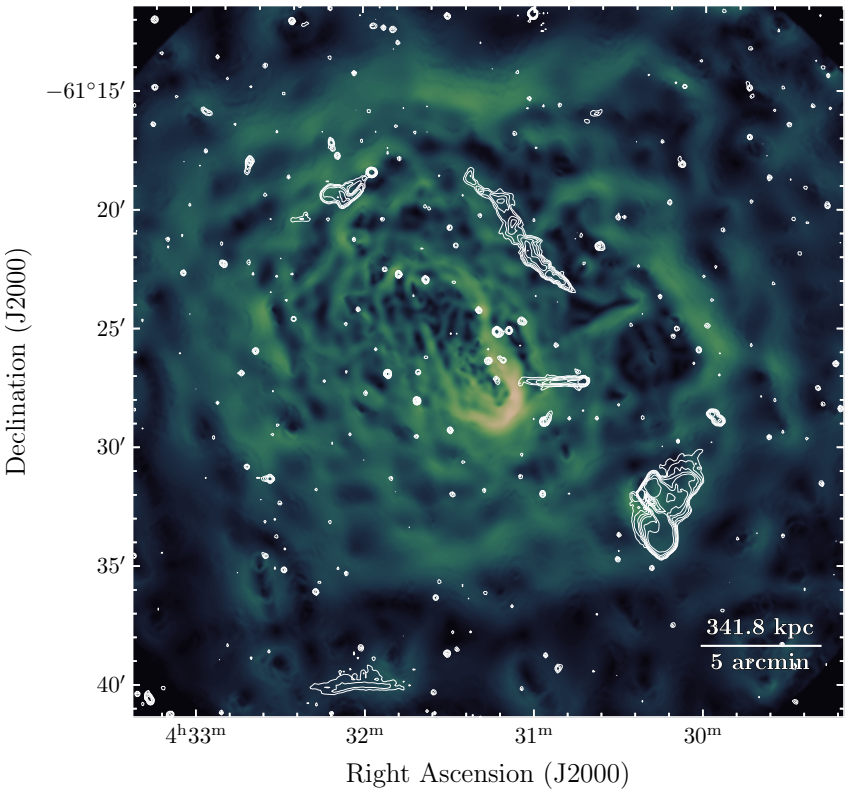

Figure 5.4: Adaptive GGM-filtered X-ray image of Abell 3266, using an SNR of 40, with MeerKAT contours overlaid. Contour levels are $1, 2, 4, 8, 16, 32, 64 \times 10\sigma$ where $\sigma = 6.9\,\mu\text{Jy beam}^{-1}$.

5.3 Abell 3376

The composite image of Abell 3376, presenting a multi-wavelength view of the cluster, highlights the cometary shape of the ICM, the prominent large-scale cluster radio shocks, and the unusual jets of A3376-RG1, which bend against the expected ram pressure from the cluster merger.

Previous studies have identified a cold front at the leading edge of this cometary structure (Urdampilleta *et al.*, 2018; Chibueze *et al.*, 2021). The GGM-filtered soft X-ray image of the cluster, shown in Figure 5.6, supports this finding by revealing a strong density discontinuity in this region, consistent with a cold front. Radio contours show that the northern jet of A3376-RG1 bends exactly along this edge, as proposed by Chibueze *et al.* (2021).

The temperature map in Figure 5.7 further confirms the presence of a cold front, showing a temperature increase across the discontinuity, verifying that it is a cold front rather than a shock.

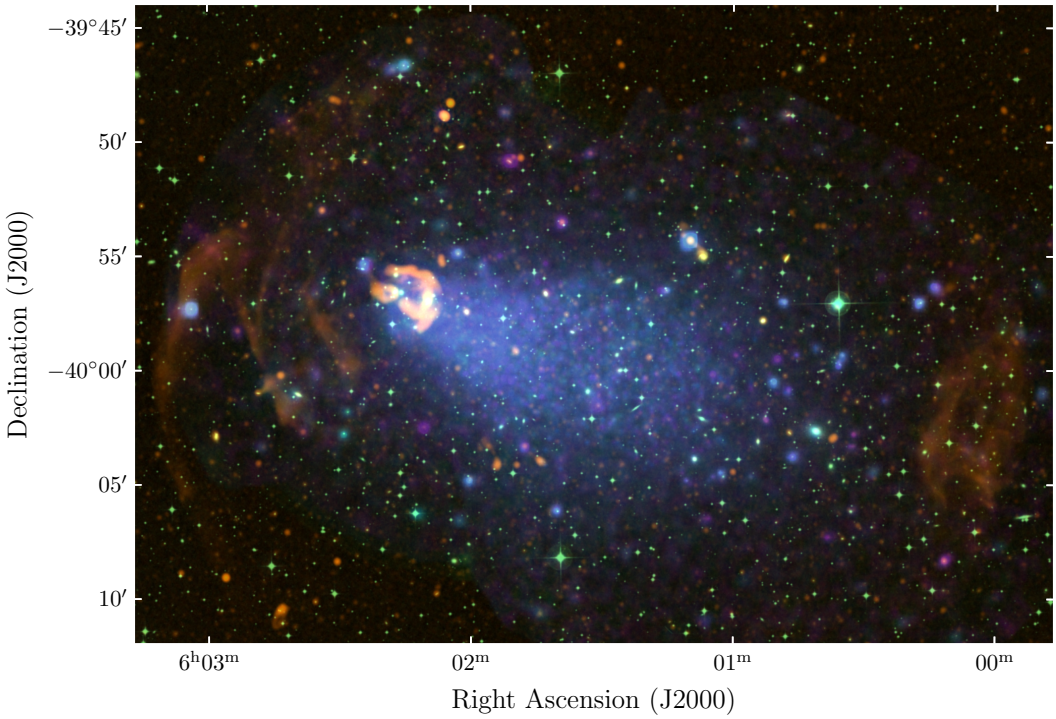

Figure 5.5: Composite radio, optical, and X-ray image of Abell 3376. The radio emission, ranging from red to orange, is based on the 10 sub-band images. The optical emission, displayed in green, is from the Digitized Sky Survey, and the X-ray emission is shown in blue to purple for the energy ranges 400 – 750 eV, 750 – 1300 eV, and 2000 – 7200 eV.

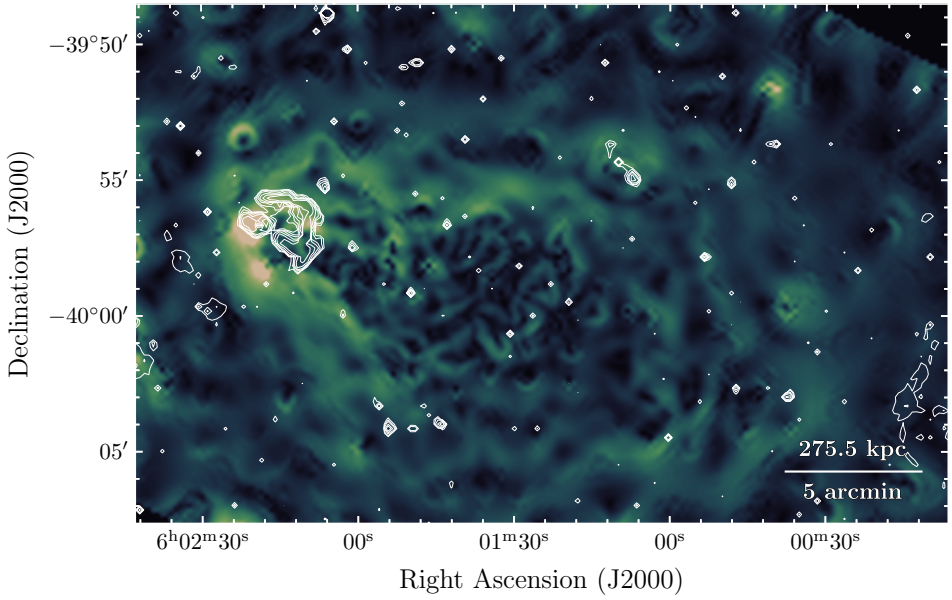

Figure 5.6: Adaptive GGM-filtered X-ray image of Abell 3376, using an SNR of 15, with MeerKAT contours overlaid. Contour levels are $1, 2, 4, 8, 16, 32 \times 10\sigma$ where $\sigma = 4.9\,\mu\text{Jy beam}^{-1}$.

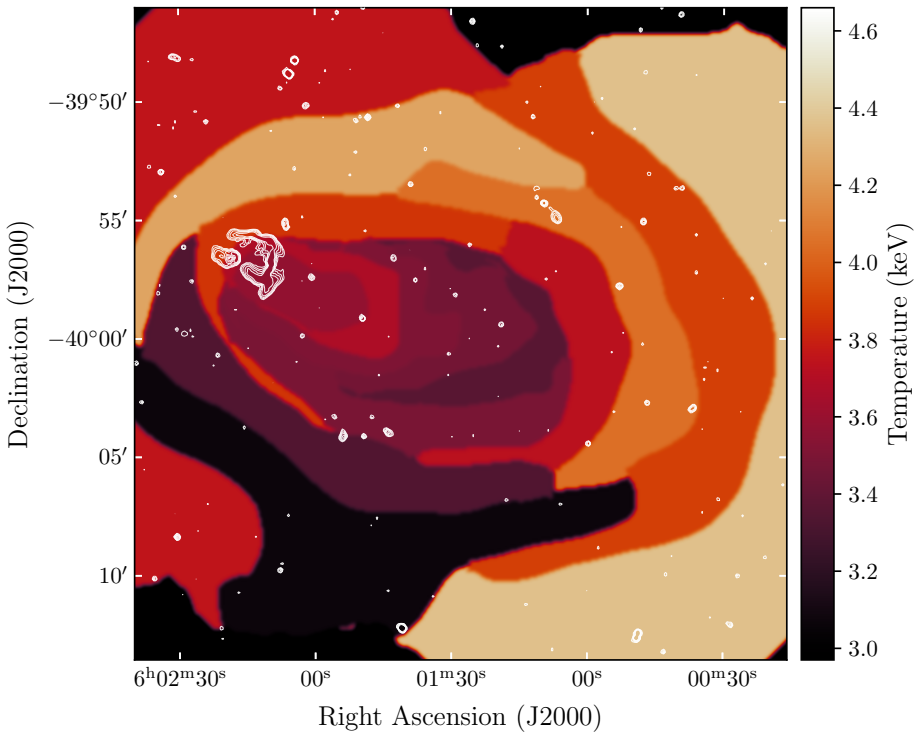

Figure 5.7: Spectroscopic temperature map of Abell 3376, showing the results of Table 4.4. The average uncertainty is 0.18 keV. Contour levels are $2, 4, 8, 16, 32 \times 10\sigma$ where $\sigma = 4.9\,\mu\text{Jy beam}^{-1}$.

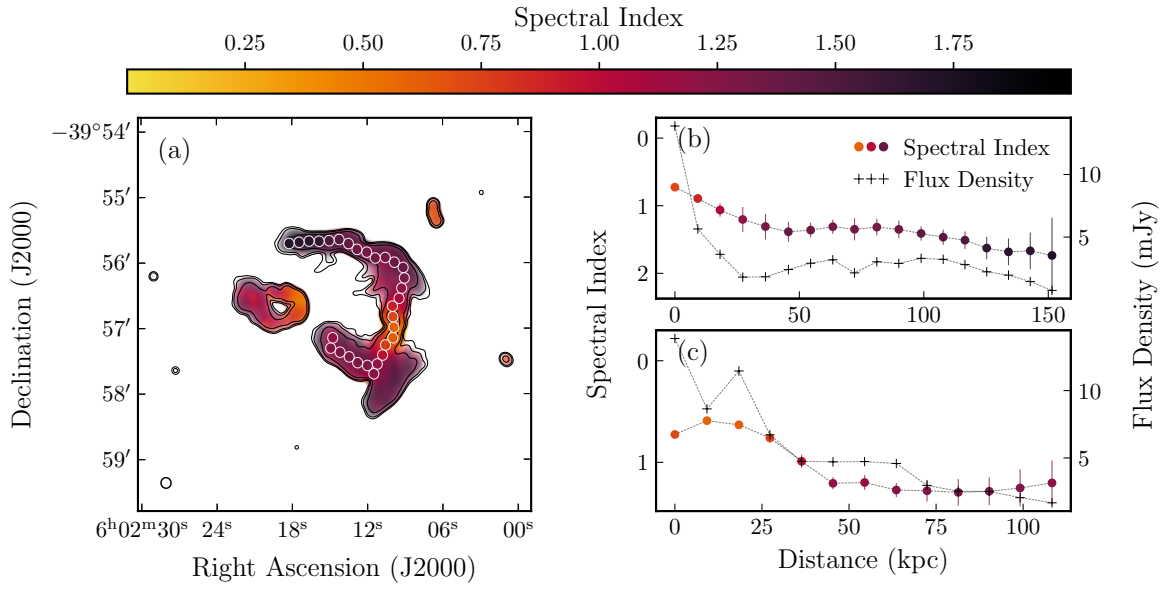

Figure 5.8: Spectral index and flux density distribution along the jets of A3376-RG1. Panel **(a)** is the spectral index map from Figure 4.21 with the spectral index error map applied as transparency scaling to mask regions with high uncertainty, overlaid with contours of the MFS MeerKAT image. Ellipses indicate the regions where the average spectral index and flux density were extracted. Panels **(b)** and **(c)** show plots of the spectral index and flux density for the northern and southern jets, respectively, as a function of the distance along the jets. The spectral index scatter plot markers are coloured according to the average spectral index in that region.

The spectral index and flux density profiles along the jets, shown in Figure 5.8, are in agreement with the trends reported by Chibueze *et al.* (2021), displaying a flattening of the spectrum and an increase in brightness in the bent jets. To validate the scenario proposed by Chibueze *et al.* (2021) where the spectral trends and the jet bending result from interactions with magnetic fields associated with the cold fronts, future work could include high-energy X-ray observations to constrain the magnetic field strength near the cold front.

5.4 Abell 3391

While the X-ray morphology of Abell 3391, shown in Figure 5.9, appears relatively relaxed, a surface brightness discontinuity is visible to the southwest of the cluster. Near this region, a large-scale filamentary structure is known to connect Abell 3391 to Abell 3395.

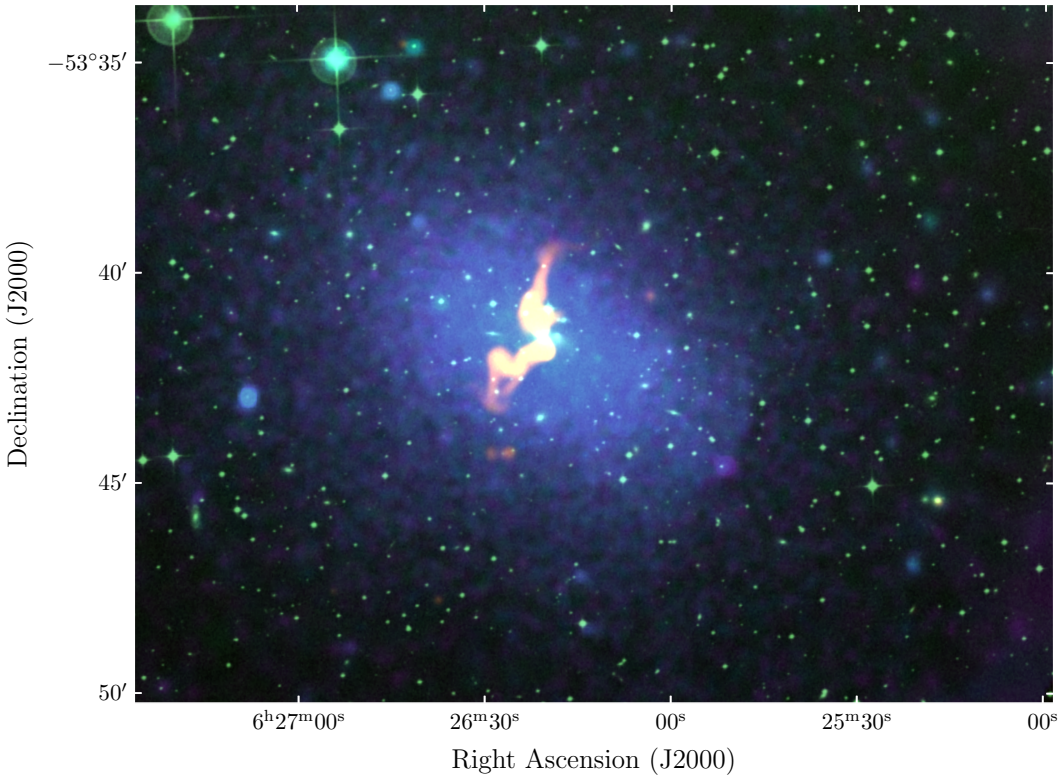

Figure 5.9: Composite radio, optical, and X-ray image of Abell 3391. The radio emission, ranging from red to orange, is based on the 10 sub-band images. The optical emission, displayed in green, is from the Digitized Sky Survey, and the X-ray emission is shown in blue to purple for the energy ranges 400 – 750 eV, 750 – 1300 eV, and 2000 – 7200 eV.

The surface brightness discontinuity is also evident in the GGM-filtered image in Figure 5.10. However, the temperature results from the spectral analysis, visualised in Figure 5.11, do not

indicate a statistically significant change in temperature across the surface brightness discontinuity. Further studies are required to determine whether this edge represents a cold front or a shock.

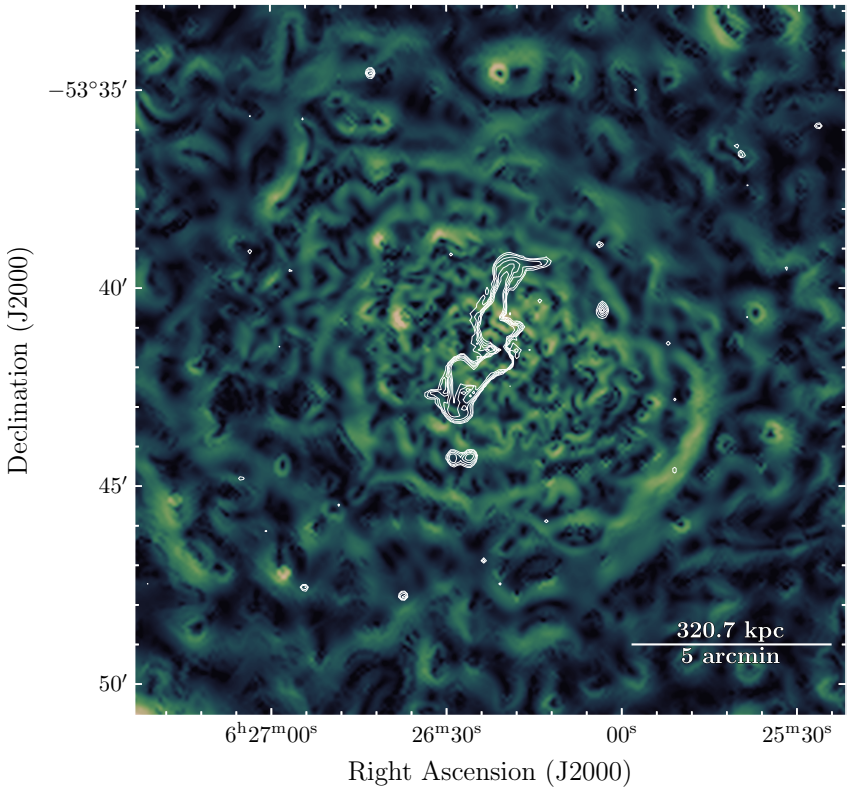

Figure 5.10: Adaptive GGM-filtered X-ray image of Abell 3391, using an SNR of 20, with MeerKAT contours overlaid. Contour levels are $2, 4, 8, 16, 32, 64 \times 10\sigma$ where $\sigma = 10\,\mu\text{Jy}\,\text{beam}^{-1}$.

The temperature map reveals a hot cluster core. The jets of the central radio galaxy exhibit bending near weak edges visible in the GGM image, and expand into plumes as they leave the hot core.

While the spectral index in the northern jet steepens gradually with distance from the core, the southern jet exhibits flattening and slight brightening near the final bend point. The reason for this would require further study.

Despite the significant improvements achieved through 3GC, the quality of the radio image remains severely affected by DDEs, particularly the presence of ring-like artefacts around the bright central radio galaxy. Brüggen *et al.* (2021) reported a similar issue in their ASKAP image of this source.

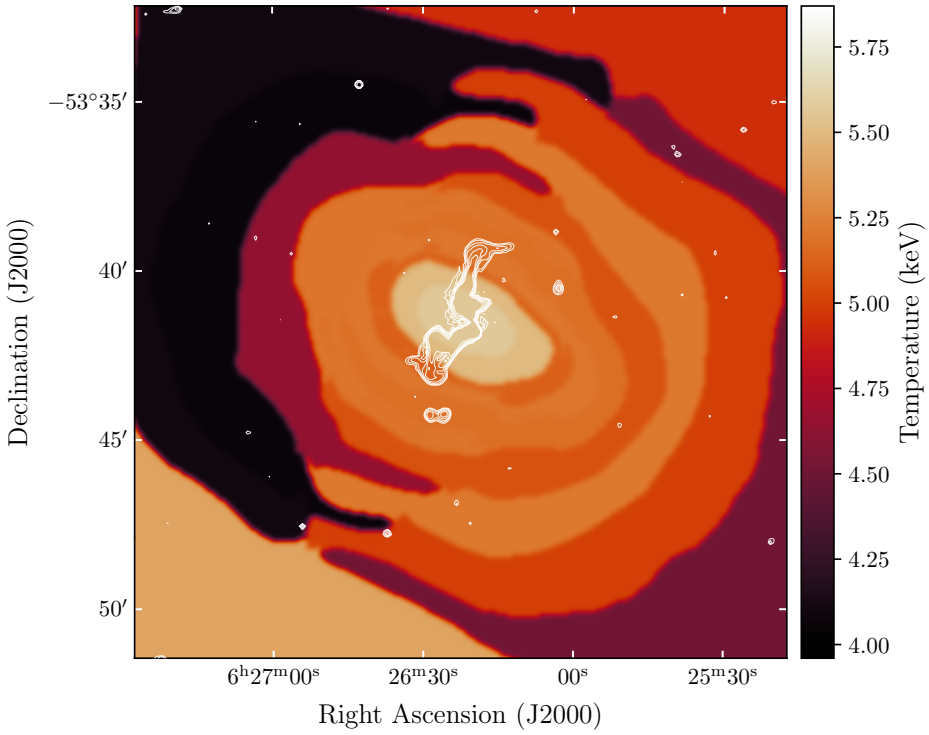

Figure 5.11: Spectroscopic temperature map of Abell 3391, showing the results of Table 4.5. Excluding region 14 to the southeast, which was not well-constrained in the fit, the average uncertainty is 0.27 keV. Contour levels are $2, 4, 8, 16, 32, 64 \times 10\sigma$ where $\sigma = 10\,\mu\text{Jy beam}^{-1}$.

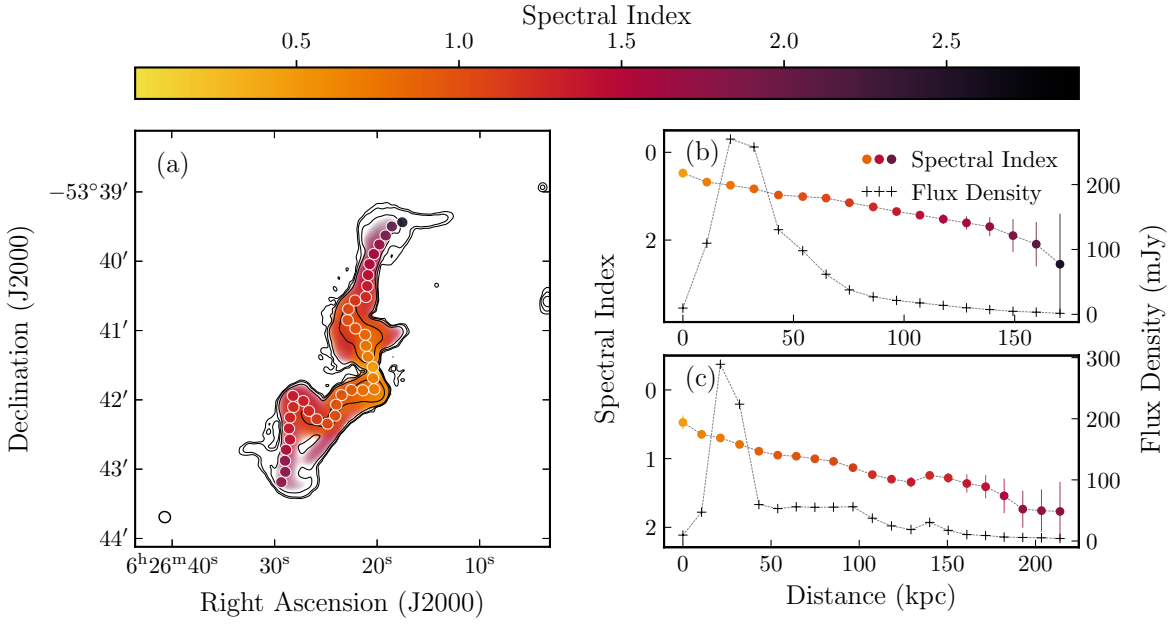

Figure 5.12: Spectral index and flux density distribution along the jets the central radio galaxy in Abell 3391. Panel layout is similar to Figure 5.8.

Chapter 6

Conclusion

This dissertation investigated the interaction between radio galaxies and the ICM in five galaxy clusters from the MGCLS in a multiwavelength analysis using radio and X-ray data. The results demonstrate significant interactions between radio galaxies and the ICM, contributing to our understanding of galaxy cluster dynamics.

This study focused on Abell 133, Abell 3266, Abell 3376, Abell 3391, and Abell 3395, using observations from *XMM-Newton* and MeerKAT. By analysing continuum radio images, X-ray images, radio spectral index maps of selected radio galaxies, and conducting spectral analysis of X-ray data, the research provided insights into the physical processes involved in the interactions between radio galaxies and the ICM.

While this study highlighted several interesting cases, it focused on only five clusters from the MGCLS, a small fraction of the 115 MGCLS clusters. An analysis of the entire sample could reveal many other clusters in the MGCLS sample with radio galaxies that interact with the ICM.

Additionally, the X-ray analysis relied on archival *XMM-Newton* data, which restricted the study to clusters with existing observations. Many MGCLS clusters have not been observed with *XMM-Newton* and were excluded from consideration. Future work could incorporate new *XMM-Newton* observations or utilise data from other X-ray observatories, such as *Chandra* and eROSITA, to expand the scope of the study.

While X-ray observations provide invaluable information about the temperature and density distributions of the ICM, these quantities are projected along the line of sight, and assumptions about the three-dimensional structure of the cluster are necessary to deproject the measure-

ments. Optical spectroscopic studies of galaxies in a cluster, such as the study of Abell 3266 by Dehghan *et al.* (2017), can be incorporated to allow the three-dimensional reconstruction of the cluster geometry from redshift information of the cluster member galaxies.

Several radio galaxies in this study exhibited signs of interaction with the ICM. However, theoretical modelling of these interactions was beyond the scope of this work. Further studies could use MHD simulations to interpret these interactions in greater detail. In addition, spectral ageing studies of the radio galaxies may be employed to explore their evolutionary states and study the re-acceleration of relativistic particles through interactions with the ICM. While these studies often make use of potentially flawed assumptions about the magnetic fields, high-energy X-ray observations could help constrain the magnetic field strengths.

As demonstrated in this work, the MGCLS provides an invaluable opportunity to study radio galaxies in cluster environments. However, data calibration and imaging strategies for MeerKAT are still being refined. This is particularly evident in the case of Abell 3391, where severe calibration artefacts persisted despite 3GC. These artefacts can obscure faint emission and distort spectral index measurements. Improvements in calibration and imaging techniques are crucial for fully utilising these datasets.

Bibliography

Abell, G. O. (1958). The distribution of rich clusters of galaxies. *Astrophysical Journal Supplement Series*, 3:211.

Abell, G. O., Corwin Jr, H. G., and Olowin, R. P. (1989). A catalog of rich clusters of galaxies. *Astrophysical Journal Supplement Series*, 70:1–138.

Alexander, E. (2022a). The traditional Fanaroff Riley classification of radio galaxies (Fanaroff & Riley, 1974). `https://commons.wikimedia.org/wiki/File:Emmaalexander_fr_blue.png`. Accessed 2024/04/11.

Alexander, E. (2022b). Unified model of AGN adapted from Urry & Padovani (1995). `https://commons.wikimedia.org/wiki/File:Emmaalexander_unified_agn.png`. Accessed 2024/04/14.

Alvarez, G. E., Randall, S. W., Bourdin, H., Jones, C., and Holley-Bockelmann, K. (2018). *Chandra* and *XMM-Newton* observations of the Abell 3395/Abell 3391 intercluster filament. *The Astrophysical Journal*, 858(1):44.

Andreas 9384 (2017a). Mirror arrangement of a Wolter telescope, Type I. `https://commons.wikimedia.org/wiki/File:Wolter-I.svg`. Accessed 2023/08/01.

Andreas 9384 (2017b). Mirror arrangement of a Wolter telescope, Type II. `https://commons.wikimedia.org/wiki/File:Wolter-II.svg`. Accessed 2023/08/01.

Andreas 9384 (2017c). Mirror arrangement of a Wolter telescope, Type III. `https://commons.wikimedia.org/wiki/File:Wolter-III.svg`. Accessed 2023/08/01.

Arnaud, K. (1996). XSPEC: the first ten years. In *Astronomical Data Analysis Software and Systems V, ASP Conference Series*, volume 101, page 17.

Arnaud, K., Gordon, C., Dorman, B., and Rutkowski, K. (2024). *XSPEC: an X-ray spectral fitting package. Users' guide for version 12.14.1.*

Arnaud, K., Smith, R., and Siemiginowska, A. (2011). *Handbook of X-ray astronomy*, volume 7. Cambridge University Press.

Arnaud, M. (2009). The β-model of the intracluster medium-commentary on: Cavaliere A. and Fusco-Femiano R., 1976, A&A, 49, 137. *Astronomy & Astrophysics*, 500(1):103–104.

Ascasibar, Y. and Markevitch, M. (2006). The origin of cold fronts in the cores of relaxed galaxy clusters. *The Astrophysical Journal*, 650(1):102.

Bagchi, J., Durret, F., Neto, G. B. L., and Paul, S. (2006). Giant ringlike radio structures around galaxy cluster Abell 3376. *Science*, 314(5800):791–794.

Baldi, R. D. (2023). The nature of compact radio sources: the case of FR 0 radio galaxies. *The Astronomy and Astrophysics Review*, 31(1):3.

Bartels, R., Zandanel, F., and Ando, S. (2015). Inverse-Compton emission from clusters of galaxies: predictions for *ASTRO-H*. *Astronomy & Astrophysics*, 582:A20.

Bean, B., Bhatnagar, S., Castro, S., Meyer, J. D., Emonts, B., Garcia, E., Garwood, R., Golap, K., Villalba, J. G., Harris, P., *et al.* (2022). CASA, Common Astronomy Software Applications for radio astronomy. *Publications of the Astronomical Society of the Pacific*, 134(1041):114501.

Beckmann, V. and Shrader, C. (2012). *Active galactic nuclei*. John Wiley & Sons.

Bernardi, G., Venturi, T., Cassano, R., Dallacasa, D., Brunetti, G., Cuciti, V., Johnston-Hollitt, M., Oozeer, N., Parekh, V., and Smirnov, O. (2015). KAT-7 observations of an unbiased sample of mass-selected galaxy clusters. *Monthly Notices of the Royal Astronomical Society*, 456(2):1259–1268.

Bîrzan, L., Rafferty, D. A., McNamara, B., Wise, M. W., and Nulsen, P. E. (2004). A systematic study of radio-induced X-ray cavities in clusters, groups, and galaxies. *The Astrophysical Journal*, 607(2):800.

Blandford, R. and Rees, M. (1974). A 'twin-exhaust' model for double radio sources. *Monthly Notices of the Royal Astronomical Society*, 169(3):395–415.

Blandford, R. D. and Znajek, R. L. (1977). Electromagnetic extraction of energy from Kerr black holes. *Monthly Notices of the Royal Astronomical Society*, 179(3):433–456.

Blanton, E., Randall, S., Clarke, T., Sarazin, C., McNamara, B., Douglass, E., and McDonald, M. (2011). A very deep *Chandra* observation of A2052: bubbles, shocks, and sloshing. *The Astrophysical Journal*, 737(2):99.

Bluem, J., Kaaret, P., Kuntz, K., Jahoda, K. M., Koutroumpa, D., Hodges-Kluck, E. J., Fuller, C. A., LaRocca, D. M., and Zajczyk, A. (2022). Widespread detection of two components in the hot circumgalactic medium of the Milky Way. *The Astrophysical Journal*, 936(1):72.

Blumenthal, G. R. and Gould, R. J. (1970). Bremsstrahlung, synchrotron radiation, and Compton scattering of high-energy electrons traversing dilute gases. *Reviews of Modern Physics*, 42(2):237.

Böhringer, H. and Werner, N. (2010). X-ray spectroscopy of galaxy clusters: studying astrophysical processes in the largest celestial laboratories. *The Astronomy and Astrophysics Review*, 18:127–196.

Bond, J. R., Kofman, L., and Pogosyan, D. (1996). How filaments of galaxies are woven into the cosmic web. *Nature*, 380(6575):603–606.

Böttcher, M., Harris, D. E., and Krawczynski, H. (2012). *Relativistic jets from active galactic nuclei*. John Wiley & Sons.

Bridle, A. H., Hough, D. H., Lonsdale, C. J., Burns, J. O., and Laing, R. A. (1994). Deep VLA imaging of twelve extended 3CR quasars. *The Astronomical Journal*, 108:766–820.

Brienza, M., Godfrey, L., Morganti, R., Prandoni, I., Harwood, J., Mahony, E., Hardcastle, M., Murgia, M., Röttgering, H., Shimwell, T. W., *et al.* (2017). Search and modelling of remnant radio galaxies in the LOFAR Lockman Hole field. *Astronomy & Astrophysics*, 606:A98.

Brüggen, M. (2013). Magnetic fields in galaxy clusters. *Astronomische Nachrichten*, 334(6):543–547.

Brüggen, M., Reiprich, T. H., Bulbul, E., Koribalski, B. S., Andernach, H., Rudnick, L., Hoang, D. N., Wilber, A. G., Duchesne, S., Veronica, A., *et al.* (2021). Radio observations of the merging galaxy cluster system Abell 3391-Abell 3395. *Astronomy & Astrophysics*, 647:A3.

Burbidge, G. R. (1956). On synchrotron radiation from Messier 87. *Astrophysical Journal*, 124:416.

Burke, B. F., Graham-Smith, F., and Wilkinson, P. N. (2019). *An introduction to radio astronomy*. Cambridge University Press.

Burns, J. O. and Owen, F. (1980). Dual curved jets in the tailed radio galaxy 1638+538 (4C53.37). *Astronomical Journal*, 85:204–214.

Camilo, F., Scholz, P., Serylak, M., Buchner, S., Merryfield, M., Kaspi, V., Archibald, R., Bailes, M., Jameson, A., Van Straten, W., *et al.* (2018). Revival of the magnetar PSR J1622–4950: observations with MeerKAT, Parkes, *XMM-Newton*, *Swift*, *Chandra*, and *NuSTAR*. *The Astrophysical Journal*, 856(2):180.

Caprioli, D. (2024). Particle acceleration at shocks: an introduction. In *Foundations of Cosmic Ray Astrophysics*, pages 143–181. IOS Press.

Carilli, C. and Taylor, G. (2002). Cluster magnetic fields. *Annual Review of Astronomy and Astrophysics*, 40(1):319–348.

Carroll, P., Line, J., Morales, M. F., Barry, N., Beardsley, A., Hazelton, B., Jacobs, D., Pober, J., Sullivan, I., Webster, R. L., *et al.* (2016). A high reliability survey of discrete Epoch of Reionization foreground sources in the MWA EoR0 field. *Monthly Notices of the Royal Astronomical Society*, 461(4):4151–4175.

Carter, J. and Sembay, S. (2008). Identifying *XMM-Newton* observations affected by solar wind charge exchange. Part I. *Astronomy & Astrophysics*, 489(2):837–848.

Cash, W. (1979). Parameter estimation in astronomy through application of the likelihood ratio. *Astrophysical Journal*, 228:939–947.

Cassano, R., Ettori, S., Giacintucci, S., Brunetti, G., Markevitch, M., Venturi, T., and Gitti, M. (2010). On the connection between giant radio halos and cluster mergers. *The Astrophysical Journal Letters*, 721(2):L82.

Cavaliere, A. and Fusco-Femiano, R. (1976). X-rays from hot plasma in clusters of galaxies. *Astronomy & Astrophysics*, 49:137–144.

Cavaliere, A. and Fusco-Femiano, R. (1978). The distribution of hot gas in clusters of galaxies. *Astronomy & Astrophysics*, 70:677.

Chibueze, J. O., Caleb, M., Spitler, L., Ashkar, H., Schüssler, F., Stappers, B., Venter, C., Heywood, I., Richards, A., Williams, D., *et al.* (2022). A MeerKAT, e-MERLIN, HESS, and *Swift* search for persistent and transient emission associated with three localized FRBs. *Monthly Notices of the Royal Astronomical Society*, 515(1):1365–1379.

Chibueze, J. O., Sakemi, H., Ohmura, T., Machida, M., Akamatsu, H., Akahori, T., Nakanishi, H., Parekh, V., van Rooyen, R., and Takeuchi, T. T. (2021). Jets from MRC 0600-399 bent by magnetic fields in the cluster Abell 3376. *Nature*, 593(7857):47–50.

Condon, J. J., Cotton, W., Greisen, E., Yin, Q., Perley, R. A., Taylor, G., and Broderick, J. (1998). The NRAO VLA Sky Survey. *The Astronomical Journal*, 115(5):1693.

Condon, J. J. and Ransom, S. M. (2016). *Essential radio astronomy*, volume 2. Princeton University Press.

Contopoulos, I., Gabuzda, D., and Kylafis, N. (2015). *The formation and disruption of black hole jets*, volume 414. Springer.

Conway, J., Cornwell, T., and Wilkinson, P. (1990). Multi-frequency synthesis–a new technique in radio interferometric imaging. *Monthly Notices of the Royal Astronomical Society, Vol. 246, NO. 3/OCT1, P. 490, 1990*, 246:490.

Cordey, R. A. (1987). IC 2476: a possible relic radio galaxy. *Monthly Notices of the Royal Astronomical Society*, 227(3):695–700.

Cornwell, T. and Wilkinson, P. (1981). A new method for making maps with unstable radio interferometers. *Monthly Notices of the Royal Astronomical Society*, 196(4):1067–1086.

Cowie, L. L. and Binney, J. (1977). Radiative regulation of gas flow within clusters of galaxies–a model for cluster X-ray sources. *Astrophysical Journal*, 215:723–732.

Coziol, R., Andernach, H., Caretta, C., Alamo-Martínez, K., and Tago, E. (2009). The dynamical state of brightest cluster galaxies and the formation of clusters. *The Astronomical Journal*, 137(6):4795.

Croston, J. H., Hardcastle, M., Harris, D., Belsole, E., Birkinshaw, M., and Worrall, D. (2005). An X-ray study of magnetic field strengths and particle content in the lobes of FR II radio sources. *The Astrophysical Journal*, 626(2):733.

Curtis, H. D. (1918). Descriptions of 762 nebulae and clusters photographed with the Crossley reflector. *Publications of Lick Observatory*, 13:9–42.

Dálya, G., Galgóczi, G., Dobos, L., Frei, Z., Heng, I. S., Macas, R., Messenger, C., Raffai, P., and de Souza, R. S. (2018). GLADE: A galaxy catalogue for multimessenger searches in the advanced gravitational-wave detector era. *Monthly Notices of the Royal Astronomical Society*, 479(2):2374–2381.

Davis, J. E. (2001). The formal underpinnings of the response functions used in X-ray spectral analysis. *The Astrophysical Journal*, 548(2):1010.

de Gasperin, F., Intema, H. T., Shimwell, T. W., Brunetti, G., Brüggen, M., Enßlin, T. A., van Weeren, R. J., Bonafede, A., and Röttgering, H. J. (2017). Gentle reenergization of electrons in merging galaxy clusters. *Science Advances*, 3(10):e1701634.

de Gasperin, F., Ogrean, G., van Weeren, R., Dawson, W., Brüggen, M., Bonafede, A., and Simionescu, A. (2015). Abell 1033: birth of a radio phoenix. *Monthly Notices of the Royal Astronomical Society*, 448(3):2197–2209.

De Grandi, S. and Molendi, S. (1999). A *BeppoSAX* observation of the merging cluster Abell 3266. *The Astrophysical Journal*, 527(1):L25.

Dehghan, S., Johnston-Hollitt, M., Colless, M., and Miller, R. (2017). Dynamics of Abell 3266–I. An optical view of a complex merging cluster. *Monthly Notices of the Royal Astronomical Society*, 468(3):2645–2654.

Dehghan, S., Johnston-Hollitt, M., Franzen, T. M., Norris, R. P., and Miller, N. A. (2014). Bent-tailed radio sources in the Australia Telescope Large Area Survey of the *Chandra* Deep Field South. *The Astronomical Journal*, 148(5):75.

Delhaize, J., Heywood, I., Prescott, M., Jarvis, M. J., Delvecchio, I., Whittam, I. H., White, S. V., Hardcastle, M. J., Hale, C. L., Afonso, J., *et al.* (2021). MIGHTEE: are giant radio galaxies more common than we thought? *Monthly Notices of the Royal Astronomical Society*, 501(3):3833–3845.

Di Mascolo, L., Mroczkowski, T., Churazov, E., Markevitch, M., Basu, K., Clarke, T. E., Devlin, M., Mason, B. S., Randall, S. W., Reese, E. D., *et al.* (2019). An ALMA+ ACA measurement of the shock in the Bullet Cluster. *Astronomy & Astrophysics*, 628:A100.

Domínguez-Fernández, P., Vazza, F., Brüggen, M., and Brunetti, G. (2019). Dynamical evolution of magnetic fields in the intracluster medium. *Monthly Notices of the Royal Astronomical Society*, 486(1):623–638.

Donnert, J., Dolag, K., Lesch, H., and Müller, E. (2009). Cluster magnetic fields from galactic outflows. *Monthly Notices of the Royal Astronomical Society*, 392(3):1008–1021.

Duchesne, S., Johnston-Hollitt, M., Riseley, C., Bartalucci, I., and Keel, S. (2022). The merging galaxy cluster Abell 3266 at low radio frequencies. *Monthly Notices of the Royal Astronomical Society*, 511(3):3525–3535.

Duchesne, S. W. and Johnston-Hollitt, M. (2019). The remnant radio galaxy associated with NGC 1534. *Publications of the Astronomical Society of Australia*, 36:e016.

Eckert, D., Jauzac, M., Shan, H., Kneib, J.-P., Erben, T., Israel, H., Jullo, E., Klein, M., Massey, R., Richard, J., *et al.* (2015). Warm–hot baryons comprise 5–10 per cent of filaments in the cosmic web. *Nature*, 528(7580):105–107.

Eilek, J. A. (1996). How radio sources stay young: spectral aging revisited. In *Energy Transport in Radio Galaxies and Quasars*, volume 100, page 281.

Ensslin, T. A., Simon, P., Biermann, P. L., Klein, U., Kohle, S., Kronberg, P. P., and Mack, K.-H. (2001). Signatures in a giant radio galaxy of a cosmological shock wave at intersecting filaments of galaxies. *The Astrophysical Journal*, 549(1):L39.

ESA/*XMM-Newton* (ca. 2005). *XMM-Newton* spacecraft model. `https://commons.wikimedia.org/wiki/File:XMM-Newton_spacecraft_model.png`. Accessed 2023/08/02.

Evrard, A. (1990). Formation and evolution of X-ray clusters–a hydrodynamic simulation of the intracluster medium. *Astrophysical Journal*, 363.

Fabian, A. and Nulsen, P. (1977). Subsonic accretion of cooling gas in clusters of galaxies. *Monthly Notices of the Royal Astronomical Society*, 180(3):479–484.

Fanaroff, B., Lal, D. V., Venturi, T., Smirnov, O. M., Bondi, M., Thorat, K., Bester, L. H., Józsa, G. I., Kleiner, D., Loi, F., *et al.* (2021). A new look at old friends–I. Imaging classical radio galaxies with uGMRT and MeerKAT. *Monthly Notices of the Royal Astronomical Society*, 505(4):6003–6016.

Fanaroff, B. L. and Riley, J. M. (1974). The morphology of extragalactic radio sources of high and low luminosity. *Monthly Notices of the Royal Astronomical Society*, 167(1):31P–36P.

Feretti, L., Fusco-Femiano, R., Giovannini, G., and Govoni, F. (2001). The giant radio halo in Abell 2163. *Astronomy & Astrophysics*, 373(1):106–112.

Feretti, L., Gioia, I. M., and Giovannini, G. (2002). *Merging processes in galaxy clusters*, volume 272. Springer Science & Business Media.

Finoguenov, A., Henriksen, M., Miniati, F., Briel, U., and Jones, C. (2006). A puzzling merger in A3266: the hydrodynamic picture from *XMM-Newton*. *The Astrophysical Journal*, 643(2):790.

Fleenor, M. C., Rose, J. A., Christiansen, W. A., Hunstead, R. W., Johnston-Hollitt, M., Drinkwater, M. J., and Saunders, W. (2005). Large-scale velocity structures in the Horologium-Reticulum supercluster. *The Astronomical Journal*, 130(3):957.

Fujita, Y., Sarazin, C. L., Kempner, J. C., Rudnick, L., Slee, O., Roy, A., Andernach, H., and Ehle, M. (2002). *Chandra* observations of the disruption of the cool core in A133. *The Astrophysical Journal*, 575(2):764.

Fujita, Y., Sarazin, C. L., Reiprich, T. H., Andernach, H., Ehle, M., Murgia, M., Rudnick, L., and Slee, O. (2004). *XMM-Newton* observations of A133: A weak shock passing through the cool core. *The Astrophysical Journal*, 616(1):157.

Gabici, S. and Blasi, P. (2003). Nonthermal radiation from clusters of galaxies: the role of merger shocks in particle acceleration. *The Astrophysical Journal*, 583(2):695.

Gabriel, C., Denby, M., Fyfe, D., Hoar, J., Ibarra, A., Ojero, E., Osborne, J., Saxton, R., Lammers, U., and Vacanti, G. (2004). The *XMM-Newton* SAS–distributed development and maintenance of a large science analysis system: a critical analysis. In *Astronomical Data Analysis Software and Systems (ADASS) XIII*, volume 314, page 759.

Gaia Collaboration (2023). Gaia Data Release 3-summary of the content and survey properties. *Astronomy & Astrophysics*, 674:A1.

Garon, A. F., Rudnick, L., Wong, O. I., Jones, T. W., Kim, J.-A., Andernach, H., Shabala, S. S., Kapińska, A. D., Norris, R. P., De Gasperin, F., *et al.* (2019). Radio galaxy zoo: the distortion of radio galaxies by galaxy clusters. *The Astronomical Journal*, 157(3):126.

Gatuzz, E., Sanders, J., Dennerl, K., Pinto, C., Fabian, A., Tamura, T., Walker, S., and ZuHone, J. (2022). Measuring sloshing, merging, and feedback velocities in the Virgo cluster. *Monthly Notices of the Royal Astronomical Society*, 511(3):4511–4527.

Gendron-Marsolais, M.-L., Hull, C. L., Perley, R., Rudnick, L., Kraft, R., Hlavacek-Larrondo, J., Fabian, A. C., Roediger, E., van Weeren, R. J., Richard-Laferrière, A., *et al.* (2021). VLA resolves unexpected radio structures in the Perseus cluster of galaxies. *The Astrophysical Journal*, 911(1):56.

Ghizzardi, S., Rossetti, M., and Molendi, S. (2010). Cold fronts in galaxy clusters. *Astronomy & Astrophysics*, 516:A32.

Gliozzi, M., Brinkmann, W., Laurent-Muehleisen, S., Takalo, L., and Sillanpaa, A. (1999). *ROSAT* HRI observations of radio-loud AGN. *arXiv preprint astro-ph/9911055*.

Gómez, P., Pinkney, J., Burns, J., Wang, Q., Owen, F., and Voges, W. (1997). *ROSAT* X-ray observations of Abell clusters with wide-angle tailed radio sources. *The Astrophysical Journal*, 474(2):580.

Gopal-Krishna and Wiita, P. (2000). Extragalactic radio sources with hybrid morphology: implications for the Fanaroff-Riley dichotomy. *Astronomy & Astrophysics*, 363:507–516.

Govoni, F. and Feretti, L. (2004). Magnetic fields in clusters of galaxies. *International Journal of Modern Physics D*, 13(08):1549–1594.

Grainge, K., Alachkar, B., Amy, S., Barbosa, D., Bommineni, M., Boven, P., Braddock, R., Davis, J., Diwakar, P., Francis, V., *et al.* (2017). Square Kilometre Array: the radio telescope of the XXI century. *Astronomy Reports*, 61:288–296.

Gupta, Y., Ajithkumar, B., Kale, H., Nayak, S., Sabhapathy, S., Sureshkumar, S., Swami, R., Chengalur, J., Ghosh, S., Ishwara-Chandra, C., *et al.* (2017). The upgraded GMRT: opening new windows on the radio Universe. *Current Science*, pages 707–714.

Hallman, E. J. and Markevitch, M. (2004). *Chandra* observation of the merging cluster A168: a late stage in the evolution of a cold front. *The Astrophysical Journal Letters*, 610(2):L81.

Hamaker, J., Bregman, J., and Sault, R. (1996). Understanding radio polarimetry. I. Mathematical foundations. *Astronomy and Astrophysics Supplement Series*, 117(1):137–147.

Han, J. (2017). Observing interstellar and intergalactic magnetic fields. *Annual Review of Astronomy and Astrophysics*, 55(1):111–157.

Hardcastle, M. (2013). Synchrotron and inverse-Compton emission from radio galaxies with non-uniform magnetic field and electron distributions. *Monthly Notices of the Royal Astronomical Society*, 433(4):3364–3372.

Hardcastle, M. and Croston, J. (2010). Searching for the inverse-Compton emission from bright cluster-centre radio galaxies. *Monthly Notices of the Royal Astronomical Society*, 404(4):2018–2027.

Hardcastle, M. and Croston, J. (2020). Radio galaxies and feedback from AGN jets. *New Astronomy Reviews*, 88:101539.

Hardcastle, M. J. and Sakelliou, I. (2004). Jet termination in wide-angle tail radio sources. *Monthly Notices of the Royal Astronomical Society*, 349(2):560–575.

Hardcastle, M. J., Sakelliou, I., and Worrall, D. (2005). A *Chandra* and *XMM-Newton* study of the wide-angle tail radio galaxy 3C 465. *Monthly Notices of the Royal Astronomical Society*, 359(3):1007–1021.

Harwood, J. J., Hardcastle, M. J., and Croston, J. H. (2015). Spectral ageing in the lobes of cluster-centre FR II radio galaxies. *Monthly Notices of the Royal Astronomical Society*, 454(4):3403–3422.

Harwood, J. J., Hardcastle, M. J., Croston, J. H., and Goodger, J. L. (2013). Spectral ageing in the lobes of FR-II radio galaxies: new methods of analysis for broad-band radio data. *Monthly Notices of the Royal Astronomical Society*, 435(4):3353–3375.

Helmholtz (1868). XLIII. On discontinuous movements of fluids. *The London, Edinburgh, and Dublin Philosophical Magazine and Journal of Science*, 36(244):337–346.

Henriksen, M., Donnelly, R. H., and Davis, D. S. (2000). Reconstructing the merger history of the A3266 galaxy cluster. *The Astrophysical Journal*, 529(2):692.

Henriksen, M. J. and Tittley, E. R. (2002). *Chandra* observations of the A3266 galaxy cluster merger. *The Astrophysical Journal*, 577(2):701.

Heywood, I., Jarvis, M., Hale, C., Whittam, I., Bester, H., Hugo, B., Kenyon, J., Prescott, M., Smirnov, O., Tasse, C., *et al.* (2022). MIGHTEE: total intensity radio continuum imaging and the COSMOS/XMM-LSS Early Science fields. *Monthly Notices of the Royal Astronomical Society*, 509(2):2150–2168.

Högbom, J. (1974). Aperture synthesis with a non-regular distribution of interferometer baselines. *Astronomy and Astrophysics Supplement Series*, 15:417.

Hong, S. E., Ryu, D., Kang, H., and Cen, R. (2014). Shock waves and cosmic ray acceleration in the outskirts of galaxy clusters. *The Astrophysical Journal*, 785(2):133.

Hubble, E. (1926). Extragalactic nebulae. *The Astrophysical Journal*, 64:321–369.

Hugo, B. V., Perkins, S., Merry, B., Mauch, T., and Smirnov, O. M. (2022). Tricolour: an optimized SumThreshold flagger for MeerKAT. *arXiv preprint arXiv:2206.09179*.

Hutschenreuter, S., Dorn, S., Jasche, J., Vazza, F., Paoletti, D., Lavaux, G., and Enßlin, T. A. (2018). The primordial magnetic field in our cosmic backyard. *Classical and Quantum Gravity*, 35(15):154001.

Jaffe, W. and Perola, G. (1973). Dynamical models of tailed radio sources in clusters of galaxies. *Astronomy & Astrophysics*, 26:423.

Jansen, F., Lumb, D., Altieri, B., Clavel, J., Ehle, M., Erd, C., Gabriel, C., Guainazzi, M., Gondoin, P., Much, R., *et al.* (2001). *XMM-Newton* observatory–I. The spacecraft and operations. *Astronomy & Astrophysics*, 365(1):L1–L6.

Jetha, N. N., Sakelliou, I., Hardcastle, M. J., Ponman, T. J., and Stevens, I. R. (2005). Interactions of radio galaxies and the intracluster medium in Abell 160 and Abell 2462. *Monthly Notices of the Royal Astronomical Society*, 358(4):1394–1404.

Jonas, J. and the MeerKAT Team (2016). The MeerKAT radio telescope. *MeerKAT Science: On the Pathway to the SKA*, page 1.

Jones, R. C. (1941). A new calculus for the treatment of optical systems I. Description and discussion of the calculus. *Josa*, 31(7):488–493.

Józsa, G. I., White, S. V., Thorat, K., Smirnov, O. M., Serra, P., Ramatsoku, M., Ramaila, A. J., Perkins, S. J., Molnár, D. C., Makhathini, S., *et al.* (2020). CARACal: Containerized automated radio astronomy calibration pipeline. Astrophysics Source Code Library, record ascl:2006.014.

Kaastra, J. and Bleeker, J. (2016). Optimal binning of X-ray spectra and response matrix design. *Astronomy & Astrophysics*, 587:A151.

Kalberla, P. M., Burton, W., Hartmann, D., Arnal, E. M., Bajaja, E., Morras, R., and Pöppel, W. G. (2005). The Leiden/Argentine/Bonn (LAB) survey of galactic HI-final data release of the combined LDS and IAR surveys with improved stray-radiation corrections. *Astronomy & Astrophysics*, 440(2):775–782.

Kale, R., Dwarakanath, K., Bagchi, J., and Paul, S. (2012). Spectral and polarization study of the double relics in Abell 3376 using the Giant Metrewave Radio Telescope and the Very Large Array. *Monthly Notices of the Royal Astronomical Society*, 426(2):1204–1211.

Kardashev, N. S. (1962). Nonstationarity of spectra of young sources of nonthermal radio emission. *Soviet Astronomy*, 6:317.

Kempner, J. C., Blanton, E. L., Clarke, T. E., Enßlin, T. A., Johnston-Hollitt, M., and Rudnick, L. (2004). Conference note: a taxonomy of extended radio sources in clusters of galaxies. In *The riddle of cooling flows in galaxies and clusters of galaxies.*

Kenyon, J., Smirnov, O., Grobler, T., and Perkins, S. (2018). CUBICAL–fast radio interferometric calibration suite exploiting complex optimization. *Monthly Notices of the Royal Astronomical Society*, 478(2):2399–2415.

Khachikian, E. Y. and Weedman, D. W. (1974). An atlas of Seyfert galaxies. *Astrophysical Journal*, 192:581–589.

King, I. (1962). The structure of star clusters. I. An empirical density law. *Astronomical Journal*, 67:471.

King, I. R. (1966). The structure of star clusters. III. Some simple dynamical models. *Astronomical Journal*, 71:64.

Knowles, K., Cotton, W., Rudnick, L., Camilo, F., Goedhart, S., Deane, R., Ramatsoku, M., Bietenholz, M., Brüggen, M., Button, C., *et al.* (2022). The MeerKAT Galaxy Cluster Legacy Survey: I. Survey overview and highlights. *Astronomy & Astrophysics*, 657:A56.

Komissarov, S. and Gubanov, A. (1994). Relic radio galaxies: evolution of synchrotron spectrum. *Astronomy & Astrophysics*, 285:27–43.

Komossa, S., Voges, W., Xu, D., Mathur, S., Adorf, H.-M., Lemson, G., Duschl, W. J., and Grupe, D. (2006). Radio-loud narrow-line type 1 quasars. *The Astronomical Journal*, 132(2):531.

Koulouridis, E., Clerc, N., Sadibekova, T., Chira, M., Drigga, E., Faccioli, L., Le Fèvre, J., Garrel, C., Gaynullina, E., Gkini, A., *et al.* (2021). The X-CLASS survey: A catalogue of 1646 X-ray-selected galaxy clusters up to $z \sim 1.5$. *Astronomy & Astrophysics*, 652:A12.

Kovalev, Y. Y., Pushkarev, A. B., Nokhrina, E. E., Plavin, A. V., Beskin, V. S., Chernoglazov, A. V., Lister, M. L., and Savolainen, T. (2020). A transition from parabolic to conical shape as a common effect in nearby AGN jets. *Monthly Notices of the Royal Astronomical Society*, 495(4):3576–3591.

Kuntz, K. and Snowden, S. (2008). The EPIC-MOS particle-induced background spectra. *Astronomy & Astrophysics*, 478(2):575–596.

Laing, R. and Bridle, A. (2014). Kinematics of kiloparsec-scale jets. *Proceedings of the International Astronomical Union*, 10(S313):108–115.

Laing, R., Guidetti, D., Bridle, A., Parma, P., and Bondi, M. (2011). Deep imaging of Fanaroff–Riley Class I radio galaxies with lobes. *Monthly Notices of the Royal Astronomical Society*, 417(4):2789–2808.

Lakhchaura, K., Singh, K., Saikia, D., and Hunstead, R. (2011). Intracluster medium of the merging cluster A3395. *The Astrophysical Journal*, 743(1):78.

Lapenta, G. and Kronberg, P. (2005). Simulation of astrophysical jets: collimation and expansion into radio lobes. *The Astrophysical Journal*, 625(1):37.

Large, M., Mills, B., Little, A., Crawford, D., and Sutton, J. (1981). The Molonglo reference catalogue of radio sources. *Monthly Notices of the Royal Astronomical Society*, 194(3):693–704.

Longair, M. S. (2010). *High energy astrophysics*. Cambridge University Press.

Lumb, D., Warwick, R., Page, M., and De Luca, A. (2002). X-ray background measurements with *XMM-Newton* EPIC. *Astronomy & Astrophysics*, 389(1):93–105.

Lyutikov, M. (2006). Magnetic draping of merging cores and radio bubbles in clusters of galaxies. *Monthly Notices of the Royal Astronomical Society*, 373(1):73–78.

Maccagni, D., Tarenghi, M., Cooke, B., Maccacaro, T., Pye, J., Ricketts, M., and Chincarini, G. (1978). An X-ray and optical study of seven clusters of galaxies. *Astronomy & Astrophysics*, 62:127–133.

Machado, R. E. and Lima Neto, G. B. (2013). Simulations of the merging galaxy cluster Abell 3376. *Monthly Notices of the Royal Astronomical Society*, 430(4):3249–3260.

Machalski, J., Kozieł-Wierzbowska, D., Jamrozy, M., and Saikia, D. (2008). J1420–0545: the radio galaxy larger than 3C 236. *The Astrophysical Journal*, 679(1):149.

Makhathini, S. (2018). *Advanced radio interferometric simulation and data reduction techniques*. PhD thesis, Rhodes University, Drosty Rd, Grahamstown, 6139, Eastern Cape, South Africa. Available via `http://hdl.handle.net/10962/57348`.

Markevitch, M., Forman, W. R., Sarazin, C. L., and Vikhlinin, A. (1998). The temperature structure of 30 nearby clusters observed with *ASCA*: similarity of temperature profiles. *The Astrophysical Journal*, 503(1):77.

Markevitch, M., Gonzalez, A., David, L., Vikhlinin, A., Murray, S., Forman, W., Jones, C., and Tucker, W. (2002). A textbook example of a bow shock in the merging galaxy cluster 1E 0657–56. *The Astrophysical Journal*, 567(1):L27.

Markevitch, M., Gonzalez, A. H., Clowe, D., Vikhlinin, A., Forman, W., Jones, C., Murray, S., and Tucker, W. (2004). Direct constraints on the dark matter self-interaction cross section from the merging galaxy cluster 1E 0657–56. *The Astrophysical Journal*, 606(2):819.

Markevitch, M., Ponman, T., Nulsen, P., Bautz, M., Burke, D., David, L., Davis, D., Donnelly, R., Forman, W., Jones, C. c., *et al.* (2000). *Chandra* observation of Abell 2142: survival of dense subcluster cores in a merger. *The Astrophysical Journal*, 541(2):542.

Markevitch, M., Sarazin, C. L., and Vikhlinin, A. (1999). Physics of the merging clusters Cygnus A, A3667, and A2065. *The Astrophysical Journal*, 521(2):526.

Markevitch, M. and Vikhlinin, A. (2007). Shocks and cold fronts in galaxy clusters. *Physics Reports*, 443(1):1–53.

Markevitch, M., Vikhlinin, A., and Mazzotta, P. (2001). Nonhydrostatic gas in the core of the relaxed galaxy cluster A1795. *The Astrophysical Journal*, 562(2):L153.

Massaro, F., Álvarez-Crespo, N., Capetti, A., Baldi, R. D., Pillitteri, I., Campana, R., and Paggi, A. (2019). Deciphering the large-scale environment of radio galaxies in the local universe: where are they born? Where do they grow? Where do they die? *The Astrophysical Journal Supplement Series*, 240(2):20.

Massaro, F., White, S., García-Pérez, A., Jimenez-Gallardo, A., Capetti, A., Cheung, C., Forman, W., Mazzucchelli, C., Paggi, A., Nesvadba, N., *et al.* (2023). Powerful radio sources in the southern sky. I. Optical identifications. *The Astrophysical Journal Supplement Series*, 265(2):32.

Matthews, T. A., Morgan, W. W., and Schmidt, M. (1964). A discussion of galaxies identified with radio sources. *Astrophysical Journal*, 140:35.

Mauch, T., Cotton, W., Condon, J., Matthews, A., Abbott, T., Adam, R., Aldera, M., Asad, K., Bauermeister, E., Bennett, T., *et al.* (2020). The 1.28 GHz Meerkat DEEP2 image. *The Astrophysical Journal*, 888(2):61.

Mauch, T., Murphy, T., Buttery, H., Curran, J., Hunstead, R., Piestrzynski, B., Robertson, J., and Sadler, E. (2003). SUMSS: a wide-field radio imaging survey of the southern sky–II. The source catalogue. *Monthly Notices of the Royal Astronomical Society*, 342(4):1117–1130.

McNamara, B. and Nulsen, P. (2012). Mechanical feedback from active galactic nuclei in galaxies, groups and clusters. *New Journal of Physics*, 14(5):055023.

Meisenheimer, K., Roser, H.-J., Hiltner, P., Yates, M., Longair, M., Chini, R., and Perley, R. (1989). The synchrotron spectra of radio hot spots. *Astronomy & Astrophysics*, 219:63–86.

Mendygral, P., Jones, T., and Dolag, K. (2012). MHD simulations of active galactic nucleus jets in a dynamic galaxy cluster medium. *The Astrophysical Journal*, 750(2):166.

Mernier, F., Cucchetti, E., Tornatore, L., Biffi, V., Pointecouteau, E., Clerc, N., Peille, P., Rasia, E., Barret, D., Borgani, S., *et al.* (2020). Constraining the origin and models of chemical enrichment in galaxy clusters using the *Athena* X-IFU. *Astronomy & Astrophysics*, 642:A90.

Mewe, R., Kaastra, J., and Liedahl, D. (1995). Update of MEKA: MEKAL. *Legacy*, 6:16.

Mingo, B., Hardcastle, M., Croston, J., Dicken, D., Evans, D., Morganti, R., and Tadhunter, C. (2014). An X-ray survey of the 2 Jy sample–I. Is there an accretion mode dichotomy in radio-loud AGN? *Monthly Notices of the Royal Astronomical Society*, 440(1):269–297.

Mingo, B., Hardcastle, M., Ineson, J., Mahatma, V., Croston, J., Dicken, D., Evans, D., Morganti, R., and Tadhunter, C. (2017). An X-ray survey of the 2 Jy sample–II. X-ray emission from extended structures. *Monthly Notices of the Royal Astronomical Society*, 470(3):2762–2779.

Missaglia, V., Massaro, F., Capetti, A., Paolillo, M., Kraft, R., Baldi, R. D., and Paggi, A. (2019). WATCAT: a tale of wide-angle tailed radio galaxies. *Astronomy & Astrophysics*, 626:A8.

Mohan, N. and Rafferty, D. (2015). PyBDSF: Python Blob Detection and Source Finder. Astrophysics Source Code Library, record ascl:1502.007.

Mohr, J. J., Fabricant, D. G., and Geller, M. J. (1993). An X-ray method for detecting substructure in galaxy clusters–application to Perseus, A2256, Centaurus, Coma, and Sersic 40/6. *Astrophysical Journal*, 413:492–505.

Molendi, S. and Pizzolato, F. (2001). Is the gas in cooling flows multiphase? *The Astrophysical Journal*, 560(1):194.

Monteiro-Oliveira, R., Lima Neto, G., Cypriano, E. S., Machado, R. E., Capelato, H. V., Laganá, T. F., Durret, F., and Bagchi, J. (2017). Weak lensing and spectroscopic analysis of the nearby dissociative merging galaxy cluster Abell 3376. *Monthly Notices of the Royal Astronomical Society*, 468(4):4566–4578.

Moretti, A., Gullieuszik, M., Poggianti, B., Paccagnella, A., Couch, W. J., Vulcani, B., Bettoni, D., Fritz, J., Cava, A., Fasano, G., *et al.* (2017). OmegaWINGS: spectroscopy in the outskirts of local clusters of galaxies. *Astronomy & Astrophysics*, 599:A81.

Morganoshell (2016). MeerKAT Radio Telescope. `https://commons.wikimedia.org/wiki/File:MeerKAT_Radio_Telescope.jpg`. Accessed 2023/05/03.

Murgia, M., Parma, P., Mack, K.-H., De Ruiter, H., Fanti, R., Govoni, F., Tarchi, A., Giacintucci, S., and Markevitch, M. (2011). Dying radio galaxies in clusters. *Astronomy & Astrophysics*, 526:A148.

Murphy, T. (1999). Diffuse radio sources in clusters of galaxies. *Thesis*.

Noordam, J. E. and Smirnov, O. M. (2010). The MeqTrees software system and its use for third-generation calibration of radio interferometers. *Astronomy & Astrophysics*, 524:A61.

O'Dea, C. P. and Owen, F. (1985). The global properties of a representative sample of 51 narrow-angle-tail radio sources in the directions of Abell clusters. *Astronomical Journal*, 90:954–972.

O'Donoghue, A. A., Eilek, J. A., and Owen, F. N. (1993). Flow dynamics and bending of wide-angle tailed radio sources. *Astrophysical Journal*, 408:428–445.

Offringa, A., McKinley, B., Hurley-Walker, N., Briggs, F., Wayth, R., Kaplan, D., Bell, M., Feng, L., Neben, A., Hughes, J., *et al.* (2014). WSCLEAN: an implementation of a fast, generic wide-field imager for radio astronomy. *Monthly Notices of the Royal Astronomical Society*, 444(1):606–619.

Oozeer, N., Rudnick, L., Bietenholz, M. F., Venturi, T., Knowles, K., Kolokythas, K., and Mhlahlo, N. (2021). Discovery of rare dying radio galaxies using MeerKAT. *Galaxies*, 9(4):102.

Otani, C., Brinkmann, W., Böhringer, H., Reid, A., and Siebert, J. (1998). *ASCA/ROSAT* observations of the radio source MRC 0625-536. *Astronomy & Astrophysics*, 339:693–700.

Owen, F. N., Ledlow, M. J., and Keel, W. C. (1995). Optical spectroscopy of radio galaxies in Abell clusters. 1: Redshifts and emission-line properties. *The Astronomical Journal*, 109:14–25.

Owen, F. N. and Rudnick, L. (1976). Radio sources with wide-angle tails in Abell clusters of galaxies. *Astrophysical Journal*, 205:L1–L4.

O'Dea, C. P. and Baum, S. A. (2023). Wide-angle-tail (WAT) radio sources. *Galaxies*, 11(3):67.

Pacholczyk, A. G. and Roberts, J. (1971). Radio astrophysics: nonthermal processes in galactic and extragalactic sources. *Physics Today*, 24(9):57–58.

Padovani, P. (2011). The microjansky and nanojansky radio sky: source population and multi-wavelength properties. *Monthly Notices of the Royal Astronomical Society*, 411(3):1547–1561.

Padovani, P. (2017). On the two main classes of active galactic nuclei. *Nature Astronomy*, 1(8):0194.

Padovani, P., Alexander, D., Assef, R., De Marco, B., Giommi, P., Hickox, R., Richards, G., Smolčić, V., Hatziminaoglou, E., Mainieri, V., *et al.* (2017). Active galactic nuclei: what's in a name? *The Astronomy and Astrophysics Review*, 25:1–91.

Pandge, M., Sebastian, B., Seth, R., and Raychaudhury, S. (2021). A detailed study of X-ray cavities in the intracluster environment of the cool core cluster Abell 3017. *Monthly Notices of the Royal Astronomical Society*, 504(2):1644–1656.

Park, J., Hada, K., Nakamura, M., Asada, K., Zhao, G., and Kino, M. (2021). Jet collimation and acceleration in the giant radio galaxy NGC 315. *The Astrophysical Journal*, 909(1):76.

Paturel, G., Petit, C., Prugniel, P., Theureau, G., Rousseau, J., Brouty, M., Dubois, P., and Cambrésy, L. (2003). HYPERLEDA-I. Identification and designation of galaxies. *Astronomy & Astrophysics*, 412(1):45–55.

Perley, R., Chandler, C., Butler, B., and Wrobel, J. (2011). The Expanded Very Large Array: a new telescope for new science. *The Astrophysical Journal Letters*, 739(1):L1.

Peterson, J., Kahn, S., Paerels, F., Kaastra, J., Tamura, T., Bleeker, J., Ferrigno, C., and Jernigan, J. (2003). High-resolution X-ray spectroscopic constraints on cooling-flow models for clusters of galaxies. *The Astrophysical Journal*, 590(1):207.

Peterson, J. R. and Fabian, A. C. (2006). X-ray spectroscopy of cooling clusters. *Physics reports*, 427(1):1–39.

Petropoulou, M., Sironi, L., Spitkovsky, A., and Giannios, D. (2019). Relativistic magnetic reconnection in electron–positron–proton plasmas: implications for jets of active galactic nuclei. *The Astrophysical Journal*, 880(1):37.

Petrov, L., de Witt, A., Sadler, E. M., Phillips, C., and Horiuchi, S. (2019). The Second LBA Calibrator Survey of southern compact extragalactic radio sources–LCS2. *Monthly Notices of the Royal Astronomical Society*, 485(1):88–101.

Planck Collaboration (2015). Planck 2013 results. XXXII. The updated Planck catalogue of Sunyaev-Zeldovich sources. *Astronomy & Astrophysics*, 581:A14.

Planck Collaboration (2016). Planck 2015 results. XXVII. The second Planck catalogue of Sunyaev-Zeldovich sources. *Astronomy & Astrophysics*, 594:A27.

Pratt, G., Arnaud, M., Biviano, A., Eckert, D., Ettori, S., Nagai, D., Okabe, N., and Reiprich, T. (2019). The galaxy cluster mass scale and its impact on cosmological constraints from the cluster population. *Space Science Reviews*, 215:1–82.

Quici, B., Hurley-Walker, N., Seymour, N., Turner, R. J., Shabala, S. S., Huynh, M., Andernach, H., Kapińska, A. D., Collier, J. D., Johnston-Hollitt, M., *et al.* (2021). Remnant radio galaxies

discovered in a multi-frequency survey. *Publications of the Astronomical Society of Australia*, 38:e008.

Quintana, H. and Melnick, J. (1982). The correlation between X-ray luminosity and velocity dispersion in clusters of galaxies. *Astronomical Journal*, 87:972–979.

Quintana, H., Ramirez, A., and Way, M. (1996). Dynamics of the cluster of galaxies A3266 (Sersic 40/60). I. Spectroscopic data. *Astronomical Journal*, 112:36.

Randall, S., Clarke, T., Nulsen, P., Owers, M., Sarazin, C., Forman, W., and Murray, S. (2010). Radio and deep *Chandra* observations of the disturbed cool core cluster Abell 133. *The Astrophysical Journal*, 722(1):825.

Reiprich, T. H., Basu, K., Ettori, S., Israel, H., Lovisari, L., Molendi, S., Pointecouteau, E., and Roncarelli, M. (2013). Outskirts of galaxy clusters. *Space Science Reviews*, 177:195–245.

Reiprich, T. H. and Boehringer, H. (2002). The mass function of an X-ray flux-limited sample of galaxy clusters. *The Astrophysical Journal*, 567(2):716.

Reiprich, T. H., Veronica, A., Pacaud, F., Ramos-Ceja, M. E., Ota, N., Sanders, J., Kara, M., Erben, T., Klein, M., Erler, J., *et al.* (2021). The Abell 3391/95 galaxy cluster system-A 15 Mpc intergalactic medium emission filament, a warm gas bridge, infalling matter clumps, and (re-) accelerated plasma discovered by combining *SRG*/eROSITA data with ASKAP/EMU and DECam data. *Astronomy & Astrophysics*, 647:A2.

Ricker, P. M. and Sarazin, C. L. (2001). Off-axis cluster mergers: effects of a strongly peaked dark matter profile. *The Astrophysical Journal*, 561(2):621.

Riseley, C., Bonnassieux, E., Vernstrom, T., Galvin, T., Chokshi, A., Botteon, A., Rajpurohit, K., Duchesne, S., Bonafede, A., Rudnick, L., *et al.* (2022). Radio fossils, relics, and haloes in Abell 3266: cluster archaeology with ASKAP-EMU and the ATCA. *Monthly Notices of the Royal Astronomical Society*, 515(2):1871–1896.

Rizza, E., Loken, C., Bliton, M., Roettiger, K., Burns, J. O., and Owen, F. N. (2000). X-ray and radio interactions in the cores of cooling flow clusters. *The Astronomical Journal*, 119(1):21.

Roediger, E., Kraft, R., Nulsen, P., Forman, W., Machacek, M., Randall, S., Jones, C., Churazov, E., and Kokotanekova, R. (2015). Stripped elliptical galaxies as probes of ICM physics. I. Tails, wakes, and flow patterns in and around stripped ellipticals. *The Astrophysical Journal*, 806(1):103.

Roettiger, K. and Flores, R. (2000). A prediction of observable rotation in the intracluster medium of Abell 3266. *The Astrophysical Journal*, 538(1):92.

Rosselli, D., Marulli, F., Veropalumbo, A., Cimatti, A., and Moscardini, L. (2023). Testing general relativity: new measurements of gravitational redshift in galaxy clusters. *Astronomy & Astrophysics*, 669:A29.

Rudnick, L., Cotton, W., Knowles, K., and Kolokythas, K. (2021). One source, two source(s): ribs and tethers. *Galaxies*, 9(4):81.

Rybicki, G. B. and Lightman, A. P. (1991). *Radiative processes in astrophysics*. John Wiley & Sons.

Saikia, D. (2022). Jets in radio galaxies and quasars: an observational perspective. *Journal of Astrophysics and Astronomy*, 43(2):97.

Saikia, D. and Jamrozy, M. (2010). Recurrent activity in active galactic nuclei. *arXiv preprint arXiv:1002.1841*.

Sand, D. J., Treu, T., Smith, G. P., and Ellis, R. S. (2004). The dark matter distribution in the central regions of galaxy clusters: implications for cold dark matter. *The Astrophysical Journal*, 604(1):88.

Sanders, J., Biffi, V., Brüggen, M., Bulbul, E., Dennerl, K., Dolag, K., Erben, T., Freyberg, M., Gatuzz, E., Ghirardini, V., *et al.* (2022). Studying the merging cluster Abell 3266 with eROSITA. *Astronomy & Astrophysics*, 661:A36.

Sanders, J., Fabian, A., Russell, H., Walker, S., and Blundell, K. (2016a). Detecting edges in the X-ray surface brightness of galaxy clusters. *Monthly Notices of the Royal Astronomical Society*, 460(2):1898–1911.

Sanders, J., Fabian, A., Taylor, G., Russell, H., Blundell, K., Canning, R., Hlavacek-Larrondo, J., Walker, S., and Grimes, C. (2016b). A very deep *Chandra* view of metals, sloshing and feedback in the Centaurus cluster of galaxies. *Monthly Notices of the Royal Astronomical Society*, 457(1):82–109.

Sanders, J. S. (2006). Contour binning: a new technique for spatially resolved X-ray spectroscopy applied to Cassiopeia A. *Monthly Notices of the Royal Astronomical Society*, 371(2):829–842.

Sarkar, A., Randall, S., Su, Y., Alvarez, G. E., Sarazin, C. L., Jones, C., Blanton, E., Nulsen, P., Chakraborty, P., Bulbul, E., *et al.* (2023). Gas sloshing and cold fronts in pre-merging galaxy cluster A98. *The Astrophysical Journal*, 944(2):132.

Sasmal, T. K., Bera, S., Pal, S., and Mondal, S. (2022). A new catalog of head–tail radio galaxies from the VLA FIRST Survey. *The Astrophysical Journal Supplement Series*, 259(2):31.

Sauvageot, J.-L., Belsole, E., and Pratt, G. W. (2005). The late merging phase of a galaxy cluster: *XMM* EPIC observations of A 3266. *Astronomy & Astrophysics*, 444(3):673–683.

Scheuer, P. (1974). Models of extragalactic radio sources with a continuous energy supply from a central object. *Monthly Notices of the Royal Astronomical Society*, 166(3):513–528.

Schneider, P. (2014). *Extragalactic astronomy and cosmology: an introduction*. Springer.

Schoenmakers, A. P., De Bruyn, A., Röttgering, H., Van Der Laan, H., and Kaiser, C. (2000). Radio galaxies with a 'double-double morphology'-I. Analysis of the radio properties and evidence for interrupted activity in active galactic nuclei. *Monthly Notices of the Royal Astronomical Society*, 315(2):371–380.

Sheardown, A., Fish, T. M., Roediger, E., Hunt, M., ZuHone, J., Su, Y., Kraft, R. P., Nulsen, P., Churazov, E., Forman, W., *et al.* (2019). A new class of X-ray tails of early-type galaxies and subclusters in galaxy clusters: slingshot tails versus ram pressure stripped tails. *The Astrophysical Journal*, 874(2):112.

Shulevski, A., Morganti, R., Harwood, J., Barthel, P., Jamrozy, M., Brienza, M., Brunetti, G., Röttgering, H., Murgia, M., White, G., *et al.* (2017). Radiative age mapping of the remnant radio galaxy B2 0924+ 30: the LOFAR perspective. *Astronomy & Astrophysics*, 600:A65.

Skrutskie, M., Cutri, R., Stiening, R., Weinberg, M., Schneider, S., Carpenter, J., Beichman, C., Capps, R., Chester, T., Elias, J., *et al.* (2006). The Two Micron All Sky Survey (2MASS). *The Astronomical Journal*, 131(2):1163.

Slee, O., Roy, A., and Andernach, H. (1996). A VLA survey of rich clusters of galaxies III. The weaker sources: maps and identifications. *Australian Journal of Physics*, 49(5):977–1062.

Slee, O., Roy, A., Murgia, M., Andernach, H., and Ehle, M. (2001). Four extreme relic radio sources in clusters of galaxies. *The Astronomical Journal*, 122(3):1172.

Smirnov, O. and Tasse, C. (2015). Radio interferometric gain calibration as a complex optimization problem. *Monthly Notices of the Royal Astronomical Society*, 449(3):2668–2684.

Smirnov, O. M. (2011). Revisiting the radio interferometer measurement equation–I. A full-sky Jones formalism. *Astronomy & Astrophysics*, 527:A106.

Smith, R. J., Hudson, M. J., Nelan, J. E., Moore, S. A., Quinney, S. J., Wegner, G. A., Lucey, J. R., Davies, R. L., Malecki, J. J., Schade, D., *et al.* (2004). NOAO Fundamental Plane Survey. I. Survey design, redshifts, and velocity dispersion data. *The Astronomical Journal*, 128(4):1558.

Smith, R. K., Brickhouse, N. S., Liedahl, D. A., and Raymond, J. C. (2001). Collisional plasma models with APEC/APED: emission-line diagnostics of hydrogen-like and helium-like ions. *The Astrophysical Journal*, 556(2):L91.

Smolčić, V., Novak, M., Bondi, M., Ciliegi, P., Mooley, K., Schinnerer, E., Zamorani, G., Navarrete, F., Bourke, S., Karim, A., *et al.* (2017). The VLA-COSMOS 3 GHz Large Project: continuum data and source catalog release. *Astronomy & Astrophysics*, 602:A1.

Snowden, S. and Kuntz, K. (2014). Cookbook for analysis procedures for *XMM-Newton* EPIC observations of extended objects and the diffuse background.

Snowden, S. and Kuntz, K. (2023). Cookbook for analysis procedures for *XMM-Newton* EPIC observations of extended objects and the diffuse background. Updated for SAS Version 21.0.

Snowden, S., Mushotzky, R., Kuntz, K., and Davis, D. S. (2008). A catalog of galaxy clusters observed by *XMM-Newton*. *Astronomy & Astrophysics*, 478(2):615–658.

Strüder, L., Briel, U., Dennerl, K., Hartmann, R., Kendziorra, E., Meidinger, N., Pfeffermann, E., Reppin, C., Aschenbach, B., Bornemann, W., *et al.* (2001). The European photon imaging camera on *XMM-Newton*: the pn-CCD camera. *Astronomy & Astrophysics*, 365(1):L18–L26.

Subrahmanyan, R., Saripalli, L., and Hunstead, R. W. (1996). Morphologies in megaparsec-size powerful radio galaxies. *Monthly Notices of the Royal Astronomical Society*, 279(1):257–274.

Sugawara, Y., Takizawa, M., Itahana, M., Akamatsu, H., Fujita, Y., Ohashi, T., and Ishisaki, Y. (2017). *Suzaku* observations of the outskirts of the galaxy cluster Abell 3395, including a filament toward Abell 3391. *Publications of the Astronomical Society of Japan*, 69(6):93.

Tasse, C. (2014). Applying Wirtinger derivatives to the radio interferometry calibration problem. *arXiv preprint arXiv:1410.8706*.

Tasse, C. (2023). killMS: direction-dependent radio interferometric calibration package. Astrophysics Source Code Library, record ascl:2305.005.

Tasse, C., Hugo, B., Mirmont, M., Smirnov, O., Atemkeng, M., Bester, L., Hardcastle, M., Lakhoo, R., Perkins, S., and Shimwell, T. (2018). Faceting for direction-dependent spectral deconvolution. *Astronomy & Astrophysics*, 611:A87.

Tasse, C., Hugo, B., Mirmont, M., Smirnov, O., Atemkeng, M., Bester, L., Hardcastle, M., Lakhoo, R., Perkins, S., and Shimwell, T. (2023). DDFacet: facet-based radio imaging package. Astrophysics Source Code Library, record ascl:2305.008.

Taylor, A. and Legodi, L. (2021). Data products for polarization of MeerKAT calibrators. *South African Radio Astronomy Observatory*.

Taylor, M. (2011). TOPCAT: tool for operations on catalogues and tables. Astrophysics Source Code Library, record ascl:1101.010.

Thompson, A. R., Moran, J. M., and Swenson, G. W. (2017). *Interferometry and synthesis in radio astronomy*. Springer Nature.

Thomson, W [Lord Kelvin] (1871). XLVI. Hydrokinetic solutions and observations. *The London, Edinburgh, and Dublin Philosophical Magazine and Journal of Science*, 42(281):362–377.

Tittley, E. R. and Henriksen, M. (2001). A filament between galaxy clusters A3391 and A3395. *The Astrophysical Journal*, 563(2):673.

Tribble, P. C. (1993). Radio spectral ageing in a random magnetic field. *Monthly Notices of the Royal Astronomical Society*, 261(1):57–62.

Trümper, J. E. and Hasinger, G. (2008). *The Universe in X-rays*. Springer Science & Business Media.

Tümer, A., Wik, D. R., Gaspari, M., Akamatsu, H., Westergaard, N. J., Tombesi, F., and Ercan, E. N. (2022). The *NuSTAR*, *XMM-Newton*, and *Suzaku* view of A3395 at the intercluster filament interface. *The Astrophysical Journal*, 930(1):83.

Turner, M. J., Abbey, A., Arnaud, M., Balasini, M., Barbera, M., Belsole, E., Bennie, P., Bernard, J., Bignami, G., Boer, M., *et al.* (2001). The European photon imaging camera on *XMM-Newton*: the MOS cameras. *Astronomy & Astrophysics*, 365(1):L27–L35.

Urdampilleta, I., Akamatsu, H., Mernier, F., Kaastra, J., De Plaa, J., Ohashi, T., Ishisaki, Y., and Kawahara, H. (2018). X-ray study of the double radio relic Abell 3376 with *Suzaku*. *Astronomy & Astrophysics*, 618:A74.

Urry, C. M. and Padovani, P. (1995). Unified schemes for radio-loud active galactic nuclei. *Publications of the Astronomical Society of the Pacific*, 107(715):803.

Valdarnini, R. and Sarazin, C. (2021). A study of cool core resiliency and entropy mixing in simulations of galaxy cluster mergers. *Monthly Notices of the Royal Astronomical Society*, 504(4):5409–5436.

van Haarlem, M. P., Wise, M. W., Gunst, A., Heald, G., McKean, J. P., Hessels, J. W., de Bruyn, A. G., Nijboer, R., Swinbank, J., Fallows, R., *et al.* (2013). LOFAR: the low-frequency array. *Astronomy & Astrophysics*, 556:A2.

Van Weeren, R., de Gasperin, F., Akamatsu, H., Brüggen, M., Feretti, L., Kang, H., Stroe, A., and Zandanel, F. (2019). Diffuse radio emission from galaxy clusters. *Space Science Reviews*, 215:1–75.

Van Weeren, R., Röttgering, H., Brüggen, M., and Cohen, A. (2009). A search for steep spectrum radio relics and halos with the GMRT. *Astronomy & Astrophysics*, 508(1):75–92.

Verner, D., Ferland, G. J., Korista, K., and Yakovlev, D. (1996). Atomic data for astrophysics. II. New analytic fits for photoionization cross sections of atoms and ions. *arXiv preprint astro-ph/9601009*.

Veronica, A., Reiprich, T. H., Pacaud, F., Ota, N., Aschersleben, J., Biffi, V., Bulbul, E., Clerc, N., Dolag, K., Erben, T., *et al.* (2024). The eROSITA view of the Abell 3391/95 field–Cluster outskirts and filaments. *Astronomy & Astrophysics*, 681:A108.

Vikhlinin, A., Markevitch, M., and Murray, S. (2001a). A moving cold front in the intergalactic medium of A3667. *The Astrophysical Journal*, 551(1):160.

Vikhlinin, A., Markevitch, M., and Murray, S. (2001b). *Chandra* estimate of the magnetic field strength near the cold front in A3667. *The Astrophysical Journal*, 549(1):L47.

Vikhlinin, A., Markevitch, M., Murray, S., Jones, C., Forman, W., and Van Speybroeck, L. (2005). *Chandra* temperature profiles for a sample of nearby relaxed galaxy clusters. *The Astrophysical Journal*, 628(2):655.

Wang, S., Liu, J., Qiu, Y., Bai, Y., Yang, H., Guo, J., and Zhang, P. (2016). *Chandra* ACIS survey of X-ray point sources: the source catalog. *The Astrophysical Journal Supplement Series*, 224(2):40.

Werner, N. and Mernier, F. (2020). Hot atmospheres of galaxies, groups, and clusters of galaxies. *Reviews in Frontiers of Modern Astrophysics: From Space Debris to Cosmology*, pages 279–310.

Wilber, A. G., Dabbech, A., Jackson, A., and Wiaux, Y. (2023a). Scalable precision wide-field imaging in radio interferometry: I. uSARA validated on ASKAP data. *Monthly Notices of the Royal Astronomical Society*, 522(4):5558–5575.

Wilber, A. G., Dabbech, A., Terris, M., Jackson, A., and Wiaux, Y. (2023b). uSARA and AIRI reconstructions of selected ASKAP observations.

Willingale, R., Starling, R., Beardmore, A. P., Tanvir, N. R., and O'Brien, P. T. (2013). Calibration of X-ray absorption in our Galaxy. *Monthly Notices of the Royal Astronomical Society*, 431(1):394–404.

Wilms, J., Allen, A., and McCray, R. (2000). On the absorption of X-rays in the interstellar medium. *The Astrophysical Journal*, 542(2):914.

Wilson, T. L., Rohlfs, K., and Hüttemeister, S. (2009). *Tools of radio astronomy*, volume 5. Springer.

Wolter, H. (1952). Spiegelsysteme streifenden Einfalls als abbildende Optiken für Röntgenstrahlen. *Annalen der Physik*, 445(1-2):94–114.

Xie, C., Van Weeren, R., Lovisari, L., Andrade-Santos, F., Botteon, A., Brüggen, M., Bulbul, E., Churazov, E., Clarke, T., Forman, W., *et al.* (2020). The discovery of radio halos in the frontier fields clusters Abell S1063 and Abell 370. *Astronomy & Astrophysics*, 636:A3.

Xu, H., Li, H., Collins, D. C., Li, S., and Norman, M. L. (2010). Evolution and distribution of magnetic fields from active galactic nuclei in galaxy clusters. I. The effect of injection energy and redshift. *The Astrophysical Journal*, 725(2):2152.

Yi, K., Park, J., Nakamura, M., Hada, K., and Trippe, S. (2024). Jet collimation and acceleration in the flat spectrum radio quasar 1928+738. *Astronomy & Astrophysics*, 688:A94.

Zhang, C., Xu, H., Zhu, Z., Li, W., Hu, D., Wang, J., Gu, J., Gu, L., Zhang, Z., Liu, C., *et al.* (2016). A *Chandra* study of the image power spectra of 41 cool core and non-cool core galaxy clusters. *The Astrophysical Journal*, 823(2):116.

Zhao, H., Peacock, J. A., and Li, B. (2013). Testing gravity theories via transverse Doppler and gravitational redshifts in galaxy clusters. *Physical Review D*, 88(4):043013.

Zhu, Z., Kovács, O. E., Simionescu, A., and Werner, N. (2023). Investigating the outskirts of Abell 133 with *Suzaku* and *Chandra* observations. *Astronomy & Astrophysics*, 678:A122.

ZuHone, J., Markevitch, M., and Johnson, R. (2010). Stirring up the pot: can cooling flows in galaxy clusters be quenched by gas sloshing? *The Astrophysical Journal*, 717(2):908.

ZuHone, J. and Su, Y. (2024). The merger dynamics of the X-ray-emitting plasma in clusters of galaxies. In *Handbook of X-ray and Gamma-ray Astrophysics*, pages 5005–5048. Springer.

ZuHone, J., Zavala, J., and Vogelsberger, M. (2019). Sloshing of galaxy cluster core plasma in the presence of self-interacting dark matter. *The Astrophysical Journal*, 882(2):119.

ZuHone, J. A. and Roediger, E. (2016). Cold fronts: probes of plasma astrophysics in galaxy clusters. *Journal of Plasma Physics*, 82(3):535820301.

Zwicky, F. (1933). Die rotverschiebung von extragalaktischen nebeln. *Helvetica Physica Acta*, 6:110–127.

Appendix A

X-ray Spectra

While example spectra for each of the clusters Abell 133, Abell 3266, Abell 3376, Abell 3391, and Abell 3395 were presented in Chapter 4, this appendix provides the complete set of spectra, shown in Figures A.1 to A.5. These figures include spectra for all regions defined in Figures 4.30 to 4.34, covering all observations listed in Table 3.2. The spectra are shown for each of the three EPIC instruments where both a source spectrum and a background spectrum were successfully extracted. In all of the figures, red represents the EPIC-MOS 1 spectra, blue represents the EPIC-MOS 2 spectra, and green represents the EPIC-pn spectra. For clusters with multiple observations, the shades of these colours indicate the observation identifier, as specified in the legends.

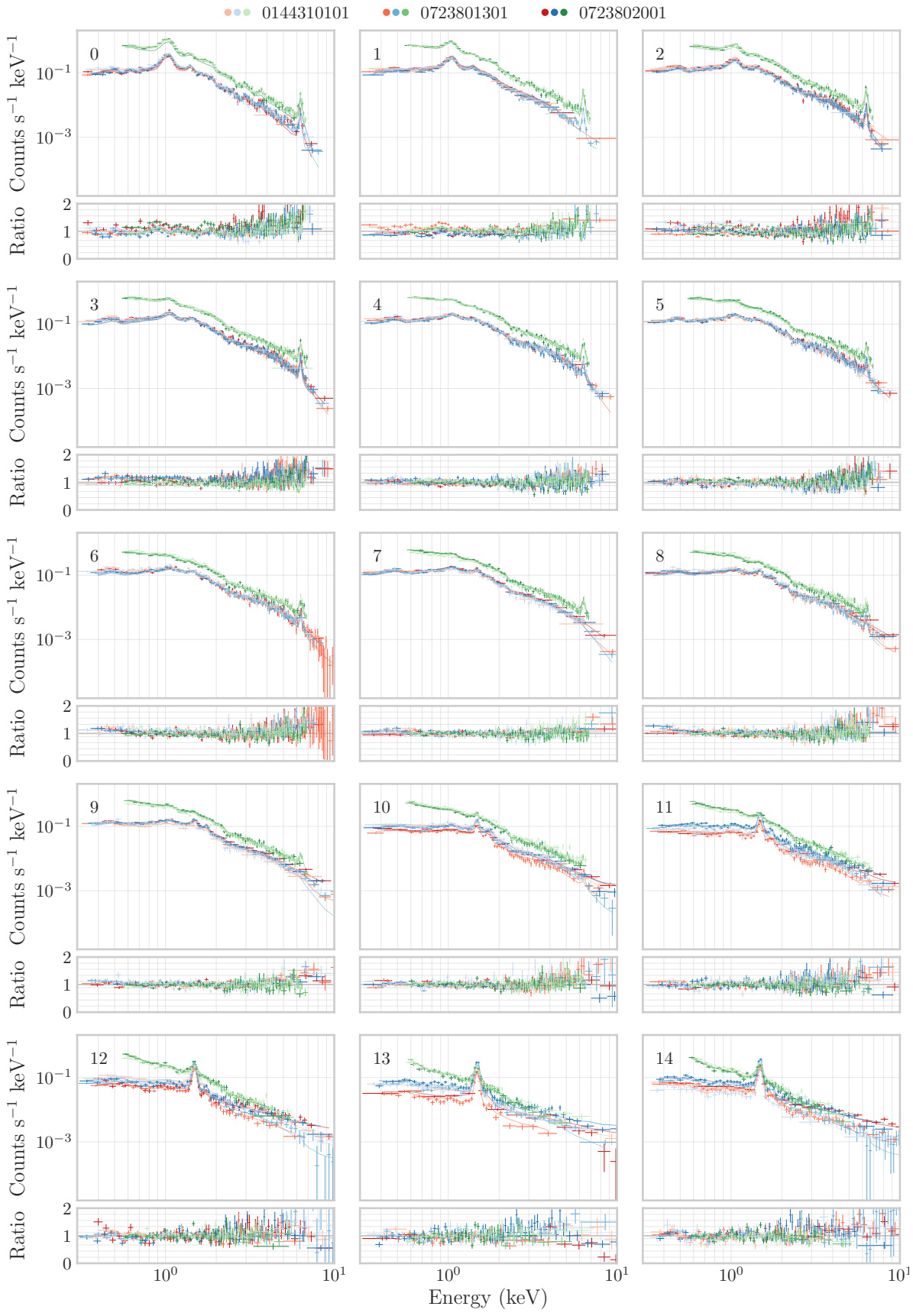

Figure A.1: Spectra of regions 0 – 14 of Abell 133. The panel below each spectrum shows the data divided by the folded model. EPIC-MOS 1, EPIC-MOS 2, and EPIC-pn spectra are coloured red, blue, and green, respectively. The reduced χ^2 for the fit is 1.95 for 7373 degrees of freedom.

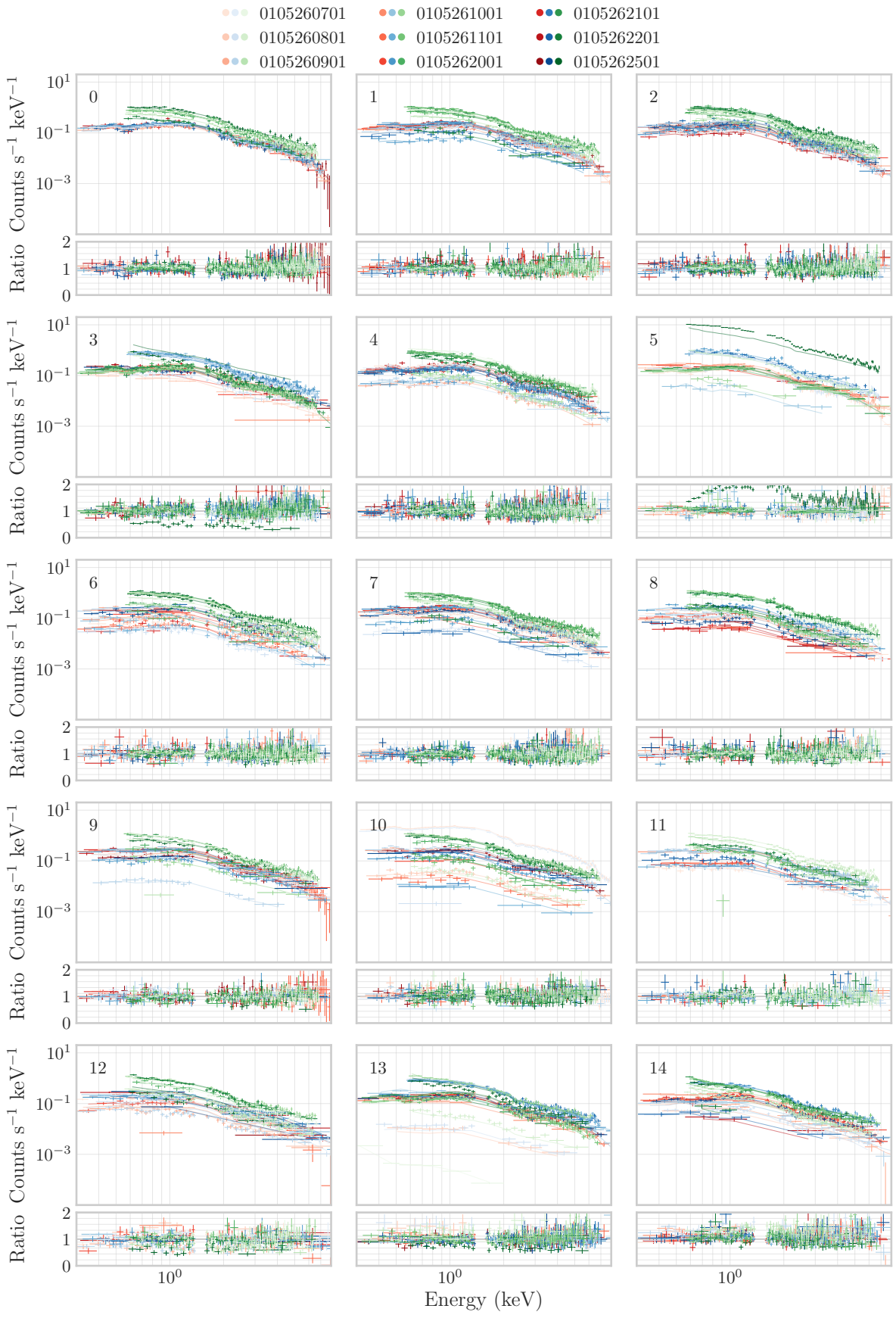

Figure A.2: Spectra of regions 0 – 14 of Abell 3266. The panel below each spectrum shows the data divided by the folded model. EPIC-MOS 1, EPIC-MOS 2, and EPIC-pn spectra are coloured red, blue, and green, respectively. The reduced χ^2 for the fit is 1.95 for 13 391 degrees of freedom.

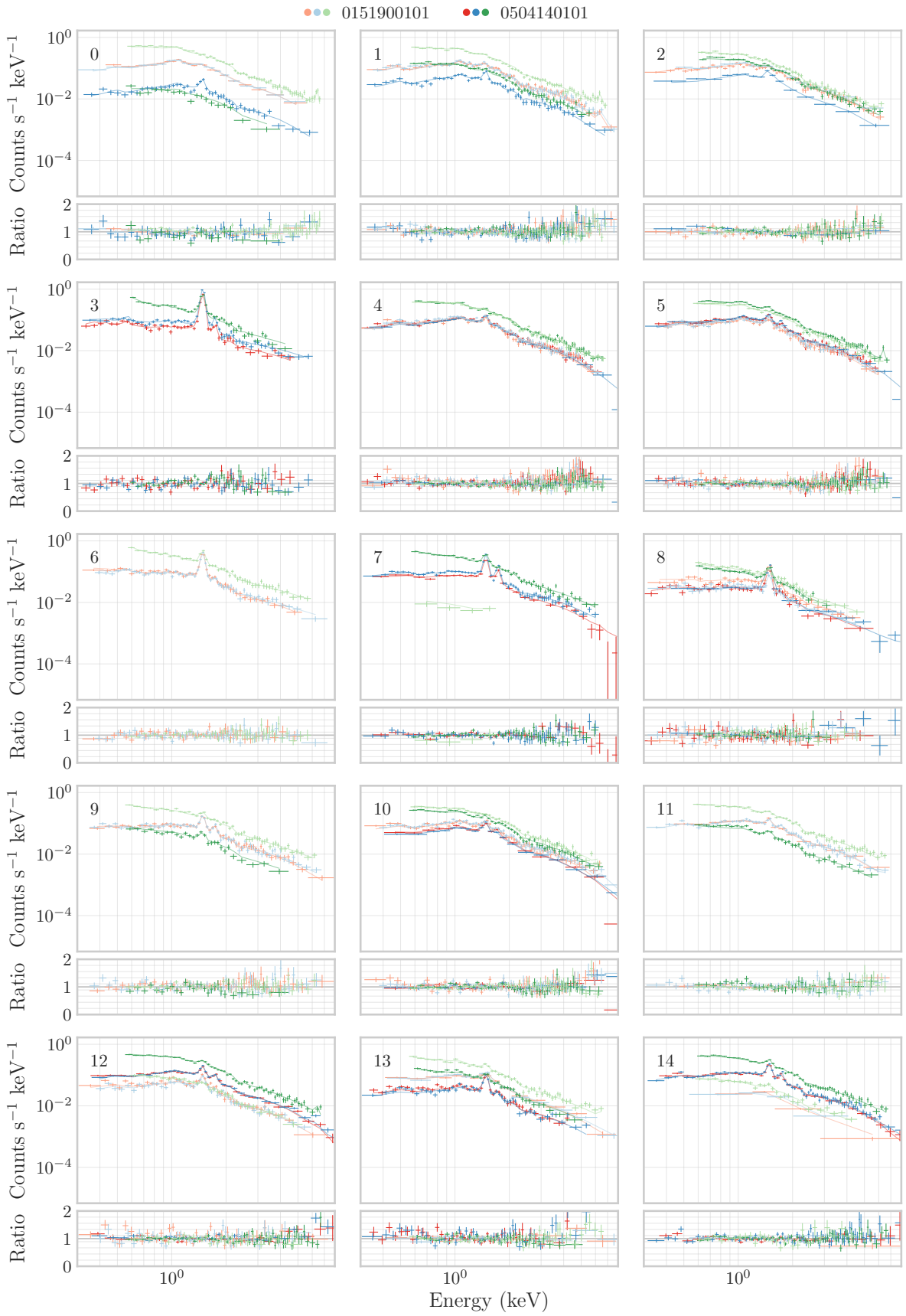

Figure A.3: Spectra of regions 0 – 14 of Abell 3376. The panel below each spectrum shows the data divided by the folded model. EPIC-MOS1, EPIC-MOS2, and EPIC-pn spectra are coloured red, blue, and green, respectively. The reduced χ^2 for the fit is 1.12 for 3313 degrees of freedom.

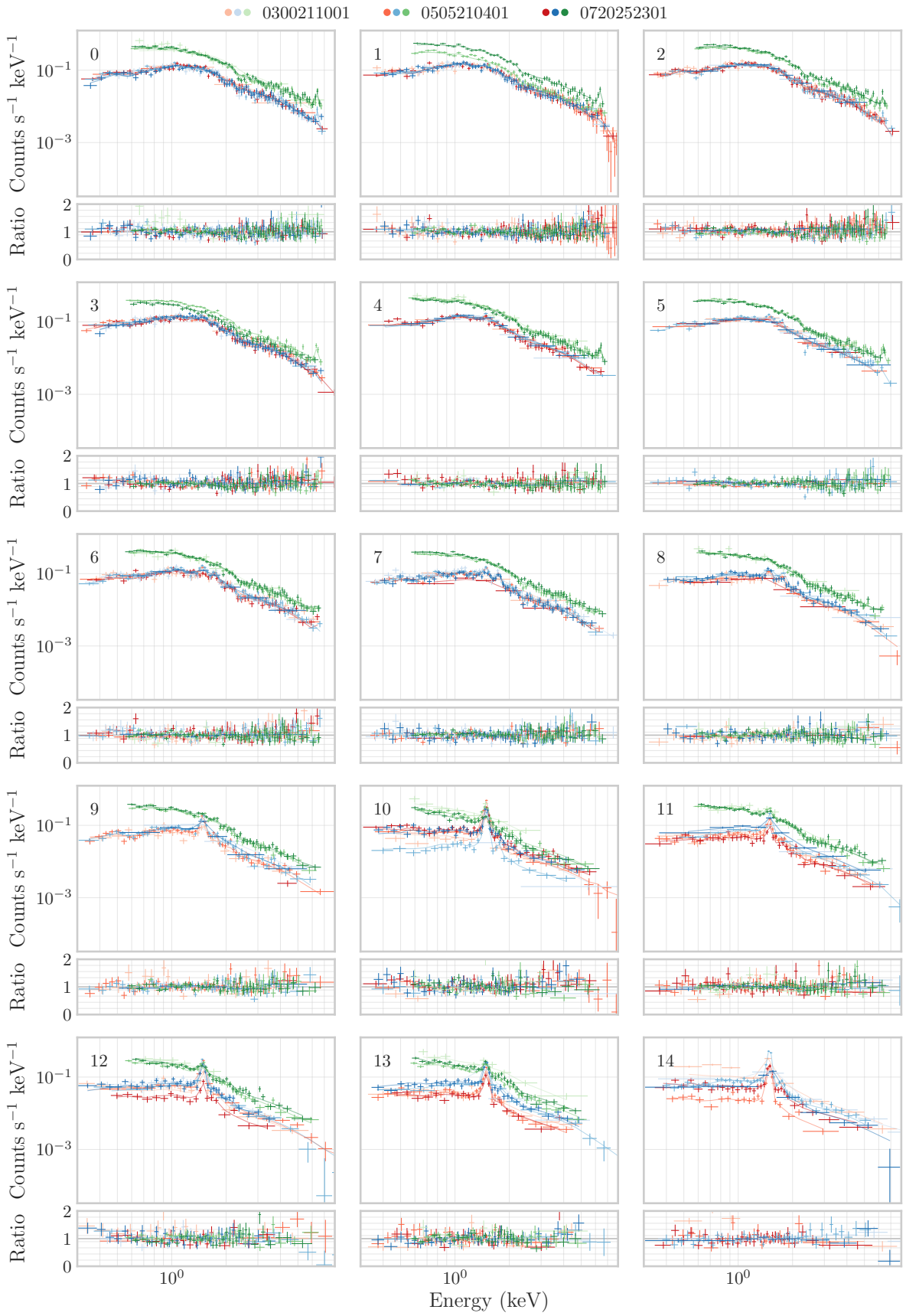

Figure A.4: Spectra of regions 0 – 14 of Abell 3391. The panel below each spectrum shows the data divided by the folded model. EPIC-MOS 1, EPIC-MOS 2, and EPIC-pn spectra are coloured red, blue, and green, respectively. The reduced χ^2 for the fit is 1.08 for 4274 degrees of freedom.

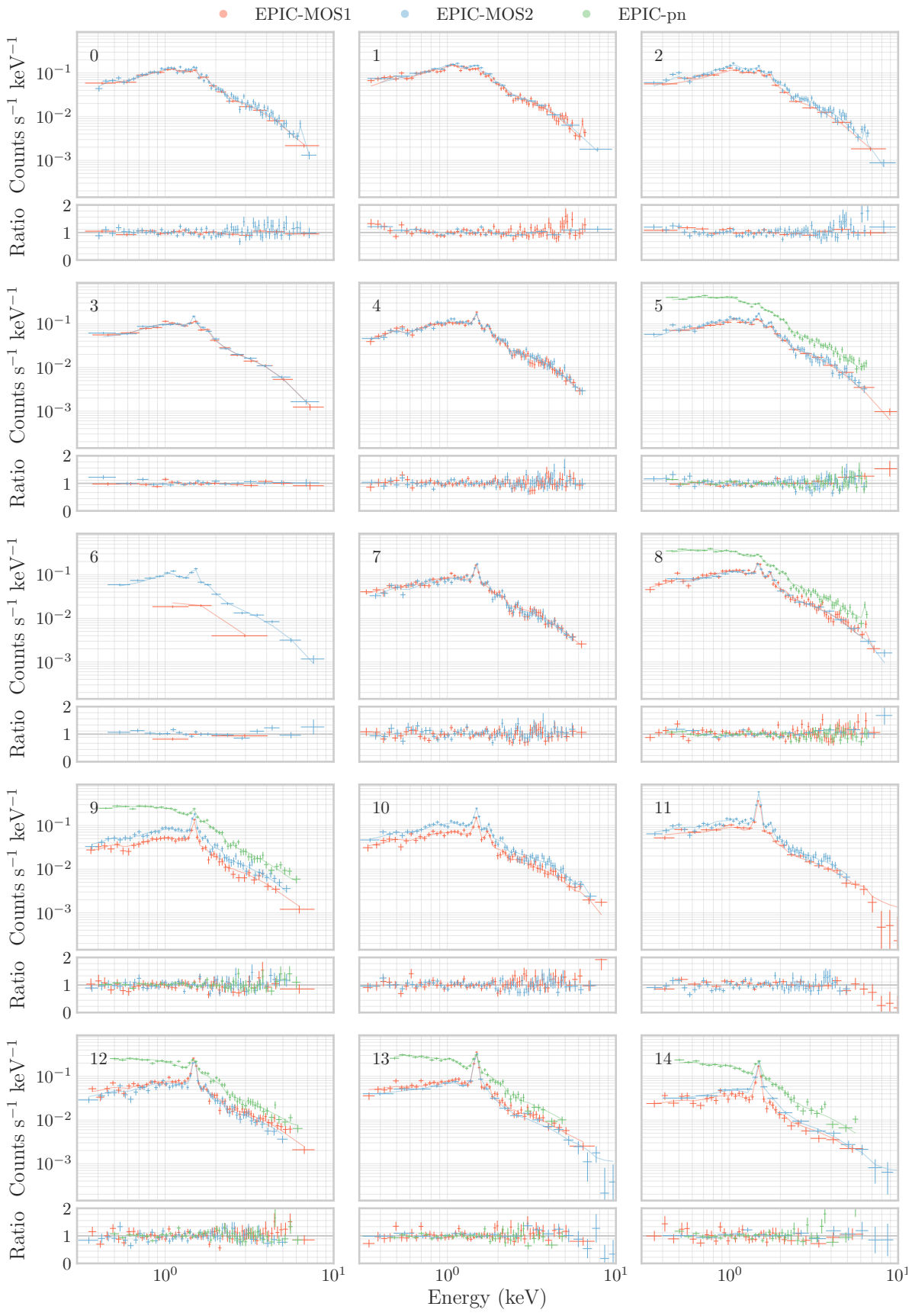

Figure A.5: Spectra of regions 0 – 14 of Abell 3395. The panel below each spectrum shows the data divided by the folded model. EPIC-MOS 1, EPIC-MOS 2, and EPIC-pn spectra are coloured red, blue, and green, respectively. The reduced χ^2 for the fit is 1.16 for 1689 degrees of freedom.